



M Ű E G Y E T E M 1 7 8 2

## PhD THESIS

# Geometric view of energy degeneracies of parameter-dependent quantum systems

György Frank

Supervisor: András Pályi  
Associate professor  
BME Department of Theoretical Physics

**Budapest University of Technology and Economics**

**2025.**

*“Never do a calculation until you know the answer.”*  
— John Archibald Wheeler

# Contents

<b>1</b>	<b>Introduction</b>	<b>5</b>
<b>2</b>	<b>Characterisation of the ground state degeneracies in the spin-orbit coupled two-spin system</b>	<b>11</b>
2.1	Total topological charge of spin systems . . . . .	11
2.2	Hamiltonian of the spin-orbit coupled two-spin system . . . . .	14
2.3	Location of ground state degeneracies . . . . .	16
2.4	Classification of degeneracy patterns . . . . .	20
2.5	Stability analysis of eigenpatterns and corresponding geometrical patterns . . . . .	24
2.6	Topological charge distribution . . . . .	27
2.7	Topological charge density of non-point-like degeneracies . . . . .	30
2.8	Conclusion . . . . .	37
2.9	Discussion . . . . .	38
<b>3</b>	<b>The geometry of the Hermitian matrix space and the Schrieffer–Wolff transformation</b>	<b>39</b>
3.1	The space of the Hermitian matrices . . . . .	40
3.2	Degeneracy of the eigenvalues . . . . .	42
3.3	The Schrieffer–Wolff transformation induces a local chart . . . . .	44
3.4	Energy splitting and the distance from $\Sigma_2$ . . . . .	47
3.5	Parameter-dependent quantum systems and Weyl points . . . . .	47
3.6	Examples . . . . .	50
3.7	Conclusions . . . . .	53
<b>4</b>	<b>Birth Quota of Non-Generic Degeneracy Points</b>	<b>55</b>
4.1	Bilayer graphene . . . . .	56
4.2	Minimal 1D model . . . . .	58
4.3	Effective Hamiltonian at a two-fold degeneracy point . . . . .	60
4.4	Birth quota . . . . .	60
4.5	Methods to calculate the birth quota . . . . .	62
4.6	Applications . . . . .	62
4.7	Conclusions . . . . .	63
4.8	Discussion . . . . .	64
	<b>Thesis statements</b>	<b>65</b>
	<b>Bibliography</b>	<b>67</b>

<b>Appendix</b>	<b>77</b>
A Spin-orbit coupled two-spin system . . . . .	77
B Schrieffer–Wolff transformation . . . . .	90
C Birth Quota of Non-Generic Degeneracy Points . . . . .	100

# Chapter 1

## Introduction

Electronic band structures are fundamental to understanding the behavior of electrons in solid materials. They describe the allowed energy levels for electrons as a function of their momentum within a crystalline lattice. This energy-momentum relationship influences a material's electrical, thermal, and optical properties, shaping its behavior as a metal, insulator, semiconductor, or a semimetal.

In particular, the study of electronic band structures is crucial for designing and discovering new materials with specific functionalities. For example, metals exhibit partially filled conduction band, allowing electrons to flow freely and conduct electricity and heat efficiently. Insulators, on the other hand, have large band gap between the valence band and the conduction band, preventing electron flow at low energies. Meanwhile, semiconductors have small band gap allowing electrons to be thermally excited leading to a low conductivity with strong dependence on the temperature.

Semimetals display properties that are intermediate between metals and insulators and similar to semiconductors. Unlike insulators and semiconductors, semimetals have no band gap, but unlike metals, semimetals have low carrier density. Therefore, they have a moderate conductivity with strong dependence on the temperature similarly to semiconductors.

Weyl semimetals [1, 2, 3, 4] are a unique type of semimetals characterized by the presence of Weyl points in their electronic band structure, where the valence and conduction bands cross. Each Weyl point carries a topological charge, or chirality, which can be positive or negative [5, 6, 7]. This topological character makes Weyl points robust against perturbations, meaning they cannot be removed or gapped out unless two Weyl points of opposite chirality annihilate each other [1, 8, 9]. These Weyl points lead to a variety of exotic phenomena such as anomalous Hall effect [10], chiral anomaly [11], negative magnetoresistance [12] and photogalvanic effect [13].

One of the most distinctive features of Weyl semimetals is the presence of Fermi arcs [1, 2, 14]. These are open-ended, continuous curves of electronic states on the surface of the material, connecting the projections of Weyl points with opposite chiralities. Fermi arcs are a direct consequence of the nontrivial topology of the bulk Weyl points and are a signature feature of Weyl semimetals.

Beyond the specific context of Weyl semimetals, Weyl points exhibit a universality that goes beyond the semimetal framework, emerging as accidental degeneracies in various parameter-dependent quantum systems. Accidental degeneracies [15, 16] occur in quantum systems when energy levels coincide due to specific values of external parameters, rather than as a consequence of inherent symmetries. These degeneracies are "accidental" in the sense that they occur only for particular settings of parameters such as magnetic and electric fields, potentials, interaction strengths, geometric parameters or other control variables.

One could argue naively that a degeneracy of a quantum system requires fine-tuning of only

one parameter, that is, the energy difference between two levels which is zero at the degeneracy. Indeed, it is the case when the two levels are "independent", for example, when the Hamiltonian describing the system has a block diagonal structure. In this case the two eigenvalues corresponding to two different blocks can coincide with the fine-tuning of only one parameter. This is the case when there is an underlying symmetry and the two blocks are corresponding to two different eigenvalues of the symmetry operator. But without symmetry or even with the symmetry within one block of the Hamiltonian, the levels are generally repelling each other giving rise to an avoided crossing (also known as anticrossing) when the system is tuned with one parameter: the two levels first approach each other and before they could meet, their distance (splitting) starts to grow again. Similarly, if the parameter space is two-dimensional, then the energy surfaces still avoid each other. Three dimensions is the first where we expect energy degeneracies and they generally appear as points which are robust against the change of further parameters.

In this thesis we give an insightful geometrical view of the appearance of Weyl points in parameter-dependent quantum systems. Neumann and Wigner [17] showed that in the  $n^2$ -dimensional space of  $n \times n$  Hermitian matrices the two-fold degenerate matrices form  $n^2 - 3$  dimensional manifolds. The Hamiltonian of a parameter-dependent quantum system maps the parameter space into the space of Hermitian matrices. If this mapping itself is non-singular, then its image appears as a manifold, too. The degeneracies of a parameter-dependent quantum system correspond to the intersections of the image of the Hamiltonian with the degeneracy manifolds (see Fig. 1.1).

If the sum of the dimension of the two manifolds equals the dimension of the ambient space the generic intersections are point-like. Moreover, the tangent space of the two manifolds at the intersection points span the tangent space of the ambient space. This type of intersection is called a transverse intersection. Transverse intersections are stable, meaning that small perturbations of the manifolds can not make the transverse intersection disappear.

For Weyl semimetals, the parameter space consists of the Cartesian components of the three-dimensional quasimomentum vector satisfying the dimension condition discussed above, and the Hamiltonian is assumed to be non-singular, which is not a strong condition. Consequently, the image of the Hamiltonian forms a 3-dimensional manifold in the space of Hermitian matrices. The two-fold degeneracy stratum, on the other hand, has dimension  $n^2 - 3$ . Since  $3 + (n^2 - 3) = n^2$ , i.e., the dimensions add up to that of the full Hermitian space, the intersection of the Hamiltonian image with the degeneracy stratum is generically transverse and consists of discrete points, stable against perturbations. The Weyl points are the preimages of these transverse intersection points under the Hamiltonian mapping, located in the quasimomentum parameter space (Brillouin zone).

The distinction between the quasimomentum and the other parameters of the crystal, e.g., external magnetic field, is based on the different role of these parameters. The quasimomentum is not an experimentally tunable parameter but rather a canonical momentum describing the motion of electrons. Their dynamics depends on the crystal's dispersion relation and the external forces. In contrast, other parameters can be tuned experimentally to explore and manipulate the crystal's behavior. However, based on solely the energy spectrum there is no qualitative difference between the parameters. For example, an artificial parameter space consists of the quasi momentum component  $k_x$ , the electric field component  $E_y$  and the magnetic field component  $B_z$  would also host Weyl points with robustness against the perturbation of the remaining components, although, this parameter space might not be justified by any relevant physics, and such parameter space lacks phenomena associated with Weyl semimetals such as the presence of Fermi arcs, etc.

A completely different type of parameter-dependent quantum system is the interacting spin system [18, 19, 20, 21]. The Hamiltonian of a spin system is quite specific, as the interaction term usually does not depend on the external magnetic field, while the Zeeman term has a

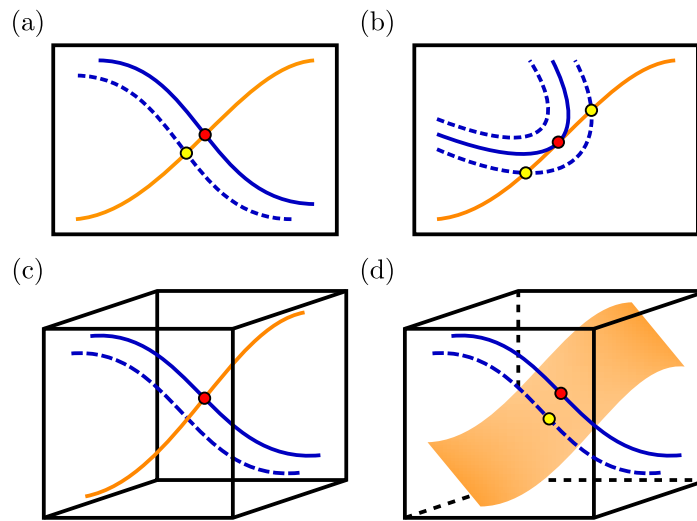


Figure 1.1: **Transverse and non-transverse intersections of manifolds.** (a) In two dimensions, curves generally intersect transversely at a point (red point). This intersection is stable under perturbation (dashed curve), meaning the intersection point cannot disappear, only shift (yellow point). (b) If two curves are tangent at the point of contact, the intersection is unstable. It can either disappear or split into multiple intersections upon perturbation. This is referred to as a non-transverse intersection. (c) In three dimensions, curves generally avoid each other. If two curves make contact, the intersection is unstable, even if the curves are not tangent, and it disappears upon perturbation. (d) A stable point-like intersection in three dimensions is realized by the intersection of a line and a surface. The sum of their dimensions  $1+2=3$  matches the dimension of the space they are in. Similarly, in a quantum system with a 3-dimensional parameter space, the Hamiltonian maps the parameter space into the  $n^2$ -dimensional space of  $n \times n$  Hermitian matrices, where two-fold degenerate matrices form an  $(n^2 - 3)$ -dimensional manifold. The dimensional equality  $3 + (n^2 - 3) = n^2$  ensures that the intersections are isolated, stable Weyl points.

linear dependence on it. Using the Cartesian components of the external magnetic field as the parameter space makes the Hamiltonian of the interacting spin system a linear map from the three-dimensional Euclidean space to the space of Hermitian matrices. Degeneracy points are often referred to as *diabolical points* in the literature [19, 20], a name that comes from the double-conical shape of the dispersion relation. This terminology is common not only in spin systems but also, for example, in molecular physics [22]. Both Weyl points in momentum space of crystals and diabolical points in magnetic (and other) systems correspond to the transverse intersection between the image of the Hamiltonian mapping and the degeneracy manifold, and in this respect, they can be considered equivalent. We refer to these degeneracies as Weyl points, regardless of the physical system [1, 16, 19, 21, 23, 24, 25] from this point onwards.

A different type of degeneracy point arises from the collision of two Weyl points with opposite topological charge [8, 9]. This degeneracy point has zero topological charge and is unstable under perturbation. The dispersion around such a point is quadratic in the direction where the two Weyl points merged. The geometric interpretation of this degeneracy point involves a non-transverse intersection, where the two manifolds are tangent at the contact point (Fig. 1.1b). The contact between manifolds can be quite complex, and their classification is possible through contact equivalence. Progressively more complex contacts give rise to increasingly complex degeneracies, which can be obtained by merging more and more Weyl points [4, 26]. This requires more finetuning, meaning that these degeneracies become increasingly unstable against perturbations.

If the sum of the dimensions of the manifolds is less than that of the ambient space, then generically the manifolds do not intersect at all. Non-transverse intersections arise when the manifolds still intersect (Fig. 1.1c). These intersections are unstable and disappear upon perturbation. A simple example of this is when a Weyl point appears in a two-dimensional parameter space. Perturbing it with a third parameter causes the Weyl point to disappear. This is the case with graphene neglecting the spin-orbit interaction. There are two-dimensional Weyl points present in the  $K$  and  $K'$  points of the Brillouin zone, but introducing the spin-orbit interaction splits these degeneracies [27]. This can be viewed in the full three-dimensional parameter space which consists of the original parameters (quasimomentum) and the perturbation (spin-orbit interaction), where the Weyl point remains stable. By isolating the perturbation parameter, we obtain two-dimensional cross-sections of the total parameter space, and varying the perturbation corresponds to moving through these cross-sections. Passing through a Weyl point in these cross-sections appears as a point degeneracy that momentarily appears and then immediately disappears.

A similar example is when a three-fold degeneracy appears in a three-dimensional parameter space. Three-fold degeneracies require the fine-tuning of 8 parameters [17], but symmetries can stabilize them [28, 29]. Breaking the symmetries splits the three-fold degeneracy into Weyl points. This example is more complex because a three-fold degeneracy can split in two different ways into two-fold degeneracies: either the upper two eigenvalues remain degenerate or the lower two remain degenerate. Furthermore, even after a small perturbation, the three near-degenerate energy levels remain close and the problem cannot be globally reduced to an effective two-level system.

If the sum of the dimensions of the manifolds exceeds that of the ambient space, then a transverse intersection is not point-like: the intersection itself is a manifold of dimension equal to the excess, and it is stable under perturbations. For example, in four-dimensional parameter spaces this intersection is generically one-dimensional, corresponding to nodal lines rather than isolated Weyl points. Equivalently, one may think of slicing the four-dimensional parameter space into three-dimensional sections, in which case the nodal line appears as a continuous family of Weyl points, reminiscent of a 3 space + 1 time description of spacetime. However, nodal lines (or even nodal surfaces) can also be stabilized by symmetries in a three-dimensional parameter space [30, 31]. This represents a non-transverse intersection, which is inherently unstable. Breaking the

symmetries causes the nodal line to break apart into Weyl points or no degeneracy [32, 33, 34].

Our approach can also be generalized to non-Hermitian systems [35], where the Hamiltonian is an arbitrary complex matrix. The intersection of the image of the Hamiltonian map with the manifold of two-fold degenerate, non-diagonalizable matrices in the space of complex matrices results in the so-called exceptional points [36, 37].

In this thesis, we present the first steps toward classifying energy degeneracies in parameter-dependent quantum systems. Our focus is solely on two-fold degeneracies, particularly, the point-like ones. In Chapter 2, we introduce the spin-orbit coupled two-spin system [21, 23], in which we provide a comprehensive characterization of the two-fold ground state degeneracy configurations achievable by elementary methods. We highlight several properties of the degeneracies, such as dimension, topological charge, and dispersion, which help differentiate them in a classification scheme. We determine the stable configurations and the generic transitions between them, and we also examine the topological charge distribution in non-point-like degeneracies.

In Chapter 3, we explore the geometrical perspective behind degeneracies [38, 39, 40]. We demonstrate that a natural parametrization near a degeneracy is provided by the Schrieffer-Wolff transformation [41, 42, 43, 44, 45], where the distance from a degeneracy stratum is proportional to the standard deviation of the eigenvalues — in the case of two-fold degeneracies, this corresponds to the gap between the two eigenvalues. We also show that Weyl points correspond to transverse intersections between manifolds and introduce the concept of the order of distance from the degeneracy stratum for parameter-dependent quantum systems.

In Chapter 4, we use the  $2 \times 2$  effective Hamiltonian to describe two-fold degeneracies. We show that multiplicity is a new topological index, serving as an upper bound on the number of newborn Weyl points that emerge upon perturbation [46].



## Chapter 2

# Characterisation of the ground state degeneracies in the spin-orbit coupled two-spin system

Nuclear and electron spins are ubiquitous constituents in condensed matter physics. Already a few interacting quantum spins exhibit a rich variety of phenomena in rather different settings such as molecular magnets [18, 19, 20], magnetic adatoms [47, 48], or spin-based quantum bits [49, 50], to name a few. When studied in the three-dimensional parameter space defined by an external magnetic field, all these quantum magnets possess an intrinsic geometrical and topological structure, characterized by concepts [5, 51] such as the Berry phase, the Berry curvature, and the Chern number. In many cases, topological considerations entail robust phenomena, governed by some global properties, insensitive to microscopic details.

### 2.1 Total topological charge of spin systems

In this thesis, we address another robust phenomenon rooted in topology, which appears in interacting spin systems subject to a magnetic field, the emergence of ground state degeneracies at certain magnetic fields. In this case, a topological invariant (an appropriately defined global Chern number, here referred to as the total topological charge) predicts the existence and global properties of ground-state degeneracy points [5, 19, 20, 21, 52, 53].

#### 2.1.1 Berry curvature and Chern number

Before introducing the specific setup and its energy degeneracies we will consider in this work, we briefly review the related geometric and topological concepts [5, 6, 7]. The Hamiltonian of a spin system  $H(\mathbf{B})$  depends on the external magnetic field vector  $\mathbf{B}$ , defining a three-dimensional parameter space. We study such a system from the viewpoint of the ground-state manifold  $|\Psi_0(\mathbf{B})\rangle$ . The topological quantities we describe here are related to the Berry phase  $\gamma_0(\mathcal{C})$ , the geometric phase which is acquired by the ground state when we adiabatically deform the Hamiltonian in a closed path  $\mathcal{C}$  of the parameter space:

$$\gamma_0(\mathcal{C}) = \oint_{\mathcal{C}} \mathcal{A}_0 \cdot d\mathbf{B} = \iint_S \mathcal{B}_0 \cdot d\mathbf{S}. \quad (2.1)$$

Here,  $\mathcal{A}_0(\mathbf{B}) = i \langle \Psi_0(\mathbf{B}) | \nabla_{\mathbf{B}} | \Psi_0(\mathbf{B}) \rangle$  is the Berry connection. The second equality in Eq. (2.1), featuring the Berry curvature  $\mathcal{B}_0(\mathbf{B}) = \nabla_{\mathbf{B}} \times \mathcal{A}_0(\mathbf{B})$ , holds whenever Stokes' theorem can be applied to the open surface  $S$  whose boundary is the path  $\mathcal{C}$ . The relation between the Berry

connection and the Berry curvature is similar to that of the magnetic vector potential and the magnetic field. Note that the Berry curvature can be measured experimentally [53].

The integral of the Berry curvature for a surface of the parameter space is analogous to the magnetic flux through a surface in real space. However, for closed surfaces, the Berry flux can be non-zero, in contrast to the magnetic flux. The Berry flux through a closed surface  $S$  in the parameter space is the Chern number associated to that surface (up to a  $2\pi$  factor):

$$Q_0(S) = \frac{1}{2\pi} \oint_S \mathcal{B}_0 \cdot d\mathbf{S}, \quad (2.2)$$

and this is an integer. The sources of this non-zero flux are the ground state degeneracies, the points in the parameter space where the Berry curvature diverge. Hence a topological charge is attributed to each isolated degeneracy point, whose value is the Chern number of a closed surface that encloses that degeneracy point but no other degeneracy points. The total topological charge of such a system is the Chern number of a closed surface that encloses all degeneracy points; this is equal to the sum of the topological charges of the degeneracy points.

### 2.1.2 Spin systems

A particular class of Hamiltonians for a spin system is given by

$$H(\mathbf{B}) = H_Z(\mathbf{B}) + H_{\text{int}} = \mu_B \mathbf{B} \cdot \sum_i \hat{\mathbf{g}}_i \mathbf{S}_i + \sum_{\langle i,j \rangle} \mathbf{S}_i \cdot (\hat{\mathbf{J}}_{ij} \mathbf{S}_j), \quad (2.3)$$

where the first term, called the Zeeman term, describes the interaction of the spins with the external magnetic field, and the second term corresponds to the interaction between the spins. In the Hamiltonian,  $\mathbf{S}_i = (S_{i,x}, S_{i,y}, S_{i,z})^T$  is a vector whose components are the spin operators acting on the  $i$ -th spin.

In the Zeeman term,  $\mu_B$  is the Bohr magneton, and  $\hat{\mathbf{g}}_i$  is the  $g$ -tensor of the  $i$ -th spin. The  $g$ -tensor is a  $3 \times 3$  real-valued matrix, which makes the Zeeman term anisotropic. The  $g$ -tensor depends on the choice of gauge and is not necessarily symmetric. However, with an appropriate gauge choice, it can be made symmetric.

The quantity  $\hat{\mathbf{J}}_{ij}$  in the interaction term is called the exchange matrix between the  $i$ -th and  $j$ -th spins. The exchange matrix is also a real-valued  $3 \times 3$  matrix that depends on the gauge choice. In special cases, such as when the spins form a 1D chain, all of the exchange matrices can be diagonalized simultaneously with an appropriate gauge choice. However, in general, this is not possible. Additionally, if the gauge is fixed to make the  $g$ -tensor symmetric, the exchange matrix is also fixed.

The exchange matrix is often decomposed into three parts: its trace (the isotropic exchange interaction), its traceless symmetric part (the dipole-dipole interaction), and its antisymmetric part (the Dzyaloshinsky–Moriya interaction).

To calculate the total topological charge of Eq. (2.3) in the magnetic parameter space we have to choose a surface which encloses all degeneracies and calculate its Chern number. For this we can choose a sphere around the origin with a finite radius  $B$  and rescaling it to infinity to contain all degeneracies:

$$Q_{0,\text{tot}} = \lim_{\lambda \rightarrow \infty} Q_0(\lambda B). \quad (2.4)$$

Using the special linear form of Eq. (2.3)

$$H(\lambda \mathbf{B}) = \lambda H_Z(\mathbf{B}) + H_{\text{int}} = \lambda \left( H_Z(\mathbf{B}) + \frac{1}{\lambda} H_{\text{int}} \right), \quad (2.5)$$

where the scaling by  $\lambda$  does not affect the eigenstates. Therefore, scaling the sphere in the magnetic parameter space by  $\lambda$  results the same integral for the ground state Chern number as scaling the interaction term by  $1/\lambda$  for a fixed sphere.

In the  $\lambda \rightarrow \infty$  limit, the Hamiltonian is interactionless, therefore, each spin aligns according to its individual Zeeman term independently, and the ground state has a tensor product form. The Chern number is additive for tensorial multiplication, therefore, each spin contributes to the Chern number by its single spin Zeeman Hamiltonian

$$H_{Z,i} = \mu_B \mathbf{B} \cdot (\hat{\mathbf{g}}_i \mathbf{S}_i). \quad (2.6)$$

Now, we can use the fact that the Chern number does not change upon perturbing the Hamiltonian as far as there is no gap closing on the surface. Assuming non-singular  $g$ -tensors, the  $i$ -th spin Hamiltonian has only a  $(2s_i + 1)$ -fold degeneracy point in the origin where the half-integer  $s_i$  is the magnitude of the spin. This does not change as we continuously deform the  $g$ -tensor as far as it remains non-singular, therefore, we can change it to the identity matrix up to a sign:

$$\hat{\mathbf{g}}_i \rightarrow (\text{sgn det } \hat{\mathbf{g}}_i) \mathbf{1}_{1 \times 1}, \quad (2.7)$$

where  $\text{sgn}$  is the sign function. The resulting isotropic Zeeman Hamiltonian has the form

$$H_{Z,\text{iso},i} = \pm \mu_B \mathbf{B} \cdot \mathbf{S}_i, \quad (2.8)$$

which has ground state Chern number [19]

$$Q_{0i} = \pm 2s_i. \quad (2.9)$$

Adding together each spin's contribution with the proper sign results the total ground state topological charge of the spin system

$$Q_{0,\text{tot}} = 2 \sum_i (\text{sgn det } \hat{\mathbf{g}}_i) s_i. \quad (2.10)$$

This formula is valid when every  $g$ -tensor is non-singular, i.e.,  $\text{det } \hat{\mathbf{g}}_i \neq 0$ . When one or more  $g$ -tensor is a singular matrix, the ground state degeneracy of the non-interacting system is not point-like and can not be enclosed by a sphere, therefore the Chern number is not defined.

The result Eq. (2.10) is valid for more general Hamiltonians where we only need to assume that in every direction for a large enough magnetic field the linear Zeeman term described in Eq. (2.6) is dominant. Anisotropy terms such as  $S_z^2$  or  $S_x^2 - S_y^2$ , many-spin-interaction terms, or constant offset magnetic fields in the Zeeman term are allowed when this condition is satisfied.

When the total ground-state Chern number is zero, the system either has no ground-state degeneracies or features degeneracies with topological charges that cancel each other. In contrast, a non-zero ground-state Chern number guarantees the presence of ground-state degeneracies. However, while a non-zero total topological charge ensures the existence of energy degeneracies, it does not provide definitive answers to certain specific questions.

- (i) What is the geometrical pattern (isolated points, lines, surfaces, or their combinations) drawn by the degeneracy points in the three-dimensional magnetic parameter space?
- (ii) How is the topological charge carried by the degeneracy points distributed among the points?
- (iii) Are different geometrical patterns and topological charge distributions stable against small perturbations of the system's Hamiltonian?

These are nontrivial questions, and answering them probably requires extensive numerical investigations, in general.

Here, we address questions (i), (ii), and (iii) for a specific, experimentally relevant setup, a spin-orbit-coupled interacting two-spin system [21, 54, 55, 56, 57, 58, 59, 60], and obtain exact results. We provide a full classification of geometrical patterns (and corresponding topological charge density patterns) of the ground-state magnetic degeneracy points of this setup; this ‘zoo’ of patterns is introduced in Tables 2.1 and 2.2. As revealed in Tables 2.1 and 2.2, the degeneracy points can be isolated, as in the electronic dispersion relation of a Weyl semimetal [1, 4], or they can form lines or surfaces, as in nodal-loop [30] or nodal-surface [31] semimetals.

## 2.2 Hamiltonian of the spin-orbit coupled two-spin system

We consider a system of two interacting localized electrons, subject to spin-orbit interaction, and assume that they are placed in a homogeneous magnetic (Zeeman) field (Fig. 2.1a). This system can be described by a  $4 \times 4$  Hamiltonian matrix [21]

$$H = H_Z + H_{\text{int}}, \quad (2.11a)$$

$$H_Z = \mu_B \mathbf{B} \cdot (\hat{\mathbf{g}}_L \mathbf{S}_L + \hat{\mathbf{g}}_R \mathbf{S}_R), \quad (2.11b)$$

$$H_{\text{int}} = J \mathbf{S}_L \cdot \hat{\mathbf{R}} \mathbf{S}_R. \quad (2.11c)$$

Here,  $H_Z$  is the Zeeman interaction with the external homogeneous magnetic field  $\mathbf{B}$ ,  $H_{\text{int}}$  is the spin-orbit-affected exchange interaction between the two electrons,  $\mu_B$  is the Bohr-magneton,  $\hat{\mathbf{g}}_L$  and  $\hat{\mathbf{g}}_R$  are the real-valued, spin-orbit-affected  $g$ -tensors of the two electrons,  $\mathbf{S}_L$  and  $\mathbf{S}_R$  are the spin vector operators represented by  $1/2$  times the spin- $1/2$  Pauli matrices,  $J > 0$  is the strength of the exchange interaction (antiferromagnetic), and  $\hat{\mathbf{R}}$  is a real,  $3 \times 3$  special orthogonal matrix accounting for the spin-orbit interaction in the exchange term.

The exchange interaction term  $H_{\text{int}}$  we use in Eq. (2.11c) was derived from a two-site Hubbard model at zero magnetic field, where spin-orbit interaction appears as a spin-dependent tunneling term [21, 61] between the two sites. The two-electron sector of this Hubbard model is a  $6 \times 6$  matrix, which can be projected to the  $4 \times 4$  exchange Hamiltonian [21, 54] above by eliminating the states with doubly occupied sites via quasidegenerate perturbation theory. It is tempting to associate a spatial direction to the spin-dependent tunneling, e.g., the direction of the rotation axis of  $\hat{\mathbf{R}}$ . Here, we avoid that, because that spatial direction is gauge dependent, that is, it depends on the choice of the Kramers-pair single-particle basis states, as discussed below.

In the Zeeman Hamiltonian of Eq. (2.11b), the  $g$ -tensors are arbitrary real matrices, which are not necessarily symmetric. One way to think about their effect is that the spins feel potentially different effective magnetic fields  $\mathbf{B}_{L/R,\text{eff}} = \hat{\mathbf{g}}_{L/R}^T \mathbf{B}$  instead of the external magnetic field. The matrix transpose is required by the convention used in the Hamiltonian, although, in many cases the  $g$ -tensors are symmetric so the distinction is irrelevant. For concreteness, let us first focus on the case when the determinants of both  $g$ -tensors are positive,  $\det(\hat{\mathbf{g}}_L), \det(\hat{\mathbf{g}}_R) > 0$ . The elements of the three  $3 \times 3$  matrices  $\hat{\mathbf{g}}_L$ ,  $\hat{\mathbf{g}}_R$ , and  $\hat{\mathbf{R}}$  are determined by microscopic details (spin-orbit interaction, confinement potential, choice of basis, etc.), but here we treat them as possibly independent phenomenological parameters.

In our topological considerations, we distinguish the three Cartesian magnetic-field components  $B_x, B_y, B_z$  in the Hamiltonian as ‘primary’ parameters, and refer to further parameters as ‘secondary’ ones. In this nomenclature, secondary parameters are fixed, while primary parameters are thought of as external parameters, varied continuously. At certain points within the space of primary parameters, the ground state of  $H$  becomes degenerate. We refer to these points as *magnetic degeneracy points*.

We have studied this two-spin system in detail in our recent work [21]. There we have shown that in the case  $\det(\hat{\mathbf{g}}_L), \det(\hat{\mathbf{g}}_R) > 0$ , (i) topological considerations guarantee the existence of

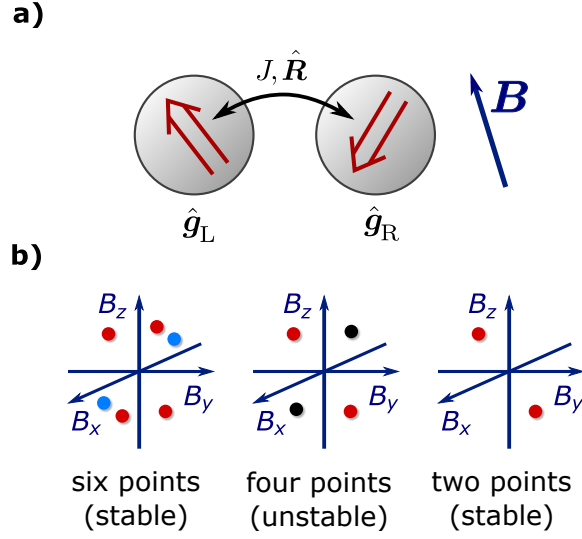


Figure 2.1: **Magnetic degeneracy points of two interacting spin-1/2 electrons.** (a) Exchange interaction between the spins is described by its strength  $J$  and a rotation  $\hat{\mathbf{R}}$ . External magnetic field  $\mathbf{B}$  couples to the spins through the  $g$ -tensors. (b) Geometry and topological charge distribution of magnetic degeneracy points for  $\det \hat{g}_L, \det \hat{g}_R > 0$ . Colors indicate topological charge: +1 (red), -1 (blue), 0 (black). Six-point and two-point patterns are stable, and the generic transition between these patterns is when two oppositely charged pairs meet and their charges annihilate each other (four points).

ground-state magnetic degeneracy points (often, but not always, Weyl points), irrespective of microscopic details of the Hamiltonian, (ii) the degeneracy points carry topological charge, and the total topological charge carried by all degeneracy points of the three-dimensional magnetic-field parameter space sums up to +2. By numerical work and intuitive considerations, we have demonstrated four different geometrical patterns formed by the magnetic degeneracy points, and the corresponding topological charge distributions:

- (A) A sphere, carrying a surface topological charge of +2. This is the case without spin-orbit interaction, when the  $g$ -tensors are isotropic and the exchange interaction is of antiferromagnetic Heisenberg type ( $J\mathbf{S}_L \cdot \mathbf{S}_R$ ). This case also provides an example where the magnetic degeneracy points are not Weyl points.
- (B) Two isolated (Weyl) points, each carrying charge +1.
- (C) Six isolated (Weyl) points, four of them carrying charge +1, two of them carrying charge -1.
- (D) Four isolated points, two of them carrying charge +1, the other two carrying no charge. (See Fig. 2.1b of this work or Fig. 4a of Ref. [21].)

We note that we use the term Weyl point to label an isolated degeneracy point that possesses all of the following properties:

- (1) the energy splitting in its vicinity increases linearly with small deviation in the parameter space, in all directions,
- (2) the degeneracy is two-fold, and

- (3) the absolute value of its topological charge is one (which, by the way, follows from (1) and (2)).

Accordingly, we did not label the charge-neutral degeneracy points in case (D) above as Weyl points, since they violate both (1) and (3). In the condensed-matter literature, band degeneracy points not showing at least one of the above three properties are sometimes called multi-Weyl points [4, 62, 63, 64], but we do not use this terminology here.

Going beyond our earlier numerical study, here we develop an analytical approach, which allows for a complete classification of the geometrical and topological structure of magnetic degeneracy points. For this analysis, it is important to distinguish cases defined by the different possible values of the total topological charge  $\mathcal{Q}_0$ . According to Eq. (2.10), for non-singular  $g$ -tensors this charge is the sum of the  $g$ -tensor determinants' sign, i.e.,

$$\mathcal{Q}_0 = \text{sgn}(\det \hat{g}_L) + \text{sgn}(\det \hat{g}_R), \quad (2.12)$$

and hence  $\mathcal{Q}_0 \in \{-2, 0, 2\}$ .

We will show that the geometrical patterns are the same in case  $\mathcal{Q}_0 = +2$  (Table 2.1) and case  $\mathcal{Q}_0 = -2$ , although the topological charges are the opposite in the two cases. Also, we will show that the geometrical patterns are distinct in the case  $\mathcal{Q}_0 = 0$  (Table 2.2). Rephrasing this in terms of the relative sign

$$\mathcal{S} = \text{sgn}[\det(\hat{g}_L) \cdot \det(\hat{g}_R)], \quad (2.13)$$

we can say that the geometrical patterns are different for different values of  $\mathcal{S}$ .

For  $\mathcal{S} = +1$  we obtain a sevenfold classification of geometrical patterns of magnetic degeneracy points (Table 2.1), corresponding to seven different topological charge distributions (i.e., three more beyond the ones identified in Ref. [21]), and further four possible classes are identified for  $\mathcal{S} = -1$ .

$\mathcal{S} = 0$ , i.e., if one or both  $g$ -tensors are singular, Eq. (2.10) does not work; the total topological charge can be only computed with searching all the ground state degeneracies and adding their individual charges together. The number of possible scenarios is quite large due to the variety of  $g$ -tensor ranks and the alignment of their null spaces. However, most of these cases are not particularly noteworthy. Therefore, we focus on the most common and illustrative case: one  $g$ -tensor being regular and the other is a co-rank-1 (rank-2) matrix. This specific scenario effectively highlights the additional phenomena that can arise compared to regular matrices.

Note that geometrical patterns of magnetic degeneracy points for a different class of Hamiltonians were studied recently in Ref. [65].

Furthermore, we use our approach to characterize the stability of these patterns against small perturbations of the Hamiltonian (see Fig. 2.1b): we find two stable and one almost stable charge configurations both for  $\mathcal{S} = +1$  and for  $\mathcal{S} = -1$ , the almost stable magnetic configuration forming a generic boundary between stable configurations, similar to bifurcations in the theory of dynamical systems [66].

The rest of the chapter is structured as follows. In Sec. 2.3 and 2.4, we give the location of degeneracies and derive a classification of the geometrical patterns and topological charge density patterns of magnetic degeneracy points, with the main results summarized in Tables 2.1 and 2.2. In Sec. 2.5, we analyze the stability of each of these patterns against perturbations of the Hamiltonian. In Sec. 2.6, we derive the topological charge distribution among the discrete degeneracy sets, and in Sec. 2.7 further extend the topological charge distribution to non-point-like degeneracies.

## 2.3 Location of ground state degeneracies

Given the Hamiltonian (2.11), it is not obvious how to analyze the geometrical patterns formed by the magnetic degeneracy points. One could, in principle, find the eigenvalues of the

$4 \times 4$  Hamiltonian (2.11) analytically, and investigate, in a very large dimensional parameter space, the conditions under which ground-state degeneracies occur. Numerical diagonalization and numerical search for the magnetic degeneracy points is also an option, but this requires a lot of computational effort and is most likely incomplete [21].

Fortunately, for the specific Hamiltonian, Eq. (2.11), a fully analytical treatment of the problem is possible. We provide an analytic result for the magnetic field value corresponding to the degeneracies. To find the degeneracies of the system, one has to solve an eigenvector problem for the direction and then solve a one variable equation for their distance from the origin.

### 2.3.1 Simplifying the Hamiltonian with a gauge transformation

As a first step, we introduce a local spin transformation  $U_{L/R}(\hat{\mathbf{O}})$  on the left/right spin. If  $\hat{\mathbf{O}}$  is a rotation around the unit vector  $\mathbf{n}$  with angle  $\alpha$ , then the corresponding unitary transformation [67] is

$$U_{L/R}(\hat{\mathbf{O}}) = \exp(-i\alpha \mathbf{n} \cdot \mathbf{S}_{L/R}). \quad (2.14)$$

This unitary transformation acts on the corresponding spin vector operator as an orthogonal rotation on its elements

$$U_{L/R}(\hat{\mathbf{O}})\mathbf{S}_{L/R}U_{L/R}^{-1}(\hat{\mathbf{O}}) = \hat{\mathbf{O}}\mathbf{S}_{L/R}. \quad (2.15)$$

Therefore, to eliminate the rotation  $\hat{\mathbf{R}}$  appearing in the exchange term, we have to rotate the right spin with the unitary transformation  $U_1 = U_R^{-1}(\hat{\mathbf{R}})$ :

$$\begin{aligned} H'(\mathbf{B}) &= U_1 H(\mathbf{B}) U_1^{-1} = \mu_B \mathbf{B} \cdot (\hat{\mathbf{g}}_L \mathbf{S}_L + \hat{\mathbf{g}}_R \hat{\mathbf{R}}^{-1} \mathbf{S}_R) + J \mathbf{S}_L \cdot \mathbf{S}_R \\ &= \mu_B (\mathbf{B}_L \cdot \mathbf{S}_L + \mathbf{B}_R \cdot \mathbf{S}_R) + J \mathbf{S}_L \cdot \mathbf{S}_R, \end{aligned} \quad (2.16)$$

where we introduce the effective magnetic fields  $\mathbf{B}_L = \hat{\mathbf{g}}_L^T \mathbf{B}$  and  $\mathbf{B}_R = \hat{\mathbf{R}} \hat{\mathbf{g}}_R^T \mathbf{B}$ . A further global rotation of both spins  $U_2 = U_L(\hat{\mathbf{O}})U_R(\hat{\mathbf{O}})$  keeps the interaction term simple because of the identity  $(\hat{\mathbf{O}}\mathbf{S}_L) \cdot (\hat{\mathbf{O}}\mathbf{S}_R) = \mathbf{S}_L \cdot \mathbf{S}_R$ . As a consequence, the effective magnetic fields rotate together, with the orthogonal matrix  $\hat{\mathbf{O}}^{-1}$ . By a proper choice we can rotate one of the effective magnetic fields (e.g. the left) to the  $z$  direction to get a simpler Hamiltonian

$$\begin{aligned} H''(\mathbf{B}) &= U_2 H'(\mathbf{B}) U_2^{-1} \\ &= \frac{1}{2} \begin{pmatrix} \mu_B (B_L + B_{R\parallel}) + J/2 & \mu_B B_{R\perp}^* & 0 & 0 \\ \mu_B B_{R\perp} & \mu_B (B_L - B_{R\parallel}) - J/2 & J & 0 \\ 0 & J & -\mu_B (B_L - B_{R\parallel}) - J/2 & \mu_B B_{R\perp}^* \\ 0 & 0 & \mu_B B_{R\perp} & -\mu_B (B_L + B_{R\parallel}) + J/2 \end{pmatrix}, \end{aligned} \quad (2.17)$$

where  $B_L = |\mathbf{B}_L|$  and  $B_{R\parallel} = (\hat{\mathbf{O}}^{-1} \mathbf{B}_R)_z = \mathbf{B}_R \cdot \mathbf{B}_L / B_L$  and  $B_{R\perp} = (\hat{\mathbf{O}}^{-1} \mathbf{B}_R)_x + i (\hat{\mathbf{O}}^{-1} \mathbf{B}_R)_y$  which latter depends on the choice of the rotation  $\hat{\mathbf{O}}$  (its complex argument can be chosen arbitrarily).

### 2.3.2 Direction of ground state degeneracies

To find the degeneracies of the matrix  $H''(\mathbf{B})$  defined in Eq. (2.17), we rephrase the degeneracy of a matrix by the rank of a related matrix. If  $\lambda$  is an eigenvalue of the  $4 \times 4$  matrix  $H$ , then, the matrix  $H - \lambda$  is singular. Its rank is less than the maximal 4, therefore, the determinant of  $H - \lambda$  is zero. Similarly, if  $\lambda$  is a degenerate eigenvalue of the  $4 \times 4$  matrix  $H$ , then, the matrix

$H - \lambda$  is ‘more’ singular. Its rank is at least 2 less than the maximal, therefore, every  $3 \times 3$  minor is zero. Erasing the first row and the last column yields a determinant

$$\begin{aligned} m_{14} &= \frac{1}{8} \begin{vmatrix} \mu_B B_{R\perp} & \mu_B (B_L - B_{R\parallel}) - J/2 - \lambda & J \\ 0 & J & -\mu_B (B_L - B_{R\parallel}) - J/2 - \lambda \\ 0 & 0 & \mu_B B_{R\perp} \end{vmatrix} \\ &= \frac{J}{8} (\mu_B B_{R\perp})^2, \end{aligned} \quad (2.18)$$

which can be zero only if (i) the interaction strength  $J$  is zero or (ii) the perpendicular component of the right effective magnetic field is zero. We are interested in the interacting case. Condition (ii) states that the two effective magnetic field can be simultaneously rotated to the  $z$  axis, which means that the effective magnetic fields have to be parallel

$$\mathbf{B}_L \parallel \mathbf{B}_R \quad (2.19)$$

$$\hat{\mathbf{g}}_L^T \mathbf{B} \parallel \hat{\mathbf{R}} \hat{\mathbf{g}}_R^T \mathbf{B}. \quad (2.20)$$

Acting with the inverse of  $\hat{\mathbf{R}} \hat{\mathbf{g}}_R^T$  leads us to the eigenvector condition

$$\hat{\mathbf{g}}_R^{-1T} \hat{\mathbf{R}}^{-1} \hat{\mathbf{g}}_L^T \mathbf{B} \parallel \mathbf{B}, \quad (2.21)$$

$$\left( \hat{\mathbf{g}}_L \hat{\mathbf{R}} \hat{\mathbf{g}}_R^{-1} \right)^T \mathbf{B} \parallel \mathbf{B}. \quad (2.22)$$

Introducing the  $3 \times 3$  matrix

$$\hat{\mathbf{M}} = \hat{\mathbf{g}}_L \hat{\mathbf{R}} \hat{\mathbf{g}}_R^{-1}, \quad (2.23)$$

the possible ground state degeneracies of the two-spin system is in the direction of the left eigenvectors of the matrix  $\hat{\mathbf{M}}$  (right eigenvector of the matrix  $\hat{\mathbf{M}}^T$ ). Note that  $\hat{\mathbf{M}}$  is real, but in general it is not symmetric. Hence, in conclusion, we have mapped the problem of finding the direction of magnetic degeneracy points to the eigenproblem of a  $3 \times 3$  non-symmetric real matrix.

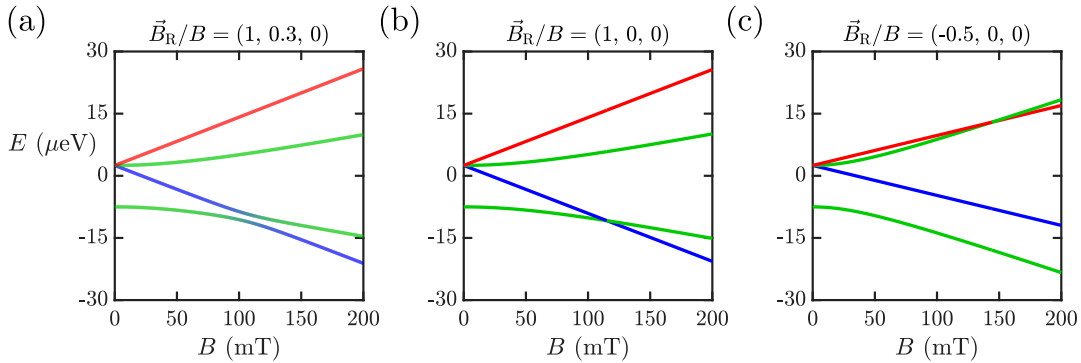


Figure 2.2: **Magnetic degeneracy points for two interacting spin-1/2 electrons.**  $J = 10 \mu\text{eV}$  and  $\mathbf{B}_L/B = (3, 0, 0)$  (a) Non-parallel effective magnetic fields do not have a level crossing at finite magnetic fields. (b) Parallel effective magnetic fields pointing in the same direction yield a ground state degeneracy point. (c) Antiparallel effective magnetic fields yield an excited state degeneracy point.

### 2.3.3 Distance of ground state degeneracies from the origin

First, we consider the case when the magnetic field vector  $\mathbf{B} = B\mathbf{v}_a$  is a left eigenvector of  $\hat{M}$  with a positive eigenvalue  $a$ , and we assume that  $\mathbf{v}_a$  is normalized. Then, the effective magnetic field vectors are parallel and point to the same direction. The transformed Hamiltonian  $H''(\mathbf{B})$  in Eq. (2.17) takes the simple form

$$H''(B\mathbf{v}_a) = \frac{1}{2} \begin{pmatrix} \mu_B g_+ B & 0 & 0 & 0 \\ 0 & \mu_B g_- B - J & J & 0 \\ 0 & J & -\mu_B g_B B - J & 0 \\ 0 & 0 & 0 & -\mu_B g_+ B \end{pmatrix} + \frac{J}{4}, \quad (2.24)$$

where

$$g_{\pm} = g_{L\mathbf{v}_a} \pm g_{R\mathbf{v}_a} \quad (2.25)$$

with the scalar  $g$ -factors

$$g_{L\mathbf{v}_a} = |\hat{\mathbf{g}}_L^T \mathbf{v}_a|, \quad (2.26)$$

$$g_{R\mathbf{v}_a} = |\hat{\mathbf{R}}\hat{\mathbf{g}}_R^T \mathbf{v}_a| = |\hat{\mathbf{g}}_R^T \mathbf{v}_a| = \frac{g_{L\mathbf{v}_a}}{a}. \quad (2.27)$$

We denote the basis states of  $H''$  by  $|\uparrow\uparrow\rangle$ ,  $|\uparrow\downarrow\rangle$ ,  $|\downarrow\uparrow\rangle$  and  $|\downarrow\downarrow\rangle$ , where  $|\uparrow\rangle$  ( $|\downarrow\rangle$ ) indicates that the spin is aligned (anti-aligned) with the corresponding effective magnetic field.

The Hamiltonian in Eq. (2.24) has a block diagonal structure corresponding to each value of the total spin  $z$  component  $S_{\text{tot},z} \in \{-1, 0, 1\}$ . Therefore, the eigenvalues of different blocks can cross upon a change of the absolute value of the external magnetic field  $B$ .

Indeed, at zero magnetic field, the ground state of  $H''(\mathbf{0})$  in Eq. (2.11) is the pseudo singlet state  $(|\uparrow\downarrow\rangle - |\downarrow\uparrow\rangle)/\sqrt{2}$  from the  $S_{\text{tot},z} = 0$  subspace, with energy  $-3J/4$ , and the remaining three states are pseudo triplets with zero energy<sup>1</sup>.

If the magnetic field is much greater than the interaction strength  $J$ , then the energy eigenstates are the product states. The ground state is the state  $|\downarrow\downarrow\rangle$  from the  $S_{\text{tot},z} = -1$  subspace with energy  $-\frac{1}{2}\mu_B g_+ B + \frac{J}{4}$ : this follows from that fact that  $|g_+| > |g_-|$ , which is implied by  $g_{L\mathbf{v}_a}, g_{R\mathbf{v}_a} > 0$ . Therefore, at a certain magnetic field strength between zero and infinity, the  $S_{\text{tot},z} = 0$  ground state must be degenerate with the  $S_{\text{tot},z} = -1$  ground state (see Fig. 2.2b). In fact, straightforward calculation shows that this level crossing degeneracy happens at the critical magnetic field strength

$$B_a = \frac{J}{2\mu_B} \left( \frac{1}{g_{L\mathbf{v}_a}} + \frac{1}{g_{R\mathbf{v}_a}} \right) \quad (2.28)$$

and the degenerate states are

$$|0\rangle = \frac{1}{\sqrt{g_L^2 + g_R^2}} (g_R |\uparrow\downarrow\rangle - g_L |\downarrow\uparrow\rangle), \quad (2.29a)$$

$$|-1\rangle = |\downarrow\downarrow\rangle, \quad (2.29b)$$

labelled with their  $S_{\text{tot},z}$  quantum number.

If, however, the direction of the magnetic field corresponds to a negative eigenvalue, then, the effective magnetic field vectors are parallel but point to the opposite direction. Therefore,

<sup>1</sup>Here ‘pseudo’ indicates that these are not genuine global singlet and triplet states, but rather singlet- and triplet-like combinations defined in the locally rotated spin frames, which nonetheless exhibit the characteristic 1+3 splitting.

the scalar  $g$ -factors have an opposite sign, which results the inequality  $|g_+| < |g_-|$ . This means that the  $|\downarrow\downarrow\rangle$  state can not reach the ground state from the  $S_{\text{tot},z} = 0$  subspace. What happens instead, is that the  $S_{\text{tot},z} = 0$  triplet state initially starts with a zero slope at  $B = 0$  and reaches  $|\uparrow\uparrow\rangle$  at a sufficiently large magnetic field (also described by Eq. (2.28) with proper signs) resulting an energy degeneracy of an excited state (see Fig. 2.2c).

If we change the  $g$ -tensors it can happen that one of them becomes singular. In such a transition,  $\hat{M}$  also becomes singular, i.e., one of its eigenvalues ( $a$ ) goes through zero (while the eigenvalue  $a$  itself and its corresponding eigenvector  $\mathbf{v}_a$  behave regularly). In the dispersion relation, no abrupt change takes place; only the relative ordering of the magnitude of  $g_+$  and  $g_-$  reverses. According to Eq. (2.28), the location of the ground state degeneracy exhibits a  $1/g_{L\mathbf{v}_a}$  fashion behavior as  $g_{L\mathbf{v}_a} \rightarrow 0^+$ , diverging to infinity. Entering negative values, an excited state degeneracy emerges from infinity.

If the real-valued matrix  $\hat{M}$  has a complex eigenvalue, then the corresponding eigenvectors are also complex, which gives non-physical solutions for the location of degeneracies.

## 2.4 Classification of degeneracy patterns

As we now show, the structure of the eigenvalues and eigenvectors of the matrix  $\hat{M}$  implies the geometrical pattern of the magnetic degeneracy points: a time-reversed pair of ground state degeneracy points corresponds to a left eigenvalue of  $\hat{M}$  which corresponds to real, positive eigenvalue. The matrix  $\hat{M}$  is a real-valued  $3 \times 3$  matrix that is not necessarily symmetric, and therefore may not be diagonalizable. However, it can still be brought into a canonical form, known as the Jordan normal form  $\hat{J}$ , via a similarity transformation using an invertible matrix  $\hat{P}$ , such that

$$\hat{J} = \hat{P}^{-1} \hat{M} \hat{P}. \quad (2.30)$$

The Jordan normal form  $\hat{J}$  consists of Jordan blocks, each corresponding to a single eigenvalue, with that eigenvalue repeated along the diagonal and ones on the superdiagonal (in the special case of a  $1 \times 1$  block, there is no superdiagonal element):

$$J_a = \begin{pmatrix} a & 1 & 0 & \cdots & 0 \\ 0 & a & 1 & \ddots & \vdots \\ 0 & 0 & a & \ddots & 0 \\ \vdots & \ddots & \ddots & \ddots & 1 \\ 0 & \cdots & 0 & 0 & a \end{pmatrix}. \quad (2.31)$$

A single eigenvalue may correspond to multiple Jordan blocks in the Jordan normal form. We can classify the eigenvector structure of a matrix according to:

- (i) the number and sizes of its Jordan blocks,
- (ii) whether different blocks share the same eigenvalue,
- (iii) and the nature of the eigenvalues — whether they are real or complex, and in the real case, whether they are positive, negative, or zero.

The possible Jordan normal forms of a  $3 \times 3$  matrix, classified by the sizes of the Jordan blocks, are:

$$J_3 = \begin{pmatrix} a & 0 & 0 \\ 0 & b & 0 \\ 0 & 0 & c \end{pmatrix}, \quad J_2 = \begin{pmatrix} a & 1 & 0 \\ 0 & a & 0 \\ 0 & 0 & b \end{pmatrix}, \quad J_1 = \begin{pmatrix} a & 1 & 0 \\ 0 & a & 1 \\ 0 & 0 & a \end{pmatrix}. \quad (2.32)$$

$J_3$  can be further classified into three classes:  $a \neq b \neq c$ ,  $a \neq b = c$  and  $a = b = c$ , and  $J_2$  can be classified into  $a \neq b$  and  $a = b$ .

The *algebraic multiplicity* of an eigenvalue is its multiplicity as a root of the characteristic polynomial; in the Jordan normal form, it corresponds to the total number of times the eigenvalue appears on the diagonal. In contrast, the *geometric multiplicity* is the dimension of the eigenspace associated with that eigenvalue (that is, the number of linearly independent eigenvectors) and equals the number of Jordan blocks for that eigenvalue. For a  $3 \times 3$  matrix, the algebraic and geometric multiplicities of each eigenvalue uniquely determine the structure of the Jordan normal form. (For larger matrices, however, this is no longer the case; additional information is needed to fully specify the Jordan structure.)

To further split the classes according to the nature of the eigenvalues, we have to use the fact that the matrix  $\hat{M}$  is real valued, and also use the sign of its determinant. This latter quantity is identical to the relative sign of the  $g$ -tensors

$$\mathcal{S} = \text{sgn}[\det(\hat{g}_L) \cdot \det(\hat{g}_R)] = \text{sgn}\left[\det\left(\hat{g}_L \hat{R} \hat{g}_R^{-1}\right)\right] = \text{sgn} \det \hat{M}, \quad (2.33)$$

because of the equalities  $\text{sgn} \det(\hat{g}_R) = \text{sgn} \det(\hat{g}_R^{-1})$  for non-singular  $\hat{g}_R$  and  $\det \hat{R} = 1$ .

#### 2.4.1 Patterns of magnetic degeneracy points for $\mathcal{S} = +1$

When the relative sign of the  $g$ -tensors is  $+1$ , there are two possibilities. Whether both  $g$ -tensors have a positive determinant, or they both have a negative determinant. These cases can be mapped to each other with the  $\hat{g}_{L/R} \rightarrow -\hat{g}_{L/R}$  sign flip. This action leaves  $\hat{M}$  invariant, therefore, location of the degeneracies is also unchanged, only their topological charge is reversed. From now we focus on the case when  $\det(\hat{g}_L), \det(\hat{g}_R) > 0$ . The total charge is  $\mathcal{Q}_0 = +2$ .

As we show below, for  $\det(\hat{g}_L), \det(\hat{g}_R) > 0$  there are 7 different cases, labelled from (I) to (VII) in Table 2.1, that are classified by the number of positive eigenvalues, and their algebraic and geometric multiplicities. We call these cases the *eigenpatterns* of the matrix  $\hat{M}$ .

For case (I), the matrix  $\hat{M}$  has three different positive eigenvalues,  $a$ ,  $b$  and  $c$ . The algebraic and geometric multiplicities are all 1. Let us denote the normalized left eigenvectors with  $\mathbf{v}_a$ ,  $\mathbf{v}_b$  and  $\mathbf{v}_c$ . Then, there are six magnetic degeneracy points, one time-reversed pair associated to each eigenvector  $\mathbf{v}_\alpha$ , appearing if the magnetic field is aligned or antialigned with those eigenvectors. The locations of the degeneracy points in the original magnetic-field parameter space are

$$\mathbf{B}_{\alpha,\pm} = \pm B_\alpha \cdot \mathbf{v}_\alpha, \quad (\alpha \in a, b, c). \quad (2.34)$$

The expressions for the critical fields  $B_\alpha$  is given in Eq. (2.28).

Two further eigenpatterns arise when  $\hat{M}$  has two different positive eigenvalues,  $a$  and  $b$ , see Table 2.1, rows (II) and (III). In these cases, one of these eigenvalues, say  $a$ , must have an algebraic multiplicity of 2. (Two different positive and one negative eigenvalue yields negative determinant which corresponds to  $\mathcal{S} = -1$ .) Then,  $a$  can have a geometric multiplicity of 2, yielding case (II) in Table 2.1, or a geometric multiplicity of 1, yielding case (III). In case (II), the magnetic degeneracy points are arranged at two isolated points along the line of  $\mathbf{v}_b$ , at  $\mathbf{B}_{b,\pm} = \pm B_b \cdot \mathbf{v}_b$ , and along an ellipse in the plane spanned by the two remaining eigenvectors,  $\mathbf{v}_{a_1}$  and  $\mathbf{v}_{a_2}$ . See Appendix A.1 for details. In case (III), the magnetic degeneracy points are arranged in four isolated points, similarly at  $\mathbf{B}_{a,\pm} = \pm B_a \cdot \mathbf{v}_a$  and  $\mathbf{B}_{b,\pm} = \pm B_b \cdot \mathbf{v}_b$ .

Four further eigenpatterns appear when  $\hat{M}$  has a single positive eigenvalue,  $a > 0$ , see rows (IV)-(VII) of Table 2.1. These eigenvalues can have an algebraic multiplicity of 3, and a geometric multiplicity of 3, yielding case (IV), where the magnetic degeneracy points form a closed surface, an ellipsoid. The simplest example is the case without spin-orbit interaction, where the  $g$ -tensors and  $\hat{R}$  are all proportional to the unit matrix, and the magnetic degeneracy

Eigenpattern label	Jordan normal form	Geometric pattern	Topological charge distribution	Stability codimension
(I)	$\begin{pmatrix} a & 0 & 0 \\ 0 & b & 0 \\ 0 & 0 & c \end{pmatrix}$		$4 \times (+1), 2 \times (-1)$	0 (stable)
(II)	$\begin{pmatrix} a & 0 & 0 \\ 0 & a & 0 \\ 0 & 0 & b \end{pmatrix}$		$2 \times (+1), 0$	3
(III)	$\begin{pmatrix} a & 1 & 0 \\ 0 & a & 0 \\ 0 & 0 & b \end{pmatrix}$		$2 \times (+1), 2 \times 0$	1 (stable transition)
(IV)	$\begin{pmatrix} a & 0 & 0 \\ 0 & a & 0 \\ 0 & 0 & a \end{pmatrix}$		2 (surface charge)	8
(V)	$\begin{pmatrix} a & 1 & 0 \\ 0 & a & 0 \\ 0 & 0 & a \end{pmatrix}$		2 (line charge)	4
(VI)	$\begin{pmatrix} a & 1 & 0 \\ 0 & a & 1 \\ 0 & 0 & a \end{pmatrix}$		$2 \times (+1)$	2
(VII)	$\begin{pmatrix} a & 0 & 0 \\ 0 & n/c & 0/1 \\ 0 & 0 & n/c \end{pmatrix}$		$2 \times (+1)$	0 (stable)

Table 2.1: **Zoo of geometrical patterns and topological charge density patterns of magnetic ground-state degeneracies of a spin-orbit-coupled two-spin system.** Classification is based on the eigenpatterns of the  $3 \times 3$  real matrix  $\hat{M}$  with positive determinant, see Eq. (2.23). In the second column, we display the Jordan normal form of  $\hat{M}$ . Each eigenpattern implies a geometrical pattern of the magnetic degeneracy points, which in turn implies a topological charge density pattern. The third column schematically shows the geometrical pattern of degeneracy points, and the topological charge of each geometrical element: +2 (orange), +1 (red), 0 (black), -1 (blue). In seventh row, the Jordan normal form may have negative or complex eigenvalues ('n/c'), and if there is a degenerate eigenvalue, then the superdiagonal element of its block can be either 0 or 1. The last column shows the stability codimension of the eigenpatterns, i.e., the number of linearly independent constraints for a small perturbation not to break the pattern.

points form a sphere. Alternatively,  $a$  can have an algebraic multiplicity of 3, and a geometric multiplicity of 2, yielding case (V), where the magnetic degeneracy points form a closed loop, an ellipse. Yet another alternative is that  $a$  has a geometric multiplicity of 1, yielding case (VI), with two isolated magnetic degeneracy points. Finally, it can also have an algebraic multiplicity of 1, and consequently a geometric multiplicity of 1, denoted as case (VII), yielding two isolated magnetic degeneracy points. The other eigenvector(s) are either negative or form a complex conjugate pair, and thus do not contribute to any further ground state degeneracy. This sevenfold classification of the relevant solutions of the eigenvalue problem implies a sixfold classification of the qualitatively different geometrical patterns of the magnetic degeneracy points, since the eigenpatterns (VI) and (VII) yield the same geometry.

### 2.4.2 Patterns of magnetic degeneracy points for $\mathcal{S} = -1$

Patterns of magnetic degeneracy points appearing for a negative relative sign  $\mathcal{S} = -1$  of the  $g$ -tensors are different from the ones discussed the previous subsection.

In this case, the total topological charge of the ground state magnetic degeneracy points is  $\mathcal{Q}_0 = 0$ . This indicates that two-spin Hamiltonians could exist without *any* magnetic degeneracy.

In fact, this expectation is confirmed by the eigenpattern analysis of the matrix  $\hat{M}$ . The analysis follows the steps of the previous subsection. The matrix  $\hat{M}$  defined in Eq. (2.23) has a negative determinant in this case, but still the magnetic degeneracy points are associated with the positive eigenvalues of  $\hat{M}$ . The negative determinant of  $\hat{M}$  implies that the combinations of algebraic and geometric multiplicities of its eigenvalues are different from the positive-determinant case. Apart from these differences, the analysis is very similar, hence we omit the details here, and summarize the results in Table 2.2.

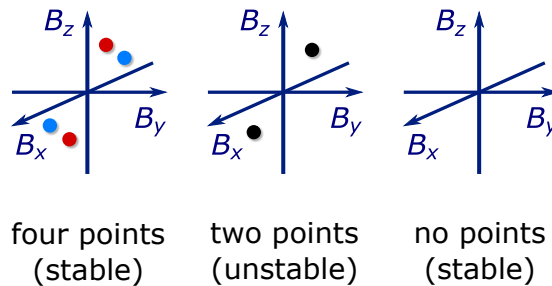


Figure 2.3: **Magnetic degeneracy points for two interacting spin-1/2 electrons, when the relative sign of the  $g$ -tensors is negative,  $\mathcal{S} = -1$ .** Color of each point indicates its topological charge: +1 (red), -1 (blue), 0 (black). Four points and no points patterns are stable, and the generic transition between them is that the two oppositely charged pairs meet and their charges annihilate each other (two points).

For a negative relative sign, we obtain four eigenpatterns: (VIII), (IX), (X), and (XI), based on the possible combinations of algebraic and geometric multiplicities of positive eigenvalues.

Pattern (XI) corresponds to the trivial case, where there is no positive eigenvalue, and therefore no degeneracy appears at any field. This pattern can be understood as pattern (VII) with the sign of one positive eigenvalue reversed, which removes a pair of degeneracy points.

Patterns (VIII), (IX), and (X) can be similarly related to patterns (I), (II) and (III), where the sign of one eigenvalue is flipped, therefore, there is no degeneracies corresponding to that eigenvalue. These cases can have either two points, four points, or a degeneracy ellipse, although not in this specific order.

Eigenpattern label	Jordan normal form	Geometric pattern	Topological charge distribution	Stability codimension
(VIII)	$\begin{pmatrix} a & 0 & 0 \\ 0 & b & 0 \\ 0 & 0 & \text{neg} \end{pmatrix}$		$2 \times (+1), 2 \times (-1)$	0 (stable)
(IX)	$\begin{pmatrix} a & 0 & 0 \\ 0 & a & 0 \\ 0 & 0 & \text{neg} \end{pmatrix}$		0	3
(X)	$\begin{pmatrix} a & 1 & 0 \\ 0 & a & 0 \\ 0 & 0 & \text{neg} \end{pmatrix}$		$2 \times 0$	1 (stable transition)
(XI)	$\begin{pmatrix} n/c & 0/1 & 0 \\ 0 & n/c & 0/1 \\ 0 & 0 & \text{neg} \end{pmatrix}$		no charge	0 (stable)

Table 2.2: **Zoo of geometrical patterns and topological charge density patterns if the  $g$ -tensors have opposite signs.** Notation and the structure of the table follows that in Table 2.1. The label ‘neg’ refers to a negative eigenvalue. In (XI) row, the Jordan normal form may have negative or complex eigenvalues (‘ $n/c$ ’). If two or three negative eigenvalues coincide, then the superdiagonal elements of the corresponding block can be either 0 or 1.

### 2.4.3 Patterns of magnetic degeneracy points for $\mathcal{S} = 0$

When one or both  $g$ -tensors are singular, a wider variety of scenarios can emerge. Depending on the ranks of the two  $g$ -tensors and the alignment of their null spaces, a large number of cases arise. However, these do not introduce fundamentally new phenomena. Therefore, we focus only on the most representative situation: when one  $g$ -tensor is regular (i.e., has a non-zero determinant), and the other is singular with rank 2 (that is, it has one zero eigenvalue with both algebraic and geometric multiplicity equal to 1). These cases correspond to transitions between configurations with  $\mathcal{S} = +1$  and  $\mathcal{S} = -1$ , where one of the eigenvalues of  $\hat{M}$  passes through zero. During this transition, as the eigenvalue changes sign from positive to negative, the associated Weyl point pair moves off to infinity and disappears. This process alters the total topological charge, since the vanishing Weyl points carry non-zero topological charge.

## 2.5 Stability analysis of eigenpatterns and corresponding geometrical patterns

In Ref. [21], we have studied random Hamiltonians for this spin-orbit-coupled two-spin model numerically, and among those random Hamiltonians, we have identified only two of the above six different geometrical patterns, the ‘six points’ pattern and the ‘two points’ pattern. Why don’t we find representatives of the other four geometrical patterns in a random ensemble of Hamiltonians? As we argue below, each eigenpattern can be characterized by a ‘degree of stability’ or ‘codimension’, denoted by  $d$ , which is a non-negative integer, familiar from the codimension property of bifurcations [66]: if  $d = 0$ , then the eigenpattern is stable, if  $d > 0$ , then the eigenpattern is unstable, and an increasing  $d$  is interpreted as decreasing stability: the larger  $d$ , the more parameters of  $H$  need to be tuned to observe the given eigenpattern and the corresponding magnetic degeneracy pattern. We will show that for  $\mathcal{S} = +1$  the ‘six points’ pattern and the ‘two points’ pattern are the only stable patterns, providing an explanation for our earlier numerical findings.

We define stability via sensitivity to small random perturbations. Consider the Hamiltonian  $H$  of Eq. (2.11) with fixed secondary parameters, which specifies the matrix  $\hat{M}$ , which in turn has a specific eigenpattern. If we slightly modify the secondary parameters, and thereby add an infinitesimal perturbation,  $H \rightarrow H' = H + \delta H$ , then the eigenpattern of  $H'$  may be the same as that of  $H$ , or it may be different. (Note that throughout this section, the prime in  $H'$  and related quantities refers to a perturbed instance of the quantity, unlike in other sections.) If the eigenpattern of  $H'$  is the same as that of  $H$  for any infinitesimal perturbation  $\delta H$ , then we call the eigenpattern of  $H$  stable. Otherwise, we call it unstable.

Instead of considering  $H$  directly, we address the question of eigenpattern stability by regarding the matrix  $\hat{M}$  as the element of a 9-dimensional vector space.<sup>2</sup> The infinitesimal perturbations  $\delta\hat{M}$  span a 9-dimensional vector space, too; we denote this vector space by  $W$ . The question of eigenpattern stability can then be phrased as follows: for a given  $\hat{M}$ , what is the dimension of the subspace  $W_s \leq W$  spanned by the infinitesimal perturbations  $\delta\hat{M}$  that preserve the eigenpattern of  $\hat{M}$  under  $\hat{M} \rightarrow \hat{M}' = \hat{M} + \delta\hat{M}$ ? If  $\dim(W_s) = 9$ , then the eigenpattern is preserved for an arbitrary infinitesimal perturbation, i.e., the eigenpattern of  $\hat{M}$  is stable. Otherwise, it is unstable, and the degree of stability can be characterized by the codimension of the stable subspace  $W_s$ , which is  $d \equiv 9 - \dim(W_s)$ , with  $d = 0$  denoting the stable case and increasing  $d$  signalling increasing instability.

We now outline a method to calculate  $d$  for a given  $\hat{M}$ . This is based on the Jordan decomposition of  $\hat{M}$ ,

$$\hat{M} = \hat{P}\hat{J}\hat{P}^{-1}, \quad (2.35)$$

with  $\hat{J}$  being the Jordan normal form of  $\hat{M}$ , and  $\hat{P}$  a similarity transformation (a real-valued non-singular  $3 \times 3$  matrix). Let us choose eigenpattern (V) as our example, so its Jordan normal form reads

$$\hat{J} = \begin{pmatrix} \lambda & 1 & 0 \\ 0 & \lambda & 0 \\ 0 & 0 & \lambda \end{pmatrix}. \quad (2.36)$$

The matrix  $\hat{M}$  has thus one eigenvalue with an algebraic multiplicity of 3 but only two linearly independent corresponding eigenvectors. Recall that this eigenpattern implies that the ground state degeneracy points are located on an ellipse.

We first characterize those perturbations of  $\hat{M}$  which preserve this eigenpattern, that is, preserve the structure of the Jordan form. For these, the Jordan form of the deformed matrix  $\hat{M}'$  must read

$$\hat{J}' = \hat{J} + \delta\hat{J} = \hat{J} + \begin{pmatrix} \delta\lambda & 0 & 0 \\ 0 & \delta\lambda & 0 \\ 0 & 0 & \delta\lambda \end{pmatrix}, \quad (2.37)$$

with an infinitesimal  $\delta\lambda$ . Since the only constraint on the perturbation is that the eigenpattern (that is, the Jordan normal form) should be preserved, an arbitrary infinitesimal change is allowed in the similarity transformation  $\hat{P}$ ,

$$\hat{P}' = \hat{P}(1 + \delta\hat{P}) \quad (2.38)$$

with an infinitesimal term

$$\delta\hat{P} = \begin{pmatrix} \delta p_{11} & \delta p_{12} & \delta p_{13} \\ \delta p_{21} & \delta p_{22} & \delta p_{23} \\ \delta p_{31} & \delta p_{32} & \delta p_{33} \end{pmatrix}. \quad (2.39)$$

<sup>2</sup>We can modify all elements of  $\hat{M}$  by changing some parameters of the original Hamiltonian.

Now we have parametrized, using 10 infinitesimal parameters (the  $\delta p_{ij}$ -s and  $\delta\lambda$ ), all matrices that are infinitesimally close to  $\hat{M}$  and have the same eigenpattern as  $\hat{M}$ ; in fact, we have overparametrized the set of matrices corresponding to eigenpattern (V) near  $\hat{M}$ . We can express the shift of the matrix  $\hat{M}$  up to linear order in these infinitesimal parameters to get the tangent space of eigenpattern (V) at  $\hat{M}$ .

$$\begin{aligned}\delta\hat{M} &= \hat{M}' - \hat{M} = \hat{P}'\hat{J}'\hat{P}'^{-1} - \hat{P}\hat{J}\hat{P}^{-1} \\ &= \hat{P}\left([\delta\hat{P}, \hat{J}] + \delta\hat{J}\right)\hat{P}^{-1} \equiv \hat{P}\delta\hat{M}\hat{P}^{-1},\end{aligned}\quad (2.40)$$

where  $\delta\hat{M}$  is the linear order change expressed in the basis of the Jordan normal form.

$$\delta\hat{M} = \begin{pmatrix} -\delta p_{21} + \delta\lambda & \delta p_{11} - \delta p_{22} & -\delta p_{23} \\ 0 & \delta p_{21} + \delta\lambda & 0 \\ 0 & \delta p_{31} & \delta\lambda \end{pmatrix}.\quad (2.41)$$

The image of  $\delta\hat{M}$  is 5-dimensional because there are 6 non-zero matrix elements and there is 1 constraint on them:

$$\delta\hat{M}_{11} + \delta\hat{M}_{22} = 2\delta\hat{M}_{33}.\quad (2.42)$$

To determine the dimension more algorithmically, we have to describe  $\delta\hat{M}(\{\delta p_{ij}\}, \delta\lambda)$  in the form of

$$\delta\hat{M}_{ij} = \sum_{\gamma=1}^{10} C_{ij,\gamma} \epsilon_{\gamma}, \quad (i, j = 1, 2, 3),\quad (2.43)$$

where  $(\{\epsilon_{\gamma}\}) = (\{\delta p_{ij}\}, \delta\lambda)$  is the 10-tuple of the infinitesimal parameters, and the coefficients of the linear relation are arranged in the  $9 \times 10$  matrix

$$C = \begin{pmatrix} 0 & 0 & 0 & -1 & -1 & 0 & 0 & 0 & 0 & 1 \\ 1 & 0 & 0 & 0 & -1 & 0 & 0 & 0 & 0 & 0 \\ 0 & 0 & 0 & 0 & 0 & -1 & 0 & 0 & 0 & 0 \\ 0 & 0 & 0 & 0 & 0 & 0 & 0 & 0 & 0 & 0 \\ 0 & 0 & 0 & 1 & 0 & 0 & 0 & 0 & 0 & 1 \\ 0 & 0 & 0 & 0 & 0 & 0 & 0 & 0 & 0 & 0 \\ 0 & 0 & 0 & 0 & 0 & 0 & 0 & 0 & 0 & 0 \\ 0 & 0 & 0 & 0 & 0 & 0 & 1 & 0 & 0 & 0 \\ 0 & 0 & 0 & 0 & 0 & 0 & 0 & 0 & 0 & 1 \end{pmatrix}.\quad (2.44)$$

The dimension of the stable subspace of perturbations is  $\dim(W_s) = \text{rank}(C)$ . A straightforward calculation shows that in this specific case,  $\dim(W_s) = \text{rank}(C) = 5$ . Correspondingly, the stability codimension is  $d = 9 - \dim(W_s) = 4$  for eigenpattern (V), cf. Table 2.1. We therefore conclude that the eigenpattern (V) has a rather high codimension  $d$ , and is therefore quite unstable, i.e., it is difficult to observe it in nature.

The stability of each of the 7 eigenpatterns in Table 2.1 can be characterized by calculating the corresponding codimension  $d$  in a similar way. The results are shown in the fifth column of Table 2.1.

### 2.5.1 Stable patterns and generic transition between them

The most important result is that the stability codimension of eigenpatterns (I) and (VII) are zero from relative sign  $\mathcal{S} = +1$ , hence these are the stable eigenpatterns, and consequently,

these provide two geometrical patterns of the magnetic degeneracy points: the ‘two points’ configuration (VII), and the ‘six points’ configuration (I). This result explains and corroborates our earlier numerical finding [21], where only these two geometrical patterns were found by studying randomized Hamiltonians.

A further question is, how transitions between stable eigenpatterns take place upon changing the secondary parameters of the Hamiltonian? If we consider two Hamiltonians from the two different stable eigenpattern classes (I) and (VII), and continuously interpolate between them, then there must be a critical point on the way where four of the six points disappear.

To describe the nature of the transition, let us simply consider that case (VII) can generically arise in two distinct ways: either two of its eigenvalues form a complex conjugate pair, or both are negative. Out of these, only the first scenario allows for a direct transition from class (I). Specifically, two of the three positive eigenvalues of the matrix  $\hat{M}$  approach each other and then become complex conjugates. At the point of direct contact, the matrix  $\hat{M}$  becomes degenerate, possessing a positive eigenvalue with algebraic multiplicity 2. This corresponds to either case (II) or (III). Among these, the generic transition is determined by the fact that case (III) has codimension exactly 1 (given by Table 2.1), i.e., it is a stable transition. In this scenario, the matrix  $\hat{M}$  is not diagonalizable but can be brought into Jordan normal form. This occurs because, during the transition, the eigenvectors also converge and eventually coincide. With further variation, they become complex.

Regarding degeneracies, this means that the degeneracies associated with the two eigenvalues merge and annihilate each other. In the direct transition, a four-point configuration emerges, of which one pair is stable (corresponding to the non-degenerate eigenvalue), and the other is unstable (associated with the degenerate eigenvalue, and formed through the merger).

It is important to emphasize that the collision of degeneracies occurs with codimension-1, despite the fact that they move in a 3D space. This implies that their motion cannot be fully independent—if it were, the degeneracies would generically avoid each other rather than collide.

To reach the remaining patterns, further fine tuning is required. An interesting example is case (VI), which geometrically yields the same pattern as case (VII), yet it is unstable. This case corresponds to a  $3 \times 3$  Jordan block, which arises when all three eigenvalues coalesce simultaneously, at which point the eigenvectors also coalesce. This implies that the associated degeneracies undergo a triple merger. Such a transition can occur either all at once, or via a sequential process in which two pairs collide first, followed by the third eigenvalue merging into them (also suggesting the codimension to be 2).

In the case of relative sign  $\mathcal{S} = -1$ , the two stable patterns are case (VIII), which features four degeneracy points, and case (XI), which has none. The stable transition between them occurs through case (X), where the degeneracies merge in a manner analogous to the transition for relative sign  $\mathcal{S} = +1$ , see Fig. 2.3.

The transition between  $\mathcal{S} = +1$  and  $\mathcal{S} = -1$  cases is discussed in Section 2.4.3: a point pair disappears at infinity as the corresponding eigenvalue goes through zero. This has codimension one because the only constraint is  $\det \hat{M} = 0$ .

## 2.6 Topological charge distribution

Additionally, we determined the topological charge distribution in the different configurations. In principle, it could happen that two different Hamiltonians yield the same geometry of degeneracy points, but the charge is distributed differently among the elements. For example, when  $\det(\hat{g}_L), \det(\hat{g}_R) > 0$ , the total topological charge  $\mathcal{Q}_0$  is  $+2$ , that is, the sum of the topological charges of each ground state degeneracies in the magnetic field parameter space. In case (II), the ellipse-shaped loop could be neutral and the isolated points could carry charge  $+1$  each, or the points could be neutral and the ellipse could carry charge  $+2$ . As we show now, in our

model, the topological charge density is uniquely determined by the geometrical pattern; in the example above, the points are charged and the loop is neutral.

To calculate the topological charge of say,  $\mathbf{B}_{a+}$ , we focus on the two degenerate ground states  $|0\rangle$  and  $|-1\rangle$  in the degeneracy point (see Eqs. (2.29)), make a linear expansion of the Hamiltonian for small deviations  $\delta\mathbf{B} = \mathbf{B} - \mathbf{B}_{a+}$  of the magnetic field from the degeneracy point, and truncate the Hamiltonian for the two-dimensional subspace spanned by  $|0\rangle$  and  $|-1\rangle$ . This reduced Hamiltonian can be written in terms of Pauli matrices,

$$H_{\text{red}}(\delta\mathbf{B}) = \mu_B \delta\mathbf{B} \cdot \hat{\mathbf{g}}_{a+} \boldsymbol{\tau}, \quad (2.45)$$

where  $\boldsymbol{\tau} = (\tau_1, \tau_2, \tau_3)$  is half times the vector of Pauli matrices, e.g.,  $\tau_3 = \frac{1}{2}(|0\rangle\langle 0| - |-1\rangle\langle -1|)$ . Because of the similarity of  $H_{\text{red}}$  and the Hamiltonian of a single spin in a magnetic field with an anisotropic  $g$ -tensor, we call  $\hat{\mathbf{g}}_{a+}$  the *effective  $g$ -tensor* of the degeneracy point  $\mathbf{B}_{a+}$ . The determinant of the effective  $g$ -tensor of a Weyl point is nonzero, and its sign provides the topological charge of the Weyl point:

$$\mathcal{Q}_{a+} = \text{sgn det}(\hat{\mathbf{g}}_{a+}). \quad (2.46)$$

To obtain an analytical result for the elements of the effective  $g$ -tensor, we evaluate  $H_{\text{red}}$  in Eq. (2.45) with  $\delta\mathbf{B} = \delta B \mathbf{e}_\alpha$  ( $\alpha = x, y, z$ ) pointing along the unit vector  $\mathbf{e}_\alpha$  of direction  $\alpha$ , multiply both sides with  $\tau_\beta$  ( $\beta = x, y, z$ ), and take the trace of both sides. This procedure yields the matrix elements

$$(\hat{\mathbf{g}}_{a+})_{\alpha\beta} = \frac{2}{\mu_B \delta B} \text{Tr}[H_{\text{red}}(\delta B \mathbf{e}_\alpha) \tau_\beta]. \quad (2.47)$$

The matrix obtained from this relation can be identified with the following basis independent expression:

$$\begin{aligned} \hat{\mathbf{g}}_{a+} \hat{\mathbf{O}} &= \frac{g_R^2 \hat{\mathbf{g}}_L + g_L^2 \hat{\mathbf{g}}_R \hat{\mathbf{R}}^{-1}}{g_L^2 + g_R^2} \mathbf{e}_z \otimes \mathbf{e}_z \\ &+ \frac{g_R \hat{\mathbf{g}}_L - g_L \hat{\mathbf{g}}_R \hat{\mathbf{R}}^{-1}}{\sqrt{g_L^2 + g_R^2}} (\mathbb{1} - \mathbf{e}_z \otimes \mathbf{e}_z), \end{aligned} \quad (2.48)$$

where  $\hat{\mathbf{O}}$  is the rotation setting the  $z$  axis along the direction of  $\hat{\mathbf{R}} \hat{\mathbf{g}}_R^T \mathbf{v}_a$  (which is the same as the direction of  $\hat{\mathbf{g}}_L^T \mathbf{v}_a$ ). Note that  $\otimes$  denotes the dyadic product of two three-dimensional real vectors.

A straightforward calculation using the matrix determinant lemma yields

$$\det \hat{\mathbf{g}}_{a+} = \frac{a(1+a)}{(1+a^2)^2} (a-b)(a-c) \det \hat{\mathbf{g}}_R, \quad (2.49)$$

where  $a$ ,  $b$  and  $c$  are the eigenvalues of the matrix  $\hat{\mathbf{M}}$ . Inserting this determinant into Eq. (2.46) and using  $a > 0$  and  $\det \hat{\mathbf{g}}_R > 0$ , we obtain

$$\mathcal{Q}_{a+} = \text{sgn}[(a-b)(a-c)] \quad \text{if } (a-b)(a-c) \neq 0. \quad (2.50)$$

The charge  $\mathcal{Q}_{a-}$  of the degeneracy in the opposite direction is the same as  $\mathcal{Q}_{a+}$  because Eq. (2.50) does not depend on how we choose the eigenvector  $\pm \mathbf{v}_a$ .

If  $(a-b)(a-c) \neq 0$ , that is,  $a \neq b$  and  $a \neq c$ , then the effective  $g$ -tensor  $\hat{\mathbf{g}}_{a+}$  is a regular matrix because  $\det \hat{\mathbf{g}}_{a+} \neq 0$ . This implies that the degeneracy will split linearly under a perturbation  $\delta\mathbf{B}$  of the magnetic field, regardless of its direction, meaning that the degeneracy point is a Weyl point.

In the case where  $a = b \neq c$  or  $a = b = c$ , the determinant of the effective  $g$ -tensor vanishes, i.e.,  $\det \hat{g}_{a+} = 0$ , meaning that  $\hat{g}_{a+}$  is singular. This implies that there exist direction(s) along which the energy splitting under a magnetic field perturbation occurs only at higher order. On top of that the simple sign formula is not enough to determine the topological charge.

If the eigenvalue  $a$  has geometric multiplicity greater than one, the degeneracy point lies on a higher-dimensional degeneracy manifold. In this case, the point is not isolated: it is part of a degeneracy curve (for multiplicity 2) or a surface (for multiplicity 3). Consequently, perturbations tangent to the degeneracy manifold do not lift the degeneracy to linear order. This is simply understood geometrically: moving tangentially to the manifold means staying closer to the degeneracy set, so the distance from degeneracy increases only at higher order, and the corresponding energy splitting is likewise nonlinear.

In contrast, if the geometric multiplicity of  $a$  is exactly one, the degeneracy is an isolated point. However, the effective  $g$ -tensor being singular implies that there still exist direction(s) in which the magnetic field perturbation does not lift the degeneracy linearly. This again reflects the fact that the point is not a Weyl point, even though it is isolated.

When the matrix  $\hat{M}$  is non-degenerate (i.e., generic) with positive determinant, there are three distinct possibilities regarding its eigenvalues:

- (i) All three eigenvalues are real and positive (case (I)). In this case, each of the three pairs of existing degeneracy points are Weyl points. According to Eq. (2.50), the pairs associated with the largest and smallest eigenvalues carry  $+1$  topological charge, while the pair associated with the intermediate eigenvalue carries  $-1$  charge. This distribution satisfies the total topological charge constraint:  $4 \times (+1) + 2 \times (-1) = +2$ .
- (ii) One eigenvalue is real and positive, while the other two are real and negative (case (VII)). In this case, only the positive eigenvalue corresponds to a ground-state Weyl point pair with  $+1$  topological charge. The other two eigenvalues are associated with excited-state degeneracies, and do not contribute to the ground-state topology. The total topological charge from ground-state degeneracies is therefore still  $+2$ .
- (iii) One eigenvalue is real and positive, while the other two form a complex-conjugate pair (also case (VII)). In this case, only the positive real eigenvalue corresponds to a Weyl point pair with  $+1$  topological charge. The complex-conjugate eigenvalues do not correspond to any physical degeneracy points. As in (ii), the total topological charge from the ground-state degeneracies is  $+2$ .

We can now understand Weyl point collisions from the perspective of topological charges as well. When transitioning from the six-point case to the two-point case, the intermediate eigenvalue merges with one of the extremal ones; that is, a Weyl point pair with charge  $-1$  collides with a pair with charge  $+1$ . The resulting degeneracy point is no longer a Weyl point, since its total charge is zero.

Moreover, based on the singularity of its effective  $g$ -tensor, we also see that its dispersion is not linear in all directions: indeed, there exists a direction along which a magnetic field perturbation causes the energy degeneracy to split quadratically while in all other directions the splitting remains linear. It can be shown that this specific direction coincides the direction along which the two oppositely charged Weyl points collided.

The total topological charge of the system remains  $+2$ , as it is preserved by the non-colliding Weyl point pair.

With further fine-tuning, it may occur that the doubly degenerate eigenvalue merges with the third one; that is, the previously formed zero-charge degeneracy pair collides with a Weyl point pair (case (VI)). As a result, a new degeneracy pair is formed whose topological charge must be  $+1$  due to charge conservation.

This new degeneracy is characterized by cubic dispersion along a special direction (in fact, not just a direction, but motion along a suitably curved path in parameter space is required to observe this), while the dispersion remains linear in all other directions.

This case also serves as an example demonstrating that Eq. (2.50) is only valid for Weyl points: here, the degeneracy pair carries topological charge +1, but the formula would incorrectly predict zero.

Let us now consider the transition where  $\det \hat{M}$  changes sign. In this case, the total topological charge is  $Q_{\text{tot}} = +2$  when  $\mathcal{S} = +1$ , and  $Q_{\text{tot}} = 0$  when  $\mathcal{S} = -1$ .

Assume that we initially start in the six-point-case, where all three eigenvalues of  $\hat{M}$  are positive, and suppose that the determinant of  $\hat{g}_{\mathbf{L}}$  goes through zero. During this transition, one of the eigenvalues also goes through zero and becomes negative. Since this can only occur for the smallest eigenvalue, the transition involves one of the +1-charged Weyl point pairs. As the determinant approaches zero, this Weyl point diverges to infinity and disappears. As a result, the system loses +2 units of topological charge, and the total charge drops to zero.

Focusing still on the  $\mathcal{S} = +1$  cases, in addition to point-like degeneracies there are also configurations where the degeneracy set includes an ellipse (case (II) and case (V)), or even an entire ellipsoid (case (IV)).

In the mixed case, where both a degeneracy point pair and an ellipse are present, the topological charge for the point pair in Eq. (2.50) simplifies to  $Q_{a\pm} = \text{sgn}[(a - b)^2] = +1$ . Thus the point pair is a Weyl point pair, each carrying charge +1, which already accounts for the entire topological charge of the system. Therefore, the ellipse must carry zero net charge. Whether this zero charge arises from a uniformly vanishing linear charge density or from a cancellation between locally positive and negative contributions along the ellipse cannot be determined based on this analysis.

In the other scenario, where only the elliptical degeneracy is present, the ellipse must carry the full charge of +2. Even in this case, one can still ask how the charge is distributed along the ellipse: whether it is continuously spread or concentrated at certain special, discrete points. Perhaps surprisingly, the latter turns out to be the case.

In case (V), all degeneracy points lie on a single ellipsoid, and therefore the total topological charge of +2 is distributed along the surface.

The results so far, concerning the total topological charge and its distribution among different types of degeneracy sets (e.g., point pairs, ellipses, ellipsoids), are summarized in Tables 2.1 and 2.2.

The internal distribution of the charge within a given degeneracy manifold, such as how it is spread along an ellipse or on an ellipsoid, will be addressed in the next section.

## 2.7 Topological charge density of non-point-like degeneracies

### 2.7.1 Linear charge density along degenerate curves

To examine the topological charge density along a line degeneracy, we must first define what we mean by it. Since the charge is fundamentally a flux through a surface, the idea is to surround the curve with a surface and integrate the Berry curvature over it. A natural choice is a tubular surface: at each point along the space curve, we consider the plane orthogonal to the tangent vector and draw a circle of fixed radius. The union of these circles forms a tube enclosing the curve. This tubular surface can be parametrized by the arc length  $s$  along the curve and an angular coordinate  $\vartheta$  around each circular cross-section. Technically, a third parameter  $r$ , the tube radius, defines a whole family of such surfaces (a tubular neighborhood of the curve) and the actual surface is the level set corresponding to fixed  $r$ .

The total topological charge enclosed in the tube is the surface integral of the Berry curvature over the tubular surface. As we shrink the radius  $r \rightarrow 0$ , the tube shrinks tightly around the

curve. The total charge remains invariant in this limit, since the enclosed topological charge is independent of the tube radius. However, the integrand becomes increasingly localized and accurately reflects the local distribution of charge along the curve.

This motivates the definition of a linear charge density of topological charge: by differentiating the total charge with respect to the arc length  $s$ , or equivalently, by integrating the flux density (i.e., the normal/radial component of the Berry curvature) over the meridional angle coordinate  $\vartheta$  (that is, over a single circular cross-section) and taking the limit  $r \rightarrow 0$ , we obtain the local topological charge per unit length.

Therefore, for a degeneracy curve, the formula revealing the linear topological charge density reads

$$\nu(s) = \frac{1}{2\pi} \lim_{r \rightarrow 0} \int_0^{2\pi} d\vartheta \mathcal{B}(\mathbf{p}_r(s, \vartheta)) \cdot (\partial_\vartheta \mathbf{p}_r \times \partial_s \mathbf{p}_r)_{s, \vartheta}, \quad (2.51)$$

where  $\mathbf{p}_r(s, \vartheta)$  is the parametrization of the tubular neighborhood. This is the quantity that we study in the following. For future reference, we introduce the *two-dimensional (2D) Berry curvature*  $\mathcal{B}_{2D}$  via

$$\mathcal{B}_{2D}(s, \vartheta) = \mathcal{B}(\mathbf{p}_r(s, \vartheta)) \cdot (\partial_\vartheta \mathbf{p}_r \times \partial_s \mathbf{p}_r)_{s, \vartheta}, \quad (2.52)$$

i.e., the integrand in Eq. (2.51). We also introduce the *apparent topological charge density*  $\tilde{\nu}_r(s)$ , which is the right hand side of Eq. (2.51), without taking the limit  $r \rightarrow 0$ :

$$\tilde{\nu}_r(s) = \frac{1}{2\pi} \int_0^{2\pi} d\vartheta \mathcal{B}_{2D}(s, \vartheta), \quad (2.53)$$

related to the charge density defined above as

$$\nu(s) = \lim_{r \rightarrow 0} \tilde{\nu}_r(s). \quad (2.54)$$

The physical dimension of the Berry curvature and the Berry flux density is magnetic field<sup>-2</sup>, whereas the dimension of the 2D Berry curvature, the apparent topological charge density and the topological charge density is magnetic field<sup>-1</sup>.

### 2.7.2 Case (II): neutral ellipse

First we consider the neutral ellipse degeneracy case (II). For this pattern, having zero total charge, one can envision two qualitatively different scenarios: (a) The charge distribution is identically zero at all points of the ellipse. (b) There is a non-zero linear charge density along the ellipse, but the negative and positive contributions cancel each other when added up for the entire ellipse. Speculation based on classical electrostatics intuition actually suggest scenario (b): if we think of the ellipse as a globally charge-neutral ‘metal’, then the two point charges outside the ellipse would ‘polarize’ the ellipse (cf. the interesting analogy with electrostatics in Section 2.7.5).

Here, we provide evidence that scenario (a) is the case, the local charge distribution along the degeneracy ellipse vanishes. This is the first key result of this work. This conclusion will be drawn from Fig. 2.4 c, but let us arrive there through a few intermediate steps.

In Fig. 2.4 a, we show the degeneracy patterns, two red points and a black ellipse. We use the specific choice of parameters where the  $g$ -tensors are

$$\hat{\mathbf{g}}_{L,II} = \begin{pmatrix} 2 & 0 & 0 \\ 0 & 2 & 0 \\ 0 & 1 & 4 \end{pmatrix}, \quad \hat{\mathbf{g}}_{R,II} = \mathbf{1}_{3 \times 3}, \quad (2.55)$$

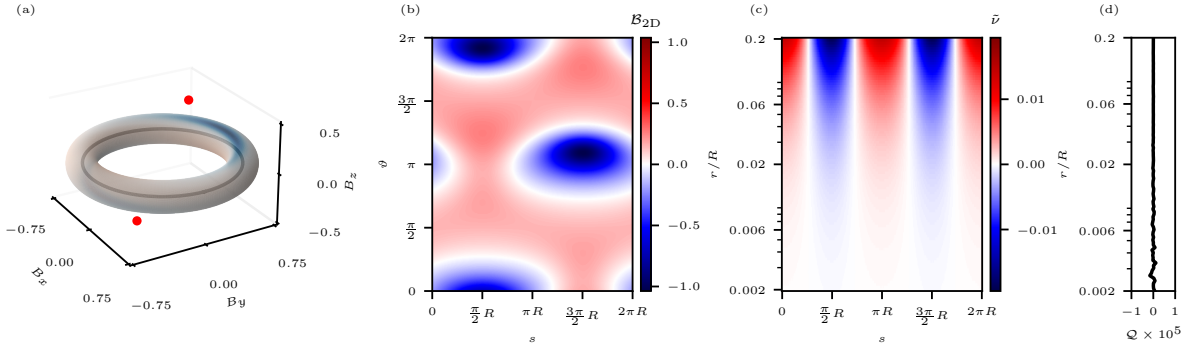


Figure 2.4: **Neutral degeneracy ellipse has vanishing linear topological charge distribution.** (a) Berry flux density  $\mathcal{B}_n$  (temperature map) on the surface of a torus surrounding a neutral degeneracy circle (black). Meridian radius,  $r/R = 0.2$  (b) Two-dimensional Berry curvature  $\mathcal{B}_{2D}(s, \vartheta)$  [Eq. (2.52)] on the parametrization of the torus, i.e., as a function of longitudinal arc length  $s$  and meridian angle  $\vartheta$ . (c) Apparent linear topological charge density  $\tilde{\nu}_r(s)$  [Eq. (2.53)], as function of longitudinal arc length  $s$  and meridian radius  $r$ . As  $r \rightarrow 0$ , this function converges to the constant zero function (white), showing that the linear topological charge density vanishes,  $\nu(s) = 0$ . (d) A benchmark for the numerical integration: numerically evaluated ground-state Chern number  $\mathcal{Q}_0$  on the torus, as function of the meridian radius  $r$ . Numerical error grows slightly as  $r \rightarrow 0$ , due to the divergence of the Berry curvature in the vicinity of the degeneracy circle, but it remains well below  $10^{-5}$  even for the smallest  $r$  values considered.

and the exchange interaction is characterized by  $J_{\text{II}} = 1$  and  $\hat{\mathbf{R}}_{\text{II}} = \mathbb{1}_{3 \times 3}$ . For simplicity, energy and magnetic field are dimensionless, unless noted otherwise (or equivalently  $J = 1 \mu\text{eV}$  and magnetic field is measured in  $\mu\text{eV}/\mu_B$ ).

The total topological charge carried by the red degeneracy points in Fig. 2.4 a is  $+2$ . These degeneracy points are located at opposite magnetic fields,

$$\mathbf{B}_{\pm} = \pm \frac{\sqrt{5}}{8} \begin{pmatrix} 0 \\ 1 \\ 2 \end{pmatrix}. \quad (2.56)$$

and each of them carry a topological charge  $+1$ . The degeneracy ellipse shown as the black loop in Fig. 2.4 is actually a circle in the  $xy$  plane for this parameter set, centered at the origin, with radius  $R = 3/4$ .

Figure 2.4 a shows the Berry flux density on a torus surrounding the degeneracy circle. The Berry flux density is defined as the normal-to-surface component of the Berry curvature vector field. For example, for a point  $\mathbf{B}$  on the torus, the Berry flux density reads

$$\mathcal{B}_n(\mathbf{B}) = \mathcal{B}(\mathbf{B}) \cdot \mathbf{n}(\mathbf{B}) \quad (\mathbf{B} \in \text{torus}), \quad (2.57)$$

where  $\mathbf{n}(\mathbf{B})$  is the normal vector of the torus at point  $\mathbf{B}$ . The torus in Fig. 2.4 a is colored according to the nonzero Berry flux density.

On the way toward the linear topological charge density, to be expressed via Eq. (2.51), we specify the parametrization of the torus surrounding the degeneracy curve as

$$\mathbf{p}_r(s, \vartheta) = R \mathbf{e}_{\text{rad}}(s) + r [\cos \vartheta \mathbf{e}_z + \sin \vartheta \mathbf{e}_{\text{rad}}(s)], \quad (2.58)$$

with

$$\mathbf{e}_{\text{rad}}(s) = \begin{pmatrix} \cos(s/R) \\ \sin(s/R) \\ 0 \end{pmatrix}, \quad \mathbf{e}_z = \begin{pmatrix} 0 \\ 0 \\ 1 \end{pmatrix}. \quad (2.59)$$

Note that the normal vector of the torus can be expressed from the parametrization via

$$\mathbf{n}(\mathbf{p}_r(s, \vartheta)) = \frac{\partial_\vartheta \mathbf{p}_r \times \partial_s \mathbf{p}_r}{|\partial_\vartheta \mathbf{p}_r \times \partial_s \mathbf{p}_r|}. \quad (2.60)$$

With the parametrization in Eq. (2.58), in Fig. 2.4 b we plot the 2D Berry curvature  $\mathcal{B}_{2\text{D}}$  (see Eq. (2.52)) on the torus, with meridian radius  $r = 0.2R$ . The data in Fig. 2.4 b is used to infer the linear topological charge density, by numerically performing the integration over the parameter  $\vartheta$  and dividing by  $2\pi$  to obtain the apparent charge density  $\tilde{\nu}_r(s)$ , and then taking the limit  $r \rightarrow 0$ . The apparent charge density as function of  $s$  and  $r$  is shown in Fig. 2.4 c. Although the value of the apparent charge density is nonzero for finite  $r$ , it does converge to zero for all values of  $s$  as  $r \rightarrow 0$ . This is numerical evidence that the degeneracy circle is charge neutral. To illustrate the accuracy of our result shown in Fig. 2.4 c, we numerically evaluate the ground-state Chern number  $\mathcal{Q}_0$  on the torus as the function of the meridian radius  $r$ , by integrating the apparent charge density over the longitudinal arc length  $s$ . The result, shown in Fig. 2.4 d, is indeed zero, exhibiting a numerical error less than  $10^{-5}$ , illustrating that our numerical procedure is rather accurate.

Up to now, we considered a specific parameter set, and we performed numerical calculations for that special case. This lead us to the finding that the neutral ellipse has an everywhere-vanishing linear charge density. Does this hold only for this special case, or is it generic for any neutral degeneracy ellipse within the spin-orbit-coupled two-spin model? We claim that the latter is true, and we outline the proof in Sec. 2.7.4.

### 2.7.3 Case (V): charged ellipse

Next we consider the charged ellipse degeneracy case (V). The question is: how is the topological charge distributed along the ellipse? Using the method of the previous subsection, we show that the topological charge is concentrated at two opposite points of the ellipse, i.e. it is not continuously distributed along the ellipse.

The example parameter set we use consists of  $g$ -tensors

$$\hat{\mathbf{g}}_{\text{L,V}} = \begin{pmatrix} 2 & 0 & 0 \\ 0 & 2 & 0 \\ 0 & 1 & 2 \end{pmatrix}, \quad \hat{\mathbf{g}}_{\text{R,V}} = \mathbf{1}_{3 \times 3}, \quad (2.61)$$

and the interaction is described by  $J_V = 1$  and  $\hat{\mathbf{R}}_V = \mathbf{1}_{3 \times 3}$ . The degeneracy ellipse is a circle with radius  $R = 3/4$  again, shown as a black line in Fig. 2.5 a.

Fig. 2.5 (in analogy with Fig. 2.4) shows (a) the Berry flux density  $\mathcal{B}_n$  on a torus surrounding the degeneracy circle, (b) the two-dimensional Berry curvature  $\mathcal{B}_{2\text{D}}(s, \vartheta)$  on the coordinates  $[0, 2\pi R) \times [0, 2\pi)$  of the torus, (c) the apparent topological charge density  $\tilde{\nu}_r(s)$  of the degeneracy circle, and (d) the numerically evaluated ground-state Chern number on the torus.

Fig. 2.5 a and b reveal a remarkable difference compared to Fig. 2.4 a and b: from Fig. 2.5 a and b, the Berry flux is concentrated in narrow regions (red spots) in the neighborhoods of two opposite points of the ellipse. Fig. 2.5 c suggests that the linear topological charge density, which corresponds to the plotted data  $\tilde{\nu}_r(s)$  in the  $r \rightarrow 0$  limit, consists of two Dirac deltas: the degeneracy circle is neutral in all points except two discrete points opposite to each other, each

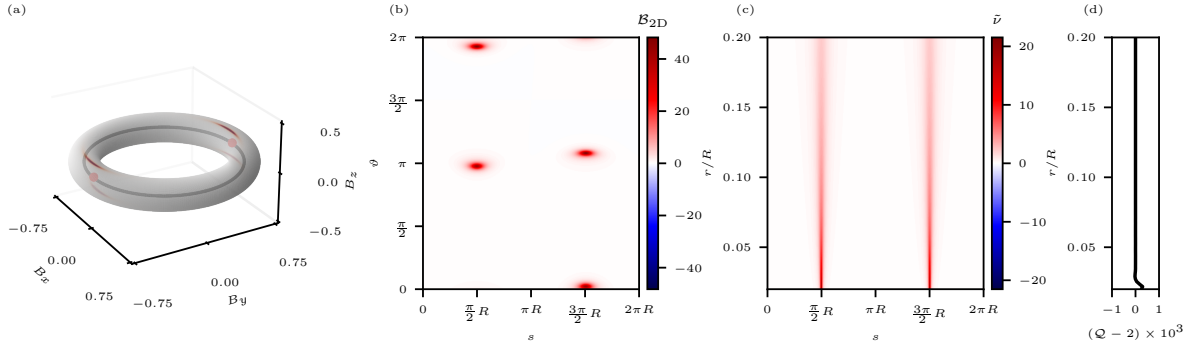


Figure 2.5: **Charged degeneracy ellipse has two charged points.** (a) Berry flux density  $\mathcal{B}_n$  (temperature map) on the surface of a torus surrounding a charged degeneracy circle (black). Meridian radius,  $r/R = 0.2$  (b) Two-dimensional Berry curvature  $\mathcal{B}_{2D}(s, \vartheta)$  [Eq. (2.52)] on the parametrization of the torus, i.e., as a function of longitudinal arc length  $s$  and meridian angle  $\vartheta$ . (c) Apparent linear topological charge density  $\tilde{\nu}_r(s)$  [Eq. (2.53)], as function of longitudinal arc length  $s$  and meridian radius  $r$ . As  $r \rightarrow 0$ , this function converges to the constant zero function (white), showing that the linear topological charge density vanishes,  $\nu(s) = 0$ . (d) A benchmark for the numerical integration: numerically evaluated ground-state Chern number on the torus, as function of the meridian radius  $r$ . Numerical error grows slightly as  $r \rightarrow 0$ , but it remains well below  $10^{-3}$  even for the smallest  $r$  values considered.

carrying a topological charge of  $+1$ . In Section 2.7.4, this numerical evidence is supported by analytical results.

Fig. 2.5 d shows that the numerical error of the Chern number is below  $10^{-3}$ , illustrating the accuracy of our numerical procedure. The feature that the error grows as the radius decreases is rather natural: for smaller radius, the Berry flux gets more focused on a smaller area, hence our numerical integration using an equidistant grid on the surface of the torus gets less accurate.

The direction of the charged points is  $(0, 1, 0)^T$ , as determined by the Jordan decomposition of  $\hat{M}$ , according to Eq. (36). From Eq. (2.28), the position of these points is expressed as:

$$\mathbf{B}_{\pm} = \pm \frac{3}{4} \begin{pmatrix} 0 \\ 1 \\ 0 \end{pmatrix}. \quad (2.62)$$

This result is in agreement with Fig. 2.5 c, where the charge density has two peaks at  $s \in \{\frac{\pi}{2}R, \frac{3\pi}{2}R\}$ .

Fig. 2.5 b shows pronounced peaks of the two-dimensional Berry curvature. These peaks appear because at each charged degeneracy point there are two opposite directions perpendicular to the tangent vector of the degeneracy circle in which the energy splitting grows quadratically as we move away from the circle, and the Berry flux density is typically greater where the splitting is smaller.

For both degeneracy points, we determine these directions analytically using Eq. (63), and we find  $(0, -1, 6)^T$ . This feature appears in the  $(s, \vartheta)$  torus of Fig. 2.5 b as red spots where the

flux density is high; the spot locations can be determined analytically as

$$\begin{aligned}
 (s_1, \vartheta_1) &= \left( \frac{\pi}{2}R, \pi - \tan^{-1} \frac{1}{6} \right), \\
 (s_2, \vartheta_2) &= \left( \frac{\pi}{2}R, 2\pi - \tan^{-1} \frac{1}{6} \right), \\
 (s_3, \vartheta_3) &= \left( \frac{3\pi}{2}R, \pi + \tan^{-1} \frac{1}{6} \right), \\
 (s_4, \vartheta_4) &= \left( \frac{3\pi}{2}R, \tan^{-1} \frac{1}{6} \right),
 \end{aligned} \tag{2.63}$$

matching the peaks seen in the numerical data.

To conclude, in this section we provided numerical evidence that the neutral degeneracy ellipse, pattern (II) of [23], has vanishing linear topological charge density, whereas the charged degeneracy ellipse, pattern (V) of [23], has all its topological charge focused in two opposite points of the ellipse. Even though the numerical results are obtained here for a specific choice of secondary parameters ( $g$ -tensors, exchange strength  $J$  and exchange rotation matrix  $\hat{\mathbf{R}}$ ), the statements are general, see Sec. 2.7.4 for the outline of the analytical proof. For example, if the secondary parameters are changed with respect to those in Section 2.7.2, such that the resulting matrix  $\hat{\mathbf{M}}$  still has the eigenpattern (II), then the degeneracy circle generically deforms into an ellipse, but all of its points remain charge-neutral. Results of Section 2.7.3 are generalized analogously. For details of these generalizations, we refer to Sec. 2.7.4.

#### 2.7.4 Linear topological charge density vanishes for rank-2 points of degeneracy curves

In this section, we outline analytical results that support the numerical evidence of topological charge distributions studied in Sections 2.7.2 and 2.7.3.

We define the *rank* of degeneracy points, by the rank of their effective  $g$ -tensor defined in Eq. (2.45). The rank of a degeneracy point of a curve and its topological charge is related. In particular, we find that a rank-2 degeneracy point located on a degeneracy curve carries no topological charge.

In Appendix A.4, we show that all degeneracy points of the neutral degeneracy ellipse are rank-2. Furthermore, in Appendix A.4 we show that in the charged degeneracy ellipse, the two points where the Berry flux density is concentrated in Fig. 2.5 are rank-1, and all other degeneracy points are rank-2. Finally, in Appendix A.5, we prove that the linear topological charge density at a rank-2 degeneracy point of a line degeneracy is zero, supporting the numerical evidence seen in Figs. 2.4c and Figs. 2.5c. We also observe that although hence there is no source of the Berry curvature on rank-2 degeneracy curves, there is always a  $\pi$  flux tube along the degeneracy, for details see Appendix A.5.

It is tempting to think about the charged ellipse degeneracy pattern (V) as a result of fine-tuning of pattern (II): upon tuning the secondary parameters ( $g$ -tensors, exchange parameters), two charged points of pattern (II) merge with the neutral degeneracy ellipse of pattern (II), forming the charged degeneracy ellipse of pattern (V). (Note the related discussion on the conversion between Weyl point and nodal lines in band structures [68].) This picture is reinforced by the fact that pattern (V) is less stable than pattern (II), signalled by their stability codimensions 4 and 3, respectively. Furthermore, in Appendix A.3, we show an example, where tuning a single parameter explicitly leads to two Weyl points merging with the neutral degeneracy ellipse.

### 2.7.5 Case (IV): continous surface charge distribution on an ellipsoid

Now consider the degenerate case (IV), the (charged) ellipsoid. We define the surface topological charge density as the jump in the component of the Berry curvature normal to the surface, between its two sides, analogous to electrostatics:

$$\sigma(\mathbf{B}_S) = \frac{1}{2\pi} (\mathcal{B}_n(\mathbf{B}_{S+}) - \mathcal{B}_n(\mathbf{B}_{S-})), \quad (2.64)$$

where  $\mathbf{B}_S$  is a point on the degeneracy surface, and  $\mathcal{B}_n(\mathbf{B}_{S\pm})$  are the components of the Berry curvature normal to the surface, evaluated in the limit  $\mathbf{B} \rightarrow \mathbf{B}_S$  from either side.

Fig. 2.6 shows this surface topological charge distribution  $\sigma(\mathbf{B}_S)$  for the example parameter set with  $g$ -tensors

$$\hat{\mathbf{g}}_{\text{L,IV}} = \begin{pmatrix} 2 & 0 & 0 \\ 0 & 6 & 0 \\ 0 & 0 & 18 \end{pmatrix}, \quad \hat{\mathbf{g}}_{\text{R,IV}} = \begin{pmatrix} 1 & 0 & 0 \\ 0 & 3 & 0 \\ 0 & 0 & 9 \end{pmatrix}, \quad (2.65)$$

and interaction described by  $J_{\text{IV}} = 1$  and  $\hat{\mathbf{R}}_{\text{IV}} = \mathbf{1}_{3 \times 3}$ . With these parameters, the degeneracy ellipsoid has its principal axes aligned with the  $(B_x, B_y, B_z)$  reference frame. The semi-axes of the ellipsoid are

$$\alpha = \frac{3}{4}, \quad \beta = \frac{1}{4}, \quad \gamma = \frac{1}{12}. \quad (2.66)$$

Contrary to the linear charge density of the ellipses, the ellipsoid shows a continuous charge distribution, which reads

$$\sigma(\mathbf{B}_S) = \frac{1}{2\pi\alpha\beta\gamma} \frac{1}{\sqrt{\frac{B_{Sx}^2}{\alpha^4} + \frac{B_{Sy}^2}{\beta^4} + \frac{B_{Sz}^2}{\gamma^4}}}. \quad (2.67)$$

This formula is obtained from the general result for the surface topological charge distribution

$$\sigma(\mathbf{B}_S) = \frac{a \det \hat{\mathbf{g}}_{\text{R}}}{\pi(a+1) |\hat{\mathbf{g}}_{\text{R}} \hat{\mathbf{g}}_{\text{R}}^{\text{T}} \mathbf{B}_S|}. \quad (2.68)$$

Here,  $a$  is the only eigenvalue of the matrix  $\hat{\mathbf{M}} = a \cdot \mathbf{1}_{3 \times 3}$  [23]. Equation (2.68) is derived in Appendix A.6.

Interestingly, the surface charge density in Eq. (2.67) has the same functional form as the electrical charge distribution of an electrically charged conducting ellipsoid [69]. Figure 2.6 exhibits the curvature effect known from electrostatics: the greater the local surface curvature, the higher the surface charge density. A further similarity is that the Berry curvature inside the ellipsoid is zero, similarly to the electric field inside a charged conductor. A difference, however, is that the Berry curvature in our example exits the surface radially with respect to the origin (i.e., it is proportional to  $\mathbf{B}/B$ ), in contrast to the electric field which exits the conductor's surface in the normal direction of the surface (i.e., it is proportional to  $\mathbf{n}(\mathbf{B})$ ). Another difference is that the curl of the Berry curvature is non-zero [65], however, the curl of the electric field induced by the charged conductor vanishes.

Given a degeneracy surface in a three-dimensional parameter space, is it a generic feature that it carries a continuous topological surface charge density? Here we argue that it is. Such a degeneracy surface divides the parameter space to two disjoint regions - in our example, the inside and the outside of the ellipsoid. The ground state changes continuously in both regions as the function of the parameters, generically implying a nonzero and continuous Berry curvature vector fields in both regions separately. But at the degeneracy surface, the ground state changes suddenly - in our example from a singlet-like state at the inside and a triplet-like state at the outside - and hence the Berry curvature also jumps, leading to a finite surface charge density according to Eq. (2.64).

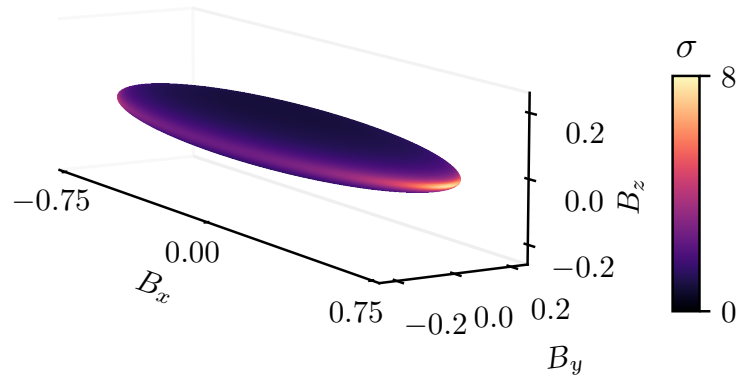


Figure 2.6: **Topological surface charge distribution on a degeneracy ellipsoid.** See Section 2.7.5 for parameter values. This topological charge distribution is the same as the electric charge distribution on the surface of a charged conducting ellipsoid.

## 2.8 Conclusion

In conclusion, we have provided a full analytical description of the geometrical patterns and topological charge distribution patterns of magnetic ground-state degeneracy points in a spin-orbit-coupled two-spin system. By recognizing the special structure of the Hamiltonian, we have mapped the problem of finding the degeneracy points to the eigenproblem of a real non-symmetric  $3 \times 3$  matrix. We have found three distinct regions in the space of (secondary) parameters, according to the total topological charge in magnetic (primary) parameter space,  $\mathcal{Q}_0 = \text{sgn}(\det \hat{g}_L) + \text{sgn}(\det \hat{g}_R)$ .

The regions  $\mathcal{Q}_0 = \pm 2$  are very similar, only the signs of the charge distributions are the opposite. In both regions, our stability analysis reveals the existence of two stable and extended (i.e., non-zero measure) regions in the secondary parameter space: in the first one, case (VII), two Weyl points carry the topological charge, while in the second one, case (I), six Weyl points carry the total charge,  $\mathcal{Q}_0 = 4 \times (+1) + 2 \times (-1)$ . There is *no other* geometrically stable region, meaning that other charge patterns exist only in special, fine-tuned Hamiltonians, realized for secondary parameters forming a set of zero measure. Some of these configurations can, however, be observed. For  $\mathcal{Q}_0 = +2$ , the unstable configuration that is the most stable is the one with two merged Weyl points, that is case (III). This configuration (III) emerges at the *boundary* between the two topologically stable phases, (I) and (VII). We naturally cross this surface in case we change some of the secondary parameters of the Hamiltonian, such that we go continuously from a region from case (I) to a region with case (VII). Approaching this surface, a positively and negatively charged pair of Weyl points must approach each other, and just merge to annihilate each other. This boundary, corresponding to case (III), includes further special patterns, corresponding to further fine-tuning of the parameters.

A similar picture emerges for the case  $\mathcal{Q}_0 = 0$ . There, two generic, extended regions are found with no degeneracy points (case (XI)), and with four Weyl points (case (VIII)), respectively. The generic surface between them corresponds to case (X), with two neutral degeneracy points, where the two pairs of Weyl points just merged. These magnetic degeneracy patterns are shown in Fig. 2.3.

The linear stability of regions (I), (VII), (VIII) and (XI) is corroborated by robust topological arguments: Weyl points cannot disappear upon infinitesimal smooth deformations of the secondary parameters. Starting from these configurations, removing Weyl points or creating new degeneracy points requires fine-tuning of the parameters: either positive and negative charges must move towards each other, and then annihilate at a very special point (this corresponds to

the boundaries (III) and (X) discussed above), or fine-tuning leads to the formation of an ellipse or an ellipsoid of degeneracy points that are not Weyl points, as their energy dispersion is flat in at least one direction. Numbers and charges of the Weyl points in regions (I), (VII), (VIII) and (XI) are constrained by the total topological charge, whereas the relative locations of these Weyl points is constrained by the fact that they always come in time-reversed pairs [21].

Additionally, we examined the charge distribution within non-point-like degeneracies. To this end, we defined both line and surface charge densities. For each of the two types of ellipses, we numerically determined the charge density for representative Hamiltonians. We found that in both cases the linear charge density vanishes, while in the charged ellipse the topological charge is concentrated at two points. We related this to the rank of the degeneracy, defined as the number of linearly independent directions along which the degeneracy splits linearly. We proved that rank-2 points along a degeneracy curve have zero linear charge density. Furthermore, we showed that the neutral ellipse consists entirely of rank-2 points, while the charged ellipse is rank-2 everywhere except at the two accumulation points, where the rank drops to 1. In contrast to the case of ellipses, for an ellipsoid the topological charge is continuously distributed over the surface. Remarkably, the distribution is exactly the same as that of electric charge on a conducting ellipsoid in electrostatics, even though the analogue of the electric field, namely the Berry curvature, is no longer strictly identical.

## 2.9 Discussion

We have seen that even in the absence of a general theory, one can get far using ad hoc methods, at least in simple settings. In our case, the Hamiltonian was a small, linearly parameterized matrix, which made it relatively easy to determine the location of degeneracies explicitly. Furthermore, by truncating the Hilbert space in a straightforward manner, we were able to compute the so-called effective  $g$ -tensor, which in turn helped to identify the charge distribution. However, in the case of linear degeneracies, we could no longer determine the full charge distribution rigorously; we merely pointed out a correlation between the rank of the degeneracy point and the localization of topological charge.

Such techniques can be useful when attempting to classify degeneracies, revealing a natural hierarchy of structural features. At the top level, degeneracies can be grouped by their dimensionality such as point-like, line-like, or surface-like. Within each class, one can further distinguish cases based on the rank, i.e., the number of linearly independent directions in which the degeneracy splits. This, in turn, has connection with the topological charge, and finally, one can consider the local stability of these structures under perturbations. These observations raise the question of whether a finite set of indices or invariants could eventually lead to a systematic classification scheme for degeneracies.

In the next chapter, we elaborate on what is actually being computed when determining the effective  $g$ -tensor. While this method is widely used in practice, it is rarely accompanied by a geometric interpretation despite the fact that it often encodes meaningful topological or structural information.

## Chapter 3

# The geometry of the Hermitian matrix space and the Schrieffer–Wolff transformation

Many physics problems are translated to matrix eigenvalue problems. For example, the frequency spectrum and the spatial patterns (modes) of small oscillations of a mechanical system are described by the eigenvalues and the eigenvectors of the dynamical matrix, which is a real symmetric matrix. Another example, which is the focus of this thesis, is quantum mechanics, where the stationary states and the energies are given by the eigenvectors and eigenvalues of the Hamiltonian, which is a Hermitian operator, often a finite-dimensional matrix.

In certain cases, a physics problem translated to a matrix eigenvalue problem is treated using perturbative methods. One of these is the Schrieffer-Wolff (SW) transformation [42, 41, 43] — also known as quasidegenerate perturbation theory [44, 45] Van Vleck perturbation theory [70], or Löwdin partitioning [71] — which decouples the subspaces of the relevant and irrelevant energy eigenstates through an appropriate unitary transformation.

In this chapter, motivated by many examples in quantum mechanics, we focus on the case, when the Hamiltonian ( $n \times n$  Hermitian matrix) of interest is in the vicinity of an *unperturbed Hamiltonian*  $H_0$  whose energy spectrum hosts a 2-fold degenerate eigenvalue, and we need to determine only those eigenvalues and eigenstates of the perturbed Hamiltonian  $H$  that correspond to the degenerate subspace of  $H_0$ . In this case, the Schrieffer-Wolff transformation takes the  $n \times n$  Hermitian matrices  $H_0$  and  $H$  as inputs, and outputs a  $2 \times 2$  Hermitian matrix  $H_{\text{eff}}$ , the *effective Hamiltonian*, whose eigenvalues and eigenvectors represent the relevant eigenvalues and eigenvectors of  $H$ . This provides a practical, useful computational method: if  $n$  is large, then computing the eigensystem of  $H_{\text{eff}}$  usually much easier than doing the same for  $H$ . Furthermore, the Schrieffer-Wolff transformation is typically applied together with an approximate, truncated power expansion of  $H_{\text{eff}}$  in the perturbation parameter(s), i.e.,  $H_{\text{eff}}$  is approximated as a low-order polynomial.

We provide a geometrical interpretation of the Schrieffer-Wolff transformation, relating the latter to the geometry of the submanifolds of degenerate matrices. The geometrical view we develop here builds a new connection between differential geometry and quantum mechanics, and hence enables the application of tools in one domain to deepen the understanding of, or solve problems in, the other domain.

Our first result is that we recognize that for any unperturbed degenerate Hamiltonian  $H_0$ , the Schrieffer-Wolff transformation provides a *canonical analytical local chart* of the manifold of Hermitian matrices, which is aligned with the corresponding degeneracy submanifold. Furthermore, we identify the effective Hamiltonian as the collection of those coordinates of this chart that lead out of the degeneracy submanifold.

Our second result is a ‘distance theorem’, which is a proportionality relation between (i) the Frobenius (a.k.a. Hilbert-Schmidt) distance between a generic Hamiltonian  $H$  and a 2-fold degeneracy submanifold, and (ii) the difference of the quasidegenerate eigenvalues of  $H$  corresponding to that degeneracy submanifold (sometimes simply called the ‘energy splitting of the degeneracy’). More precisely, the distance from the 2-fold degeneracy stratum equals the energy splitting divided by  $\sqrt{2}$ .

Our third result is a rigorous proof of the ‘protection’ of Weyl points, which are degeneracy points appearing, e.g., in the electronic band structure of crystalline materials [1]. Making use of the relations developed here, we show that the protection of Weyl points against perturbations is analogous to the protection of the crossing point of two lines drawn on a paper sheet, and we formalize this analogy by a common underlying theorem, namely the transversality theorem.

### 3.1 The space of the Hermitian matrices

The Hermitian matrices (of size  $n \times n$ ) are the complex matrices  $H$  with  $H = H^\dagger$ . Their set  $\text{Herm}(n)$  is a real vector space, it is a subspace of  $\mathbb{C}^{n \times n}$  of all  $n \times n$  complex matrices. Although  $\mathbb{C}^{n \times n}$  is a complex vector space (of dimension  $n^2$ ),  $\text{Herm}(n)$  inherits only real vector space structure, because it is not closed under the multiplication by the imaginary unit  $i$ .

The dimension of  $\text{Herm}(n)$  over  $\mathbb{R}$  is  $n^2$ . We fix a basis of  $\text{Herm}(n)$ , which we will refer to as ‘canonical basis’, which enables to identify  $\text{Herm}(n)$  with  $\mathbb{R}^{n^2}$ . This basis is formed by three families of matrices, the real off-diagonal parts ( $(n^2 - n)/2$  matrices), imaginary parts ( $(n^2 - n)/2$  matrices) and the diagonal parts ( $n$  matrices):

$$\sigma_{ab}^{(\text{real})} = \frac{1}{\sqrt{2}}(e_b \cdot e_a^\dagger + e_a \cdot e_b^\dagger) = \frac{1}{\sqrt{2}} \begin{pmatrix} \vdots & \vdots \\ \dots & 0 & \dots & 1 & \dots \\ \vdots & \vdots \\ \dots & 1 & \dots & 0 & \dots \\ \vdots & \vdots \\ a & b \end{pmatrix} \quad (\text{for } a < b), \quad (3.1)$$

$$\sigma_{ab}^{(\text{im})} = \frac{i}{\sqrt{2}}(e_b \cdot e_a^\dagger - e_a \cdot e_b^\dagger) = \frac{1}{\sqrt{2}} \begin{pmatrix} \vdots & \vdots \\ \dots & 0 & \dots & -i & \dots \\ \vdots & \vdots \\ \dots & i & \dots & 0 & \dots \\ \vdots & \vdots \\ a & b \end{pmatrix} \quad (\text{for } a < b), \quad (3.2)$$

$$\sigma_{aa}^{(\text{diag})} = e_a \cdot e_a^\dagger = \begin{pmatrix} 0 & & & & \\ & \ddots & & & \\ & & 1 & & \\ & & & \ddots & \\ & & & & 0 \end{pmatrix} a, \quad (3.3)$$

where  $e_1, \dots, e_n$  is the standard basis of  $\mathbb{C}^n$ . For any other unitary basis  $u_1, \dots, u_n$  of  $\mathbb{C}^n$  (where  $u_a = Ue_a$  is the  $a$ -th column of a unitary matrix  $U \in U(n)$ ), there is an associated basis of  $\text{Herm}(n)$  (over  $\mathbb{R}$ ), obtained from Equations (3.1), (3.2), (3.3) by replacing  $e_a$  with  $u_a$ , resulting  $\sigma_{ab}^U = U\sigma_{ab}U^\dagger$ .

For brevity, we denote the canonical basis of  $\text{Herm}(n)$  by  $C = (c_1, \dots, c_{n^2})$ , where  $c_a$ -s are the above defined  $\sigma$  matrices in an appropriate order where the first  $k^2$  elements generate the upper left  $k \times k$  block. For example,

$$c_1 = \sigma_{11}^{(\text{diag})}, c_2 = \sigma_{12}^{(\text{real})}, c_3 = \sigma_{12}^{(\text{im})}, c_4 = \sigma_{22}^{(\text{diag})}, c_5 = \sigma_{13}^{(\text{real})}, c_6 = \sigma_{13}^{(\text{im})}, \dots \quad (3.4)$$

Similarly, we denote the basis associated with a unitary matrix  $U \in U(n)$  by  $C^U = (c_1^U, \dots, c_{n^2}^U)$ , with  $c_a^U = U c_a U^\dagger$ , therefore,  $c_1^U, \dots, c_{k^2}^U$  span the subspace of  $\text{Herm}(n)$  consisting of the matrices acting on the subspace of  $\mathbb{C}^n$  spanned by  $u_1, \dots, u_k$ .

For  $k < n$ ,  $\text{Herm}(k)$  is embedded in  $\text{Herm}(n)$  as the subspace that consists of the matrices having zero entries outside the upper left  $k \times k$  block, that is, the subspace spanned by  $c_1, \dots, c_{k^2}$ . We often identify  $\text{Herm}(k)$  with this subspace of  $\text{Herm}(n)$ .

The complex vector space  $\mathbb{C}^{n \times n}$  is endowed with a Hermitian inner product (Frobenius inner product) defined as

$$\langle M, N \rangle = \text{tr}(M^\dagger \cdot N) = \sum_{a=1}^n \sum_{b=1}^n M_{ab}^* N_{ab}, \quad (3.5)$$

where  $z^*$  denotes the complex conjugate of  $z \in \mathbb{C}$ . That is, the inner product of two matrices agrees with the inner product of the vectors formed by the entries.

Although, this inner product takes complex values, its restriction to  $\text{Herm}(n)$  is real valued because every summand on the right side of Equation (3.5) has its complex conjugate too. Therefore, the Frobenius inner product on  $\text{Herm}(n)$  simplifies as  $\langle H, K \rangle = \text{tr}(H \cdot K) \in \mathbb{R}$ , making  $\text{Herm}(n)$  a Euclidean space. The basis  $C^U$  of  $\text{Herm}(n)$  associated to  $U \in U(n)$  (in particular, the canonical basis  $C$ ) is orthonormal with respect to the Frobenius inner product. If the coordinates of  $H$  and  $K$  in the basis  $C^U$  are  $h_a^U$  and  $k_b^U$ , respectively, then

$$\langle H, K \rangle = \sum_{a=1}^{n^2} h_a^U k_a^U. \quad (3.6)$$

The induced Frobenius norm of a Hermitian matrix is  $\|H\| = \sqrt{\text{tr}(H^2)}$ . The distance of two matrices  $H, G \in \text{Herm}(n)$  induced by the Frobenius norm is denoted by  $d(H, G) = \|H - G\|$ . This distance induces a topology on  $\text{Herm}(n)$ . An open neighborhood, or simply a neighborhood of  $H$  in  $\text{Herm}(n)$  is an open subset  $A \subset \text{Herm}(n)$  which contains an open ball around  $H$ , that is, there is a radius  $0 < r$  such that  $d(H, G) < r$  implies that  $G \in A$ .

**Lemma 3.7.** *The scalar product is invariant under the conjugation by unitary matrices. That is,  $\langle UH U^\dagger, UK U^\dagger \rangle = \langle H, K \rangle$  holds for every  $H, K \in \text{Herm}(n)$  and  $U \in U(n)$ .*

*Proof.*  $\langle UH U^\dagger, UK U^\dagger \rangle = \text{tr}(UH^\dagger U^\dagger UK U^\dagger) = \text{tr}(U^\dagger UH^\dagger K) = \text{tr}(H^\dagger K) = \langle H, K \rangle. \quad \square$

Let  $\text{Herm}_0(n) \subset \text{Herm}(n)$  be the subspace consisting of the matrices with zero trace. The dimension of  $\text{Herm}_0(n)$  over  $\mathbb{R}$  is  $n^2 - 1$ . A basis  $\check{c}_1, \dots, \check{c}_{n^2-1}$  is formed by the  $\sigma_{ij}^{(\text{real})}$  and  $\sigma_{ij}^{(\text{im})}$  matrices, extended with an orthonormal basis of the diagonal matrices with zero trace. This latter basis of traceless diagonal matrices replaces the matrices  $\sigma_{ii}^{(\text{diag})}$ , which are not contained in  $\text{Herm}_0(n)$ . For example, for  $n = 2$  one can choose the normalized Pauli matrices as a basis of  $\text{Herm}_0(2)$ :

$$\frac{1}{\sqrt{2}} \sigma_x = \frac{1}{\sqrt{2}} \begin{pmatrix} 0 & 1 \\ 1 & 0 \end{pmatrix} = \sigma_{12}^{(\text{real})}, \quad (3.8)$$

$$\frac{1}{\sqrt{2}} \sigma_y = \frac{1}{\sqrt{2}} \begin{pmatrix} 0 & -i \\ i & 0 \end{pmatrix} = \sigma_{12}^{(\text{im})}, \quad (3.9)$$

$$\frac{1}{\sqrt{2}} \sigma_z = \frac{1}{\sqrt{2}} \begin{pmatrix} 1 & 0 \\ 0 & -1 \end{pmatrix} = \frac{1}{\sqrt{2}} \left( \sigma_{11}^{(\text{diag})} - \sigma_{22}^{(\text{diag})} \right). \quad (3.10)$$

### 3.2 Degeneracy of the eigenvalues

Hermitian matrices have real eigenvalues and they can be diagonalized by a unitary basis transformation. Furthermore, for each  $H \in \text{Herm}(n)$ , one can choose a unitary matrix  $U \in U(n)$  such that

$$\Lambda = U^{-1} \cdot H \cdot U \tag{3.11}$$

is diagonal with the eigenvalues in increasing order  $\lambda_1 \leq \lambda_2 \leq \dots \leq \lambda_n$ . The ordered eigenvalues are continuous functions  $\lambda_i : \text{Herm}(n) \rightarrow \mathbb{R}$ , as it can be proven e.g. using Weyl's inequality [72]. However, the diagonalizing matrix  $U$  is not unique; each column, in fact, can be independently multiplied by an arbitrary phase factor. Moreover, in the case of degenerate eigenvalues  $\lambda_i = \lambda_{i+1}$ , the corresponding columns of  $U$  form a unitary basis of the corresponding 2-dimensional eigenspace. This basis can be transformed by any unitary action of  $U(2)$  to obtain a different matrix  $U'$  that still diagonalizes  $H$ .

The *degeneracy set*  $\Sigma \subset \text{Herm}(n)$  is the set of matrices with at least two coinciding eigenvalues. This degeneracy set  $\Sigma$  is a subvariety, i.e., an algebraic subset defined by polynomial equations. Indeed, indeed, it can be defined by one polynomial equation, namely,  $\Sigma$  is the zero locus of the discriminant of the characteristic polynomial. By the Neumann–Wigner theorem [17] the codimension of  $\Sigma$  is 3. For convenience, we summarize the original proof in Table 3.1. Our work provides an alternative proof, as a byproduct of the SW chart, see Corollary 3.17.

	Non-degenerate matrices		2-fold ground state degenerate matrices	
	Diagonalization structure	Number of parameters	Diagonalization structure	Number of parameters
$\Lambda$	$\lambda_1 < \dots < \lambda_n$	$n$	$\lambda_1 = \lambda_2 < \dots < \lambda_n$	$n - 1$
$U$	$[U] \in \underbrace{\frac{U(n)}{U(1) \times \dots \times U(1)}}_{n \text{ times}}$	$n^2 - n$	$[U] \in \frac{U(n)}{U(2) \times \underbrace{U(1) \times \dots \times U(1)}_{n-2 \text{ times}}}$	$n^2 - 4 - (n - 2)$
$H$		$n^2$		$n^2 - 3$

Table 3.1: Summary of the proof of the Neumann–Wigner theorem for 2-fold (ground state) degeneracy. Consider a Hermitian matrix in form  $H = U\Lambda U^{-1}$ , where  $\Lambda$  is diagonal, containing the ordered eigenvalues, and the columns of the unitary matrix  $U \in U(n)$  are eigenvectors of  $H$ . The dimension of  $U(n)$  is  $n^2$ , since every unitary matrix sufficiently close to the identity can be written as  $e^{iK}$  with  $K \in \text{Herm}(n)$  (in other words, the Lie algebra of the Lie group  $U(n)$  is the space  $\mathfrak{u}(n) = i \cdot \text{Herm}(n)$  of the anti-Hermitian matrices). If we construct a non-degenerate  $H$ , every column of  $U$  can be modified by a  $U(1)$  action providing the same matrix  $H$ . Hence the choice of  $U$  has  $n^2 - n$  free parameters, which together with the  $n$  parameters of  $\Lambda$  verifies that the dimension of the non-degenerate matrices (i.e., the generic part of  $\text{Herm}(n)$ ) is  $n^2$ . If we construct a 2-fold degenerate  $H$  ( $\lambda_1 = \lambda_2 < \lambda_3$ ), then the eigenvectors  $u_1, u_2$  spanning the degenerate eigenspace can be modified by a  $U(2)$  action. Hence the choice of  $U$  has  $n^2 - 4 - (n - 2)$  free parameters, which together with the  $n - 1$  parameters of  $\Lambda$  verifies that the dimension of the 2-fold degeneracy is  $n^2 - 3$ , hence, its codimension is 3 independently of  $n$ .

The set  $\Sigma$  can be decomposed into the disjoint union of different *strata* based on the type of the degeneracy, i.e., which eigenvalues coincide [39]. In this context, this decomposition or partitioning of  $\Sigma$  is often called *stratification*. Each stratum can be labeled by an ordered partition of  $n$  in the following way. Let  $\kappa = (k_1, \dots, k_l)$  be a sequence of integers  $1 \leq k_i \leq n$  of length  $1 \leq l < n$  such that  $n = \sum_{i=1}^l k_i$ , defining  $\kappa$  as an ordered partition of  $n$ . The number of the ordered partitions of  $n$  is  $2^{n-1}$ , (including the case with  $l = n$ ). The associated stratum  $\Sigma_\kappa$  of  $\Sigma$  consists of the matrices with coinciding eigenvalues  $\lambda_1 = \dots = \lambda_{k_1} < \lambda_{k_1+1} = \dots = \lambda_{k_1+k_2} < \dots$

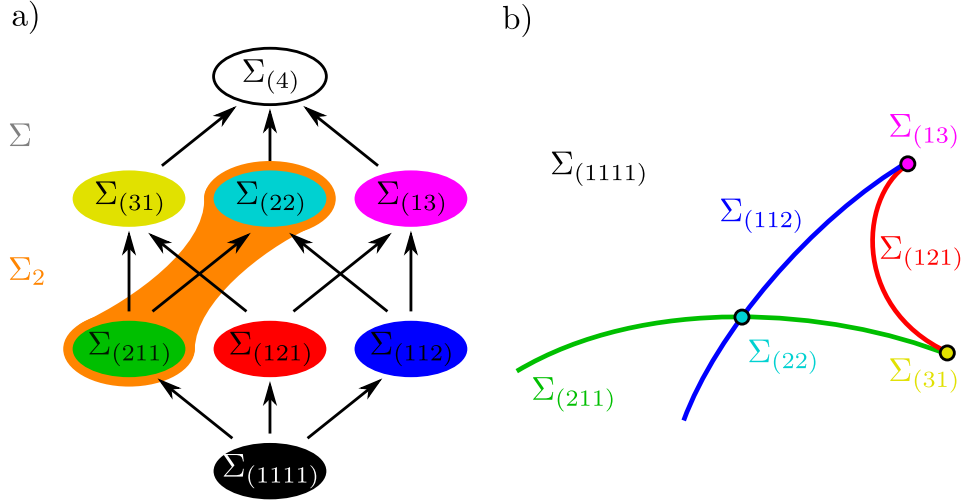


Figure 3.1: The stratification of  $\text{Herm}(4)$ , the space of  $4 \times 4$  Hermitian matrices. (a) The strata are labeled with the ordered partitions of 4, whose number is  $2^3 = 8$ . The non-degenerate matrices form an open and dense subset  $\Sigma_{(1111)}$  in  $\text{Herm}(4)$ . Its complement is the degeneracy set  $\Sigma$  (grey), the set of matrices with at least two coinciding eigenvalues. For example,  $\lambda_1 = \lambda_2 < \lambda_3 < \lambda_4$  in  $\Sigma_{(211)}$ , and  $\lambda_1 = \lambda_2 < \lambda_3 = \lambda_4$  in  $\Sigma_{(22)}$ . The two-fold ground state degeneracy set  $\Sigma_2$  (orange) consists of the matrices with  $\lambda_1 = \lambda_2 < \lambda_3$ , that is,  $\Sigma_2 = \Sigma_{(2,2)} \cup \Sigma_{(2,1,1)}$ . (b)  $\Sigma$  is a subvariety of  $\text{Herm}(4)$ . Although, each stratum is a (non-closed) smooth submanifold of  $\text{Herm}(4)$ , however,  $\Sigma$  is not a smooth manifold. The smooth points of  $\Sigma$  are the exactly two-fold degenerate matrices in  $\Sigma_{(211)} \cup \Sigma_{(121)} \cup \Sigma_{(112)}$ . The two-fold ground state degeneracy set  $\Sigma_2$  is a smooth submanifold in  $\text{Herm}(4)$ . Its generic points belong to  $\Sigma_{(211)}$ . At the points of  $\Sigma_{(22)}$ ,  $\Sigma_2$  is smooth, but  $\Sigma$  is not smooth. Indeed,  $\Sigma_{(2,2)}$  is the (transverse) intersection of the smooth branches  $\Sigma_2$  and  $\Sigma_{(1,1,2)} \cup \Sigma_{(2,2)}$ .

The partition with  $l = n$  and  $k_i = 1$  marks the complement of  $\Sigma$ , the set of non-degenerate matrices. Each stratum  $\Sigma_\kappa$  is a (not closed) smooth submanifold of  $\text{Herm}(n)$ , whose dimension is  $\dim \Sigma_\kappa = n^2 - \sum_{i=1}^l (k_i^2 - 1)$  by the Neumann–Wigner theorem [17], cf. Table 3.1. The closure  $\text{cl}(\Sigma_\kappa)$  contains the higher degeneracies. The smooth points of  $\Sigma$  are the strictly two-fold degenerate matrices, that is, exactly 2 eigenvalues coincide and all the others are different. The set  $\Sigma$  is singular at all other points, see Figure 3.1. We refer to [39, 73] for details.

In this chapter we restrict our study to the subset  $\Sigma_2$  of  $\Sigma$  consisting of 2-fold ground-state degenerate matrices, that is, matrices with  $\lambda_1 = \lambda_2 < \lambda_3$ . Since higher eigenvalues can coincide with each other,  $\Sigma_2$  is the union of all strata  $\Sigma_\kappa$  corresponding to  $\kappa = (k_1, \dots, k_l)$  with  $k_1 = 2$ . The generic points of  $\Sigma_2$  belong to the stratum corresponding to  $(2, 1, \dots, 1)$ .

The set  $\Sigma_2$  is a smooth, not closed submanifold in  $\text{Herm}(n)$  of codimension 3, that is,  $\dim(\Sigma_2) = n^2 - 3$ , cf. Figure 3.1. This follows from the Neumann–Wigner theorem, see Table 3.1 for a sketch of the proof.

In addition to  $\Sigma_2$ , its closure  $\text{cl}(\Sigma_2)$  contains the higher degeneracies as well, it precisely decomposes as the disjoint union  $\text{cl}(\Sigma_2) = \Sigma_2 \cup \Sigma_3 \cup \dots \cup \Sigma_n$ . The proof is the following. If an infinite sequence  $H_1, H_2, \dots$  of elements  $H_i \in \Sigma_2$  is convergent in  $\text{Herm}(n)$ , then its limit  $\lim_{i \rightarrow \infty} H_i$  is in  $\text{cl}(\Sigma_2)$  by the definition of the closure. As a consequence of the continuity of the eigenvalues, the lowest two eigenvalues of  $\lim_{i \rightarrow \infty} H_i$  are degenerate, and it might happen that one or more other eigenvalues also converge to them.

Our results can be naturally adapted to arbitrary  $k$ -fold degeneracy, which is not necessarily ground state, i.e., the set of matrices with  $\lambda_i < \lambda_{i+1} = \dots = \lambda_{i+k} < \lambda_{i+k+1}$ .

We introduce one more notation. Let  $\Sigma_{[k,k+1]} \subset \Sigma$  denote the set of matrices  $H \in \text{Herm}(n)$  with  $\lambda_k = \lambda_{k+1}$ , that is, the closure of the two-fold degeneracy stratum corresponding to  $\lambda_k = \lambda_{k+1}$ . For example, in  $\text{Herm}(4)$  we have  $\Sigma_{[2,3]} = \Sigma_{(1,2,1)} \cup \Sigma_{(1,3)} \cup \Sigma_{(3,1)} \cup \Sigma_{(4)}$ , its complement is  $\Sigma_{(1,1,1,1)} \cup \Sigma_{(2,1,1)} \cup \Sigma_{(1,1,2)} \cup \Sigma_{(2,2)}$ , cf. Figure 3.1.

### 3.3 The Schrieffer–Wolff transformation induces a local chart

We consider matrices  $H \in \text{Herm}(n)$  in a sufficiently small neighborhood  $\mathcal{V}_0$  of a fixed 2-fold ground-state degenerate matrix  $H_0 \in \Sigma_2$ . For simplicity, we assume that  $H_0$  is diagonal in the canonical basis of  $\mathbb{C}^n$  with increasing order of the eigenvalues.

As we mentioned before, the choice of the unitary matrix  $U \in U(n)$  in the diagonalization (3.11) of  $H$  is not unique. Furthermore,  $U$  cannot be chosen to depend continuously on  $H$  in any (open) neighborhood of  $H_0$  in  $\text{Herm}(n)$ . This is because the eigenvectors corresponding to degenerate eigenvalues cannot be chosen continuously<sup>1</sup>. Instead, what happens if our objective is to attain only a block diagonal structure

$$\tilde{B} = U^{-1}HU, \quad (3.12)$$

where  $\tilde{B}$  consists of a  $2 \times 2$  and a  $(n-2) \times (n-2)$  block? It turns out that such a family of unitary matrices  $U \in U(n)$  can be chosen not only as a continuous, but an analytical function of  $H$  as well. Moreover, if  $U$  is assumed to be of the form  $U = e^{iS}$  with  $S$  a block off-diagonal Hermitian matrix, the decomposition (3.12) is essentially unique. It is formulated by our first statement as follows.

**Theorem 3.13** (Exact SW decomposition, cf. Figure 3.2). *Fix a diagonal matrix  $H_0 \in \Sigma_2$  with increasing order of its eigenvalues along its diagonal. Then, there are neighborhoods  $\mathcal{V}_0, \mathcal{W}_0 \subset \text{Herm}(n)$  of  $H_0$  and a neighborhood  $\mathcal{X}_0 \subset \text{Herm}(n)$  of 0 such that for every  $H \in \mathcal{V}_0$  there is a unique decomposition*

$$H = e^{iS} \cdot \tilde{B} \cdot e^{-iS}, \quad (3.14)$$

where  $\tilde{B}$  and  $S$  are  $n \times n$  Hermitian matrices with the following special properties:

1.  $\tilde{B} \in \mathcal{W}_0$  is a block diagonal matrix with  $2 \times 2$  and  $(n-2) \times (n-2)$  blocks.
2.  $S \in \mathcal{X}_0$  is an off-block matrix, i.e., its  $2 \times 2$  and  $(n-2) \times (n-2)$  blocks along the diagonal are zero. Non-zero entries are in the  $2 \times (n-2)$  and  $(n-2) \times 2$  off-diagonal blocks.
3. The first two columns of  $e^{iS}$  span the sum of the eigenspaces of  $H$  corresponding to the lowest two eigenvalues.

Furthermore, the dependence of  $S$  and  $\tilde{B}$  on  $H \in \mathcal{V}_0$  is (real) analytic.

Actually, the theorem gives an exact formulation of the well-known method called Schrieffer–Wolff transformation [41, 42, 43, 44, 45], by breaking up  $\tilde{B}$  into parts according to the blocks as follows, cf. Figure 3.2:

$$H = e^{iS} \cdot (H_0 + B + T + H_{\text{eff}}) \cdot e^{-iS}, \quad (3.15)$$

where  $T, B, H_{\text{eff}}$  and  $S$  are  $n \times n$  Hermitian matrices with the following special properties:

1.  $B$  is block diagonal matrix and it has non-zero entries only in the  $(n-2) \times (n-2)$  bottom right block.

---

<sup>1</sup>The eigenspaces form a complex line bundle over the non-degenerate matrices, which is nontrivial. For example, it is always possible to find a small 2-sphere  $S^2$  around  $H_0$  in  $\text{Herm}(n) \setminus \Sigma$ , such that the first Chern number of the lowest eigenstate is non-zero, showing the impossibility of a continuous choice of eigenvectors.

$$H = e^{i \begin{array}{|c|c|} \hline 0 & \\ \hline & 0 \\ \hline \end{array}} \cdot \begin{array}{|c|c|} \hline & 0 \\ \hline 0 & \\ \hline \end{array} \cdot e^{-i \begin{array}{|c|c|} \hline 0 & \\ \hline & 0 \\ \hline \end{array}}$$

$$\underbrace{\begin{array}{|c|c|} \hline \diagdown & 0 \\ \hline 0 & \diagup \\ \hline \end{array}}_{H_0} + \begin{array}{|c|c|} \hline 0 & 0 \\ \hline 0 & \\ \hline \end{array} + \begin{array}{|c|c|} \hline \diagdown & 0 \\ \hline 0 & 0 \\ \hline \end{array} + \begin{array}{|c|c|} \hline & 0 \\ \hline 0 & 0 \\ \hline \end{array} \\
 H_{\text{eff}}$$

Figure 3.2: The exact SW decomposition (3.15). By Theorem 3.13 the block diagonalization of a matrix  $H$  close enough to  $H_0$  is unique, if the unitary matrix has the special form  $e^{iS}$ , where  $S$  is off-block, and both  $S$  and the block diagonal matrix are sufficiently close to 0. Decomposing the block diagonal matrix into parts gives the ‘non-interesting block’  $B$ , the scalar matrix  $T$  in the ‘interesting block’ carrying the trace of this block, and the traceless effective Hamiltonian  $H_{\text{eff}}$ .

2.  $T$  is a scalar matrix in the  $2 \times 2$  upper left block and all the other entries are zero.
3. The traceless *effective Hamiltonian*  $H_{\text{eff}}$  has a traceless  $2 \times 2$  block and all the other entries are zero.
4.  $S$  is an off-block matrix, see above (point (2) in Theorem 3.13).

Assuming that  $(S, T, B, H_{\text{eff}})$  is in a sufficiently small neighborhood of  $(0, 0, 0, 0)$ , then the decomposition is unique, and the dependence of  $S$ ,  $T$ ,  $B$  and  $H_{\text{eff}}$  on  $H \in \mathcal{V}_0$  is (real) analytic, by Theorem 3.13. Note that in the literature the effective Hamiltonian is usually defined together with its trace, i.e.,  $H_{\text{eff}} + T$ .

The proof of Theorem 3.13, and hence the unique decomposition (3.15) is based on the analytic inverse function theorem, see Section B.1. The unitary transformation  $e^{iS}$  is described in [43] as a ‘direct rotation’ between the eigenspaces of  $H$  and  $H_0$  corresponding to the lowest two eigenvalues. In the following, we clarify the relation of [43] with Theorem 3.13, and we adapt the results of [43] to specify the validity range of decomposition (3.15).

By the convention introduced in Section 3.1,  $H_{\text{eff}}$  can be considered as a traceless  $2 \times 2$  Hermitian matrix, that is,  $H_{\text{eff}} \in \text{Herm}_0(2) \subset \text{Herm}(n)$ . Let  $y_1, y_2, y_3$  denote its coordinates in the orthonormal basis  $\check{c}_1, \check{c}_2, \check{c}_3$  of  $\text{Herm}_0(2)$  introduced in Section 3.3

$$H_{\text{eff}} = y_1 \check{c}_1 + y_2 \check{c}_2 + y_3 \check{c}_3 = \frac{1}{\sqrt{2}}(y_1 \sigma_x + y_2 \sigma_y + y_3 \sigma_z). \quad (3.16)$$

The number of the (possibly) nonzero coordinates of the matrices  $B$ ,  $T$  and  $S$  in the canonical basis of  $\text{Herm}(n)$  is

1.  $B$ :  $(n - 2)^2$ ,
2.  $T$ : 1,
3.  $S$ :  $4(n - 2)$ .

Together these are  $n^2 - 3$  coordinates, let  $x_1, \dots, x_{n^2-3}$  denote them.

**Corollary 3.17** (SW decomposition induces a local chart, cf. Figure 3.3). (a) *The map  $\varphi : \mathcal{V}_0 \rightarrow \mathbb{R}^{n^2}$  with coordinate functions  $x_i$  and  $y_j$  is a local chart on  $\text{Herm}(n)$  around  $H_0$ , and  $\varphi$  is analytic in the canonical coordinates on  $\text{Herm}(n)$ .*

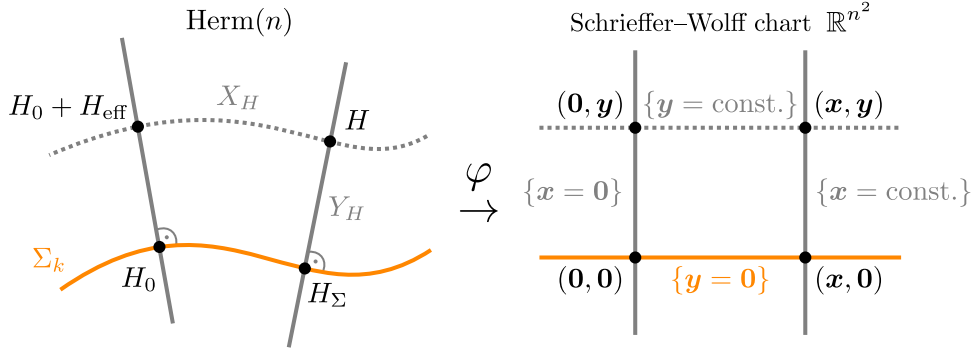


Figure 3.3: A schematic picture showing the local chart induced by the SW decomposition around the fixed  $H_0$ . A matrix  $H \in \mathcal{V}_0$  is endowed with two sets of coordinates: (1) the projection  $H_{\text{proj}} = H_\Sigma$  of  $H$  to  $\Sigma_2$  is described by the coordinates of  $S$ ,  $B$  and  $T$  (these are  $n^2 - 3$  coordinates denoted by  $x_i$ ), (2) the traceless effective Hamiltonian  $H_{\text{eff}}$  is described by 3 coordinates denoted by  $y_i$ . The constant level set of the  $y$  and  $x$  coordinates through  $H$  is denoted by  $X_H$  and  $Y_H$ , respectively. The  $Y_H$  sets are affine subspaces in  $\text{Herm}(n)$  of dimension 3. As an essential step of the proof of Theorem 3.23 (see Proposition 117 in Appendix B.2) we will show that the line joining  $H$  and  $H_\Sigma$  is orthogonal to  $\Sigma_2$  at  $H_\Sigma$ , or equivalently, the  $Y_H$  subspaces are orthogonal to  $\Sigma_2$ , moreover,  $H_\Sigma$  is the closest point of  $\Sigma_2$  to  $H$ .

(b) In this local chart the set  $\Sigma_2$  of 2-fold ground state degenerate matrices is the common zero locus of the coordinates  $y_j$ , that is,

$$\Sigma_2 \cap \mathcal{V}_0 = \{H \in \mathcal{V}_0 \mid y_1(H) = y_2(H) = y_3(H) = 0\}. \quad (3.18)$$

This chart shows that  $\Sigma_2$  is a codimension-3 submanifold in  $\text{Herm}(n)$ , providing an alternative proof for the Neumann–Wigner theorem (whose original proof is summarised in Table 3.1).

Consider the projection  $H_{\text{proj}}$  of  $H$  to  $\Sigma_2$  by omitting  $H_{\text{eff}}$  from the SW decomposition (3.15), that is,

$$H_{\text{proj}} = e^{iS} \cdot (H_0 + B + T) \cdot e^{-iS}. \quad (3.19)$$

This can be rephrased in the SW chart picture as making the  $y_j$  coordinates 0, see Figure 3.3. We show that  $H_{\text{proj}}$  can be constructed without using the SW decomposition. The following construction works for the large set  $H \in \text{Herm}(n) \setminus \Sigma_{[2,3]}$  of Hermitian matrices, not only on the domain  $\mathcal{V}_0$  of the SW decomposition around an  $H_0$ . Let  $\Lambda = U^{-1}HU$  be a diagonalization of  $H$ , containing the eigenvalues  $\lambda_1 \leq \lambda_2 < \lambda_3 \leq \dots \leq \lambda_n$  of  $H$ . Let

$$\bar{\lambda} = \frac{\lambda_1 + \lambda_2}{2}. \quad (3.20)$$

be the average of the lowest two eigenvalues. Let  $\Lambda_\Sigma$  be the diagonal matrix obtained from  $\Lambda$  by replacing the first 2 entries  $\lambda_j$  ( $j = 1, 2$ ) with  $\bar{\lambda}$ . Define

$$H_\Sigma = U \cdot \Lambda_\Sigma \cdot U^{-1}, \quad (3.21)$$

the matrix obtained from  $H$  by ‘collapsing the lowest two eigenvalues’. Observe that  $H_\Sigma \in \Sigma_2$ . In Section B.1 we show that  $H_\Sigma$  does not depend on the choice of the unitary matrix  $U$ , and  $H_\Sigma$  depends on  $H$  in analytic way, although  $U$  cannot be chosen continuously. The following statement will be also proved in Appendix B.1.

**Theorem 3.22** (Projection to  $\Sigma_2$ , cf. Figure 3.3). *If the SW decomposition (3.15) of  $H$  with respect to  $H_0 \in \Sigma_2$  is defined, then it holds that  $H_\Sigma = H_{\text{proj}}$ .*

### 3.4 Energy splitting and the distance from $\Sigma_2$

Recall the distance of two matrices  $H, G \in \text{Herm}(n)$  induced by the Frobenius metric is denoted by  $d(H, G) = \|H - G\|$ . The distance  $d(H, A)$  of an element  $H \in \text{Herm}(n)$  and a subset  $A \subset \text{Herm}(n)$  is the infimum of the distances  $d(H, G)$ ,  $G \in A$ .

**Theorem 3.23** (Distance from  $\Sigma_2$ ). *For every  $H \in \text{Herm}(n) \setminus \Sigma_{[2,3]}$*

$$d(H, \Sigma_2) = d(H, H_\Sigma) = \frac{1}{\sqrt{2}} \cdot |\lambda_2 - \lambda_1| = \|H_{\text{eff}}\|, \quad (3.24)$$

where  $\lambda_1$  and  $\lambda_2$  are the lowest two eigenvalues of  $H$  and  $H_{\text{eff}}$  is the effective Hamiltonian of  $H$  with respect to any  $H_0 \in \Sigma_2$  for which the exact SW decomposition (3.15) of  $H$  is defined.

The first equation expresses that  $H_\Sigma$  is the closest point of  $\Sigma_2$  to  $H$ . We note that the first and second equations hold also for  $H \in \Sigma_{[2,3]}$ , although, the projection  $H_\Sigma$  is not unique, as it depends on the choice of  $U$ .

### 3.5 Parameter-dependent quantum systems and Weyl points

Parameter-dependent quantum systems are described by a smooth ( $\mathcal{C}^\infty$ ) map from a manifold  $M$  of dimension  $m$  to the space of Hamiltonians, i.e., Hermitian matrices  $\text{Herm}(n)$ . Slightly abusing the notation again, we denote this map by  $H$ . So from now on  $H : M \rightarrow \text{Herm}(n)$  is a smooth map with  $H(p_0) = H_0 \in \Sigma_2$  for a point  $p_0 \in M$ , which is called degeneracy point. For simplicity, assume that  $H_0$  is diagonal.

As above, let  $\mathcal{V}_0$  denote a neighborhood of  $H_0$  where the SW decomposition is unique. Then, consider the corresponding neighborhood  $\mathcal{W}_0 \subset H^{-1}(\mathcal{V}_0)$  of  $p_0$  in  $M$ . On this  $\mathcal{W}_0$ , the (traceless) effective Hamiltonian map is defined by the SW decomposition, that is,

$$H_{\text{eff}} : \mathcal{W}_0 \rightarrow \text{Herm}_0(2). \quad (3.25)$$

By introducing a local chart in  $\mathcal{W}_0$  centered at  $p_0$  (i.e.,  $p_0 = 0$ ) and expressing  $H_{\text{eff}}$  in the basis  $\check{c}_i$  of  $\text{Herm}_0(k)$  (cf. Sec. 3.3), we obtain a map

$$h : \mathbb{R}^m \rightarrow \mathbb{R}^3 \quad (3.26)$$

defined in a neighborhood of the origin, satisfying  $h(0) = 0$ . The  $i$ -th component of  $h$  is  $h_i = y_i \circ H$  ( $i = 1, 2, 3$ ), where  $y_i$  are the effective coordinates of the SW chart in Corollary 3.17. This is illustrated in Fig. 3.4.

If we want to describe the ‘type’ of the degeneracy point  $p_0$ , this problem leads to the description of the intersection of  $H$  and  $\Sigma_2$  at  $H_0$ , which can be reduced to the description of the ‘type’ of the root of  $h$  at 0. For this it is necessary to know  $h$  in an arbitrarily small neighborhood of the origin. This description of the degeneracy point leads to the study of map germs  $h : (\mathbb{R}^m, 0) \rightarrow (\mathbb{R}^3, 0)$ , and their classifications in singularity theory. Although this relation between degeneracy points and singularities implicitly appears in several works, see e.g. [74, 75, 46, 76], this relation is essentially based on the geometric picture described here. We illustrate this relation on the characterization of Weyl points. Weyl points represent the simplest type of degeneracy, and we show that they correspond to the simplest type of intersection called transverse intersection of  $H$  and  $\Sigma$ , and also to the simplest singularity type of  $h$ . These relations explain the protected nature of Weyl points, as a straightforward consequence of transversality.

Recall that in the physics terminology, Weyl points are isolated two-fold degeneracy points in a 3-dimensional parameter space, with linear energy splitting in every direction. We formalize this informal description below.

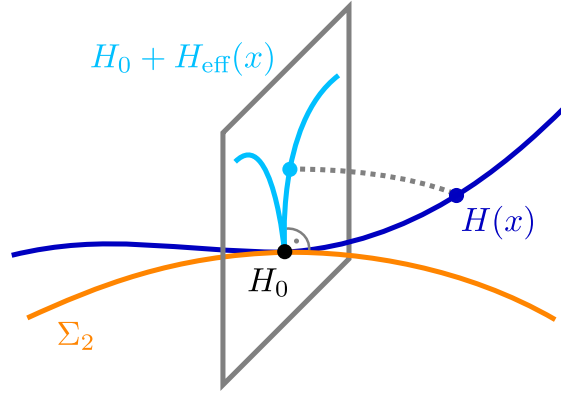


Figure 3.4: Illustration of the effective Hamiltonian map. The image of the parameter-dependent Hamiltonian  $H : M \rightarrow \text{Herm}(n)$  touches the two-fold degeneracy set  $\Sigma_2$  at  $H_0$ . The effective Hamiltonian  $H_{\text{eff}} \rightarrow \text{Herm}_0(2)$  is obtained by taking the SW chart in the neighborhood of  $H_0$ , and keeping only the three outgoing  $y_i$  components. In the example shown the reduced map  $H_{\text{eff}}$  becomes singular at the contact point because  $H$  is tangent to  $\Sigma_2$ .

First, we define what is the order of energy splitting of a degeneracy along a curve. For a curve  $\gamma : (\mathbb{R}, 0) \rightarrow (M, p_0)$  and  $\gamma'(0) \neq 0$ . The energy splitting along  $H \circ \gamma$  is measured by

$$(\Delta_{12} \circ \gamma)(t) := \lambda_2((H \circ \gamma)(t)) - \lambda_1((H \circ \gamma)(t)). \quad (3.27)$$

By Theorem 3.23 this agrees with the distance function up to a scalar factor, that is,

$$(\Delta_{12} \circ \gamma)(t) = \sqrt{2}d((H \circ \gamma)(t), \Sigma_2) = \sqrt{2}\|(H_{\text{eff}} \circ \gamma)(t)\|. \quad (3.28)$$

**Definition 3.29** (Order of energy splitting).

$$r(\gamma) := \text{ord}_0(H_{\text{eff}} \circ \gamma) \equiv \text{ord}_0(h \circ \gamma) \equiv \min_{1 \leq i \leq 3} \{\text{ord}_0(h_i \circ \gamma)\} = \frac{\text{ord}_0(\Delta_{12}^2 \circ \gamma)}{2}, \quad (3.30)$$

where  $\text{ord}_0(f)$  denotes the order of the function  $f$  at  $t = 0$ .

The last equation comes from  $\Delta_{12}^2 = 2\|H_{\text{eff}}\|^2$ . The squaring is needed, because  $\Delta_{12} \circ \gamma$  is not always a smooth function at  $t = 0$ .

**Remark 3.31.** One might wonder why we consider arbitrary curves rather than just straight lines through the point of degeneracy. The following example illustrates the issue. Take the effective map

$$h(x, y, z) = (x - z^2, y, z^3). \quad (3.32)$$

Along any line with nonzero  $x$ - or  $y$ -component, the splitting is linear. Along the  $z$ -axis one obtains quadratic splitting, since  $h(0, 0, t) = (-t^2, 0, t^3)$ . However, by considering a more general curve one can reach higher order. For instance, with the parabola  $\gamma(t) = (t^2, 0, t)$  we obtain

$$h \circ \gamma(t) = (0, 0, t^3), \quad (3.33)$$

so the splitting is cubic along  $\gamma$ . This is not a far-fetched example: already in the spin-orbit coupled two-spin system degeneracy pattern (VI) introduced in Section 2.4.1 gives rise to such degeneracy points with cubic splitting along the appropriate curve. The splitting was explicitly mentioned in Section 2.6.

Now we formalize what is a Weyl point. Recall the notion of transversality, see e.g. [77, 78]. Consider smooth manifolds  $M$  and  $N$ , a smooth submanifold  $Z \subset N$  of  $N$ , and a smooth map  $f : M \rightarrow N$  with  $f(p) \in Z$  for a point  $p \in M$ . The tangent map  $df_p$  is a linear map from the tangent space  $T_p M$  of  $M$  at  $p$  to the tangent space  $T_{f(p)} N$  of  $N$  at  $f(p)$ . In local coordinates  $(df)_p$  is the Jacobian matrix. Then,  $f$  is *transverse* to  $Z$  at  $p$  if

$$T_{f(p)} Z + (df)_p(T_p M) = T_{f(p)} N \quad (3.34)$$

holds. That is, the tangent space of the submanifold  $Z$  and the image of the tangent map  $(df)_p$  span the tangent space of  $N$  at  $f(p)$ , see panel (a) and (d) in Figure 1.1.

Transversality implies the expected dimension of the preimage, namely, if  $f$  is transverse to  $Z$  at every point of  $f^{-1}(Z)$ , then  $f^{-1}(Z)$  is a submanifold of  $M$  of dimension  $\dim(f^{-1}(Z)) = \dim(M) + \dim(Z) - \dim(N)$ , see [77, pg. 28]. By the statements closely related to the transversality theorem [77, pg. 35, 68-69], transversality with respect to a fixed submanifold is a stable and generic property of smooth maps, cf. Figure 1.1.

**Theorem 3.35** (Characterization of Weyl points). *Given a parameter-dependent quantum system by a  $C^\infty$  map  $H : M^3 \rightarrow \text{Herm}(n)$  and a two-fold ground state degeneracy point  $p_0 \in M^3$ ,  $H(p_0) = H_0 \in \Sigma_2$  and the induced effective map germ  $h : (\mathbb{R}^3, 0) \rightarrow (\mathbb{R}^3, 0)$ , the following properties are equivalent:*

1. *The map  $H$  is transverse to  $\Sigma_2$  at  $p_0$ ,*
2. *The rank of the Jacobian of  $h$  at 0 has maximal rank, i.e.  $\text{rk}((dh)_0) = 3$ .*
3. *Taking any curve  $\gamma : (\mathbb{R}, 0) \rightarrow (M^3, p_0)$  with  $\gamma(0) = p_0$  and  $\gamma'(0) \neq 0$ , for the composition  $(h \circ \gamma)'(0) \neq 0$  holds.*
4. *Taking any curve  $\gamma : (\mathbb{R}, 0) \rightarrow (M^3, p_0)$  with  $\gamma(0) = p_0$  and  $\gamma'(0) \neq 0$ , for the composition  $H \circ \gamma$  the energy splitting is linear.*

A two-fold degeneracy point  $p_0$  satisfying any, hence all of the properties (1)–(4) is called Weyl point. Note that (4) formulates the physicist definition.

**Remark 3.36.** *By (2), the characterization of Weyl points is already determined by the first-order part of the exact effective map  $h$ . It implies that in the approximate computation of the SW transformation (see e.g. [44, 45]) to the first-order term is sufficient to decide whether a degeneracy point  $p_0 \in M^3$  is a Weyl point or not. Namely, it can be decided by the following steps, cf. Example 3.6.3:*

1. *Take the first-order SW transformation, i.e. the upper-left traceless  $2 \times 2$  block of  $H(p)$ .*
2. *Via the Pauli decomposition it can be considered as a map  $h^{(1)} : \mathbb{R}^3 \rightarrow \mathbb{R}^3$ , defined in a neighborhood of the origin  $p_0 = 0$ .*
3.  *$p_0$  is a Weyl point if and only if  $\text{rk}((dh^{(1)})_0) = 3$ .*

**Remark 3.37.** *Note that the Jacobian matrix of the first-order effective map  $(dh^{(1)})_0$  is the effective  $g$ -tensor (up to a  $\sqrt{2}$  factor) of the degeneracy point defined in Eq. (2.45).*

**Remark 3.38.** *Observe that the codimension of  $\Sigma_2$  in  $\text{Herm}(n)$  is 3, and we also take the parameter space  $M$  to be 3-dimensional. This situation arises in many physical contexts (such as 3D crystals or magnetic fields, see Chapter 2 and Chapter 4). The coincidence of these dimensions allows point-like transverse intersections, which in turn gives rise to Weyl points.*

The properties of the transversality mentioned above imply the following corollaries.

**Corollary 3.39** (Weyl points are isolated). *Every Weyl point  $p_0$  is an isolated degeneracy point, in the sense that there is a neighborhood  $\mathcal{W}_0 \subset M^3$  of  $p_0$  such that  $H(p) \notin \Sigma_2$  for  $p_0 \neq p \in \mathcal{W}_0$ .*

Intuitively, the protected nature of Weyl points includes the following phenomena:

- (a) *Weyl points are stable:* For any small perturbation, a Weyl point does not disappear, it only gets displaced by a small amount in  $M$  (if at all).
- (b) *Weyl points are generic:* Under a generic perturbation, any degeneracy that is not a Weyl point either splits into Weyl points or disappears.

To translate (a) and (b) into rigorous claims, we consider one-parameter perturbations  $H_t$  of  $H$ . Formally, these are  $\mathcal{C}^\infty$  maps (germs) from  $M^3 \times \mathbb{R}$  to  $\text{Herm}(n)$  defined on a neighborhood of  $(p_0, 0)$ , such that  $H_{t=0} = H$ . For simplicity we formulate the statement in a local version for isolated two-fold degeneracy points, although, it can be generalized for non-isolated or multifold degeneracy points, see Remark 139.

**Corollary 3.40** (Weyl points are stable and generic). *Let  $H : M^3 \rightarrow \text{Herm}(n)$  be a parameter-dependent quantum system with an isolated two-fold ground state degeneracy point  $p_0 \in M^3$ ,  $H(p_0) = H_0 \in \Sigma_2$ . Let  $\mathcal{W}_0 \subset M^3$  be a neighborhood of  $p_0$  whose closure  $\text{cl}(\mathcal{W}_0)$  is compact and it does not contain other ground state degeneracy points, that is,  $H^{-1}(\text{cl}(\Sigma_2)) \cap \text{cl}(\mathcal{W}_0) = \{p_0\}$ .*

- (a) *If  $p_0$  is a Weyl point, then for every one-parameter perturbation  $H_t$  of  $H_{t=0} = H$ , there is an  $0 < \epsilon$ , such that for  $|t| < \epsilon$  the perturbed Hamiltonian  $H_t$  has exactly one degeneracy point in  $\mathcal{W}_0$ , and it is a Weyl point. Moreover, there is a  $\mathcal{C}^\infty$  curve  $\gamma : (-\epsilon, \epsilon) \rightarrow M^3$  such that  $\gamma(t)$  is the unique Weyl point of  $H_t$  in  $\mathcal{W}_0$ .*
- (b) *If  $p_0$  is not a Weyl point, then for every  $0 < \epsilon$  there is a  $K \in \text{Herm}(n)$  with  $\|K\| < \epsilon$ , such that every degeneracy point of the perturbed map  $H_K : p \mapsto H_K(p) = H(p) + K$  in  $\mathcal{W}_0$  is a Weyl point.*

Finally, Property (2) of Theorem 3.35 implies that the topological charge of a Weyl point is  $\pm 1$ . Indeed, the topological charge is equal to the local degree  $\text{deg}_0 h$  of  $h$  at 0, which is  $\text{sgn det dh}_0$ , if  $\text{rk}(dh_0) = 3$ , see Section 4.4. (Note that in the physics literature the topological charge is defined as the first Chern number of the eigenvector bundle corresponding to the lowest eigenvalue, evaluated on a small sphere in  $M^3$  around  $p_0$ , but it is equal to the local degree  $\text{deg}_0 h$  of  $h$  at 0.)

## 3.6 Examples

### 3.6.1 $3 \times 3$ Hermitian matrices in the vicinity of $\text{diag}(0,0,1)$

In the case of  $3 \times 3$  matrices, the exact SW decomposition 3.13 can be given in a closed form using Cardano’s formula to determine the diagonalization, then, to get the block-diagonalized form, one needs to perform the exact direct rotation between the near-degenerate subspaces. However, the resulting expressions are extremely complicated. As an alternative to exact decomposition, one might use a series expansion [44] to approximate the terms of the decomposition.

As an example, we take a general  $H \in \text{Herm}(3)$  around  $H_0 = \text{diag}(0, 0, 1) \in \Sigma_2$  with the elements as coordinates such that

$$H = \begin{pmatrix} 0 & 0 & 0 \\ 0 & 0 & 0 \\ 0 & 0 & 1 \end{pmatrix} + \begin{pmatrix} v + z & x - iy & p - iq \\ x + iy & v - z & r - is \\ p + iq & r + is & w \end{pmatrix}. \quad (3.41)$$

The SW decomposition up to second order reads

$$iS^{(2)} = \begin{pmatrix} 0 & 0 & (1+v-w+z)(p-iq) + (x-iy)(r-is) \\ 0 & 0 & (1+v-w-z)(r-is) + (x+iy)(p-iq) \\ -\text{h.c.} & -\text{h.c.} & 0 \end{pmatrix} + \dots, \quad (3.42)$$

$$B^{(2)} = (1+w+p^2+q^2+r^2+s^2+\dots) \begin{pmatrix} 0 & 0 & 0 \\ 0 & 0 & 0 \\ 0 & 0 & 1 \end{pmatrix}, \quad (3.43)$$

$$T^{(2)} = \left( v - \frac{p^2+q^2+r^2+s^2}{2} + \dots \right) \begin{pmatrix} 1 & 0 & 0 \\ 0 & 1 & 0 \\ 0 & 0 & 0 \end{pmatrix}, \text{ and} \quad (3.44)$$

$$\begin{aligned} H_{\text{eff}}^{(2)} &= \begin{pmatrix} z & x-iy & 0 \\ x+iy & -z & 0 \\ 0 & 0 & 0 \end{pmatrix} - \frac{1}{2} \begin{pmatrix} p^2+q^2-r^2-s^2 & 2(p-iq)(r+is) & 0 \\ 2(p+iq)(r-is) & -p^2-q^2+r^2+s^2 & 0 \\ 0 & 0 & 0 \end{pmatrix} + \dots \\ &= (x-pr-qs+\dots)\sigma_x \\ &+ (y+ps-qr+\dots)\sigma_y \\ &+ \left( z - \frac{p^2+q^2-r^2-s^2}{2} + \dots \right) \sigma_z. \end{aligned} \quad (3.45)$$

Recall that in the last equation  $H_{\text{eff}}$  is considered as a  $2 \times 2$  matrix of trace zero. Note that the effective Hamiltonian in the first-order  $H_{\text{eff}}^{(1)}$  is the truncation of  $H$  to its near-degenerate upper-left  $2 \times 2$  block.

### 3.6.2 Exact SW decomposition

In the special case  $p = q = r = s = 0$  in Eq. (3.41) it is trivial to perform the SW decomposition, as  $H$  is already block diagonal, and  $S = 0$ .

For a simple non-trivial example we take the 2 dimensional section of  $\text{Herm}(n)$

$$H(p, r) = \begin{pmatrix} 0 & 0 & p \\ 0 & 0 & r \\ p & r & 1 \end{pmatrix}. \quad (3.46)$$

The components  $S$ ,  $B$ ,  $T$ ,  $H_{\text{eff}}$  of the SW decomposition (3.15) of  $H$  with respect to  $H_0$  can be expressed explicitly as functions of  $p$  and  $r$  as:

$$iS(p, r) = \frac{1}{\sqrt{p^2+r^2}} \tan^{-1} \left( \frac{\sqrt{1+4p^2+4r^2}-1}{2\sqrt{p^2+r^2}} \right) \begin{pmatrix} 0 & 0 & p \\ 0 & 0 & r \\ -p & -r & 0 \end{pmatrix}, \quad (3.47)$$

$$B(p, r) = \frac{1+\sqrt{1+4p^2+4r^2}}{2} \begin{pmatrix} 0 & 0 & 0 \\ 0 & 0 & 0 \\ 0 & 0 & 1 \end{pmatrix}, \quad (3.48)$$

$$T(p, r) = \frac{1-\sqrt{1+4p^2+4r^2}}{4} \begin{pmatrix} 1 & 0 & 0 \\ 0 & 1 & 0 \\ 0 & 0 & 0 \end{pmatrix}, \text{ and} \quad (3.49)$$

$$\begin{aligned} H_{\text{eff}}(p, r) &= \frac{1-\sqrt{1+4p^2+4r^2}}{4(p^2+r^2)} \begin{pmatrix} p^2-r^2 & 2pr & 0 \\ 2pr & -p^2+r^2 & 0 \\ 0 & 0 & 0 \end{pmatrix} \\ &= \frac{1-\sqrt{1+4p^2+4r^2}}{4(p^2+r^2)} (2pr\sigma_x + (p^2-r^2)\sigma_z). \end{aligned} \quad (3.50)$$

Observe that every term  $S$ ,  $B$ ,  $T$  and  $H_{\text{eff}}$  is an analytic function of  $(p, r)$  in a neighborhood of  $(0, 0)$ , although this is not obvious at first sight. The non-analytic behaviour of these maps far from  $(0, 0)$  shows that the SW decomposition can only be defined locally.

### 3.6.3 Explicit example of a Weyl point

In Sec. 3.5 we have discussed the generic nature of Weyl points in a mathematical context. This discussion is relevant to many physical setups. Weyl points arise as spectral features in the electronic, phononic, photonic, magnonic band structures of crystalline materials, or metamaterials. More generally, Weyl points also arise in quantum systems described by a Hamiltonian depending on three parameters. One example is an interacting spin system in a homogeneous magnetic field, where the manifold of parameters is  $M = \mathbb{R}^3$ , corresponding to the external magnetic field vector [21, 23]. Another example is a multiterminal Josephson junction, where the manifold of parameters is the three-dimensional torus, hosting the values of three magnetic flux biases piercing the loops of the superconducting circuit [79, 24, 80].

An explicit  $3 \times 3$  example for a Hamiltonian with a Weyl point is the following:

$$H(x, y, z) = \begin{pmatrix} z & x - iy & y - iz \\ x + iy & -z & x - iz \\ y + iz & x + iz & 1 + xyz \end{pmatrix}. \quad (3.51)$$

This matrix has a two-fold ground state degeneracy at  $x = y = z = 0$ . This is a Weyl point according to Remark 3.36 as the first-order effective Hamiltonian is

$$H_{\text{eff}}^{(1)}(x, y, z) = x\sigma_x + y\sigma_y + z\sigma_z, \quad (3.52)$$

which, expanded in the orthonormal Pauli basis, corresponds to the effective map

$$h^{(1)}(x, y, z) = \sqrt{2}(x, y, z). \quad (3.53)$$

The Jacobian of  $h^{(1)}$  is  $\sqrt{2}$  times the identity, hence it has maximal rank 3. Note that the off-block matrix elements can be arbitrary functions of  $x, y$  and  $z$  with constant term 0, so that the resulting Hamiltonian still describes a Weyl point at the origin. Moreover, one can also perturb the  $2 \times 2$  block with higher-order terms without destroying the Weyl point, as they do not change the Jacobian (and hence its rank) of the first-order effective map  $h^{(1)}$  at the origin. Off-block and higher-order terms have significant effect, with the possibility of creating new degeneracy points, only far from the origin.

### 3.6.4 Parameter-dependent quantum systems exhibiting non-generic degeneracy points

A  $4 \times 4$  example of a point-like degeneracy that is not a Weyl point occurs in A-B-stacked bilayer graphene. The linearized tight binding model around the  $K$  point reads [81]

$$H(\mathbf{k}) = \begin{pmatrix} 0 & \hbar v(k_x - ik_y) & 0 & 0 \\ \hbar v(k_x + ik_y) & 0 & \gamma_1 & 0 \\ 0 & \gamma_1 & 0 & \hbar v(k_x - ik_y) \\ 0 & 0 & \hbar v(k_x + ik_y) & 0 \end{pmatrix}, \quad (3.54)$$

where the 2D quasimomentum vector  $\mathbf{k}$  is measured from  $K$ ,  $v$  is the intralayer band velocity and  $\gamma_1$  is the vertical interlayer hopping. This matrix exhibits a degeneracy between the two

middle states at 0. For the excited states, the Schrieffer–Wolff transformation still applies, and by computing the second-order effective Hamiltonian we obtain

$$H_{\text{eff}}^{(2)}(\mathbf{k}) = \frac{\hbar^2}{2m} \begin{pmatrix} 0 & (k_x - ik_y)^2 \\ (k_x + ik_y)^2 & 0 \end{pmatrix} \quad (3.55)$$

$$= \frac{\hbar^2}{2m} ((k_x^2 - k_y^2)\sigma_x + (2k_x k_y)\sigma_y), \quad (3.56)$$

where  $m = \gamma_1/2v^2$ .

Notice that Eq.(3.54) defines a linear Hamiltonian. Hence its image, in the 16-dimensional space of  $4 \times 4$  Hermitian matrices, is a two-dimensional plane. For this Hamiltonian the energy splitting is quadratic along any curve  $\gamma : \mathbb{R} \rightarrow \mathbb{R}^2$  with  $\gamma(0) = 0$  and  $\gamma'(0) \neq 0$ . By the distance theorem (Theorem 3.23), which states that the energy splitting equals the distance from the degeneracy manifold, this implies that the image plane of the Hamiltonian map is tangent to the degeneracy stratum  $\Sigma_2$  in every direction.

Moreover, the effective map is not equidimensional, so a generic small perturbation completely removes the degeneracy; cf. panel (c) in Figure 1.1.

The absence of the  $\sigma_z$  component in Eq. (3.56) is a consequence of chiral symmetry. Therefore the effective Hamiltonian can be viewed as a map  $M^2 \rightarrow \mathbb{R}^2$ . If the system is perturbed by chiral-symmetry-preserving terms, the Hamiltonian remains equidimensional, and the degeneracy typically splits into 2D Weyl points rather than disappearing entirely (although this is not strictly excluded). In the next chapter we will investigate this scenario.

If we compare Eq.(3.56) with Eq.(3.50), the similarity is striking. Indeed, after a simple rescaling and a permutation of the Pauli matrices, the two effective Hamiltonians agree to leading order. This provides an example where, if we interpret Eq. (3.46) as a linear Hamiltonian map  $\mathbb{R}^2 \rightarrow \text{Herm}(3)$ , then both Hamiltonians exhibit a twofold degeneracy at the origin, which are equivalent in a suitable sense, although the original maps are quite different.

### 3.7 Conclusions

In this chapter, we investigated the geometry of the  $n^2$ -dimensional Euclidean space of  $n \times n$  Hermitian matrices in relation to their degeneracies. We began by introducing a coordinate system for Hermitian matrices and describing their stratification according to eigenvalue degeneracies. Throughout this work, we focused on two-fold ground state degeneracies, although in Ref. [40] we have generalized our results to higher-order and excited-state degeneracies as well.

We showed that the Schrieffer–Wolff (SW) transformation provides a local chart around a degeneracy: it yields a coordinate system in which  $n^2 - 3$  parameters vary within the degeneracy manifold, while the remaining 3 coordinates, which form the effective Hamiltonian, correspond to directions transverse to it.

We also demonstrated that the distance of a Hamiltonian from the ground state degeneracy manifold is proportional to the splitting of lowest to eigenvalues. Moreover, in the case of parameter-dependent Hamiltonians, the SW transformation defines an effective Hamiltonian as a smooth map from the parameter space to  $\mathbb{R}^3$ , whose zero set corresponds to the degeneracy locus. This reduces the problem of characterizing degeneracies to the study of zero sets of multivariable functions, allowing techniques from singularity theory to be applied.

As a concrete example, we identified Weyl points as transverse intersections, which are therefore generic and stable. We argued that transversality is already encoded at first order, which allows us to identify Weyl points purely based on the maximal rank of the effective  $g$ -tensor.



## Chapter 4

# Birth Quota of Non-Generic Degeneracy Points

In Chapter 2 we explored degeneracies from a naive perspective and in Chapter 3 established a connection between degeneracies and the zero sets of vector-valued functions. The focus of this chapter is to show how the well-known concept of root multiplicity manifests itself in the context of degeneracies in quantum systems

In this chapter, we continue to study point-like degeneracies, but now we turn our attention to non-generic cases. Previously, we encountered such points in the context of Weyl-point collisions, where non-generic degeneracies can emerge. Crystal symmetries, however, can stabilize isolated non-generic two-fold degeneracy points, such as multi-Weyl points, in the electronic band structure of three-dimensional solids [4, 26, 82, 29]. If the symmetry is broken, e.g., by changing an external magnetic (Zeeman) field or applying mechanical strain, the non-generic degeneracy point splits into multiple Weyl points [4]. As the symmetry-breaking perturbation is switched on gradually, these newly born Weyl points follow continuous trajectories in the Brillouin zone, originating from the original degeneracy point.

The question naturally arises: For a given non-generic degeneracy point, how many Weyl points can emerge upon perturbation? From topological charge conservation and the generic character of Weyl points, it follows that the minimum number of newborn Weyl points upon a generic perturbation is the absolute value  $|Q|$  of the topological charge  $Q$  associated to the non-generic degeneracy point (e.g. the Chern number in 3D). The same consideration implies that the number of newborn Weyl points may also be  $|Q| + 2M$  with  $M$  being a positive integer, in such a way that  $M$  of the excess Weyl points have unit positive charge and  $M$  have unit negative charge, hence the sum of the charges of the newborn Weyl points equals  $Q$ . Is there also a ‘birth quota’, i.e., an upper limit of the number of newborn Weyl points? This is a fundamental question, which has only been studied to a limited extent in the mathematical physics literature [74], and the implications to realistic physical systems remain unexplored.

In this chapter, we answer this question positively, and show that such a non-generic degeneracy point does have a birth quota, which turns out to be the so-called *local multiplicity* known in singularity theory. Our result is not exclusive to Weyl points in three dimensions (3D), we also obtain an analogous result for two-dimensional (2D) crystals with chiral symmetry illustrated on the example of bilayer graphene, as well as a minimal example in 1D (Fig. 4.2). We emphasize that our analysis covers the effect of *any* possible perturbation. While this may sound surprising, it is possible to derive such general results using singularity theory.

We showcase the power of these results on quasiparticle (electronic, photonic, phononic) band structures: we compute the birth quota of all four types of two-fold degeneracies stabilised by the 230 crystalline space groups [29] (Table 4.1). However, the notion of the birth quota is more generic: it is applicable to quantum systems controlled by external parameters, such as

interacting spin systems [18, 19, 21, 23, 80] or quantum circuits [24, 34]; more generally, it is applicable to any physical system that is described by a matrix, e.g., linearly coupled mechanical oscillators or electromagnetic modes.

## 4.1 Bilayer graphene

We illustrate the birth of Weyl points from a non-generic degeneracy point by the already mentioned example of electrons in A-B-stacked bilayer graphene (Fig. 4.1). This is a two-dimensional crystal, whose simplest band-structure models have chiral (a.k.a. sublattice) symmetry, which protects the accidental degeneracies (2D Weyl points) in the two-dimensional Brillouin zone. A simple tight-binding model of delocalized electrons in graphene yields the following  $2 \times 2$  Hamiltonian (see Section 3.6.4), valid in the vicinity of the high-symmetry point  $K$  (and  $K'$ ) of the Brillouin zone [81, 83]:

$$H = \frac{\hbar^2}{2m} \begin{pmatrix} 0 & (k_x - ik_y)^2 \\ (k_x + ik_y)^2 & 0 \end{pmatrix}. \quad (4.1)$$

Here,  $k_{x,y}$  are momentum components measured from  $K$ , and the matrix represents a combined layer-sublattice degree of freedom. The effective mass is  $m \approx 0.035 m_e$  [81, 83].

This Hamiltonian exemplifies a non-generic degeneracy point in 2D, located at  $(k_x, k_y) = 0$  with dispersion  $E_{\pm} = \pm \hbar^2 k^2 / 2m$  quadratic in momentum (Fig. 4.1a). To illustrate the structure of this degeneracy point, we first decompose the Hamiltonian with Pauli matrices,  $H \propto (k_x^2 - k_y^2) \sigma_x + 2k_x k_y \sigma_y$ , where chiral symmetry forbids the  $\sigma_z$  term [7]. It also forbids a  $\sigma_0$  term, but as it does not affect the band-degeneracies, we ignore such terms in the following. This allows us to reinterpret the Hamiltonian as the dimensionless *effective Hamiltonian map*

$$h : \mathbb{R}^2 \rightarrow \mathbb{R}^2, (k_x, k_y) \mapsto (k_x^2 - k_y^2, 2k_x k_y). \quad (4.2)$$

We plot how the signs (color coded) of the value of this map change on the  $(k_x, k_y)$  plane in Fig. 4.1b. The meeting point of all colors defines the degeneracy point, and the color pattern in its neighborhood shows that this point has a winding number (or charge) of  $Q_{2D} = 2$ .

One type of perturbation to this degeneracy point is mechanical strain: applying it along  $x$  adds the perturbation term<sup>1</sup>

$$H_s = - \begin{pmatrix} 0 & w \\ w & 0 \end{pmatrix} \quad (4.3)$$

to  $H$ ; strain of 1% yields  $w \approx 6$  meV [84]. The effect of the strain is shown in Fig. 4.1c,d: the non-generic degeneracy point is split to two 2D Weyl points at

$$\mathbf{k}_{\pm} = \left( \pm \frac{\sqrt{2mw}}{\hbar}, 0 \right), \quad (4.4)$$

both having charge  $Q_{2D} = 1$ , i.e., the total charge is conserved upon perturbation.

Another type of perturbation appears when the skew interlayer hopping is taken into account, causing *trigonal warping*. This perturbation term is described by

$$H_{tw} = -\hbar v_3 \begin{pmatrix} 0 & k_x + ik_y \\ k_x - ik_y & 0 \end{pmatrix}, \quad (4.5)$$

<sup>1</sup>This is the effective form of the perturbation. In reality, strain modifies the hopping amplitudes of the original  $4 \times 4$  Hamiltonian, which in turn descend to the  $2 \times 2$  model in the form given here.

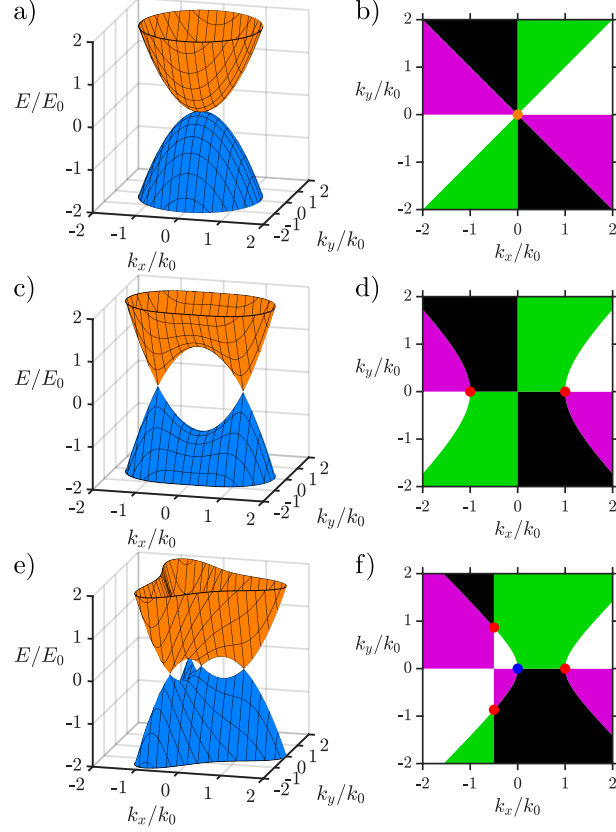


Figure 4.1: Birth of 2D Weyl points from a non-generic degeneracy point in bilayer graphene. a-b) Non-generic degeneracy point. a) Dispersion relation of the valence band (blue surface) and conduction band (orange surface) based on Eq. (4.1). b) Colored plane shows the sign pattern of the effective Hamiltonian map  $h$  of bilayer graphene, see Eq. (4.2). White denotes  $(+, +)$  regions, i.e., where both components of  $h(k_x, k_y)$  are positive. Gray:  $(-, +)$ . Black:  $(-, -)$ . Green:  $(+, -)$ . Degeneracies are located where all four colors meet and their charge is equal to the signed number of white-gray-black-green cycles as we go around them counter clockwise. c-d) Two 2D Weyl points born due to mechanical strain, both having charge +1, see Eq. (4.3). e-f) Four 2D Weyl points born due to trigonal warping, see Eq. (4.5). The three outer 2D Weyl points has charge +1, while the inner one has charge  $-1$ . The energy scale is  $E_0 = \hbar^2 k_0^2 / 2m$ , with the wave vector scale  $k_0 = \sqrt{2mw}/\hbar$  for c-d) and  $k_0 = 2mv_3/\hbar$  for e-f). The non-generic degeneracy point of a-b) is scale-invariant.

where  $v_3 \approx 10^5 \frac{\text{m}}{\text{s}}$  [81, 83]. The effect of this perturbation is shown in Fig. 4.1e,f: the non-generic degeneracy point of Fig. 4.1a,b is split to 4 2D Weyl points: 3 having charge  $Q_{2\text{D}} = 1$ , located at

$$\mathbf{k}_n = \frac{2mv_3}{\hbar} \left( \cos \frac{2\pi n}{3}, \sin \frac{2\pi n}{3} \right) \quad n \in \{1, 2, 3\}, \quad (4.6)$$

and 1 having  $Q_{2\text{D}} = -1$ , located at  $\mathbf{k}_4 = (0, 0)$ . Again, the charge of the degeneracy point of  $H$  is conserved by the perturbation.

The observation that the non-generic degeneracy point at  $K$  can split to 2 or 4 2D Weyl points triggers the question: is there a perturbation of  $H$  such that the number of newborn 2D Weyl points is different from 2 or 4? One implication of our analysis below is that the answer is ‘no’, i.e., Fig. 4.1 covers all possibilities. The lower bound (2) is governed by topological charge conservation, whereas the upper bound (4), i.e., the ‘birth quota’, follows from our analysis below.

## 4.2 Minimal 1D model

First, we consider a minimal mathematical model of the birth quota effect: the birth of generic roots (‘1D Weyl points’) of the polynomial  $f : \mathbb{R} \rightarrow \mathbb{R}$ ,  $f(x) = x^3$ , from its non-generic root at the origin  $x = 0$ . Any generic perturbation of the form  $f_t(x) = x^3 + t_1x^2 + t_2x + t_3$  has one or three real roots, and all of them converge to 0 as the vector of control parameters  $t = (t_1, t_2, t_3)$  tends to 0. We draw such perturbations in Fig. 4.2a, where, for simplicity, we set  $(t_1, t_2, t_3) = (0, p, q)$ . In the case of three roots (green region), two of them have positive signs (i.e. the function is increasing, charge +1, red dot), and one has negative sign (the function is decreasing, charge -1, blue dot). In the case of one root (orange region), it has positive sign (charge +1). Hence the sum of the charges is +1, same as the charge of the root of the unperturbed function  $f$ , exemplifying charge conservation.

The number of the real roots changes when the control vector  $t$  steps through the zero locus  $\mathcal{D} = \{(t_1, t_2, t_3) \in \mathbb{R}^3 \mid D(t_1, t_2, t_3) = 0\}$  of the discriminant  $D$  of  $f$  (see Appendix C.2). This *discriminant set*  $\mathcal{D}$  in the control space is illustrated as the purple solid line in Fig. 4.2a.

Importantly, when we consider the complexification<sup>2</sup>  $f_{\mathbb{C},t} : \mathbb{C} \rightarrow \mathbb{C}$ , the *complex discriminant set*  $\mathcal{D}_{\mathbb{C}}$  does not separate different root configurations: one can always find a path between different configurations such that the roots avoid collision in the complex plane. In fact,  $f_{\mathbb{C},t}$  has three distinct complex roots for any  $t \in \mathbb{C}^3 \setminus \mathcal{D}_{\mathbb{C}}$ . This is illustrated by Fig. 4.2b,c,d, displaying the (c) unperturbed map  $f_{\mathbb{C}}$  and (b,d) two perturbed maps, and the roots of those  $\mathbb{C} \rightarrow \mathbb{C}$  maps as red points. The number of complex roots born upon perturbation from the root of  $f_{\mathbb{C}}(x) = x^3$  is called the *local multiplicity*  $\text{mult}_0 f_{\mathbb{C}} = 3$  of  $f_{\mathbb{C}}$  at the root  $x = 0$ . As illustrated in Fig. 4.2c, this local multiplicity is the winding number of  $f_{\mathbb{C}}$  evaluated on a small circle (green) around the root; the value 3 can be read off.

This winding number is also called the *local degree*  $\text{deg}_0 f_{\mathbb{C}}$ , which is defined as the local degree  $\text{deg}_0 f_{\mathbb{C},\mathbb{R}}$  of the real-imaginary decomposition (‘realification’)

$$\begin{aligned} f_{\mathbb{C},\mathbb{R}} &: \mathbb{R}^2 \rightarrow \mathbb{R}^2, \\ (u, v) &\mapsto (\text{Re}(f_{\mathbb{C}}(u + iv)), \text{Im}(f_{\mathbb{C}}(u + iv))) \end{aligned} \quad (4.7)$$

of the complexification  $f_{\mathbb{C}}$ . Here, the explicit form of  $f_{\mathbb{C},\mathbb{R}}$  reads  $f_{\mathbb{C},\mathbb{R}}(u, v) = (u^3 - 3uv^2, 3u^2v - v^3)$ . Since every generic root of  $f_t$  is also a generic root of  $f_{\mathbb{C},t}$ , we conclude that the number of roots born from the original root of  $f$  at  $x = 0$  upon perturbation is upper-bounded by  $\text{deg}_0 f_{\mathbb{C},\mathbb{R}}$ .

<sup>2</sup>For a real analytic function  $f : \mathbb{R}^m \rightarrow \mathbb{R}^n$ , its complexification is defined as the function  $f_{\mathbb{C}} : \mathbb{C}^m \rightarrow \mathbb{C}^n$  that has the same power series as  $f$ .

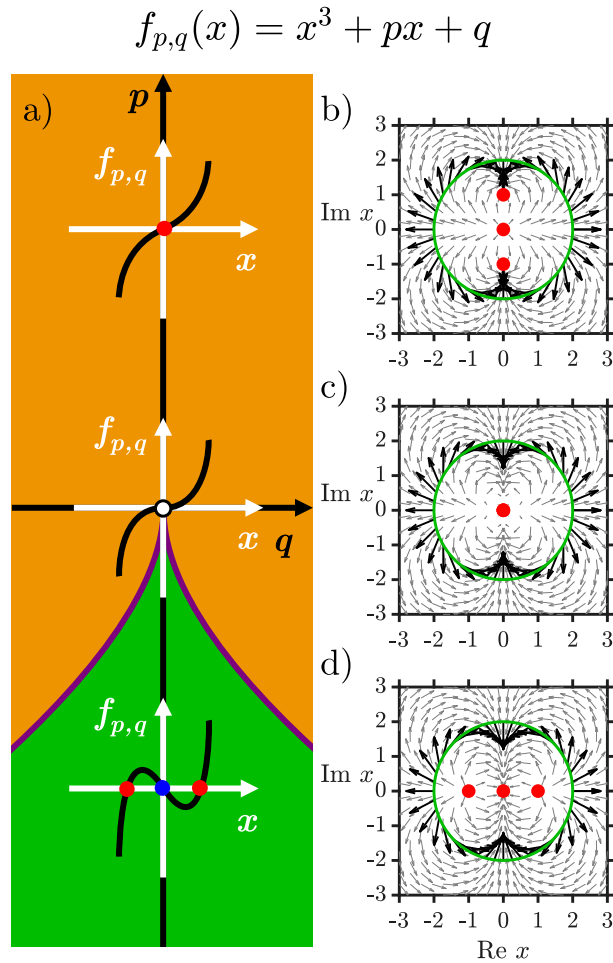


Figure 4.2: Number of generic roots ('1D Weyl points') born from the non-generic root of  $f(x) = x^3$  is lower-bounded by the charge of the root (which is 1) and upper-bounded by the local multiplicity of the root ( $\text{mult}_0 f = 3$ ). a) Phase diagram of perturbations of  $f(x) = x^3$  of the form  $f_{p,q}(x) = x^3 + px + q$ . Orange: perturbation has one generic root. Green: perturbation has three generic roots. Purple line: perturbation has one generic root and one non-generic root. b) Complexified perturbation  $f_{\mathbb{C},p,q}$  with  $p = 1, q = 0$ . c) Complexified map  $f_{\mathbb{C}}(x) = x^3$ , exhibiting a single root with a winding number or local multiplicity  $\text{mult}_0 f = 3$ . d) Complexified perturbation  $f_{\mathbb{C},p,q}$  with  $p = -1, q = 0$ . The complex values of the function are represented as arrows, so phase windings can be read off. b), d) exhibits three complex roots with winding number 1 each, even though the real function  $f_{p,q}$  has b) one real root and d) three real roots.

Note that higher-degree perturbations of  $f$  can have more than three roots, but these extra roots are ‘born at infinity’, not from the original root at  $x = 0$ . For example, the root  $x = 1/t$  of the perturbed map  $f_t(x) = x^3 - tx^4 = -tx^3(x - 1/t)$  goes to infinity as  $t$  tends to 0.

In the rest of this chapter, we outline the generalization of this minimal model, and use it to derive the birth quota of non-generic isolated two-fold degeneracy points.

### 4.3 Effective Hamiltonian at a two-fold degeneracy point

The models we study, e.g., tight-binding models of the electronic band structure, are described by a Hamiltonian map  $H : M^m \rightarrow \text{Herm}(N)$ . Here,  $M^m$  is an  $m$ -manifold, and  $\text{Herm}(N)$  is the real vector space of  $N \times N$  Hermitian matrices. We focus on the example when  $M^m = \text{BZ}$  is the Brillouin zone of a 3D crystal ( $m = 3$ ), but will also comment on the 2D case ( $m = 2$ ), relevant for bilayer graphene described above.

A key quantity in our analysis of the birth quota, analogous to the function  $f$  in the minimal model above, is the *effective Hamiltonian map*  $h$  associated to the non-generic isolated two-fold degeneracy point  $P \in \text{BZ}$ . Denote the ordinal number of the degenerate levels by  $i$  and  $i + 1$ . Then, for the eigenvalues of  $H(P)$ , it holds that  $E_{i-1} < E_i = E_{i+1} < E_{i+2}$ , and  $E_i < E_{i+1}$  holds in a neighborhood  $U_P$  of  $P \in \text{BZ}$ . The effective Hamiltonian map  $h$  is obtained by an exact Schrieffer–Wolff transformation (see Chapter 3) at  $P$ , which provides a map from the neighborhood  $U_P$  of the degeneracy point  $P$  into the space of traceless Hermitian  $2 \times 2$  matrices. The latter matrix space is identified with  $\mathbb{R}^3$  via the standard Pauli-matrix decomposition,  $X\sigma_x + Y\sigma_y + Z\sigma_z \equiv (X, Y, Z)$ , hence the Schrieffer–Wolff transformation yields the effective Hamiltonian map  $h : U_P \rightarrow \mathbb{R}^3$ .

The fact that  $P$  is an isolated degeneracy point can be reformulated as  $h^{-1}(0) = \{P\}$ , i.e. the preimage set of the origin  $0 \in \mathbb{R}^3$  contains only one point. We assume that in the natural wave-vector coordinates of the BZ, measured from  $P$  as the reference point,  $h$  is an analytic map, that is, its Taylor series is convergent and it produces  $h^3$ . This results in an  $h : (\mathbb{R}^3, 0) \rightarrow (\mathbb{R}^3, 0)$  map, consisting of 3 locally convergent power series  $h_1, h_2$  and  $h_3$  of 3 variables, fulfilling  $h(0) = 0$ . Our following analysis works for  $m = 3$  in general, and also for  $m = 2$  assuming chiral symmetry, when the degeneracy is at zero energy. The latter conditions imply  $h_3 = 0$  and provide a map  $h : (\mathbb{R}^2, 0) \rightarrow (\mathbb{R}^2, 0)$ <sup>4</sup>.

### 4.4 Birth quota

Up to now, we converted band-structure features to an  $h : \mathbb{R}^3 \rightarrow \mathbb{R}^3$  analytic map. This enables us to establish the birth quota of a non-generic degeneracy point using concepts and relations from singularity theory. The *local degree*  $\text{deg}_0 h$  of the effective Hamiltonian map  $h : (\mathbb{R}^m, 0) \rightarrow (\mathbb{R}^m, 0)$  at 0 is the *global degree* of the normalised map (‘pseudospin texture’ [26])  $\tilde{h} = \frac{h}{|h|} : S_\epsilon^{m-1} \rightarrow S^{m-1}$  defined on a sufficiently small sphere  $S_\epsilon^{m-1}$  around the origin, see [86, 87, 88, 89, 90] for details. For  $m = 2$  the local degree is a winding number, and for  $m = 3$  it agrees with the first Chern number of the eigenstate corresponding to the  $i$ -th eigenvalue, see [7]. For both cases, the local degree is often referred to as the (topological) charge of the degeneracy

<sup>3</sup>Note that our analysis also works in  $\mathcal{C}^\infty$  (i.e. smooth) category, using the notion of *map germs*, however the analytic condition simplifies the discussion.

<sup>4</sup>Similarly, spinless  $PT$  symmetry restricts the Hamiltonian to be real valued, yielding  $h_2 = 0$ . Hamiltonians with both chiral and  $PT$  symmetry correspond to the case  $m = 1$  with effective Hamiltonian map  $h : (\mathbb{R}, 0) \rightarrow (\mathbb{R}, 0)$ . Such symmetric 1D systems can provide a physical realization of the minimal example with  $H(k) = f(k)\sigma_x$ . Moreover, in systems with fermionic time-reversal symmetry, twofold-degenerate Kramers pairs can meet to form a fourfold degeneracy in a 5-dimensional parameter space, known as an instanton [85].

point. We will also refer to the complexification  $h_{\mathbb{C}} : (\mathbb{C}^m, 0) \rightarrow (\mathbb{C}^m, 0)$  of  $h$ , and its local degree  $\deg_0 h_{\mathbb{C}}$ .

The effect of a physical perturbation on the crystal electrons, e.g., mechanical strain or a change of the magnetic (Zeeman) field, is described in our framework as a *deformation* of the effective Hamiltonian map  $h$ . An unfolding of  $h$  with  $k$  control parameters is an analytic map  $\mathcal{H} : \mathbb{R}^3 \times \mathbb{R}^k \rightarrow \mathbb{R}^3 \times \mathbb{R}^k$  of the special form  $\mathcal{H}(x, y, z, t) = (h_t(x, y, z), t)$ , where  $t \in \mathbb{R}^k$ , such that  $h_0 = h$ . For fixed control parameters  $t$ , we call  $h_t$  an analytic deformation, or simply deformation, of  $h$ . To derive the birth quota of  $h$ , we will use the complex generalizations of these concepts: a holomorphic unfolding  $\mathcal{H}_{\mathbb{C}}$  and the corresponding complex deformation  $h_{\mathbb{C},t}$  of the complexification  $h_{\mathbb{C},0} = h_{\mathbb{C}}$  are defined similarly to the real case above [90, 87].

We call the points of  $h_t^{-1}(0) \subset \mathbb{R}^3$  *degeneracy points* of  $h_t$ , and the points of  $h_{\mathbb{C},t}^{-1}(0) \subset \mathbb{C}^3$  *complex degeneracy points*. A complex degeneracy point  $p$  is generic, and we call it a *complex Weyl point*, if the Jacobian of  $h_{\mathbb{C},t}$  at  $p$  has maximal rank, i.e., rank 3. A real degeneracy point  $p$  is generic, and we call it a (real) *Weyl point*, if the Jacobian of  $h_t$  at  $p$  has maximal rank. This happens if and only if  $p$  is generic as a complex degeneracy point. At a real Weyl point  $p$ , the local degree is  $\deg_p h_t = \pm 1$ , determined by the sign of the Jacobian determinant, cf. [4]. At a complex Weyl point  $p$ , the local degree of  $h_{\mathbb{C},t}$  is always  $\deg_p h_{\mathbb{C},t} = 1$ .

Our goal is to characterize the birth of (real) Weyl points from a non-generic degeneracy point. Hence, we need to distinguish between Weyl points born from the original degeneracy point, and all other Weyl points. This we already noted in the minimal model above, by pointing out that 1D Weyl points can be born at infinity. To make this distinction here, we consider the complex case first. We take a spherical boundary  $S_{\epsilon}^5 \subset \mathbb{C}^3$  in the configuration space, centered at the origin, which we call the *separator*, such that the only degeneracy point of  $h_{\mathbb{C}}$  inside this sphere is the origin. The separator bounds the closed ball  $B_{\epsilon}^6 \subset \mathbb{C}^3$ . When a deformation is applied continuously, the degeneracy points  $h_{\mathbb{C},t}^{-1}(0)$  follow continuous trajectories in the complex configuration space. Therefore, there is a neighborhood  $\mathcal{U}_{\mathbb{C}}$  of the origin of the control space such that for all  $t \in \mathcal{U}_{\mathbb{C}}$ , (i) the degeneracy points born from the original degeneracy point do not reach the separator, and (ii) the degeneracy points of the undeformed map  $h_{\mathbb{C}}$  that are outside of the separator do stay outside. For convenience, we take a neighborhood  $\mathcal{U}_{\mathbb{C}}$  that is an open ball centered at the origin of the control space. Furthermore, from now on, we restrict the unfolding  $\mathcal{H}_{\mathbb{C}}$  onto  $B_{\epsilon}^6 \times \mathcal{U}_{\mathbb{C}}$ .

We define the *complex discriminant set*  $\mathcal{D}_{\mathbb{C}} \subset \mathcal{U}_{\mathbb{C}}$  as those control vectors  $t$  for which  $h_{\mathbb{C},t}$  has non-generic complex degeneracy points in  $B_{\epsilon}^6$ . That is, for any control vector  $t \in \mathcal{U}_{\mathbb{C}} \setminus \mathcal{D}_{\mathbb{C}}$ , all degeneracy points of  $h_{\mathbb{C},t}$  are complex Weyl points. A key observation is that the number of complex Weyl points within  $B_{\epsilon}^6$ , denoted as  $\#h_{\mathbb{C},t}^{-1}(0)$ , is the same for any control vector  $t \in \mathcal{U}_{\mathbb{C}} \setminus \mathcal{D}_{\mathbb{C}}$ . This is related to the fact that the complex codimension of the discriminant set  $\mathcal{D}_{\mathbb{C}}$  is at least 1, and therefore the real codimension is at least 2. This implies that  $\mathcal{U}_{\mathbb{C}} \setminus \mathcal{D}_{\mathbb{C}}$  is path-connected, and hence the number  $\#h_{\mathbb{C},t}^{-1}(0)$  of complex Weyl points cannot change along any control trajectory in  $\mathcal{U}_{\mathbb{C}} \setminus \mathcal{D}_{\mathbb{C}}$ . For details, we refer to Appendix C.1 and [90]. In conclusion, the number of preimages of 0,  $\#h_{\mathbb{C},t}^{-1}(0)$  is a property of  $h_{\mathbb{C}}$ , and hence a property of  $h$ . It is called the *local multiplicity* of  $h_{\mathbb{C}}$  ( $\text{mult}_0 h_{\mathbb{C}}$ ), and also called the *local multiplicity* of  $h$  ( $\text{mult}_0 h$ ).

In the band-structure context, the effective Hamiltonian map  $h$  is a real map. We denote the set of real control vectors  $t \in \mathbb{R}^k$  in  $\mathcal{U}_{\mathbb{C}}$  and  $\mathcal{D}_{\mathbb{C}}$  by  $\mathcal{U}$  and  $\mathcal{D}$ , respectively. With these, we can express the key message of this work: the local multiplicity  $\text{mult}_0 h$  is the birth quota of the original non-generic degeneracy point, i.e,  $\text{mult}_0 h$  is the upper bound of the number of Weyl points born from the original degeneracy point:

$$\#h_t^{-1}(0) \leq \text{mult}_0 h. \quad (4.8)$$

Here,  $h_t$  is restricted to  $B_{\epsilon}^3$  and  $t \in \mathcal{U} \setminus \mathcal{D}$ . Equation (4.8) is a consequence of the previous paragraph, and the fact that a real Weyl point is also a complex Weyl point.

## 4.5 Methods to calculate the birth quota

We mention three different methods to compute the birth quota  $\text{mult}_0 h_{\mathbb{C}}$ . The first one is the direct application of the definition for the *constant deformation*  $h_{\mathbb{C},q}(x) = h_{\mathbb{C}} - q$  with  $q \in \mathbb{C}^3$  close to 0. Note that by Sard's lemma [86], for almost all values  $q$ , all degeneracy points of  $h_{\mathbb{C},q}$  are generic. By definition, the number of the roots of  $h_{\mathbb{C},q}$  inside the ball  $B_{\epsilon}^6$  is the local multiplicity. Hence the computation of the birth quota  $\text{mult}_0 h_{\mathbb{C}}$  reduces to solving the equation  $h_{\mathbb{C}} = q$ , which, in general, can be done numerically.

Another method is based on the fact that the local multiplicity is equal to the local degree  $\text{deg}_0 h_{\mathbb{C}}$  of the complexification  $h_{\mathbb{C}}$ , see [90, E.3]. Here, the local degree is understood in the sense described for the minimal model, i.e. it is the local degree of the real-imaginary decomposition (realification)  $h_{\mathbb{C},\mathbb{R}} : \mathbb{R}^6 \rightarrow \mathbb{R}^6$ . The computation of the local degree also allows the use of integral formulas, see e.g. in [91, 7].

We note that an alternative, commonly used definition of the local multiplicity uses algebraic methods: the local multiplicity is defined as the dimension of the so-called *local algebra* of  $h$  at 0, see Appendix C.3 and Refs. [87, 90]. This definition also provides a practical computational method of the birth quota. In the physical applications below, we computed the birth quotas using deformations, as well as this algebraic method.

## 4.6 Applications

In what follows, we derive the local multiplicity for two different families of isolated two-fold degeneracy points: for chiral symmetric band-structure models of few-layer graphene, and for all stable isolated two-fold degeneracy points that arise in time-reversal-symmetric crystals. The results are summarised in Table 4.1.

For bilayer graphene, discussed above, we find that the local multiplicity of the unperturbed effective Hamiltonian map  $h$  is 4, confirming that the number of newborn 2D Weyl points upon a generic deformation is either 2 or 4. For chiral-symmetric models of trilayer graphene with ABC stacking, or multi-layer ( $n$ -layer) graphene with ABCA... stacking, the local degree of the degeneracy point at the  $K$  point is  $n$ , whereas the local multiplicity is  $n^2$ , as shown in the top panel of Table 4.1. (For derivation, see Example 2 in Appendix C.3.)

Our methods provide the birth quota for non-generic degeneracy points appearing in 3D crystals as well. We focus on time-reversal symmetric crystals, which are classified in 230 space groups. It is known [29] that there are four types of isolated two-fold degeneracy points in the quasiparticle band structures of such crystals, listed in the bottom panel of Table 4.1.

The charge-1 Weyl point is the generic degeneracy point (called Weyl point throughout this thesis), whereas the charge-2, -3, -4 Weyl points are non-generic degeneracy points showing non-linear dispersion in certain directions. Charge-2 and -3 Weyl points have been proposed in Ref. [4], with effective Hamiltonians in the form  $H = ak_z\sigma_z + (bk_+^n + ck_-^n)\sigma_+ + \text{h.c.}$  with  $n \in \{2, 3\}$ ,  $|b| \neq |c|$ ,  $k_{\pm} = k_x \pm ik_y$  and  $\sigma_{\pm} = \sigma_x \pm i\sigma_y$ . The charge-4 Weyl point has been proposed in Ref. [26], and is described by the effective Hamiltonian  $H = Ak_xk_yk_z\sigma_z + B(k_x^2 + \omega k_y^2 + \omega^2 k_z^2)\sigma_+ + \text{h.c.}$  with  $\omega = \exp(-2\pi i/3)$ . Note that this map corresponds to the map studied in Ref. [89, Pg. 24], and also that such charge-4 Weyl points have been observed experimentally [92, 93].

We have computed the local multiplicities of these degeneracy points, and list the results in Table 4.1. (Derivations are shown in Example 2 and Example 3 in Appendix C.3.) The table also indicates the number of space groups where the corresponding non-generic degeneracy points are stabilised by symmetries.

$\mathbb{R}^2 \rightarrow \mathbb{R}^2$	local degree (winding number, top. charge)	local multiplicity (birth quota)
monolayer graphene	1	1
bilayer graphene (AB)	2	4
$n$ -layer graphene (ABCA...)	$n$	$n^2$

$\mathbb{R}^3 \rightarrow \mathbb{R}^3$	local degree (Chern number, top. charge)	local multiplicity (birth quota)	#SG SO	#SG nSO
Charge-1 Weyl point	1	1		
Charge-2 Weyl point	2	4	36	48
Charge-3 Weyl point	3	9	26	12
Charge-4 Weyl point	4	12	-	13

Table 4.1: Local multiplicities of isolated two-fold degeneracy points. The upper panel ( $\mathbb{R}^2 \rightarrow \mathbb{R}^2$ ) lists the absolute value of the local degree, and the local multiplicity, associated to the electronic quasiparticles that emerge in the simplest chiral-symmetric tight-binding models of mono- or multilayer graphene. The lower panel ( $\mathbb{R}^3 \rightarrow \mathbb{R}^3$ ) lists the same invariants, for all four types of isolated two-fold degeneracy points in crystals. The absolute value of the local degree is the minimum number of newborn Weyl points upon a generic deformation. The local multiplicity is the birth quota, i.e., the maximum number of newborn Weyl points. The last two columns of the lower panel indicate the number of space groups where symmetries stabilise non-generic degeneracy points, based on Ref. [29]. The label SO (nSO) denotes band structures with (without) spin-orbit coupling, e.g. electronic (phononic, photonic) band structures.

## 4.7 Conclusions

We have shown that when a non-generic degeneracy point is split, the number of resulting Weyl points is not only bounded from below by the absolute value of the topological charge of the original degeneracy but also bounded from above. The key step is to apply a Schrieffer–Wolff transformation, which reduces the Hamiltonian near the degeneracy to a smaller effective Hamiltonian. In this form, the problem is no longer a map into Hermitian matrices but it is a vector field: the components of the effective Hamiltonian define a function whose zeros coincide with the band degeneracies.

The advantage is that the behavior of zeros of vector fields is much better understood. In particular, for the complexified effective Hamiltonian map, the number of zeros created under perturbation is fixed: it always equals the multiplicity of the original zero. The real Weyl points correspond to a subset of these complex zeros, and therefore their number is always bounded above by the multiplicity.

We have also outlined several ways to compute this multiplicity. For numerical work, the most practical method is to expand the Hamiltonian to the required order, interpret the resulting power series as a complex polynomial, add a generic constant term, and solve for its complex roots, thus, obtaining the multiplicity directly.

This “birth quota” is not restricted to 3D Weyl points: it also applies to 2D Weyl points protected by chiral symmetry, and even to 1D cases where the effective Hamiltonian reduces to a scalar function. Finally, we have systematically enumerated the symmetry-protected two-fold degeneracies known in solid-state systems and determined their corresponding birth quotas.

## 4.8 Discussion

Our results establish a strong link between singularity theory and the theory of topological semimetals. While the examples discussed here were primarily drawn from electronic band structures, the framework naturally extends to other types of Bloch band systems, such as phononic, magnonic, or photonic crystals. More broadly, the approach applies to general parameter-dependent quantum systems, including, for instance, multi-terminal Josephson junctions, magnetically controlled quantum spin systems, and any physical system described by families of Hermitian matrices such as linearly coupled mechanical oscillators or linear electronic circuits.

This perspective invites a more systematic classification of degeneracies, by treating them as zero locus of the effective Hamiltonian map. In this context, the natural notion of equivalence is contact equivalence [90, 76], rather than the more commonly used topological classifications.

The advantage of the algebraic tools presented in the final chapter is that they go beyond pure geometry. While the Hamiltonian defines a parameterized family of matrices, the degeneracy set is an algebraic variety, i.e. a locus specified by equations. It is therefore natural to substitute the parameterization directly into these defining equations and treat them algebraically. Geometrically, this means that the Hamiltonian map is allowed to be singular. Moreover, the two-fold degeneracy manifold become singular near a higher degeneracy, so in their neighborhood an effective two-level model no longer exists. Nevertheless, the degeneracy set remains tractable algebraically: one is studying the intersection of singular varieties, which can still be organized and classified [94].

A possible direction for future work is to investigate further invariants under contact equivalence, such as the order of determinacy, which characterizes the minimal degree beyond which higher-order perturbations do not affect the equivalence class of the singularity. It also indicates the order at which perturbative calculations can be truncated without altering the qualitative structure.

In addition to analyzing the lowest-order (linear) splitting behavior near degeneracies, we also suggest that the maximal splitting order of eigenvalues, evaluated along a space curve departing from the degeneracy point, is an interesting quantity to consider. Based on examples, we conjecture a connection between the order of determinacy and the maximal splitting order.

Finally, we observe that the contact class obtained from the effective Hamiltonian corresponds to the isomorphism class of the local algebra associated with the degeneracy. This raises the question of whether the algebraic structure of a degeneracy can be determined without explicitly calculating the effective Hamiltonian — a particularly relevant issue when dealing with higher-order degeneracies, where truncating the Hilbert space is no longer feasible, and the splitting into simpler structures, such as Weyl points, must be understood directly from the full system.

# Thesis statements

## New scientific results

The new scientific results presented in my dissertation can be summarized in the following thesis points:

1. **Characterization of degeneracy patterns in a two-spin system** As part of my research, I studied the ground-state degeneracies of a two-spin system realized in a double quantum dot. I derived an analytical expression for the location of degeneracies, which allowed for a classification of all possible degeneracy configurations within the system. I identified the stable configurations and described the generic transitions between them. For the fine-tuned (non-generic) cases, I calculated their instability, i.e., the number of parameters that must be tuned to realize them.

In addition, I determined the distribution of topological charge for each configuration. For line and surface degeneracies, I introduced appropriate notions of topological charge density. I found that line degeneracies typically carry zero charge density, while surface degeneracies exhibit continuous charge density.

Related publications: I., II.

2. **Effective Hamiltonian and its relation to degeneracies**

I investigated the relationship between the degeneracies of a Hamiltonian operator and the effective Hamiltonian derived via quasi-degenerate perturbation theory (specifically, the Schrieffer–Wolff transformation). I proved that the Schrieffer–Wolff transformation provides a natural local coordinate system near the degeneracy manifold of Hermitian matrices, in which the effective Hamiltonian is expressed using coordinates transverse to the degeneracy.

I proved that the splitting of eigenvalues of a Hamiltonian is proportional to the distance of the Hamiltonian from the degeneracy manifold in the space of Hermitian matrices. Since degeneracies appear as the zero locus of the effective Hamiltonian map, I proposed identifying them with the map. This framework allows degeneracies to be analyzed using tools from singularity theory.

Within this setting, I provided several ways to define Weyl points, proved their equivalence, and proved that Weyl points are stable and generic degeneracies, analogous to the transversal intersection of two curves in the plane.

Related publication: III.

3. **Birth quota of non-generic degeneracy points**

I showed that upon perturbation of non-generic point-like degeneracies, there is not only a minimum number of Weyl points that are born (as determined by the topological charge), but also a maximum number, which we refer to as the birth quota. I provided three methods

to obtain the birth quota, all starting by applying the Schrieffer–Wolff transformation to the Hamiltonian and interpreting the resulting effective Hamiltonian as a multivariable vector-valued function.

I have shown that the birth quota of the degeneracy corresponds to the multiplicity of this function, similarly as the topological charge (minimum number) corresponds to the degree.

I have computed the birth quota for the isolated non-generic twofold degeneracy points of the electronic band structure of  $n$ -layer ABCA-stacked graphene, as well as for all such symmetry-enforced degeneracy points of three-dimensional materials.

Related publication: IV.

## Publications related to thesis points:

- I. **Gy. Frank**, Z. Scherübl, Sz. Csonka, G. Zaránd, and A. Pályi, *Magnetic degeneracy points in interacting two-spin systems: Geometrical patterns, topological charge distributions, and their stability*. Physical Review B **101** 245409 (2020).
- II. **Gy. Frank**, D. Varjas, P. Vrana, G. Pintér, and A. Pályi, *Topological charge distributions of an interacting two-spin system*. Physical Review B **105** 035414 (2022).
- III. G. Pintér, **Gy. Frank**, D. Varjas, A. Pályi, *The geometry of the Hermitian matrix space and the Schrieffer–Wolff transformation*. Quantum Journal, under review, arXiv:2407.10478.
- IV. G. Pintér, **Gy. Frank**, D. Varjas, A. Pályi, *Upper bound on the number of Weyl points born from a nongeneric degeneracy point*. Physical Review B **110** 245124 (2024).

## Other publications:

- V. A. Sen, **Gy. Frank**, B. Kolok, J. Danon, and A. Pályi, *Classification and magic magnetic field directions for spin-orbit-coupled double quantum dots*. Physical Review B **108** 245406 (2023).
- VI. **Gy. Frank**, D. Varjas, G. Pintér, and A. Pályi, *Weyl-point teleportation*. Physical Review B **109** 205415 (2024).
- VII. G. Naselli, **Gy. Frank**<sup>5</sup>, D. Varjas, I. C. Fulga, G. Pintér, A. Pályi, and V. Könye, *Stability of Weyl node merging processes under symmetry constraints*. Physical Review Letters **133** 196602 (2024).
- VIII. Z. Guba, **Gy. Frank**, G. Pintér, and A. Pályi, *Weyl points in ball-and-spring mechanical systems*. Physical Review B **111** 224109 (2025).
- IX. **Gy. Frank**, G. Pintér, and A. Pályi, *Singularity theory of Weyl-point creation and annihilation*. Physical Review B, under review, arXiv:2309.05506.
- X. **Gy. Frank**<sup>5</sup>, G. Pintér, D. Varjas, and A. Pályi, *Multifold degeneracy points of quantum systems and singularities of matrix varieties*. Research in the Mathematical Sciences, under review, arXiv:2507.17485.

---

<sup>5</sup>Shared first authorship.

# Acknowledgements

I would like to thank my supervisor, András Pályi, for making this project possible by proposing the research topic and supporting its realization.

I am especially grateful to Gergő Pintér for the intellectually stimulating and rewarding collaboration, and for introducing me to the more abstract aspects of mathematics. Working with him was not only exciting but also personally meaningful.

I thank Dániel Varjas for the many discussions and for providing a physicist's perspective that consistently served as a reliable and intuitive point of reference. I am also thankful to Péter Vrana for his precise mathematical feedback.

I would like to thank János Asbóth as well, whose thoughtful questions and genuine curiosity often led to engaging conversations, both during discussions related to research and in more personal moments shared over coffee breaks.

Finally, I would like to thank all fellow PhD students for the time shared, both in work and in everyday life during these years.



# Bibliography

- [1] N. P. Armitage, E. J. Mele, and A. Vishwanath, “Weyl and Dirac semimetals in three-dimensional solids,” *Rev. Mod. Phys.*, vol. 90, p. 015001, Jan 2018.
- [2] B. Yan and C. Felser, “Topological materials: Weyl semimetals,” *Annual Review of Condensed Matter Physics*, vol. 8, no. 1, pp. 337–354, 2017.
- [3] A. Bernevig, H. Weng, Z. Fang, and X. Dai, “Recent progress in the study of topological semimetals,” *Journal of the Physical Society of Japan*, vol. 87, no. 4, p. 041001, 2018.
- [4] C. Fang, M. J. Gilbert, X. Dai, and B. A. Bernevig, “Multi-Weyl topological semimetals stabilized by point group symmetry,” *Phys. Rev. Lett.*, vol. 108, p. 266802, Jun 2012.
- [5] M. V. Berry, “Quantal phase factors accompanying adiabatic changes,” *Proceedings of the Royal Society of London A: Mathematical, Physical and Engineering Sciences*, vol. 392, no. 1802, pp. 45–57, 1984.
- [6] A. Bohm, A. Mostafazadeh, H. Koizumi, Q. Niu, and J. Zwanziger, *The Geometric Phase in Quantum Systems*. Springer-Verlag Berlin Heidelberg, 2003.
- [7] J. K. Asbóth, L. Oroszlány, and A. Pályi, *A Short Course on Topological Insulators*. Springer International Publishing, 2016.
- [8] S. Murakami and S.-I. Kuga, “Universal phase diagrams for the quantum spin Hall systems,” *Phys. Rev. B*, vol. 78, p. 165313, Oct 2008.
- [9] J. Liu and D. Vanderbilt, “Weyl semimetals from noncentrosymmetric topological insulators,” *Physical Review B*, vol. 90, no. 15, p. 155316, 2014.
- [10] A. Burkov, “Anomalous hall effect in weyl metals,” *Physical review letters*, vol. 113, no. 18, p. 187202, 2014.
- [11] A. Zyuzin and A. Burkov, “Topological response in weyl semimetals and the chiral anomaly,” *Physical Review B—Condensed Matter and Materials Physics*, vol. 86, no. 11, p. 115133, 2012.
- [12] X. Huang, L. Zhao, Y. Long, P. Wang, D. Chen, Z. Yang, H. Liang, M. Xue, H. Weng, Z. Fang, *et al.*, “Observation of the chiral-anomaly-induced negative magnetoresistance in 3d weyl semimetal taas,” *Physical Review X*, vol. 5, no. 3, p. 031023, 2015.
- [13] E. König, H.-Y. Xie, D. Pesin, and A. Levchenko, “Photogalvanic effect in weyl semimetals,” *Physical Review B*, vol. 96, no. 7, p. 075123, 2017.
- [14] Z. Liu, L. Yang, Y. Sun, T. Zhang, H. Peng, H. Yang, C. Chen, Y. f. Zhang, Y. Guo, D. Prabhakaran, *et al.*, “Evolution of the fermi surface of weyl semimetals in the transition metal pnictide family,” *Nature materials*, vol. 15, no. 1, pp. 27–31, 2016.

- [15] C. Herring, “Accidental degeneracy in the energy bands of crystals,” *Phys. Rev.*, vol. 52, pp. 365–373, Aug 1937.
- [16] M. V. Berry and M. Wilkinson, “Diabolical points in the spectra of triangles,” *Proceedings of the Royal Society of London. A. Mathematical and Physical Sciences*, vol. 392, no. 1802, pp. 15–43, 1984.
- [17] von Neuman, J. and Wigner, E., “Über merkwürdige diskrete Eigenwerte. Über das Verhalten von Eigenwerten bei adiabatischen Prozessen,” *Physikalische Zeitschrift*, vol. 30, pp. 467–470, Jan. 1929.
- [18] W. Wernsdorfer and R. Sessoli, “Quantum phase interference and parity effects in magnetic molecular clusters,” *Science*, vol. 284, no. 5411, pp. 133–135, 1999.
- [19] P. Bruno, “Berry phase, topology, and degeneracies in quantum nanomagnets,” *Phys. Rev. Lett.*, vol. 96, p. 117208, Mar 2006.
- [20] A. Garg, “Berry phases near degeneracies: Beyond the simplest case,” *American Journal of Physics*, vol. 78, pp. 661–670, 07 2010.
- [21] Z. Scherübl, A. Pályi, G. Frank, I. E. Lukács, G. Fülöp, B. Fülöp, J. Nygård, K. Watanabe, T. Taniguchi, G. Zaránd, and S. Csonka, “Observation of spin-orbit coupling induced Weyl points in a two-electron double quantum dot,” *Communications Physics*, vol. 2, pp. 1–6, Sept. 2019.
- [22] D. R. Yarkony, “Diabolical conical intersections,” *Rev. Mod. Phys.*, vol. 68, pp. 985–1013, Oct 1996.
- [23] G. Frank, Z. Scherübl, S. Csonka, G. Zaránd, and A. Pályi, “Magnetic degeneracy points in interacting two-spin systems: Geometrical patterns, topological charge distributions, and their stability,” *Physical Review B*, vol. 101, no. 24, p. 245409, 2020.
- [24] V. Fatemi, A. R. Akhmerov, and L. Bretheau, “Weyl Josephson circuits,” *Physical Review Research*, vol. 3, mar 2021.
- [25] Z. Guba, G. Frank, G. m. H. Pintér, and A. Pályi, “Weyl points in ball-and-spring mechanical systems,” *Phys. Rev. B*, vol. 111, p. 224109, Jun 2025.
- [26] T. Zhang, R. Takahashi, C. Fang, and S. Murakami, “Twofold quadruple Weyl nodes in chiral cubic crystals,” *Phys. Rev. B*, vol. 102, p. 125148, Sep 2020.
- [27] C. L. Kane and E. J. Mele, “Quantum spin hall effect in graphene,” *Physical review letters*, vol. 95, no. 22, p. 226801, 2005.
- [28] B. Bradlyn, J. Cano, Z. Wang, M. Vergniory, C. Felser, R. J. Cava, and B. A. Bernevig, “Beyond dirac and weyl fermions: Unconventional quasiparticles in conventional crystals,” *Science*, vol. 353, no. 6299, p. aaf5037, 2016.
- [29] Z.-M. Yu, Z. Zhang, G.-B. Liu, W. Wu, X.-P. Li, R.-W. Zhang, S. A. Yang, and Y. Yao, “Encyclopedia of emergent particles in three-dimensional crystals,” *Science Bulletin*, vol. 67, pp. 375–380, feb 2022.
- [30] C. Fang, Y. Chen, H.-Y. Kee, and L. Fu, “Topological nodal line semimetals with and without spin-orbital coupling,” *Phys. Rev. B*, vol. 92, p. 081201, Aug 2015.

- [31] W. Wu, Y. Liu, S. Li, C. Zhong, Z.-M. Yu, X.-L. Sheng, Y. X. Zhao, and S. A. Yang, “Nodal surface semimetals: Theory and material realization,” *Phys. Rev. B*, vol. 97, p. 115125, Mar 2018.
- [32] J. Nissinen and G. E. Volovik, “Dimensional crossover of effective orbital dynamics in polar distorted  $^3\text{He}-\text{A}$ : Transitions to antispacetime,” *Phys. Rev. D*, vol. 97, p. 025018, Jan 2018.
- [33] J. Li, H. Wang, and H. Pan, “Tunable topological phase transition from nodal-line semimetal to Weyl semimetal by breaking symmetry,” *Phys. Rev. B*, vol. 104, p. 235136, Dec 2021.
- [34] G. Frank, D. Varjas, G. Pintér, and A. Pályi, “Weyl-point teleportation,” *Physical Review B*, vol. 109, no. 20, p. 205415, 2024.
- [35] Y. Ashida, Z. Gong, and M. Ueda, “Non-hermitian physics,” *Advances in Physics*, vol. 69, no. 3, pp. 249–435, 2020.
- [36] W. D. Heiss, “The physics of exceptional points,” *Journal of Physics A: Mathematical and Theoretical*, vol. 45, p. 444016, oct 2012.
- [37] I. Mandal and E. J. Bergholtz, “Symmetry and higher-order exceptional points,” *Physical review letters*, vol. 127, no. 18, p. 186601, 2021.
- [38] V. I. Arnold, “On matrices depending on parameters,” *Russian Mathematical Surveys*, vol. 26, no. 2, p. 29, 1971.
- [39] V. I. Arnold, “Remarks on eigenvalues and eigenvectors of Hermitian matrices, Berry phase, adiabatic connections and quantum Hall effect,” *Selecta Mathematica-new Series*, vol. 1, pp. 1–19, Mar. 1995.
- [40] G. Pintér, G. Frank, D. Varjas, and A. Pályi, “The geometry of the hermitian matrix space and the schrieffer–wolff transformation,” *arXiv preprint arXiv:2407.10478*, 2024.
- [41] J. M. Luttinger and W. Kohn, “Motion of electrons and holes in perturbed periodic fields,” *Phys. Rev.*, vol. 97, pp. 869–883, Feb 1955.
- [42] J. R. Schrieffer and P. A. Wolff, “Relation between the Anderson and Kondo Hamiltonians,” *Phys. Rev.*, vol. 149, pp. 491–492, Sep 1966.
- [43] S. Bravyi, D. P. DiVincenzo, and D. Loss, “Schrieffer–Wolff transformation for quantum many-body systems,” *Annals of Physics*, vol. 326, no. 10, pp. 2793–2826, 2011.
- [44] R. Winkler, S. Papadakis, E. De Poortere, and M. Shayegan, *Spin-orbit coupling in two-dimensional electron and hole systems*, vol. 41. Springer, 2003.
- [45] I. A. Day, S. Miles, H. K. Kerstens, D. Varjas, and A. R. Akhmerov, “Pymablock: an algorithm and a package for quasi-degenerate perturbation theory,” *arXiv preprint arXiv:2404.03728*, 2024.
- [46] G. Pintér, G. Frank, D. Varjas, and A. Pályi, “Upper bound on the number of weyl points born from a nongeneric degeneracy point,” *Physical Review B*, vol. 110, no. 24, p. 245124, 2024.
- [47] R. Wiesendanger, “Spin mapping at the nanoscale and atomic scale,” *Rev. Mod. Phys.*, vol. 81, pp. 1495–1550, Nov 2009.

- [48] A. Spinelli, M. Gerrits, R. Toskovic, B. Bryant, M. Ternes, and A. F. Otte, “Exploring the phase diagram of the two-impurity Kondo problem,” *Nature Communications*, vol. 6, p. 10046, 11 2015.
- [49] R. Hanson, L. P. Kouwenhoven, J. R. Petta, S. Tarucha, and L. M. K. Vandersypen, “Spins in few-electron quantum dots,” *Rev. Mod. Phys.*, vol. 79, pp. 1217–1265, Oct 2007.
- [50] F. A. Zwanenburg, A. S. Dzurak, A. Morello, M. Y. Simmons, L. C. L. Hollenberg, G. Klimeck, S. Rogge, S. N. Coppersmith, and M. A. Eriksson, “Silicon quantum electronics,” *Rev. Mod. Phys.*, vol. 85, pp. 961–1019, Jul 2013.
- [51] F. Wilczek and A. Shapere, *Geometric phases in physics*, vol. 5. World Scientific, 1989.
- [52] V. Gritsev and A. Polkovnikov, “Dynamical quantum Hall effect in the parameter space,” *Proceedings of the National Academy of Sciences*, vol. 109, no. 17, pp. 6457–6462, 2012.
- [53] P. Roushan, C. Neill, Y. Chen, M. Kolodrubetz, C. Quintana, N. Leung, M. Fang, R. Barends, B. Campbell, Z. Chen, B. Chiaro, A. Dunsworth, E. Jeffrey, J. Kelly, A. Megrant, J. Mutus, P. J. J. O’Malley, D. Sank, A. Vainsencher, J. Wenner, T. White, A. Polkovnikov, A. N. Cleland, and J. M. Martinis, “Observation of topological transitions in interacting quantum circuits,” *Nature*, vol. 515, p. 241, 11 2014.
- [54] K. V. Kavokin, “Symmetry of anisotropic exchange interactions in semiconductor nanostructures,” *Phys. Rev. B*, vol. 69, p. 075302, Feb 2004.
- [55] K. C. Nowack, F. H. L. Koppens, Y. V. Nazarov, and L. M. K. Vandersypen, “Coherent control of a single electron spin with electric fields,” *Science*, vol. 318, no. 5855, pp. 1430–1433, 2007.
- [56] S. Nadj-Perge, S. M. Frolov, E. P. A. M. Bakkers, and L. P. Kouwenhoven, “Spin-orbit qubit in a semiconductor nanowire,” *Nature*, vol. 468, p. 1084, 2010.
- [57] S. Nadj-Perge, V. S. Pribiag, J. W. G. van den Berg, K. Zuo, S. R. Plissard, E. P. A. M. Bakkers, S. M. Frolov, and L. P. Kouwenhoven, “Spectroscopy of spin-orbit quantum bits in indium antimonide nanowires,” *Phys. Rev. Lett.*, vol. 108, p. 166801, Apr 2012.
- [58] M. D. Schroer, K. D. Petersson, M. Jung, and J. R. Petta, “Field tuning the  $g$  factor in InAs nanowire double quantum dots,” *Phys. Rev. Lett.*, vol. 107, p. 176811, Oct 2011.
- [59] P. Harvey-Collard, N. T. Jacobson, C. Bureau-Oxton, R. M. Jock, V. Srinivasa, A. M. Mounce, D. R. Ward, J. M. Anderson, R. P. Manginell, J. R. Wendt, T. Pluym, M. P. Lilly, D. R. Luhman, M. Pioro-Ladrière, and M. S. Carroll, “Spin-orbit interactions for singlet-triplet qubits in silicon,” *Phys. Rev. Lett.*, vol. 122, p. 217702, May 2019.
- [60] T. Tanttu, B. Hensen, K. W. Chan, C. H. Yang, W. W. Huang, M. Fogarty, F. Hudson, K. Itoh, D. Culcer, A. Laucht, A. Morello, and A. Dzurak, “Controlling spin-orbit interactions in silicon quantum dots using magnetic field direction,” *Phys. Rev. X*, vol. 9, p. 021028, May 2019.
- [61] J. Danon and Y. V. Nazarov, “Pauli spin blockade in the presence of strong spin-orbit coupling,” *Phys. Rev. B*, vol. 80, p. 041301, Jul 2009.
- [62] Z. Yan and Z. Wang, “Floquet multi-Weyl points in crossing-nodal-line semimetals,” *Phys. Rev. B*, vol. 96, p. 041206, Jul 2017.

- [63] S. Ahn, E. J. Mele, and H. Min, “Optical conductivity of multi-Weyl semimetals,” *Phys. Rev. B*, vol. 95, p. 161112, Apr 2017.
- [64] Z.-M. Huang, J. Zhou, and S.-Q. Shen, “Topological responses from chiral anomaly in multi-Weyl semimetals,” *Phys. Rev. B*, vol. 96, p. 085201, Aug 2017.
- [65] T. Souza, M. Tomka, M. Kolodrubetz, S. Rosenberg, and A. Polkovnikov, “Enabling adiabatic passages between disjoint regions in parameter space through topological transitions,” *Phys. Rev. B*, vol. 94, p. 094106, Sep 2016.
- [66] J. Guckenheimer and P. Holmes, *Nonlinear Oscillations, Dynamical Systems, and Bifurcations of Vector Fields*. Springer, 1983.
- [67] L. Diósi, *A Short Course in Quantum Information Theory: An Approach From Theoretical Physics*. Springer-Verlag Berlin Heidelberg, 01 2007.
- [68] X.-Q. Sun, S.-C. Zhang, and T. Bzdusek, “Conversion rules for Weyl points and nodal lines in topological media,” *Phys. Rev. Lett.*, vol. 121, p. 106402, Sep 2018.
- [69] T. Curtright, Z. Cao, S. Huang, J. Sarmiento, S. Subedi, D. Tarrence, and T. Thapaliya, “Charge densities for conducting ellipsoids,” *European Journal of Physics*, vol. 41, no. 3, p. 035204, 2020.
- [70] J. H. Van Vleck, “On  $\sigma$ -type doubling and electron spin in the spectra of diatomic molecules,” *Phys. Rev.*, vol. 33, pp. 467–506, Apr 1929.
- [71] P. Löwdin, “Studies in Perturbation Theory. IV. Solution of Eigenvalue Problem by Projection Operator Formalism,” *Journal of Mathematical Physics*, vol. 3, pp. 969–982, 09 1962.
- [72] H. Weyl, “Das asymptotische Verteilungsgesetz der Eigenwerte linearer partieller Differentialgleichungen (mit einer Anwendung auf die Theorie der Hohlraumstrahlung),” *Mathematische Annalen*, vol. 71, no. 4, pp. 441–479, 1912.
- [73] V. A. Vassiliev, “Spaces of Hermitian operators with simple spectra and their finite-order cohomology,” *arXiv preprint arXiv:1407.7238*, 2014.
- [74] H. Teramoto, K. Kondo, S. Izumiya, M. Toda, and T. Komatsuzaki, “Classification of Hamiltonians in neighborhoods of band crossings in terms of the theory of singularities,” *Journal of Mathematical Physics*, vol. 58, no. 7, 2017.
- [75] H. Teramoto, A. Tsuchida, K. Kondo, S. Izumiya, M. Toda, and T. Komatsuzaki, “Application of singularity theory to bifurcation of band structures in crystals,” *Journal of Singularities*, vol. 21, pp. 289–302, 2020.
- [76] G. Naselli, G. Frank, D. Varjas, I. C. Fulga, G. Pintér, A. Pályi, and V. Könye, “Stability of Weyl node merging processes under symmetry constraints,” *arXiv preprint arXiv:2403.08518*, 2024.
- [77] V. Guillemin and A. Pollack, *Differential topology*, vol. 370. American Mathematical Soc., 2010.
- [78] M. Golubitsky and V. Guillemin, *Stable mappings and their singularities*. Springer New York, NY, 2012.
- [79] R.-P. Riwar, M. Houzet, J. S. Meyer, and Y. V. Nazarov, “Multi-terminal Josephson junctions as topological matter,” *Nature Communications*, vol. 7, p. 11167, Apr. 2016.

- [80] G. Frank, D. Varjas, P. Vrana, G. m. H. Pintér, and A. Pályi, “Topological charge distributions of an interacting two-spin system,” *Phys. Rev. B*, vol. 105, p. 035414, Jan 2022.
- [81] E. McCann and M. Koshino, “The electronic properties of bilayer graphene,” *Reports on Progress in Physics*, vol. 76, p. 056503, apr 2013.
- [82] M. M. Hirschmann, A. Leonhardt, B. Kilic, D. H. Fabini, and A. P. Schnyder, “Symmetry-enforced band crossings in tetragonal materials: Dirac and Weyl degeneracies on points, lines, and planes,” *Phys. Rev. Materials*, vol. 5, p. 054202, May 2021.
- [83] C. G. Péterfalvi, L. Oroszlány, C. J. Lambert, and J. Cserti, “Intraband electron focusing in bilayer graphene,” *New Journal of Physics*, vol. 14, no. 6, p. 063028, 2012.
- [84] M. Mucha-Kruczyński, I. L. Aleiner, and V. I. Fal’ko, “Strained bilayer graphene: Band structure topology and Landau level spectrum,” *Phys. Rev. B*, vol. 84, p. 041404, Jul 2011.
- [85] M. Johnsson and I. Aitchison, “The  $su(2)$  instanton and the adiabatic evolution of two kramers doublets,” *Journal of Physics A: Mathematical and General*, vol. 30, no. 6, p. 2085, 1997.
- [86] J. Milnor and D. W. Weaver, *Topology from the differentiable viewpoint*. Princeton university press, 1965.
- [87] V. I. Arnold, A. N. Varchenko, and S. M. Gusein-Zade, *Singularities of Differentiable Maps: Volume II Monodromy and Asymptotic Integrals*, vol. 83. Springer Science & Business Media, 2012.
- [88] D. Eisenbud, “An algebraic approach to the topological degree of a smooth map,” *Bulletin of the American Mathematical Society*, vol. 84, no. 5, pp. 751–764, 1978.
- [89] D. Eisenbud, H. I. Levine, and B. Teissier, “An algebraic formula for the degree of a  $C^\infty$  map germ / Sur une inégalité à la Minkowski pour les multiplicités,” *Annals of Mathematics*, vol. 106, no. 1, pp. 19–44, 1977.
- [90] D. Mond and J. J. Nuño-Ballesteros, *Singularities of mappings: The local behaviour of smooth and complex analytic mappings*, vol. 357. Springer, 2020.
- [91] R. Bott, L. W. Tu, *et al.*, *Differential forms in algebraic topology*, vol. 82. Springer, 1982.
- [92] L. Luo, W. Deng, Y. Yang, M. Yan, J. Lu, X. Huang, and Z. Liu, “Observation of quadruple Weyl point in hybrid-Weyl phononic crystals,” *Phys. Rev. B*, vol. 106, p. 134108, Oct 2022.
- [93] Q. Chen, F. Chen, Y. Pan, C. Cui, Q. Yan, L. Zhang, Z. Gao, S. A. Yang, Z.-M. Yu, H. Chen, *et al.*, “Discovery of a maximally charged weyl point,” *Nature Communications*, vol. 13, no. 1, p. 7359, 2022.
- [94] G. Frank, G. Pintér, D. Varjas, and A. Pályi, “Multifold degeneracy points of quantum systems and singularities of matrix varieties,” *arXiv preprint arXiv:2507.17485*, 2025.
- [95] S. G. Krantz and H. R. Parks, *A primer of real analytic functions*. Birkhäuser Boston, MA, 2002.
- [96] R. L. Foote, “Regularity of the distance function,” *Proceedings of the American Mathematical Society*, vol. 92, no. 1, pp. 153–155, 1984.
- [97] T. De Jong and G. Pfister, *Local analytic geometry: Basic theory and applications*. Springer Science & Business Media, 2000.

- 
- [98] S. Lojasiewicz, *Introduction to complex analytic geometry*. Birkhäuser, 1991.
- [99] V. Könye, A. Bouhon, I. C. Fulga, R.-J. Slager, J. van den Brink, and J. I. Facio, “Chirality flip of Weyl nodes and its manifestation in strained MoTe<sub>2</sub>,” *Physical Review Research*, vol. 3, no. 4, p. L042017, 2021.
- [100] W. Fulton, “Algebraic curves,” *An Introduction to Algebraic Geom*, vol. 54, 2008.



# Appendix

## A Spin-orbit coupled two-spin system

### A.1 Closed degeneracy curves are ellipses, closed degeneracy surfaces are ellipsoids

In Table 2.1, the eigenpattern (IV) implies that the degeneracy points form a closed surface. Here we show that this surface is an ellipsoid. A similar proof shows that the loops formed by the degeneracy points in cases (II), (V), and (X) are ellipses.

In case (IV), the matrix  $\hat{M}$  has a single eigenvalue  $a$  and the normalized eigenvectors form the three-dimensional unit sphere. So, any  $\mathbf{v}$  unit vector is an eigenvector, and we can apply the results (2.27) and (2.28) to obtain the locations of the degeneracy points

$$\mathbf{B}_a(\mathbf{v}) = \frac{J(1+a)}{2\mu_B} \frac{\mathbf{v}}{|\hat{\mathbf{g}}_L^T \mathbf{v}|} = \frac{J(1+a)}{2\mu_B} \frac{\mathbf{v}}{|\hat{\mathbf{G}}_L \mathbf{v}|}. \quad (9)$$

In the second step, we have made use  $\hat{\mathbf{G}}_L = \sqrt{\hat{\mathbf{g}}_L \hat{\mathbf{g}}_L^T}$ , which is the real symmetric component of the polar decomposition. In the principal reference frame of  $\hat{\mathbf{G}}_L$ , the location of the degeneracy point associated to  $\mathbf{v}$  reads

$$\begin{pmatrix} B_{ax} \\ B_{ay} \\ B_{az} \end{pmatrix} = \frac{J(1+a)}{2\mu_B} \frac{1}{\sqrt{G_x^2 v_x^2 + G_y^2 v_y^2 + G_z^2 v_z^2}} \begin{pmatrix} v_x \\ v_y \\ v_z \end{pmatrix}, \quad (10)$$

where  $(G_x, G_y, G_z)$  are the principal values of  $\hat{\mathbf{G}}_L$ . Acting with  $\hat{\mathbf{G}}_L$  on both sides of the equation, and taking the length-squared of the resulting vectors, we obtain the equation

$$G_x^2 B_{ax}^2 + G_y^2 B_{ay}^2 + G_z^2 B_{az}^2 = \left[ \frac{J(1+a)}{2\mu_B} \right]^2, \quad (11)$$

which implies that the degeneracy points form an ellipsoid.

For cases (II), (V), and (X), we have an additional constraint:  $\mathbf{v}$  has to be in the degenerate subspace of  $\hat{M}$ . This intersects the ellipsoid with a plane passing through the origin. Since the intersection of a plane and an ellipsoid is always an ellipse, we conclude that the degeneracy points in these cases are ellipses.

### A.2 Effective $g$ -tensor determinant

Here, we provide the derivation of the determinant of

$$\hat{g}_{a+} \hat{O} = \frac{g_R^2 \hat{\mathbf{g}}_L + g_L^2 \hat{\mathbf{g}}_R \hat{\mathbf{R}}^{-1}}{g_L^2 + g_R^2} \hat{O}^{-1} \mathbf{e}_z \otimes \mathbf{e}_z \hat{O} + \frac{g_R \hat{\mathbf{g}}_L - g_L \hat{\mathbf{g}}_R \hat{\mathbf{R}}^{-1}}{\sqrt{g_L^2 + g_R^2}} \hat{O}^{-1} (\mathbf{1} - \mathbf{e}_z \otimes \mathbf{e}_z) \hat{O} \quad (12)$$

Using that  $\hat{\mathbf{O}}^{-1} \mathbf{e}_z = \tilde{\mathbf{v}}_a = \hat{\mathbf{g}}_L^\top \mathbf{v}_a / g_L$ , where and hence we have

$$\hat{\mathbf{g}}_{a+} \hat{\mathbf{O}} = \frac{g_R^2 \hat{\mathbf{g}}_L + g_L^2 \hat{\mathbf{g}}_R \hat{\mathbf{R}}^{-1}}{g_L^2 + g_R^2} \tilde{\mathbf{v}}_a \otimes \tilde{\mathbf{v}}_a + \frac{g_R \hat{\mathbf{g}}_L - g_L \hat{\mathbf{g}}_R \hat{\mathbf{R}}^{-1}}{\sqrt{g_L^2 + g_R^2}} (\mathbf{1} - \tilde{\mathbf{v}}_a \otimes \tilde{\mathbf{v}}_a) \quad (13)$$

Dividing both the numerators and the denominators by  $g_R^2$ , we have

$$\hat{\mathbf{g}}_{a+} \hat{\mathbf{O}} = \frac{\hat{\mathbf{g}}_L + \frac{g_L^2}{g_R^2} \hat{\mathbf{g}}_R \hat{\mathbf{R}}^{-1}}{1 + \frac{g_L^2}{g_R^2}} \tilde{\mathbf{v}}_a \otimes \tilde{\mathbf{v}}_a + \frac{\hat{\mathbf{g}}_L - \frac{g_L}{g_R} \hat{\mathbf{g}}_R \hat{\mathbf{R}}^{-1}}{\sqrt{1 + \frac{g_L^2}{g_R^2}}} (\mathbf{1} - \tilde{\mathbf{v}}_a \otimes \tilde{\mathbf{v}}_a) \quad (14)$$

Using the relation  $g_L/g_R = a$ , this simplifies to

$$\hat{\mathbf{g}}_{a+} \hat{\mathbf{O}} = \frac{\hat{\mathbf{g}}_L + a^2 \hat{\mathbf{g}}_R \hat{\mathbf{R}}^{-1}}{1 + a^2} \tilde{\mathbf{v}}_a \otimes \tilde{\mathbf{v}}_a + \frac{\hat{\mathbf{g}}_L - a \hat{\mathbf{g}}_R \hat{\mathbf{R}}^{-1}}{\sqrt{1 + a^2}} (\mathbf{1} - \tilde{\mathbf{v}}_a \otimes \tilde{\mathbf{v}}_a) \quad (15)$$

Inserting the unit matrix as  $\mathbf{1}_{3 \times 3} = \hat{\mathbf{R}} \hat{\mathbf{g}}_R^{-1} \hat{\mathbf{g}}_R \hat{\mathbf{R}}^{-1}$  on the right of  $\hat{\mathbf{g}}_L$ , we obtain

$$\begin{aligned} \hat{\mathbf{g}}_{a+} \hat{\mathbf{O}} &= \frac{\hat{\mathbf{g}}_L \hat{\mathbf{R}} \hat{\mathbf{g}}_R^{-1} \hat{\mathbf{g}}_R \hat{\mathbf{R}}^{-1} + a^2 \hat{\mathbf{g}}_R \hat{\mathbf{R}}^{-1}}{1 + a^2} \tilde{\mathbf{v}}_a \otimes \tilde{\mathbf{v}}_a \\ &+ \frac{\hat{\mathbf{g}}_L \hat{\mathbf{R}} \hat{\mathbf{g}}_R^{-1} \hat{\mathbf{g}}_R \hat{\mathbf{R}}^{-1} - a \hat{\mathbf{g}}_R \hat{\mathbf{R}}^{-1}}{\sqrt{1 + a^2}} (\mathbf{1} - \tilde{\mathbf{v}}_a \otimes \tilde{\mathbf{v}}_a) \end{aligned} \quad (16)$$

Using the earlier definition  $\hat{\mathbf{M}} = \hat{\mathbf{g}}_L \hat{\mathbf{R}} \hat{\mathbf{g}}_R^{-1}$  from Eq. (2.23), we find

$$\hat{\mathbf{g}}_{a+} \hat{\mathbf{O}} = \frac{\hat{\mathbf{M}} + a^2}{1 + a^2} \hat{\mathbf{g}}_R \hat{\mathbf{R}}^{-1} \tilde{\mathbf{v}}_a \otimes \tilde{\mathbf{v}}_a + \frac{\hat{\mathbf{M}} - a}{\sqrt{1 + a^2}} \hat{\mathbf{g}}_R \hat{\mathbf{R}}^{-1} (\mathbf{1} - \tilde{\mathbf{v}}_a \otimes \tilde{\mathbf{v}}_a)$$

Now we rearrange the terms to express  $\hat{\mathbf{g}}_{a+} \hat{\mathbf{O}}$  as the sum of a matrix and a dyadic product, a form revealing the applicability of the matrix determinant lemma:

$$\hat{\mathbf{g}}_{a+} \hat{\mathbf{O}} = \frac{\hat{\mathbf{M}} - a}{\sqrt{1 + a^2}} \hat{\mathbf{g}}_R \hat{\mathbf{R}}^{-1} + \left[ \left( \frac{\hat{\mathbf{M}} + a^2}{1 + a^2} - \frac{\hat{\mathbf{M}} - a}{\sqrt{1 + a^2}} \right) \hat{\mathbf{g}}_R \hat{\mathbf{R}}^{-1} \tilde{\mathbf{v}}_a \right] \otimes \tilde{\mathbf{v}}_a \quad (17)$$

The matrix determinant lemma states that for an invertible matrix  $\hat{\mathbf{A}}$  and two vectors  $\mathbf{u}$  and  $\mathbf{v}$ , it holds that

$$\det(\hat{\mathbf{A}} + \mathbf{u} \otimes \mathbf{v}) = (1 + \mathbf{v} \cdot \hat{\mathbf{A}}^{-1} \mathbf{u}) \det\{\hat{\mathbf{A}}\}, \quad (18)$$

It is tempting to identify the quantities of Eq. (17) with those appearing in the matrix determinant lemma Eq. (18) as follows:

$$\hat{\mathbf{A}} = \frac{\hat{\mathbf{M}} - a}{\sqrt{1 + a^2}} \hat{\mathbf{g}}_R \hat{\mathbf{R}}^{-1} \quad (19a)$$

$$\hat{\mathbf{B}} = \frac{\hat{\mathbf{M}} + a^2}{1 + a^2} \hat{\mathbf{g}}_R \hat{\mathbf{R}}^{-1} \quad (19b)$$

$$\mathbf{u} = \left( \frac{\hat{\mathbf{M}} + a^2}{1 + a^2} - \frac{\hat{\mathbf{M}} - a}{\sqrt{1 + a^2}} \right) \hat{\mathbf{g}}_R \hat{\mathbf{R}}^{-1} \tilde{\mathbf{v}}_a = (\hat{\mathbf{B}} - \hat{\mathbf{A}}) \tilde{\mathbf{v}}_a \quad (19c)$$

$$\mathbf{v} = \tilde{\mathbf{v}}_a \quad (19d)$$

An important caveat is that our matrix  $\hat{\mathbf{A}}$  is not invertible, since  $a$  is one of the eigenvalues of  $\hat{\mathbf{M}}$ . Therefore, we can not use the matrix determinant lemma directly. Therefore, we will use the matrix determinant lemma for auxiliary quantities  $\hat{\mathbf{A}}'$  and  $\mathbf{u}'$  that are infinitesimally close to  $\hat{\mathbf{A}}$  and  $\mathbf{u}$ , respectively, defining  $\hat{\mathbf{A}}'$  as an invertible matrix, and take the limit  $\hat{\mathbf{A}}' \rightarrow \hat{\mathbf{A}}$  and  $\mathbf{u}' \rightarrow \mathbf{u}$  as the last step of the calculation. We define the auxiliary quantities as follows:

$$\hat{\mathbf{A}}' = \frac{\hat{\mathbf{M}} - a'}{\sqrt{1 + a'^2}} \hat{\mathbf{g}}_{\mathbf{R}} \hat{\mathbf{R}}^{-1}, \quad (20)$$

$$\mathbf{u}' = (\hat{\mathbf{B}} - \hat{\mathbf{A}}') \tilde{\mathbf{v}}_a, \quad (21)$$

and we will take the limit  $a' \rightarrow a$  as the last step of the calculation.

Now, we use the matrix determinant lemma for  $\hat{\mathbf{A}}'$ ,  $\mathbf{u}'$ , and  $\mathbf{v}$  to evaluate the determinant of Eq. (17), and express  $\mathbf{u}'$  and  $\mathbf{v}$  via Eqs. (21) and (19d), respectively:

$$\det \hat{\mathbf{g}}_{a+} \hat{\mathbf{O}} = \left(1 + \tilde{\mathbf{v}}_a \cdot \hat{\mathbf{A}}'^{-1} (\hat{\mathbf{B}} - \hat{\mathbf{A}}') \tilde{\mathbf{v}}_a\right) \det \hat{\mathbf{A}}' \quad (22)$$

We use in Eq. (22) the fact that  $\hat{\mathbf{O}}$  is a rotation, which implies  $\det \hat{\mathbf{O}} = 1$ , and furthermore we use the relations  $\hat{\mathbf{A}}'^{-1} \hat{\mathbf{A}}' = \mathbf{1}_{3 \times 3}$  and  $\tilde{\mathbf{v}}_a \cdot \tilde{\mathbf{v}}_a = 1$  to obtain

$$\det \hat{\mathbf{g}}_{a+} = \tilde{\mathbf{v}}_a \cdot \hat{\mathbf{A}}'^{-1} \hat{\mathbf{B}} \tilde{\mathbf{v}}_a \det \hat{\mathbf{A}}', \quad (23)$$

Then,  $\hat{\mathbf{A}}'$  is expressed using Eq. (20):

$$\det \hat{\mathbf{g}}_{a+} = \tilde{\mathbf{v}}_a \cdot \left( \frac{\hat{\mathbf{M}} - a'}{\sqrt{1 + a'^2}} \hat{\mathbf{g}}_{\mathbf{R}} \hat{\mathbf{R}}^{-1} \right)^{-1} \frac{\hat{\mathbf{M}} + a^2}{1 + a^2} \hat{\mathbf{g}}_{\mathbf{R}} \hat{\mathbf{R}}^{-1} \tilde{\mathbf{v}}_a \det \left( \frac{\hat{\mathbf{M}} - a'}{\sqrt{1 + a'^2}} \hat{\mathbf{g}}_{\mathbf{R}} \hat{\mathbf{R}}^{-1} \right) \quad (24)$$

Using the relation for the inverse of a matrix product, we rearrange the first matrix inverse to obtain

$$\det \hat{\mathbf{g}}_{a+} = \tilde{\mathbf{v}}_a \cdot \hat{\mathbf{R}} \hat{\mathbf{g}}_{\mathbf{R}}^{-1} \left( \frac{\hat{\mathbf{M}} - a'}{\sqrt{1 + a'^2}} \right)^{-1} \frac{\hat{\mathbf{M}} + a^2}{1 + a^2} \hat{\mathbf{g}}_{\mathbf{R}} \hat{\mathbf{R}}^{-1} \tilde{\mathbf{v}}_a \det \left( \frac{\hat{\mathbf{M}} - a'}{\sqrt{1 + a'^2}} \hat{\mathbf{g}}_{\mathbf{R}} \hat{\mathbf{R}}^{-1} \right) \quad (25)$$

Now we use  $\tilde{\mathbf{v}}_a = \left( \hat{\mathbf{g}}_{\mathbf{R}} \hat{\mathbf{R}}^{-1} \right)^{\mathbf{T}} \mathbf{v}_a / g_{\mathbf{R}}$ , yielding

$$\det \hat{\mathbf{g}}_{a+} = \frac{\mathbf{v}_a}{g_{\mathbf{R}}} \cdot \left[ \left( \frac{\hat{\mathbf{M}} - a'}{\sqrt{1 + a'^2}} \right)^{-1} \frac{\hat{\mathbf{M}} + a^2}{1 + a^2} \right] \hat{\mathbf{g}}_{\mathbf{R}} \hat{\mathbf{R}}^{-1} \tilde{\mathbf{v}}_a \det \left( \frac{\hat{\mathbf{M}} - a'}{\sqrt{1 + a'^2}} \hat{\mathbf{g}}_{\mathbf{R}} \hat{\mathbf{R}}^{-1} \right). \quad (26)$$

The next step is to make use of the fact that  $\mathbf{v}_a$  is a left eigenvector of  $\hat{\mathbf{M}}$  with eigenvalue  $a$ , that is,  $\mathbf{v}_a^{\mathbf{T}} \hat{\mathbf{M}} = a \mathbf{v}_a^{\mathbf{T}}$ :

$$\det \hat{\mathbf{g}}_{a+} = \left[ \left( \frac{a - a'}{\sqrt{1 + a'^2}} \right)^{-1} \frac{a + a^2}{1 + a^2} \right] \frac{1}{g_{\mathbf{R}}} \mathbf{v}_a \cdot \hat{\mathbf{g}}_{\mathbf{R}} \hat{\mathbf{R}}^{-1} \tilde{\mathbf{v}}_a \det \left( \frac{\hat{\mathbf{M}} - a'}{\sqrt{1 + a'^2}} \hat{\mathbf{g}}_{\mathbf{R}} \hat{\mathbf{R}}^{-1} \right) \quad (27)$$

Expressing  $\mathbf{v}_a$  cancels the  $g$ -tensor and the rotation, and using  $\tilde{\mathbf{v}}_a \cdot \tilde{\mathbf{v}}_a = 1$ , we find

$$\det \hat{\mathbf{g}}_{a+} = \frac{\sqrt{1 + a'^2}}{a - a'} \cdot \frac{a + a^2}{1 + a^2} \cdot \det \left( \frac{\hat{\mathbf{M}} - a'}{\sqrt{1 + a'^2}} \right) \det \hat{\mathbf{g}}_{\mathbf{R}} \det \hat{\mathbf{R}}^{-1}. \quad (28)$$

Finally, expressing the first determinant via the eigenvalues, and invoking  $\det \hat{\mathbf{R}}^{-1} = 1$ , we obtain

$$\begin{aligned} \det \hat{\mathbf{g}}_{a+} &= \frac{\sqrt{1 + a'^2}}{a - a'} \cdot \frac{a + a^2}{1 + a^2} \cdot \frac{(a - a')(b - a)(c - a)}{(\sqrt{1 + a'^2})^3} \det \hat{\mathbf{g}}_{\mathbf{R}} \\ &= \frac{a(1 + a)}{(1 + a^2)^2} (a - b)(a - c) \det \hat{\mathbf{g}}_{\mathbf{R}}, \end{aligned} \quad (29)$$

where the  $a' \rightarrow a$  limit was taken in the last step.

### A.3 Jordan normal forms for the examples in Section 2.7

In this section, we revisit the Jordan decomposition of  $3 \times 3$  real matrices, and discuss the relation between the matrix  $\hat{M}$  introduced in Eq. (2.23) of the main text, its Jordan decomposition, and the magnetic degeneracy points.

In the main text, we have introduced the real valued non-symmetric matrix  $\hat{M}$  in Eq. (2.23), as the central quantity of the two-spin problem. Also, we claimed that the directions of the degeneracy points in the magnetic-field parameter space are described by the left eigenvectors (left *ordinary eigenvectors*) of this matrix  $\hat{M}$ . Because of the non-symmetric property,  $\hat{M}$  is not always diagonalizable. Instead, it can be written as

$$\hat{M} = \hat{P} \hat{J} \hat{P}^{-1} = \begin{bmatrix} | & | & | \\ \mathbf{w}_1 & \mathbf{w}_2 & \mathbf{w}_2 \\ | & | & | \end{bmatrix} \hat{J} \begin{bmatrix} - & \mathbf{v}_1^T & - \\ - & \mathbf{v}_2^T & - \\ - & \mathbf{v}_3^T & - \end{bmatrix}, \quad (30)$$

which is called the Jordan decomposition. Here,  $\hat{P}^{-1}$  ( $\hat{P}$ ) is a non-singular matrix whose rows (columns) are the left (right) *generalized eigenvectors* of  $\hat{M}$ . From  $\hat{P}^{-1} \hat{P} = \mathbb{1}$  it follows that  $\mathbf{v}_i^T \mathbf{w}_j = \delta_{ij}$ . It is important to note that the left (right) generalized eigenvectors are not necessarily orthogonal to each other and not necessarily normalized. Also, the transformation matrix  $\hat{P}$  is not unique. The matrix  $\hat{J}$  is the Jordan normal form of  $\hat{M}$ , which has a block-diagonal structure formed of Jordan blocks.

A left generalized eigenvector of rank  $m \in \{1, 2, 3\}$  corresponding to eigenvalue  $\lambda$  satisfies

$$\mathbf{v}^T (\hat{M} - \lambda \mathbb{1})^m = 0 \quad (31)$$

and

$$\mathbf{v}^T (\hat{M} - \lambda \mathbb{1})^{m-1} \neq 0. \quad (32)$$

The parallel condition in Eq. (2.19) is fulfilled by the left *ordinary eigenvectors* denoted as  $\mathbf{b}$  which are the rank-1 generalized left eigenvectors. The  $i$ -th row in  $\hat{P}^{-1}$  is an ordinary left eigenvector of  $\hat{M}$  if the  $i$ -th row in  $\hat{J}$  does not contain a superdiagonal 1 element. Linear combinations of ordinary eigenvectors corresponding to the same eigenvalue are also ordinary eigenvectors.

In the following subsections we provide the Jordan normal forms corresponding to the Hamiltonians and degeneracy patterns discussed in subsections 2.7.2, and 2.7.3, and section 2.7.5. Note that in examples (II) and (V) discussed in the main text, we set both the interaction matrix  $\hat{R} = \mathbb{1}_{3 \times 3}$  and the right  $g$ -tensor  $\hat{g}_R = \mathbb{1}_{3 \times 3}$  as the  $3 \times 3$  unit matrix, and hence the matrix  $\hat{M}$  equals the left  $g$ -tensor  $\hat{g}_L$ .

#### Degeneracy pattern (II), section 2.7.2

For the example Hamiltonian producing the degeneracy pattern (II), treated in section 2.7.2, the left  $g$ -tensor was specified in Eq. (2.55), leading to

$$\hat{M}_{\text{II}} = \hat{g}_{L,\text{II}} \hat{R}_{\text{II}} \hat{g}_{R,\text{II}}^{-1} = \hat{g}_{L,\text{II}} = \begin{pmatrix} 2 & 0 & 0 \\ 0 & 2 & 0 \\ 0 & 1 & 4 \end{pmatrix}. \quad (33)$$

The matrices of the Jordan decomposition [see Eq. (30)] of this matrix  $\hat{M}_{\text{II}}$  read:

$$\hat{J}_{\text{II}} = \begin{pmatrix} 4 & 0 & 0 \\ 0 & 2 & 0 \\ 0 & 0 & 2 \end{pmatrix}, \quad \hat{P}_{\text{II}} = \frac{1}{2} \begin{pmatrix} 0 & 0 & 2 \\ 0 & 2 & 0 \\ 1 & -1 & 0 \end{pmatrix}, \quad \hat{P}_{\text{II}}^{-1} = \begin{pmatrix} 0 & 1 & 2 \\ 0 & 1 & 0 \\ 1 & 0 & 0 \end{pmatrix}. \quad (34)$$

The Jordan normal form  $\hat{\mathbf{J}}_{\text{II}}$  is diagonal, it consists of three Jordan blocks: two blocks of the form  $\hat{\mathbf{J}}_{1 \times 1}(2)$ , and one block of the form  $\hat{\mathbf{J}}_{1 \times 1}(4)$ .

As seen from Eqs. (30) and (34), the left eigenvector corresponding to the eigenvalue 4 is  $\mathbf{v}_1 = (0, 1, 2)^T$ . As claimed in Eq. (2.56), there are two Weyl points, forming a time-reversed pair, along the B-field direction set by  $\mathbf{v}_1$ . It is also seen in Eq. (34) that two left eigenvectors corresponding to the eigenvalue 2 are  $\mathbf{v}_2 = (0, 1, 0)^T$  and  $\mathbf{v}_3 = (1, 0, 0)^T$ . In fact, all vectors in the subspace  $\text{Span}(\mathbf{v}_2, \mathbf{v}_3)$  are eigenvectors with eigenvalue 2. According to Eqs. (2.28) and (2.55), the corresponding magnetic degeneracy points form a circle with radius  $R = 3/4$ .

### Degeneracy pattern (V), section 2.7.3

In section 2.7.3, describing the charged ellipse degeneracy pattern (V), the left  $g$ -tensor and hence the matrix  $\hat{\mathbf{M}}$  was set to

$$\hat{\mathbf{M}}_{\text{V}} = \begin{pmatrix} 2 & 0 & 0 \\ 0 & 2 & 0 \\ 0 & 1 & 2 \end{pmatrix}. \quad (35)$$

A Jordan decomposition of this matrix is:

$$\hat{\mathbf{J}}_{\text{V}} = \begin{pmatrix} 2 & 1 & 0 \\ 0 & 2 & 0 \\ 0 & 0 & 2 \end{pmatrix}, \quad \hat{\mathbf{P}}_{\text{V}} = \begin{pmatrix} 0 & 0 & 1 \\ 0 & 1 & 0 \\ 1 & 0 & 0 \end{pmatrix}, \quad \hat{\mathbf{P}}_{\text{V}}^{-1} = \begin{pmatrix} 0 & 0 & 1 \\ 0 & 1 & 0 \\ 1 & 0 & 0 \end{pmatrix}. \quad (36)$$

The Jordan normal form  $\hat{\mathbf{J}}_{\text{V}}$  consists of the Jordan blocks  $\hat{\mathbf{J}}_{1 \times 1}(2)$  and  $\hat{\mathbf{J}}_{2 \times 2}(2)$ . There is a superdiagonal 1 element in the first row, hence  $\mathbf{v}_1 = (0, 0, 1)^T$  is not an ordinary left eigenvector but a rank-2 generalized left eigenvector.

The ordinary eigenvectors are in the subspace  $\text{Span}(\mathbf{v}_2, \mathbf{v}_3)$ , similarly to the previous case. As a consequence of this, and Eq. (2.28), the corresponding degeneracies are on a circle with radius  $R = 3/4$  in the  $xy$ -plane again. This is similar to the degeneracy circle of pattern (II), but there the circle was neutral, while here it is charged.

Using Figs. 2.5 a, b, c, we argued in the main text that the topological charge of this charged degeneracy circle is localized on two opposite points of the circle. Here we claim that the charge is located in the  $\mathbf{v}_2$  direction. This can be illustrated by studying a parameter-dependent matrix  $\hat{\mathbf{M}}$  that exemplifies a transition from the degeneracy pattern (II) formed by two equally-charged Weyl points and a neutral circle, to the degeneracy pattern (V) formed by the charged circle:

$$\hat{\mathbf{M}}_{\text{II} \rightarrow \text{V}}(\epsilon) = \begin{pmatrix} 2 & 0 & 0 \\ 0 & 2 & 0 \\ 0 & 1 & 2 + \epsilon \end{pmatrix}. \quad (37)$$

For  $\epsilon > 0$ , this matrix has a Jordan decomposition analogous to (34), i.e., it implies the degeneracy pattern (II). In particular, its largest eigenvalue is  $2 + \epsilon$ , with an ordinary left eigenvector  $\mathbf{v}_1 = (0, 1, \epsilon)^T$ . As  $\epsilon$  is tuned continuously to zero, then  $\mathbf{v}_1$  coalesces with the ( $\epsilon$ -independent) second left ordinary eigenvector  $\mathbf{v}_2 = (0, 1, 0)^T$ . During this transition the Weyl points approach the neutral ellipse and then merge with it at  $\epsilon = 0$ .

### Degeneracy pattern (IV), section 2.7.5

In section 2.7.5, describing the charged ellipsoid degeneracy pattern (IV), the matrix  $\hat{\mathbf{M}}$  was set to

$$\hat{\mathbf{M}}_{\text{IV}} = 2 \cdot \mathbf{1}_{3 \times 3} \quad (38)$$

Every vector is an eigenvector, hence there are degeneracies in every direction. The distance of the degeneracy points from the origin is given by Eq. (2.28).

#### A.4 Rank of the effective $g$ -tensor in the points of the degeneracy ellipses

Figure 2.4 of the main text provides numerical evidence that the topological charge density of the neutral degeneracy ellipse, of pattern (II), is zero. Similarly, Fig. 2.5 shows that the topological charge density of the charged degeneracy ellipse, pattern (V), is concentrated at two charged points, whereas the linear charge density in all other points of the ellipse is zero. In this section, we show that the above charge distributions are related to the ranks of the effective  $g$ -tensors  $\hat{\mathbf{g}}_{\text{eff}}(\mathbf{B}_0)$  of the degeneracy points, defined in Eq. (2.45). Namely, the effective  $g$ -tensor is a rank-1 matrix for the charged points of the charged ellipse, and a rank-2 matrix for the uncharged points of the charged ellipse and for every point of the neutral ellipse, too. The rank-2 property implies a first-order energy splitting of the degeneracy as we leave the degenerate line in any perpendicular direction. In the case of a rank-1 effective  $g$ -tensor there exist a direction perpendicular to the tangent vector of the degeneracy circle, with the property that the energy splitting is of higher-than-linear order if we leave the circle in that particular direction.

The effective  $g$ -tensor for a ground-state degeneracy point at  $\mathbf{B}_0 = B_0 \mathbf{b}$  reads (Eq. (17))

$$\hat{\mathbf{g}}_{\text{eff}}(\mathbf{B}_0) \hat{\mathbf{O}} = \left( \frac{\hat{M} + a^2}{1 + a^2} - \frac{\hat{M} - a}{\sqrt{1 + a^2}} \right) \hat{\mathbf{g}}_{\text{R}} \hat{\mathbf{R}}^{-1} \tilde{\mathbf{b}} \tilde{\mathbf{b}}^{\text{T}} + \frac{\hat{M} - a}{\sqrt{1 + a^2}} \hat{\mathbf{g}}_{\text{R}} \hat{\mathbf{R}}^{-1}, \quad (39)$$

where

$$\tilde{\mathbf{b}} = \hat{\mathbf{R}} \hat{\mathbf{g}}_{\text{R}}^{\text{T}} \mathbf{b} / |\hat{\mathbf{g}}_{\text{R}}^{\text{T}} \mathbf{b}|. \quad (40)$$

Note that, here,  $\mathbf{b}$  and  $\tilde{\mathbf{b}}$  is used for  $\mathbf{v}_a$  and  $\tilde{\mathbf{v}}_a$ . Also, compared to the previous section, here we denote the dyadic product as a matrix product  $\tilde{\mathbf{b}} \tilde{\mathbf{b}}^{\text{T}}$  of a column vector and a row vector, instead of the alternative notation  $\tilde{\mathbf{b}} \otimes \tilde{\mathbf{b}}$ . The orthogonal matrix  $\hat{\mathbf{O}}$ , is an (ambiguous) rotation fulfilling  $\hat{\mathbf{O}} \tilde{\mathbf{b}} = \mathbf{e}_z$  (e.g., it can be the  $\pi$  rotation around the bisector of  $\tilde{\mathbf{b}}$  and  $\mathbf{e}_z$ ).

Equation (39) for the effective  $g$ -tensor is too complicated to determine rank  $[\hat{\mathbf{g}}_{\text{eff}}(\mathbf{B}_0)]$  directly. Instead, in the forthcoming calculation, we show that the rank is reflected by the rank of a simpler matrix  $\hat{\mathbf{A}}_Q$ , which we express below in Eq. (55). Then, in subsections A.4 and A.4, we use this matrix  $\hat{\mathbf{A}}_Q$  to derive the rank of the effective  $g$ -tensor on degeneracy ellipses.

As a first step in our calculation, we substitute  $\tilde{\mathbf{b}}$  with  $\mathbf{b}$  according to Eq. (40), into Eq. (39), and multiply the latter with  $\hat{\mathbf{O}}^{-1}$  from the right:

$$\hat{\mathbf{g}}_{\text{eff}}(\mathbf{b}) = \left[ \left( \frac{\hat{M} + a^2}{1 + a^2} - \frac{\hat{M} - a}{\sqrt{1 + a^2}} \right) \hat{\mathbf{g}}_{\text{R}} \hat{\mathbf{g}}_{\text{R}}^{\text{T}} \mathbf{b} \mathbf{b}^{\text{T}} + \frac{\hat{M} - a}{\sqrt{1 + a^2}} \mathbf{b}^{\text{T}} \hat{\mathbf{g}}_{\text{R}} \hat{\mathbf{g}}_{\text{R}}^{\text{T}} \mathbf{b} \right] \hat{\mathbf{g}}_{\text{R}} \hat{\mathbf{R}}^{-1} \hat{\mathbf{O}}^{-1}. \quad (41)$$

Here, we use  $\mathbf{b}$  instead of  $\mathbf{B}_0$  in the argument of  $\hat{\mathbf{g}}_{\text{eff}}$ , because the latter quantity does not depend on the norm  $B_0$ .

In cases (II) and (V), where degeneracy ellipses appear, the directions of the magnetic degeneracy points are in the subspace of the second and third left generalized eigenvectors. That is, the degeneracy points can be parameterized by the angle  $\varphi \in [0, 2\pi[$  via

$$\mathbf{b} = \beta_2 \mathbf{v}_2 + \beta_3 \mathbf{v}_3 = \beta (\mathbf{v}_2 \cos \varphi + \mathbf{v}_3 \sin \varphi), \quad (42)$$

with  $\beta = \sqrt{\beta_2^2 + \beta_3^2}$ . Since  $\mathbf{v}_2$  and  $\mathbf{v}_3$  are not necessarily orthogonal and normalized,  $\beta$  is not necessarily  $|\mathbf{b}|$  and  $\varphi$  is not necessarily the angle between  $\mathbf{b}$  and  $\mathbf{v}_2$ .

The forthcoming steps lack an a priori intuitive justification, but a posteriori they prove to be particularly useful. First, let us recall that according to Eq. (30), the left generalized eigenvectors form the rows in the similarity transformation matrix  $\hat{\mathbf{P}}^{-1}$  in the Jordan decomposition of  $\hat{\mathbf{M}}$ . Using this,  $\mathbf{b}^{\text{T}}$  can be written as the second row of the matrix  $\hat{\mathbf{Q}} \hat{\mathbf{P}}^{-1}$ , that is

$$\mathbf{b}^{\text{T}} = \left( \hat{\mathbf{Q}} \hat{\mathbf{P}}^{-1} \right)_{2,}, \quad (43)$$

where

$$\hat{\mathbf{Q}} = \beta \begin{pmatrix} 1 & 0 & 0 \\ 0 & \cos \varphi & \sin \varphi \\ 0 & -\sin \varphi & \cos \varphi \end{pmatrix}. \quad (44)$$

Inserting a unit matrix in the form of  $\hat{\mathbf{P}}^{-1} \hat{\mathbf{P}}$  to Eq. (43) yields

$$\mathbf{b}^T = \left( \hat{\mathbf{P}}^{-1} \hat{\mathbf{P}} \hat{\mathbf{Q}} \hat{\mathbf{P}}^{-1} \right)_{2..} \equiv \left( \hat{\mathbf{P}}^{-1} \hat{\mathbf{Q}}' \right)_{2..} = \mathbf{v}_2^T \hat{\mathbf{Q}}'. \quad (45)$$

Here the sign  $\equiv$  denotes the definition of  $\hat{\mathbf{Q}}'$  and in the last step, we used Eq. (30).

Substituting Eq. (45) to the effective  $g$ -tensor of Eq. (41), we obtain

$$\hat{\mathbf{g}}_{\text{eff}}(\hat{\mathbf{Q}}'^T \mathbf{v}_2) = \left[ \left( \frac{\hat{M} + a^2}{1 + a^2} - \frac{\hat{M} - a}{\sqrt{1 + a^2}} \right) \hat{\mathbf{D}} + \frac{\hat{M} - a}{\sqrt{1 + a^2}} \right] \hat{\mathbf{g}}_{\text{R}} \hat{\mathbf{R}}^{-1} \hat{\mathbf{O}}^{-1}, \quad (46)$$

where we introduced the shorthand

$$\hat{\mathbf{D}} = \frac{\hat{\mathbf{g}}_{\text{R}} \hat{\mathbf{g}}_{\text{R}}^T \hat{\mathbf{Q}}'^T \mathbf{v}_2 \mathbf{v}_2^T \hat{\mathbf{Q}}'}{\mathbf{v}_2^T \hat{\mathbf{Q}}' \hat{\mathbf{g}}_{\text{R}} \hat{\mathbf{g}}_{\text{R}}^T \hat{\mathbf{Q}}'^T \mathbf{v}_2}, \quad (47)$$

which is a dyadic product.

Next, we further transform  $\hat{\mathbf{M}}$  and  $\hat{\mathbf{D}}$  in Eq. (46), starting with the latter. Substituting unit matrices into Eq. (47) yields

$$\hat{\mathbf{D}} = \frac{\left( \hat{\mathbf{Q}}'^{-1} \hat{\mathbf{P}} \hat{\mathbf{P}}^{-1} \hat{\mathbf{Q}}' \right) \hat{\mathbf{g}}_{\text{R}} \hat{\mathbf{g}}_{\text{R}}^T \hat{\mathbf{Q}}'^T \mathbf{v}_2 \mathbf{v}_2^T \hat{\mathbf{Q}}'}{\mathbf{v}_2^T \left( \hat{\mathbf{P}} \hat{\mathbf{P}}^{-1} \right) \hat{\mathbf{Q}}' \hat{\mathbf{g}}_{\text{R}} \hat{\mathbf{g}}_{\text{R}}^T \hat{\mathbf{Q}}'^T \mathbf{v}_2}. \quad (48)$$

Then, using the associative nature of matrix multiplication, we obtain

$$\hat{\mathbf{D}} = \frac{\hat{\mathbf{Q}}'^{-1} \hat{\mathbf{P}} \left( \hat{\mathbf{P}}^{-1} \hat{\mathbf{Q}}' \hat{\mathbf{g}}_{\text{R}} \hat{\mathbf{g}}_{\text{R}}^T \hat{\mathbf{Q}}'^T \mathbf{v}_2 \right) \mathbf{v}_2^T \hat{\mathbf{Q}}'}{\mathbf{v}_2^T \hat{\mathbf{P}} \left( \hat{\mathbf{P}}^{-1} \hat{\mathbf{Q}}' \hat{\mathbf{g}}_{\text{R}} \hat{\mathbf{g}}_{\text{R}}^T \hat{\mathbf{Q}}'^T \mathbf{v}_2 \right)} = \frac{\hat{\mathbf{Q}}'^{-1} \hat{\mathbf{P}} \mathbf{r} \mathbf{v}_2^T \hat{\mathbf{Q}}'}{\mathbf{v}_2^T \hat{\mathbf{P}} \mathbf{r}}, \quad (49)$$

where we introduced

$$\mathbf{r} = \hat{\mathbf{P}}^{-1} \hat{\mathbf{Q}}' \hat{\mathbf{g}}_{\text{R}} \hat{\mathbf{g}}_{\text{R}}^T \hat{\mathbf{Q}}'^T \mathbf{v}_2. \quad (50)$$

Then, we substitute the definition of  $\hat{\mathbf{Q}}'$  from Eq. (45) to Eq. (49), yielding

$$\hat{\mathbf{D}} = \frac{\hat{\mathbf{P}} \hat{\mathbf{Q}}^{-1} \hat{\mathbf{P}}^{-1} \hat{\mathbf{P}} \mathbf{r} \mathbf{v}_2^T \hat{\mathbf{P}} \hat{\mathbf{Q}} \hat{\mathbf{P}}^{-1}}{\mathbf{v}_2^T \hat{\mathbf{P}} \mathbf{r}} = \hat{\mathbf{P}} \hat{\mathbf{Q}}^{-1} \frac{\mathbf{r}}{r_2} \begin{pmatrix} 0 & 1 & 0 \end{pmatrix} \hat{\mathbf{Q}} \hat{\mathbf{P}}^{-1}. \quad (51)$$

The denominator  $r_2$ , which is the second vector component of  $\mathbf{r}$ , appears from the scalar product of  $\mathbf{r}$  with  $\mathbf{v}_2^T \hat{\mathbf{P}} \equiv (0 \ 1 \ 0)$ . Note that  $r_2 = |\hat{\mathbf{g}}_{\text{R}}^T \mathbf{b}|^2$ , which follows, e.g., from Eqs. (50) and (45), and it guarantees that the denominator in Eq. (51) is nonzero.

According to Eq. (51), the matrix  $\hat{\mathbf{D}}$  can be thought of as a result of a similarity transformation generated by  $\hat{\mathbf{P}} \hat{\mathbf{Q}}^{-1}$ . Now, we transform the terms of Eq. (46) containing  $\hat{\mathbf{M}}$  to a similar form. Multiplying  $\hat{\mathbf{M}}$  with appropriately composed unit matrices, using its Jordan decomposition, and introducing the *transformed Jordan normal form* via

$$\hat{\mathbf{J}}_{\mathbf{Q}} = \hat{\mathbf{Q}} \hat{\mathbf{J}} \hat{\mathbf{Q}}^{-1}, \quad (52)$$

we find

$$\hat{M} = \left( \hat{P} \hat{Q}^{-1} \hat{Q} \hat{P}^{-1} \right) \left( \hat{P} \hat{J} \hat{P}^{-1} \right) \left( \hat{P} \hat{Q}^{-1} \hat{Q} \hat{P}^{-1} \right) = \hat{P} \hat{Q}^{-1} \hat{J}_Q \hat{Q} \hat{P}^{-1}. \quad (53)$$

Inserting Eqs. (51) and (53) into Eq. (46), we find the following expression for the effective  $g$ -tensor:

$$\hat{g}_{\text{eff}}(\mathbf{b}) = \hat{P} \hat{Q}^{-1} \hat{A}_Q \hat{Q} \hat{P}^{-1} \hat{g}_R \hat{R}^{-1} \hat{O}^{-1}, \quad (54)$$

where we introduced

$$\hat{A}_Q = \left( \frac{\hat{J}_Q + a^2}{1 + a^2} - \frac{\hat{J}_Q - a}{\sqrt{1 + a^2}} \right) \frac{\mathbf{r}}{r_2} \begin{pmatrix} 0 & 1 & 0 \end{pmatrix} + \frac{\hat{J}_Q - a}{\sqrt{1 + a^2}}. \quad (55)$$

Matrix  $\hat{A}_Q$  has the same rank as the effective  $g$ -tensor, because they only differ by multiplications of non-singular matrices. In what follows, we will determine the rank of the  $g$ -tensor at the points of the degeneracy ellipses by determining the rank of  $\hat{A}_Q$ .

### Neutral ellipse

In Eq. (34), we have shown an example Jordan decomposition corresponding to a degeneracy pattern including a neutral ellipse. More generally, the normal form of that degeneracy pattern has a two-fold degeneracy of the following kind:

$$\hat{J}_{\text{II}} = \begin{pmatrix} b & 0 & 0 \\ 0 & a & 0 \\ 0 & 0 & a \end{pmatrix}, \quad (56)$$

where  $a, b > 0$  and  $a \neq b$ . Since its second Jordan block is proportional to the  $2 \times 2$  unit matrix, the transformation with  $\hat{Q}$  defined in Eq. (44) leaves the normal form invariant:

$$\hat{J}_{Q,\text{II}} = \hat{J}_{\text{II}}, \quad (57)$$

for every  $\varphi$ . That means that every point of a neutral ellipse has the same rank effective  $g$ -tensor. Then, expressing  $\hat{A}_Q$  from Eqs. (55), (57) and (56) yields

$$\begin{aligned} \hat{A}_Q &= \begin{pmatrix} \frac{b+a^2}{1+a^2} - \frac{b-a}{\sqrt{1+a^2}} & 0 & 0 \\ 0 & \frac{a+a^2}{1+a^2} & 0 \\ 0 & 0 & \frac{a+a^2}{1+a^2} \end{pmatrix} \begin{pmatrix} r_1/r_2 \\ 1 \\ r_3/r_2 \end{pmatrix} \begin{pmatrix} 0 & 1 & 0 \end{pmatrix} + \begin{pmatrix} \frac{b-a}{\sqrt{1+a^2}} & 0 & 0 \\ 0 & 0 & 0 \\ 0 & 0 & 0 \end{pmatrix} \\ &= \begin{pmatrix} \frac{b-a}{\sqrt{1+a^2}} & \left[ \frac{b+a^2}{1+a^2} - \frac{b-a}{\sqrt{1+a^2}} \right] \frac{r_1}{r_2} & 0 \\ 0 & \frac{a(1+a)}{1+a^2} & 0 \\ 0 & \frac{a(1+a)}{1+a^2} \frac{r_3}{r_2} & 0 \end{pmatrix}. \end{aligned} \quad (58)$$

$\hat{A}_Q$  cannot be a dyadic product because the condition  $A_{Q,11}A_{Q,22} = A_{Q,12}A_{Q,21}$  cannot be satisfied as  $A_{Q,11}, A_{Q,22} \neq 0$  and  $A_{Q,21} = 0$ . That means  $\text{rank}(\hat{g}_{\text{eff}}) > 1$ . The determinant of the effective  $g$ -tensor is zero [Eq. (2.49) with  $c = a$ ], therefore  $\text{rank}(\hat{g}_{\text{eff}}) < 3$ . This way we proved that the rank is 2 for every points of the neutral degeneracy ellipse.

### Charged ellipse

In Eq. (36), we have shown an example for a Jordan decomposition corresponding to a degeneracy pattern of a charged ellipse. More generally, the Jordan normal form of that degeneracy pattern has a three-fold eigenvalue degeneracy, and a single 1 element in the superdiagonal:

$$\hat{\mathbf{J}}_{\mathbf{V}} = \begin{pmatrix} a & 1 & 0 \\ 0 & a & 0 \\ 0 & 0 & a \end{pmatrix}, \quad (59)$$

with  $a > 0$ . Now  $\hat{\mathbf{J}}_{Q,\mathbf{V}}$  does depend on the angle  $\varphi$  parameterizing the degeneracy point along the degeneracy ellipse:

$$\hat{\mathbf{J}}_{Q,\mathbf{V}} = \begin{pmatrix} a & \cos \varphi & -\sin \varphi \\ 0 & a & 0 \\ 0 & 0 & a \end{pmatrix}. \quad (60)$$

Expressing  $\hat{\mathbf{A}}_Q$  from Eqs. (55) and (60) yields

$$\begin{aligned} \hat{\mathbf{A}}_Q &= \begin{pmatrix} \frac{a+a^2}{1+a^2} & \cos \varphi \left[ \frac{1}{1+a^2} - \frac{1}{\sqrt{1+a^2}} \right] & -\sin \varphi \left[ \frac{1}{1+a^2} - \frac{1}{\sqrt{1+a^2}} \right] \\ 0 & \frac{a+a^2}{1+a^2} & 0 \\ 0 & 0 & \frac{a+a^2}{1+a^2} \end{pmatrix} \begin{pmatrix} r_1/r_2 \\ 1 \\ r_3/r_2 \end{pmatrix} \begin{pmatrix} 0 & 1 & 0 \end{pmatrix} \\ &+ \begin{pmatrix} 0 & \frac{\cos \varphi}{\sqrt{1+a^2}} & \frac{-\sin \varphi}{\sqrt{1+a^2}} \\ 0 & 0 & 0 \\ 0 & 0 & 0 \end{pmatrix} = \begin{pmatrix} 0 & A_{Q,12} & -\frac{\sin(\varphi)}{\sqrt{1+a^2}} \\ 0 & \frac{a(1+a)}{1+a^2} & 0 \\ 0 & A_{Q,32} & 0 \end{pmatrix}, \end{aligned} \quad (61)$$

where the elements  $A_{Q,12}$  and  $A_{Q,32}$  are given by lengthy but unimportant expressions. Similarly to the neutral ellipse, the condition  $A_{Q,12}A_{Q,23} = A_{Q,13}A_{Q,22}$  is not satisfied for  $\sin \varphi \neq 0$ , hence the rank of the effective  $g$ -tensor is 2 for those points. However, if  $\sin \varphi = 0$ , i.e., if the magnetic field is along the direction of  $\mathbf{v}_2$ , the matrix  $\hat{\mathbf{A}}$  is clearly a dyadic product and not a zero matrix, hence its rank is 1, implying that the rank of the effective  $g$ -tensor is also 1.

Finally, let us consider this latter case, when the rank of the effective  $g$ -tensor is 1. Starting at the degeneracy point  $\mathbf{B}_0$ , and changing the magnetic field by  $\delta\mathbf{B}$  along the degeneracy line as  $\mathbf{B} = \mathbf{B}_0 + \delta\mathbf{B}$ , the energy splitting induced by  $\delta\mathbf{B}$  is at least of second order in  $\delta\mathbf{B}$ . Since the rank of the effective  $g$ -tensor is 1, there must be a plane of higher-order splitting, that is, a plane along which the energy splitting is at least of second order in  $\delta\mathbf{B}$ . Which is the second direction, which spans this plane together with the direction of the degeneracy ellipse?

This question can be answered by recasting the rank-1 effective  $g$ -tensor as a dyadic product of two vectors. Without the derivation, we claim that one way this can be done is as follows:

$$\hat{\mathbf{g}}_{\text{eff}}(\mathbf{v}_2) = \mathbf{d}_1 \mathbf{d}_2^T, \quad (62)$$

where

$$\mathbf{d}_1 = \frac{1}{1+a^2} \left[ a(1+a) \frac{\hat{\mathbf{g}}_{\mathbf{R}} \hat{\mathbf{g}}_{\mathbf{R}}^T \mathbf{v}_2}{\mathbf{v}_2^T \hat{\mathbf{g}}_{\mathbf{R}} \hat{\mathbf{g}}_{\mathbf{R}}^T \mathbf{v}_2} + \mathbf{w}_1 \right], \quad \mathbf{d}_2 = \hat{\mathbf{O}} \hat{\mathbf{R}} \hat{\mathbf{g}}_{\mathbf{R}}^T \mathbf{v}_2 \quad (63)$$

with  $\mathbf{w}_1$  is the right generalized eigenvector defined in Eq. (30). The column vector  $\mathbf{d}_1$  in the square bracket defines the direction of maximal linear splitting in  $\delta\mathbf{B}$ , cf. Eq. (2.45). If  $\delta\mathbf{B}$  lies in the plane perpendicular to that vector, then the energy splitting is at least second order in  $\delta\mathbf{B}$ .

## A.5 Rank-2 points of a degeneracy curve carry zero linear topological charge density

In this section, we show that, in general, degeneracy curves consisting of rank-2 points carry zero linear topological charge density. For simplicity, we assume that the degeneracy line is along the  $B_z$  axis.

We use  $x \equiv B_x$ ,  $y \equiv B_y$  and  $z \equiv B_z$  for brevity, and we shift the coordinate system of the magnetic parameter space such that the rank-2 point we consider is in the origin, where  $(x, y, z) = 0$ . From now on, we further simplify notation by using  $\psi_0(s, \vartheta)$  instead of  $\hat{\psi}_0(s, \vartheta)$ .

According to Eq. (2.53), our goal is to evaluate

$$\nu(0) = \frac{1}{2\pi} \lim_{r \rightarrow 0} \int_0^{2\pi} d\vartheta \mathcal{B}_{2D}(s, \vartheta) = \frac{1}{2\pi} \lim_{r \rightarrow 0} \int_0^{2\pi} d\vartheta (-2) \text{Im} [\langle \partial_\vartheta \psi_0 | \partial_s \psi_0 \rangle]. \quad (64)$$

For the parameter-space geometry we consider, the relation between the Cartesian coordinates and the torus parameters is  $x = r \cos \vartheta$ ,  $y = r \sin \vartheta$ , and  $s = z$ . Our strategy is to evaluate the above  $\vartheta$  integral, i.e., to show that it vanishes, by using an approximate ground state  $\psi_0$  for  $r \rightarrow 0$ , obtained via a  $z$ -dependent two-level effective Hamiltonian.

Along the  $z$  axis, in the small neighborhood of the degeneracy point, we take an orthonormal basis  $(\eta(z), \chi(z))$  of the degenerate ground-state subspace for each  $z$ , such that the two basis states depend on  $z$  continuously. Using this basis, we define the effective Hamiltonian of the degeneracy point  $(0, 0, z)$  as follows:

$$H_{\text{eff}}(z) = P(z)H(x, y, z)P(z), \quad (65)$$

where  $P(z) = |\eta(z)\rangle \langle \eta(z)| + |\chi(z)\rangle \langle \chi(z)|$  projects on the two-dimensional ground-state subspace (this projector  $P$  should not be confused by the similarity transformation  $\hat{P}$ ).

This effective Hamiltonian can also be written as

$$H_{\text{eff}}(z) = \mathbf{x} \cdot \hat{\mathbf{g}}_{2 \times 3}(z) \boldsymbol{\tau}(z), \quad (66)$$

where  $\mathbf{x} = (x, y)^T$ , and  $\boldsymbol{\tau} = (\tau_x, \tau_y, \tau_z)^T$  are the Pauli operators acting on the states  $(\eta(z), \chi(z))$ , e.g.,  $\tau(z) = \frac{1}{2} (|\eta(z)\rangle \langle \eta(z)| - |\chi(z)\rangle \langle \chi(z)|)$ . Furthermore,  $\hat{\mathbf{g}}_{2 \times 3}$  is a  $2 \times 3$  matrix of the form

$$\hat{\mathbf{g}}_{2 \times 3} = \begin{pmatrix} g_{xx} & g_{xy} & g_{xz} \\ g_{yx} & g_{yy} & g_{yz} \end{pmatrix}. \quad (67)$$

The coordinate  $z$  is absent from Eq. (66), since our degeneracy point is on a degeneracy line of direction  $z$ , i.e., the two energy levels of the Hamiltonian must be degenerate as we move along the  $z$  axis.

The matrix  $\hat{\mathbf{g}}_{2 \times 3}(z)$  is of size  $2 \times 3$  and of rank 2, hence it can be further simplified to a block matrix with a nonzero  $2 \times 2$  block and a vanishing  $2 \times 1$  block (see Eq. (72) below), using a  $z$ -dependent unitary transformation of the basis  $(|\eta(z)\rangle, |\chi(z)\rangle)$ . To this end, we introduce the vectors  $\mathbf{g}_x = (g_{xx}, g_{xy}, g_{xz})^T$  and  $\mathbf{g}_y = (g_{yx}, g_{yy}, g_{yz})^T$  which are linearly independent because of the rank. We further introduce the vector

$$\mathbf{g}_\perp(z) = \mathbf{g}_x(z) \times \mathbf{g}_y(z), \quad (68)$$

for which it holds that

$$\hat{\mathbf{g}}_{2 \times 3} \mathbf{g}_\perp = 0. \quad (69)$$

Now we introduce the orthogonal matrix  $\hat{\mathbf{O}}(z)$  which rotates  $\mathbf{g}_\perp(z)$  to the  $z$  direction

$$\hat{\mathbf{O}} \mathbf{g}_\perp = g e_z, \quad (70)$$

with  $g(z) = |\mathbf{g}_\perp(z)|$ . One possible choice for  $\hat{\mathbf{O}}(z)$  is an orthogonal matrix which rotates  $180^\circ$  around the bisector  $\mathbf{t}(z)$  of  $\mathbf{e}_z$  and  $\mathbf{g}_\perp(z)$ . Now we substitute the identity  $\hat{\mathbf{O}}^{-1}\hat{\mathbf{O}}$  into Eq. (69) to obtain

$$\hat{\mathbf{g}}_{2\times 3}\mathbf{g}_\perp = \left(\hat{\mathbf{g}}_{2\times 3}\hat{\mathbf{O}}^{-1}\right)\left(\hat{\mathbf{O}}\mathbf{g}_\perp\right) = \hat{\mathbf{g}}'_{2\times 3}g\mathbf{e}_z = 0, \quad (71)$$

where we introduced  $\hat{\mathbf{g}}'_{2\times 3}(z) = \hat{\mathbf{g}}_{2\times 3}(z)\hat{\mathbf{O}}^{-1}(z)$ , which has the form

$$\hat{\mathbf{g}}'_{2\times 3} = \begin{pmatrix} g'_{xx} & g'_{xy} & 0 \\ g'_{yx} & g'_{yy} & 0 \end{pmatrix}. \quad (72)$$

After these steps we finally simplify the effective Hamiltonian defined in Eq. (66) with a unitary transformation. Substituting  $\hat{\mathbf{O}}^{-1}\hat{\mathbf{O}}$  yields

$$H_{\text{eff}}(z) = \mathbf{x} \cdot \hat{\mathbf{g}}_{2\times 3}(z)\hat{\mathbf{O}}^{-1}(z)\hat{\mathbf{O}}(z)\boldsymbol{\tau}(z) = \mathbf{x} \cdot \hat{\mathbf{g}}'_{2\times 3}(z)\boldsymbol{\tau}'(z), \quad (73)$$

where the new Pauli operator reads

$$\boldsymbol{\tau}'(z) = \hat{\mathbf{O}}(z)\boldsymbol{\tau}(z) = U(z)\boldsymbol{\tau}(z)U^\dagger(z). \quad (74)$$

After the first equation sign,  $\hat{\mathbf{O}}$  transforms the vector components of  $\boldsymbol{\tau}$ , while after the second equation sign, the corresponding unitary matrix  $U(z) = \exp(-i\pi\mathbf{t}(z) \cdot \boldsymbol{\tau}(z)) = -i\mathbf{t}(z) \cdot \boldsymbol{\tau}(z)$  transforms the operators in the Hilbert space. In Eq. (73) the Pauli operator  $\tau'_z$  does not appear, thus we can simplify the effective Hamiltonian by introducing the  $2 \times 2$  nonzero block  $\hat{\mathbf{g}}_{2\times 2}$  of the matrix  $\hat{\mathbf{g}}'_{2\times 3}$  in Eq. (72), and the 2-component vector operator  $\boldsymbol{\tau}_2 = (\tau'_x, \tau'_y)^\text{T}$ , yielding

$$H_{\text{eff}}(z) = \mathbf{x} \cdot \hat{\mathbf{g}}_{2\times 2}(z)\boldsymbol{\tau}_2(z). \quad (75)$$

This two-level effective Hamiltonian is straightforward to diagonalize, and its diagonalization provides a formula for the unique ground state away from the  $z$  axis:

$$|\psi_0(s, \vartheta)\rangle \equiv |\psi_0(z, \vartheta)\rangle \approx \frac{1}{\sqrt{2}} \left( |\eta'(z)\rangle - e^{i\alpha(z, \vartheta)} |\chi'(z)\rangle \right), \quad (76)$$

where

$$|\nu'(z)\rangle = U(z)|\nu(z)\rangle \quad (77)$$

$$|\chi'(z)\rangle = U(z)|\chi(z)\rangle \quad (78)$$

are the transformed basis states and  $\alpha(z, \vartheta)$  is the polar angle of the vector  $\hat{\mathbf{g}}_{2\times 2}^\text{T}\mathbf{x}$ . A key property of this angle is

$$\alpha(z, \vartheta + \pi) = \alpha(z, \vartheta) + \pi. \quad (79)$$

As we show below, this property implies  $\mathcal{B}_{2\text{D}}(s, \vartheta) = -\mathcal{B}_{2\text{D}}(s, \vartheta + \pi)$ , and hence a vanishing result of the integral in Eq. (64).

To compute the integrand of Eq. (64), we first evaluate the derivatives of the ground state (76):

$$|\partial_\vartheta\psi_0\rangle = \frac{-i}{\sqrt{2}}(\partial_\vartheta\alpha)e^{i\alpha}|\chi'\rangle, \quad (80)$$

$$|\partial_z\psi_0\rangle = \frac{1}{\sqrt{2}}\left(|\partial_z\eta'\rangle - e^{i\alpha}|\partial_z\chi'\rangle - i(\partial_z\alpha)e^{i\alpha}|\chi'\rangle\right). \quad (81)$$

Then, the scalar product in the integrand of Eq. (64) reads

$$\langle \partial_\vartheta \psi_0 | \partial_z \psi_0 \rangle = \frac{1}{2} [i(\partial_\vartheta \alpha) e^{-i\alpha} \langle \chi' | \partial_z \eta' \rangle + i(\partial_\vartheta \alpha) \langle \chi' | \partial_z \chi' \rangle + (\partial_\vartheta \alpha)(\partial_z \alpha)]. \quad (82)$$

The second term in the square bracket is real, since

$$\text{Re} \langle \chi' | \partial_z \chi' \rangle = \frac{1}{2} (\langle \chi' | \partial_z \chi' \rangle + \langle \partial_z \chi' | \chi' \rangle) = \frac{1}{2} \partial_z \langle \chi' | \chi' \rangle = 0. \quad (83)$$

Furthermore, the third term is also real, since  $\alpha$ , defined as an angle, is real-valued.

As a consequence, the imaginary part of the scalar product in the integrand of Eq. (64) reads

$$\text{Im} \langle \partial_\vartheta \psi_0 | \partial_z \psi_0 \rangle = \frac{1}{4} [(\partial_\vartheta \alpha) e^{-i\alpha} \langle \chi' | \partial_z \eta' \rangle + c.c.]. \quad (84)$$

From this result, using Eq. (79), it follows that

$$\text{Im} \langle \partial_\vartheta \psi_0(z, \vartheta + \pi) | \partial_z \psi_0(z, \vartheta + \pi) \rangle = -\text{Im} \langle \partial_\vartheta \psi_0(z, \vartheta) | \partial_z \psi_0(z, \vartheta) \rangle. \quad (85)$$

Finally, Eq. (85) implies that the  $\vartheta$  integral of Eq. (64) vanishes.

While the topological charge density vanishes at rank-2 points of a degeneracy curve, the Berry curvature is not identically zero. To see this, we consider a small disk  $D$  intersecting the degeneracy curve and calculate the integral of the Berry connection  $\mathcal{A} = i \langle \psi_0 | \nabla \psi_0 \rangle$  around the perimeter of the disk, which is a loop surrounding the line degeneracy:

$$\oint_{\partial D} \mathcal{A} \cdot d\mathbf{l} = i \int_0^{2\pi} \langle \psi_0 | \partial_\vartheta \psi_0 \rangle d\vartheta = \frac{1}{2} \int_0^{2\pi} \partial_\vartheta \alpha(z, \vartheta) d\vartheta = \frac{1}{2} [\alpha(z, 2\pi) - \alpha(z, 0)] = \pi. \quad (86)$$

This result is independent of the radius of the disk chosen.

If the degeneracy is broken by some perturbation, the Berry curvature becomes well defined and finite everywhere, with a large Berry curvature along the position of the degeneracy curve. In this case, the integral of the Berry curvature for the disk equals the integral of the Berry connection around the perimeter

$$\iint_D \mathcal{B} \cdot d\mathbf{A} = \oint_{\partial D} \mathcal{A} \cdot d\mathbf{l}. \quad (87)$$

The connection integral changes continuously with perturbations of the Hamiltonian, while the curvature diverges at the degeneracy. This allows us to interpret this result in the degenerate case as half a quantum of Berry flux concentrated in a line-like flux tube along the line degeneracy.

## A.6 Surface charge density of the ellipsoid

Here, we derive the surface charge density of the charged ellipsoid, a result quoted in the main text as Eq. (2.67). To do this, first, we transform the Hamiltonian to a simple form, where the Berry curvature is easy to determine, then we transform it back to obtain the surface charge density.

### Berry curvature in a simplified Hamiltonian

The Hamiltonian of the two-spin system can be simplified with the following steps. A global unitary transformation  $U$  which changes the right spin as  $\mathbf{S}'_R = \hat{\mathbf{R}} \mathbf{S}_R$  changes the interaction to be isotropic

$$H'(\mathbf{B}) = UH(\mathbf{B})U^\dagger = \mathbf{B} \cdot (\hat{\mathbf{g}}_L \mathbf{S}_L + \hat{\mathbf{g}}_R \hat{\mathbf{R}}^{-1} \mathbf{S}'_R) + J \mathbf{S}_L \cdot \mathbf{S}'_R. \quad (88)$$

This transformation changes the right  $g$ -tensor too. Now, we simplify the Zeeman term of the right spin with a linear transformation

$$\mathbf{B}' = \hat{\mathbf{R}}\hat{\mathbf{g}}_{\mathbf{R}}^{\mathbf{T}}\mathbf{B}. \quad (89)$$

To do this, we substitute the unit matrix  $\hat{\mathbf{g}}_{\mathbf{R}}\hat{\mathbf{R}}^{-1}\hat{\mathbf{R}}\hat{\mathbf{g}}_{\mathbf{R}}^{-1}$ , we get

$$H'(\mathbf{B}) = \mathbf{B} \cdot \hat{\mathbf{g}}_{\mathbf{R}}\hat{\mathbf{R}}^{-1} \left( \hat{\mathbf{R}}\hat{\mathbf{g}}_{\mathbf{R}}^{-1}\hat{\mathbf{g}}_{\mathbf{L}}\mathbf{S}_{\mathbf{L}} + \mathbf{S}'_{\mathbf{R}} \right) + J\mathbf{S}_{\mathbf{L}} \cdot \mathbf{S}'_{\mathbf{R}}. \quad (90)$$

This changes the left  $g$ -tensor to a transformed  $\hat{\mathbf{M}}$  matrix

$$\hat{\mathbf{R}}\hat{\mathbf{g}}_{\mathbf{R}}^{-1}\hat{\mathbf{g}}_{\mathbf{L}} = \hat{\mathbf{g}}_{\mathbf{L}}^{-1}\hat{\mathbf{g}}_{\mathbf{L}}\hat{\mathbf{R}}\hat{\mathbf{g}}_{\mathbf{R}}^{-1}\hat{\mathbf{g}}_{\mathbf{L}} = \hat{\mathbf{g}}_{\mathbf{L}}^{-1}\hat{\mathbf{M}}\hat{\mathbf{g}}_{\mathbf{L}} = \hat{\mathbf{M}}'. \quad (91)$$

The result is a Hamiltonian with  $\hat{\mathbf{R}}' = \mathbb{1}_{3 \times 3}$  and  $\hat{\mathbf{g}}'_{\mathbf{R}} = \mathbb{1}_{3 \times 3}$

$$H'(\mathbf{B}') = \mathbf{B}' \cdot \left( \hat{\mathbf{M}}'\mathbf{S}_{\mathbf{L}} + \mathbf{S}'_{\mathbf{R}} \right) + J\mathbf{S}_{\mathbf{L}} \cdot \mathbf{S}'_{\mathbf{R}}. \quad (92)$$

The global unitary transformation leaves the Berry curvature invariant but the linear transformation in the parameter space changes it, as we derive it in the next subsection.

For degeneracy ellipsoids  $\hat{\mathbf{M}} = a\mathbb{1}_{3 \times 3}$  is proportional to the unit matrix,

$$H'(\mathbf{B}') = \mathbf{B}' \cdot (a\mathbf{S}_{\mathbf{L}} + \mathbf{S}'_{\mathbf{R}}) + J\mathbf{S}_{\mathbf{L}} \cdot \mathbf{S}'_{\mathbf{R}}. \quad (93)$$

The result is an isotropic Hamiltonian. It has a degeneracy sphere with radius

$$R = \frac{1}{2} \left( 1 + \frac{1}{a} \right). \quad (94)$$

carrying a total topological charge 2. The Berry curvature in the transformed parameter space can be calculated using Gauss's law because of the isotropy

$$\mathcal{B}'(\mathbf{B}') = \begin{cases} 0 & B' < R \\ \frac{B'}{B'^3} & B' > R. \end{cases} \quad (95)$$

### Transformation of the Berry curvature in 3 dimensional parameter space

To obtain an isotropic Hamiltonian we did a global unitary transformation on the Hilbert space which preserves the Berry curvature, but we also did a linear transformation on the parameter space which, however, changes the curvature. In this subsection we derive the transformation of the Berry curvature in 3-dimensional parameter spaces.

We assume that Berry curvature with the transformed argument  $\mathbf{x}'(\mathbf{x})$  is known, this transformed curvature is given by  $\mathcal{B}'_i(\mathbf{x}') \equiv i\epsilon_{ijk} \langle \partial'_j \psi | \partial'_k \psi \rangle$  where  $\partial'_k$  is the derivative with respect to  $x'_k$ . We want to find the curvature with respect to the variable  $\mathbf{x}$ , given by  $\mathcal{B}_i(\mathbf{x}) \equiv i\epsilon_{ijk} \langle \partial_j \psi | \partial_k \psi \rangle$ . For the  $i$ -th component we get

$$\mathcal{B}_i(\mathbf{x}) = i\epsilon_{ijk} \langle \partial_l \psi | \partial_m \psi \rangle = i\epsilon_{ijk} \langle \partial_j \psi(\mathbf{x}'(\mathbf{x})) | \partial_k \psi(\mathbf{x}'(\mathbf{x})) \rangle = i\epsilon_{ijk} (\partial_j x'_l) (\partial_k x'_m) \langle \partial'_l \psi | \partial'_m \psi \rangle, \quad (96)$$

where we used the chain rule. The partial derivative  $\partial_j x'_l = J_{lj}$  is an element of the Jacobian matrix. This shows that the Berry curvature transforms as a 2-form. Multiplying with the Jacobian from the left yields

$$J_{ni}\mathcal{B}_i(\mathbf{x}) = i\epsilon_{ijk} J_{ni} J_{lj} J_{mk} \langle \partial'_l \psi | \partial'_m \psi \rangle = i(\det \hat{\mathbf{J}}) \epsilon_{nlm} \langle \partial'_l \psi | \partial'_m \psi \rangle = (\det \hat{\mathbf{J}}) \mathcal{B}'_n(\mathbf{x}'(\mathbf{x})), \quad (97)$$

where the Berry curvature with the transformed argument  $\mathcal{B}'(\mathbf{x}')$  appeared. From this we write the transformation rule specific to 3-dimensional parameter space:

$$\mathcal{B}(\mathbf{x}) = (\det \hat{\mathbf{J}}) \hat{\mathbf{J}}^{-1} \mathcal{B}'(\mathbf{x}'(\mathbf{x})). \quad (98)$$

For a linear transformation  $\mathbf{x}'(\mathbf{x}) = \hat{\mathbf{J}}\mathbf{x}$  the Jacobian is the coefficient matrix.

### Berry curvature in the parameter space of the ellipsoid

Now we can use the transformation of the Berry curvature derived in Eq. (98) to the Berry curvature in Eq. (95) with the transformation introduced in Eq. (89)

$$\mathcal{B}(\mathbf{B}) = (\det \hat{\mathbf{J}}) \hat{\mathbf{J}}^{-1} \mathcal{B}'(\mathbf{B}'(\mathbf{B})). \quad (99)$$

Here  $\hat{\mathbf{J}} = \hat{\mathbf{R}} \hat{\mathbf{g}}_{\mathbf{R}}^{\mathbf{T}}$ . Outside the ellipsoid we get

$$\mathcal{B}(\mathbf{B}_{S+}) = \det \left( \hat{\mathbf{R}} \hat{\mathbf{g}}_{\mathbf{R}}^{\mathbf{T}} \right) \left( \hat{\mathbf{R}} \hat{\mathbf{g}}_{\mathbf{R}}^{\mathbf{T}} \right)^{-1} \frac{\hat{\mathbf{R}} \hat{\mathbf{g}}_{\mathbf{R}}^{\mathbf{T}} \mathbf{B}_S}{|\hat{\mathbf{R}} \hat{\mathbf{g}}_{\mathbf{R}}^{\mathbf{T}} \mathbf{B}_S|^3} = \det(\hat{\mathbf{g}}_{\mathbf{R}}) \frac{\mathbf{B}_S}{|\hat{\mathbf{g}}_{\mathbf{R}}^{\mathbf{T}} \mathbf{B}_S|^3}, \quad (100)$$

inside we get

$$\mathcal{B}(\mathbf{B}_{S-}) = 0. \quad (101)$$

From Eq. (2.28) we get the equation for the degeneracy ellipsoid  $\mathbf{B}_S = B_S \mathbf{b}$

$$|\hat{\mathbf{g}}_{\mathbf{R}}^{\mathbf{T}} \mathbf{B}_S| = B_S |\hat{\mathbf{g}}_{\mathbf{R}}^{\mathbf{T}} \mathbf{b}| = B_S g_{\mathbf{R}} = \frac{1}{2} \left( 1 + \frac{1}{a} \right). \quad (102)$$

To get an expression for the surface normal of the ellipsoid, we consider the scalar field

$$f(\mathbf{B}) = \left( \hat{\mathbf{g}}_{\mathbf{R}}^{\mathbf{T}} \mathbf{B} \right)^2 \quad (103)$$

that is constant on the degeneracy ellipsoid. Hence the gradient

$$\nabla f = 2 \hat{\mathbf{g}}_{\mathbf{R}} \hat{\mathbf{g}}_{\mathbf{R}}^{\mathbf{T}} \mathbf{B} \quad (104)$$

is proportional to the normal vector of the surface. Thus, the normal vector for the degeneracy ellipsoid at  $\mathbf{B}_S$  reads

$$\mathbf{n}(\mathbf{B}_S) = \frac{\hat{\mathbf{g}}_{\mathbf{R}} \hat{\mathbf{g}}_{\mathbf{R}}^{\mathbf{T}} \mathbf{B}_S}{|\hat{\mathbf{g}}_{\mathbf{R}} \hat{\mathbf{g}}_{\mathbf{R}}^{\mathbf{T}} \mathbf{B}_S|}. \quad (105)$$

The surface topological charge density is proportional to the jump of the normal component of the Berry curvature

$$\sigma(\mathbf{B}_S) = \frac{1}{2\pi} [\mathcal{B}(\mathbf{B}_{S+}) - \mathcal{B}(\mathbf{B}_{S-})] \cdot \mathbf{n}(\mathbf{B}_S) = \frac{\det \hat{\mathbf{g}}_{\mathbf{R}}}{2\pi |\hat{\mathbf{g}}_{\mathbf{R}}^{\mathbf{T}} \mathbf{B}_S| \cdot |\hat{\mathbf{g}}_{\mathbf{R}} \hat{\mathbf{g}}_{\mathbf{R}}^{\mathbf{T}} \mathbf{B}_S|} = \frac{a \det \hat{\mathbf{g}}_{\mathbf{R}}}{\pi(a+1) |\hat{\mathbf{g}}_{\mathbf{R}} \hat{\mathbf{g}}_{\mathbf{R}}^{\mathbf{T}} \mathbf{B}_S|} \quad (106)$$

where in the last step Eq. (102) was used.

This calculation shows that the topological surface charge density is finite if the degenerate surface separates the parameter space into two regions with different Berry curvatures.

## B Schrieffer–Wolff transformation

This section contains the proofs and further details of the statements in Chapter 3.

### B.1 The Schrieffer–Wolff transformation induces a local chart

*Proof of Theorem 3.13 on the exact SW decomposition.* Recall that the diagonal matrix  $H_0 \in \Sigma_2$  is fixed, and define  $\check{B} := B + T + H_{\text{eff}} = \check{B} - H_0$ , see decomposition (3.15) and Figure 3.2 for notations.  $\check{B}$  is a block diagonal matrix of  $2 \times 2$  and  $(n-2) \times (n-2)$  blocks. The correspondence

$$(S, \check{B}) \mapsto H = f(S, \check{B}) := e^{iS} \cdot (H_0 + \check{B}) \cdot e^{-iS} \quad (107)$$

defines a real analytic map  $f : \mathbb{R}^{n^2} \rightarrow \mathbb{R}^{n^2}$ , in fact, the dimension of the space of  $(S, \check{B})$  is  $(n-2)^2 + 2^2 + 2 \cdot 2 \cdot (n-2) = n^2$ . We apply the analytic inverse function theorem [95, pg. 47, Thm. 2.5.1.].

We show that the Jacobian of  $H$  at 0 has maximal rank, that is,  $\text{rk}((df)_0) = n^2$ . This is equivalent to the fact that for every fix  $(S, \check{B}) \neq (0, 0)$ , the first-order part of  $f(tS, t\check{B}) = e^{itS} \cdot (H_0 + t\check{B}) \cdot e^{-itS}$  at  $t = 0$  is nonzero. That is,

$$\left. \frac{d}{dt} \left( e^{itS} \cdot (H_0 + t\check{B}) \cdot e^{-itS} \right) \right|_{t=0} = i[S, H_0] + \check{B} \neq 0. \quad (108)$$

To show that  $i[S, H_0] + \check{B} \neq 0$ , consider the entry  $a, b$  of the commutator:

$$[S, H_0]_{a,b} = \sum_{l=1}^n (S_{a,l} H_{0;l,b} - H_{0;a,l} S_{l,b}) = S_{a,b} (\lambda_b - \lambda_a). \quad (109)$$

It shows that  $[S, H_0]$  is an off-block matrix, and it is nonzero if  $S \neq 0$ . Indeed,  $S_{a,b} \neq 0$  can happen only if the index  $a, b$  satisfies  $a \leq 2 < b$  or  $b \leq 2 < a$ , hence in this case  $\lambda_b - \lambda_a \neq 0$ . Since  $\check{B}$  is block diagonal, for this  $a, b$  index  $\check{B}_{a,b} = 0$ , therefore it cannot cancel  $[S, H_0]_{a,b} \neq 0$ . That is,  $(i[S, H_0] + \check{B})_{a,b} \neq 0$ , if  $S_{a,b} \neq 0$ , implying that  $i[S, H_0] + \check{B} = 0$  only if  $S = 0$  and  $\check{B} = 0$ .

By the analytic inverse function theorem, there is a neighborhood  $\widetilde{\mathcal{W}}_0$  of  $(0, 0) \in \mathbb{R}^{n^2}$  (in the  $(S, \check{B})$  space) and  $\mathcal{V}_0$  of  $H_0 \in \text{Herm}(n)$  such that  $f|_{\widetilde{\mathcal{W}}_0} : \widetilde{\mathcal{W}}_0 \rightarrow \mathcal{V}_0$  is a bijection, whose inverse is also analytic. This gives the unique decomposition if  $H \in \mathcal{V}_0$  and  $(\check{B}, S) \in \widetilde{\mathcal{W}}_0$ , and the analytic dependence of  $\check{B}$  and  $S$  on  $H$ .

Moreover, we have to show that the ‘lowest two state property’ is satisfied, that is, the first two columns of  $e^{iS}$  span the sum of the eigenspaces of  $H$  corresponding to the lowest two eigenvalues. This is an additional property, which possibly requires the choice of smaller neighborhoods  $\mathcal{V}_0$  and  $\widetilde{\mathcal{W}}_0$ . Observe the following:

- (a) The eigenvalues of  $\check{B}$  and  $H$  are equal.
- (b) The subspace spanned by the first two columns of  $e^{iS}$  is exactly the sum of the eigenspaces of the  $2 \times 2$  block of  $\check{B}$ .

Therefore, the lowest two state property is equivalent to the statement that  $\lambda < \mu$  holds for each eigenvalue  $\lambda$  of the  $2 \times 2$  block of  $\check{B}$  and  $\mu$  of the  $(n-2) \times (n-2)$  block of  $\check{B}$ . The inequality  $\lambda < \mu$  holds for  $H = H_0$ , and the eigenvalues are continuous functions of  $H$ . Therefore, the inequality, and hence, the lowest two state property holds for every  $H$  in a sufficiently small neighborhood of  $H_0$ . □

**Remark 110.** *Surprisingly, in our proof the continuous behaviour of the eigenvalues implies the analytic behaviour of the sum of the eigenspaces corresponding to the lowest two eigenvalues around  $H_0 \in \Sigma_2$  (more precisely, the projector onto this eigenspace). Indeed, the dependence of  $S$  on  $H$  is analytic, and the sum of the eigenspaces is equal to the subspace spanned by the first two columns of  $e^{iS}$ , which is deduced from the continuous behaviour of the eigenvalues, and it implies the analytic dependence of the projector.*

In the Appendix we provide exact conditions for the neighborhoods  $\mathcal{V}_0$ ,  $\mathcal{W}_0$  and  $\mathcal{S}_0$  based on the results in [43].

*Proof of Corollary 3.17 on the local chart induced by the SW decomposition.* (a) The proof of Theorem 3.13 shows that the correspondence  $H \mapsto (x_i, y_j)$  is an analytic bijection with analytic inverse between the neighborhood  $\mathcal{V}_0 \subset \text{Herm}(n)$  of  $H_0$  and a neighborhood of  $0 \in \mathbb{R}^{n^2}$ . (b) Equation (3.18) is a straightforward consequence of the construction. Indeed,  $y_j = 0$  means that  $H_{\text{eff}} = 0$ , and in this case  $H \in \Sigma_2$  by equation (3.15). □

**Remark 111.** *The existence of the SW chart fitting to  $\Sigma_2$  in the sense of Corollary 3.17 gives an alternative proof for the Neumann–Wigner theorem, stating that  $\Sigma_2$  is a submanifold of codimension 3 (see Table 3.1 for the sketch of the original proof).*

*Proof of Theorem 3.22 on the projection to  $\Sigma_2$ .* Let  $\mathcal{P}$  denote the subspace spanned by the first  $k$  columns of  $e^{iS}$ , which is equal to the sum of the eigenspaces of the lowest two eigenvalues of  $H$ . Let  $\mathcal{P}^\perp$  denote its Hermitian complement, this is the subspace spanned by the last  $n - 2$  columns of  $e^{iS}$ , and it also agrees with the sum of the eigenspaces of the highest  $n - 2$  eigenvalues of  $H$ . In particular,  $\mathcal{P}$  and  $\mathcal{P}^\perp$  are invariant subspaces of  $H_\Sigma$  and  $H_{\text{proj}}$ . We show that the restrictions of  $H_{\text{proj}}$  and  $H_\Sigma$  to both  $\mathcal{P}$  and  $\mathcal{P}^\perp$  are equal.

Both  $H_\Sigma$  and  $H_{\text{proj}}$  has  $k$ -fold degeneracy, and  $\mathcal{P}$  is the eigenspace corresponding to the lowest two degenerate eigenvalues of  $H_{\text{proj}}$ , and also  $H_\Sigma$ . Moreover the degenerate eigenvalues of these matrices are also equal. Indeed, the trace of the  $2 \times 2$  block of  $H_{\text{proj}}$  is equal to  $\lambda_1 + \lambda_2$  (where  $\lambda_{1,2}$  denotes the eigenvalues of  $H$ ), since  $H_{\text{eff}}$  has trace 0. Hence the restrictions of  $H_{\text{proj}}$  and  $H_\Sigma$  to their common degenerate eigensubspace  $\mathcal{P}$  are equal.

On the other hand, their restrictions to  $\mathcal{P}^\perp$  are equal to the restriction of  $H$ . Then  $H_{\text{proj}}$  and  $H_\Sigma$  agree on both  $\mathcal{P}$  and  $\mathcal{P}^\perp$ , hence  $H_{\text{proj}} = H_\Sigma$ . □

## B.2 Energy splitting and the distance from $\Sigma_2$

In this subsection we prove Theorem 3.23 on the distance from  $\Sigma_2$ . We start with its easy parts.

**Proposition 112.**  $d(H, H_\Sigma) = \|H_{\text{eff}}\| = \frac{\lambda_2 - \lambda_1}{\sqrt{2}}$ .

*Proof.*  $d(H, H_\Sigma) = \|H - H_\Sigma\| = \|e^{iS} \cdot H_{\text{eff}} \cdot e^{-iS}\| = \|H_{\text{eff}}\|$ , the second equation follows from the eigenvalues of a  $2 \times 2$  matrix:

$$\lambda_{1,2} = \mp \sqrt{y_1^2 + y_2^2 + y_3^2} = \frac{\|H_{\text{eff}}\|}{\sqrt{2}}. \quad (113)$$

□

Next we show the harder part, namely, for every  $H \in \text{Herm}(n) \setminus \Sigma_{[2,3]}$  the unique closest point of  $\Sigma_2$  to  $H$  is  $H_\Sigma$ . First of all, notice that  $\Sigma_2$  is not a compact set, hence, theoretically it might happen that  $\Sigma_2$  does not have closest point to  $H$ , more precisely, the distance function  $d_H : \text{Herm}(n) \rightarrow \mathbb{R}$  defined as  $d_H(G) = d(H, G)$  does not have a minimum on  $\Sigma_2$ . Avoiding this possibility causes several complications, which are managed at the end of this subsection. But before this, we first observe that a minimum point of the restricted function  $d_H|_{\Sigma_2}$  is also critical point of it, therefore we have the following.

**Proposition 114.** *If  $\mu$  is a minimum value of  $d_H$  on  $\Sigma_2$ , that is,  $\mu = \min\{d(H, G) \mid G \in \Sigma_2\}$ , and  $K \in \Sigma_2$  satisfies  $d(H, K) = \mu$ , then the line  $\{tK + (1 - t)H \mid t \in \mathbb{R}\}$  is orthogonal to  $\Sigma_2$  at  $K$ .*

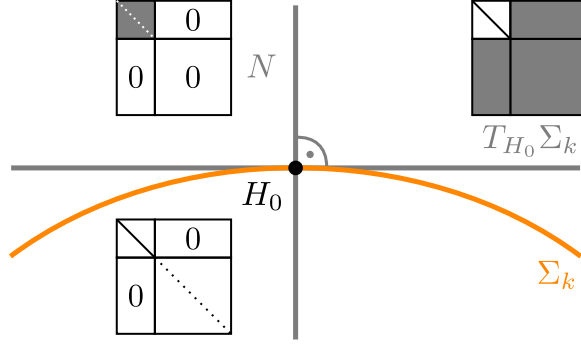


Figure 3: The matrix form of the elements of the tangent space  $T_{H_0}\Sigma_2$  and normal space  $N$  of  $\Sigma_2$  at a diagonal matrix  $H_0 \in \Sigma_2$ . By Lemma 118, the tangent space consists of matrices whose upper-left  $2 \times 2$  block is a scalar matrix. The normal space, i.e. the orthogonal complement of the tangent space agrees with the space of effective Hamiltonians  $\text{Herm}_0(2) \subset \text{Herm}(n)$ : its elements have only a traceless upper left  $2 \times 2$  block and zero entries everywhere else.

*Proof.*  $d_H$  has a global minimum at  $K$ , in particular, it is a local minimum. Since  $\Sigma_2$  is a smooth manifold, every local minimum of a smooth function is a critical point, meaning that the differential  $(d(d_H|_{\Sigma_2}))_K$  of  $d_H|_{\Sigma_2}$  at  $K$  is 0. It means that the gradient of  $d_H$  at  $K$  is orthogonal to  $\Sigma_2$ . Indeed, for any tangent vector  $v \in T_K\Sigma_2$  of  $\Sigma_2$  at  $K$  the evaluation of the differential is

$$(d(d_H|_{\Sigma_2}))_K(v) = (d(d_H))_K(v) = \langle \text{grad}_K(d_H), v \rangle, \quad (115)$$

where the first equality comes from the definition of the restriction, and second equality is definition of the gradient. Hence  $(d(d_H|_{\Sigma_2}))_K$  is zero for every  $v \in T_K\Sigma_2$  if and only if  $\text{grad}_K(d_H)$  is orthogonal to  $T_K\Sigma_2$ .

On the other hand, since  $d_H$  is the distance from  $H$ , the gradient  $\text{grad}_K(d_H)$  is parallel to  $K - H$ , hence it is parallel to the line joining  $H$  and  $K$ . Therefore, this line is orthogonal to the tangent space  $T_K\Sigma_2$ , hence to  $\Sigma_2$  at  $K$ .  $\square$

From now on we look for all the lines through  $H$  orthogonal to  $\Sigma_2$ . According to Proposition 114, the intersection points of these lines with  $\Sigma_2$  are the candidates for the closest point of  $\Sigma_2$  to  $H$ . Let

$$L_H = \{tH_\Sigma + (1-t)H \mid t \in \mathbb{R}\} \quad (116)$$

be the line joining  $H$  and  $H_\Sigma$ .

**Proposition 117.**  $L_H$  is orthogonal to  $\Sigma_2$  at the intersection point  $H_\Sigma$ .

Before the proof we highlight its essential step, the description of the tangent space.

**Lemma 118.** Let  $H_0 \in \Sigma_2$  be a diagonal matrix. Then the tangent space  $T_{H_0}\Sigma_2$  of  $\Sigma_2$  at  $H_0$  consists of the Hermitian matrices whose upper-left  $2 \times 2$  block is a scalar matrix. See Figure 3.

*Proof of Lemma 118.* By the SW decomposition (3.15) and Corollary 3.17,  $\Sigma_2$  is locally given by the equation  $H_{\text{eff}} = 0$ , that is,  $y_1 = y_2 = y_3 = 0$ . Hence the tangent space  $T_{H_0}\Sigma_2$  consists of the directions orthogonal to the  $H_{\text{eff}}$  directions, which includes everything in the  $(n-2) \times (n-2)$  block, in the off-block, and the trace of the  $2 \times 2$  block, proving the lemma.  $\square$

**Remark 119.** *A more precise analysis also highlights the role of the off-block form of the exponent  $S$  in SW decomposition (3.15): its variation changes the off-block elements of  $H_0$  up to first order. Indeed, by Equation (108), every tangent vector can be written in form  $i[S, H_0] + \check{B}$  with an off-block  $S$  and a block diagonal  $\check{B}$ , where now  $\check{B} = B + T$ , that is,  $H_{\text{eff}} = 0$ , since we are in  $\Sigma_2$ . By Equation (109), the entries of this tangent vector are  $iS_{a,b}(\lambda_b - \lambda_a) + \check{B}_{a,b}$ , showing that  $S$  generates the off-block elements, and  $\check{B}$  generates the  $(n-2) \times (n-2)$  block and the trace of the  $2 \times 2$  block.*

Moreover, one can prove Lemma 118 without referring to the SW decomposition, but starting from an over-parametrization of  $\Sigma_2$  around  $H_0$  of the form  $e^{iG}(H_0 + \check{B})e^{-iG}$ , where  $\check{B} = B + T$  as above, but now  $G$  can be any element of  $\text{Herm}(n)$ . This leads to tangent vectors of the form  $i[G, H_0] + \check{B}$  with entries  $iG_{a,b}(\lambda_b - \lambda_a) + \check{B}_{a,b}$ , which also shows that the off-diagonal elements of a tangent vector depend on the off-block entries of  $G$  and it can be arbitrary, since  $\lambda_b - \lambda_a \neq 0$  between different blocks; the  $2 \times 2$  block of  $G$  is irrelevant, since  $\lambda_b - \lambda_a = 0$  if  $a, b \leq 2$ ; and the  $(n-2) \times (n-2)$  block of  $G$  contributes only to the  $(n-2) \times (n-2)$  block of the tangent vector, which can be arbitrary by a choice of  $\check{B}$ , as well as the trace of the  $2 \times 2$  block.

*Proof of Proposition 117.* It is enough to show that  $H - H_\Sigma$  is orthogonal to the tangent space  $T_{H_\Sigma}\Sigma_2$  of  $\Sigma_2$  at  $H_\Sigma$ . Because of Lemma 3.7 it is enough to show the orthogonality in the diagonal case, namely,  $\Lambda - \Lambda_\Sigma$  is orthogonal to  $T_{\Lambda_\Sigma}\Sigma_2$ . But  $\Lambda - \Lambda_\Sigma$  is a diagonal matrix with nonzero elements only in the  $2 \times 2$  block, and its trace is 0. More precisely, the diagonal elements are  $\lambda_i - \bar{\lambda}$  ( $i = 1, 2$ ) where  $\lambda_i$  are lowest two eigenvalues of  $H$  and  $\bar{\lambda} = (\lambda_1 + \lambda_2)/2$  is their mean value. By Lemma 118, the  $2 \times 2$  block of each tangent vector  $K \in T_{\Lambda_\Sigma}\Sigma_2$  is a scalar matrix, we denote its diagonal entries by  $c$ . Then

$$\langle \Lambda - \Lambda_\Sigma, K \rangle = c(\lambda_1 - \bar{\lambda}) + c(\lambda_2 - \bar{\lambda}) = 0, \quad (120)$$

proving the proposition.  $\square$

**Remark 121.** *If  $H$  is sufficiently close to  $\Sigma_2$ , then the orthogonality of  $L_H$  to  $\Sigma_2$  implies that  $H_\Sigma$  is the unique closest point of  $\Sigma_2$  to  $H$ . This follows from the tubular neighborhood theorem [96] (see also [77, pg. 74, exercise 3.]): if a point  $p \in \mathbb{R}^n$  is sufficiently close to a submanifold  $N \subset \mathbb{R}^n$ , then it has a unique closest point  $p' \in N$ , characterised by the orthogonality of the line joining  $p$  and  $p'$  to  $N$ . However, it is not enough for the global version of Theorem 3.23, that is, for every  $H \in \text{Herm}(n) \setminus \Sigma_{[k, k+1]}$ .*

In the following we characterise the lines orthogonal to  $\Sigma_2$  at a point.

**Proposition 122.** *Let  $L$  be a line in  $\text{Herm}(n)$  through a point  $H_0 \in \Sigma_2$ . Then the following are equivalent:*

1.  $L = L_H$  for an element  $H \in L \setminus \{H_0\}$  (in particular,  $H_\Sigma = H_0$ ).
2.  $L$  is orthogonal to  $\Sigma_2$  at  $H_0$ .
3.  $L$  can be parametrized as follows: Starting with any diagonalization  $H_0 = U\Lambda_0U^{-1}$  with increasing order of the eigenvalues, we choose a  $2 \times 2$  diagonal matrix  $D$  of trace 0 with increasing order of the diagonal elements in the upper-left block, and take the parametrization

$$t \mapsto U(\Lambda_0 + tD)U^{-1}. \quad (123)$$

4.  $L = L_H$  for every  $H \in L \setminus \{H_0\}$  sufficiently close to  $H_0$  (in particular,  $H_\Sigma = H_0$ ).

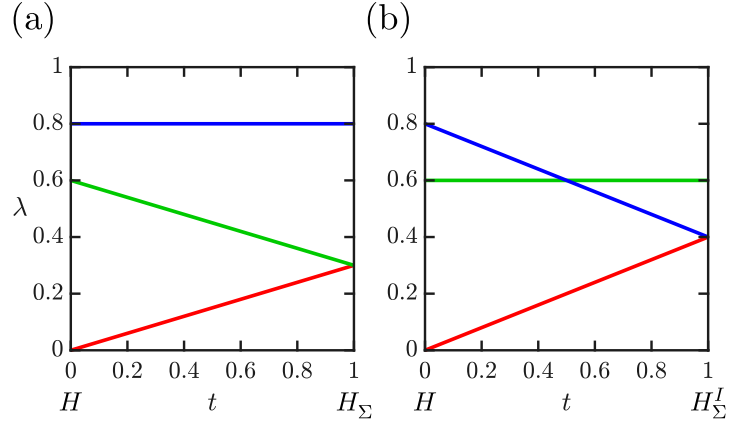


Figure 4: The projections of  $H$  onto  $\Sigma_2$  for  $n = 3$ , illustrating the proof of Proposition 131. Panel (a) ((b) respectively):  $H_\Sigma = H_\Sigma^{\{1,2\}}$  ( $H_\Sigma^I = H_\Sigma^{\{1,3\}}$ ) is constructed by contracting the eigenvalues  $\lambda_1$  and  $\lambda_2$  ( $\lambda_1$  and  $\lambda_3$ ) of  $H$  to their mean value. The linear motion of the eigenvalues (red, green and blue line segments) realizes the line segments of  $L_H$  ( $L_H^I$ ), joining  $H$  with  $H_\Sigma$  ( $H_\Sigma^I$ ).

*Proof.* (1)  $\Rightarrow$  (2): Follows from Proposition 117.

(1)  $\Rightarrow$  (3): Follows directly from the construction of  $H_\Sigma$ , by choosing  $D = \Lambda - \Lambda_0$ , with any choice of  $U$  diagonalizing  $H$  (hence, also  $H_0$ ), where  $\Lambda = U^{-1}HU$  is diagonal.

(3)  $\Rightarrow$  (4): Consider an element  $G = U(\Lambda_0 + tD)U^{-1} \in L$ , then  $G_\Sigma = H_0$  if the diagonal elements of  $\Lambda_\Sigma + tD$  are still in increasing order, that is, until the line reaches the  $\Sigma_{[2,3]}$  degeneracy stratum. This holds for sufficiently small  $t$ .

(4)  $\Rightarrow$  (1) is obvious. Until now we proved the equivalence of (1), (3) and (4), and any of them implies (2).

(2)  $\Rightarrow$  (3): It follows by counting the dimensions, cf. Table 3.1 for a similar method. First note that (3) implies (2), that is, the parametrization (123) provides orthogonal lines to  $\Sigma_2$  at  $H_0$ . Then we count how many dimensions can be covered by such a parametrization. The choice of  $D$  up to a real scalar factor gives  $2 - 1$  dimensions. The choice of the lowest two eigenspaces, that is, the first two columns of  $U$  up to  $U(1)$  rotations gives  $2^2 - 2$  dimensions. Hence, the dimension of the subspace of matrices which can be reached by a parametrization in form (123) has  $2 - 1 + 2^2 - 2 = 3$  dimensions, therefore it covers the whole normal space of  $\Sigma_2$  at  $H_0$ .

The above implications imply the equivalence, proving the theorem.  $\square$

**Remark 124.** By point (3) of the above proposition, the orthogonal lines to  $\Sigma_2$  at  $H_0$  can be described as ‘spreading the eigenvalues linearly’. Although this construction seems to be insightful, its difficulty is that the direction of the line depends on both  $D$  and the unitary matrix  $U$  – more precisely, on the subspaces spanned by its first two columns. Another way to characterize the orthogonal lines via SW decomposition is ‘turning an effective Hamiltonian on’: Starting from the unique SW decomposition (3.19) of  $H_0$  (with respect to a possibly different base point  $H_0^I$ ), we choose a  $2 \times 2$  Hermitian matrix  $H_{\text{eff}}$  of trace 0 in the upper left block. The corresponding line is parametrized as

$$t \mapsto H_0 + t \cdot e^{iS} \cdot H_{\text{eff}} \cdot e^{-iS}, \quad (125)$$

which is orthogonal to  $\Sigma_2$  at  $H_0$ , cf. Lemma 118.

Next we characterise the lines through a point  $H \in \text{Herm}(n) \setminus \Sigma_{[2,3]}$  which intersect  $\Sigma_2$  orthogonally.  $L_H$  is one of these lines. To find the others, first consider an example, a matrix

$H \in \text{Herm}(3)$  with eigenvalues  $\lambda_1 < \lambda_2 < \lambda_3$ . To obtain its projection  $H_\Sigma^{\{1,2\}} = H_\Sigma \in \Sigma_2$ , we contract  $\lambda_1$  and  $\lambda_2$  to their mean value  $\bar{\lambda}^{\{1,2\}} = (\lambda_1 + \lambda_2)/2$ , then the line through  $H_\Sigma$  and  $H$  is  $L_H^{\{1,2\}} = L_H$ .

Another possibility is the contraction of  $\lambda_1$  and  $\lambda_3$  to  $\bar{\lambda}^{\{1,3\}} = (\lambda_1 + \lambda_3)/2$ . If  $\bar{\lambda}^{\{1,3\}} < \lambda_2$ , then we obtain a point  $H_\Sigma^{\{1,3\}} \in \Sigma_2$ . Consider the line

$$L_H^{\{1,3\}} = \{tH_\Sigma^{\{1,3\}} + (1-t)H \mid t \in \mathbb{R}\} \quad (126)$$

joining  $H_\Sigma^{\{1,3\}}$  and  $H$ . It consists of the matrices

$$\begin{aligned} tH_\Sigma^{\{1,3\}} + (1-t)H &= U \begin{pmatrix} \lambda_1 + \frac{t}{2}(\lambda_3 - \lambda_1) & 0 & 0 \\ 0 & \lambda_2 & 0 \\ 0 & 0 & \lambda_3 + \frac{t}{2}(\lambda_1 - \lambda_3) \end{pmatrix} U^{-1} \\ &= U' \begin{pmatrix} \lambda_1 + \frac{t}{2}(\lambda_3 - \lambda_1) & 0 & 0 \\ 0 & \lambda_3 + \frac{t}{2}(\lambda_1 - \lambda_3) & 0 \\ 0 & 0 & \lambda_2 \end{pmatrix} (U')^{-1}, \end{aligned} \quad (127)$$

where  $U'$  is the product of  $U$  with the transposition of the 2nd and 3th basis elements. The role of  $U'$  is to satisfy the increasing order of the eigenvalues, if we want to have a conventional form. Then, by Proposition 122,  $L_H^{\{1,3\}}$  is orthogonal to  $\Sigma_2$  at  $H_\Sigma^{\{1,3\}}$ . However, it crosses the stratum  $\Sigma_{(12)}$  of  $\Sigma$  (corresponding to the degeneracy  $\lambda_2 = \lambda_3$ ) between  $H_\Sigma^{\{1,3\}}$  and  $H$ , namely, for  $t = 2(\lambda_3 - \lambda_2)/(\lambda_3 - \lambda_1)$ . See Figure 4.

The third possibility, the contraction of  $\lambda_2$  and  $\lambda_3$  to  $\bar{\lambda}^{\{2,3\}}$  results a matrix  $H_\Sigma^{\{2,3\}}$ , which is not in  $\Sigma_2$ , since  $\bar{\lambda}^{\{2,3\}} > \lambda_1$ .

The same can be done in general, for an  $H \in \text{Herm}(n) \setminus \Sigma_{[2,3]}$ . Choose two indices  $1 \leq i_1 < i_2 \leq n$ , and let  $I = \{i_1, i_2\}$  denote their set. Let  $H_\Sigma^I$  denote the matrix obtained from  $H$  by replacing the eigenvalues  $\lambda_{i_1}, \lambda_{i_2}$  with their mean  $\bar{\lambda}^I = (\lambda_{i_1} + \lambda_{i_2})/2$ . More precisely, let  $\Lambda_\Sigma^I$  be the diagonal matrix obtained from  $\Lambda = U^{-1}HU = \text{diag}(\lambda_1, \dots, \lambda_n)$  by replacing  $\lambda_i$  with  $\bar{\lambda}^I$  for  $i \in I$ , and define

$$H_\Sigma^I = U \cdot \Lambda_\Sigma^I \cdot U^{-1}. \quad (128)$$

In general,  $H_\Sigma^I$  can depend on the choice of  $U$ . In fact, if there is a degeneracy  $\lambda_i = \lambda_{i'}$  of eigenvalues of  $H$  with  $i \in I$  and  $i' \notin I$ , then their separation depends on the choice of the diagonalization inside the degenerate eigenspace. For simplicity we omit the  $U$  dependence from the notation, and  $H_\Sigma^I$  denotes any of the possible choices.

If  $\bar{\lambda}^I$  is smaller than the lowest omitted eigenvalue  $\lambda_m$ , where  $m = \min(\{1, \dots, n\} \setminus I)$ , then  $H_\Sigma^I \in \Sigma_2$ . Let

$$L_H^I = \{tH_\Sigma^I + (1-t)H \mid t \in \mathbb{R}\} \quad (129)$$

be the line joining  $H_\Sigma^I$  and  $H$ . Obviously,  $L_H^I$  crosses other strata of  $\Sigma$  between  $H$  and  $H_\Sigma^I$ . By Proposition 122, the lines  $L_H^I$  are orthogonal to  $\Sigma_2$  at  $H_\Sigma^I$ , moreover:

**Proposition 130.** *The only lines through  $H \in \text{Herm}(n) \setminus \Sigma_{[2,3]}$  which are orthogonal to  $\Sigma_2$  are the  $L_H^I$  lines with  $I \subset \{1, \dots, n\}$  satisfying  $H_\Sigma^I \in \Sigma_2$ .*

*Proof.* Assume that a line  $L$  through  $H$  intersects  $\Sigma_2$  orthogonally at  $H_0 \in \Sigma_2$ . By point (3) of Proposition 122,  $L$  has a special parametrization in form (123). The linear motion of the degenerate eigenvalues of  $H_0$  arrives at 2 eigenvalues of  $H$  corresponding to the indices  $\{i_1, i_2\} = I$ , and then,  $H_0 = H_\Sigma^I$  by the construction.  $\square$

Recall that our goal is to prove that  $H_\Sigma$  is the closest point of  $\Sigma_2$  to  $H$ . Towards this goal the next step is to show that  $H_\Sigma^I$  cannot be a closest point of  $\Sigma_2$  to  $H$  if  $I \neq \{1, 2\}$ . Recall that it does not imply directly that  $H_\Sigma$  is the closest point, until we prove that there is a closest point, which will be the last step.

**Proposition 131.** *The closest  $H_\Sigma^I \in \Sigma_2$  (with a fixed unitary matrix  $U$  diagonalizing  $H$ , cf. Equation (128)) to  $H$  has the index  $I = \{1, 2\}$ .*

*Proof.* If  $1 < i_1$ , then  $\lambda_1 < \frac{\lambda_{i_1} + \lambda_{i_2}}{2}$ , therefore,  $H_\Sigma^I \notin \Sigma_2$ . If  $i_1 = 1$  and  $2 < i_2$ , then  $H_\Sigma^{\{1, 2\}}$  is closer to  $\Sigma_2$  than  $H_\Sigma^I$  because  $\lambda_2 - \lambda_1 < \lambda_{i_2} - \lambda_1$ .  $\square$

Comparing Proposition 114, 117, 130 and 131, we conclude the following.

**Corollary 132.** *If the distance function  $d_H$  has a global minimum  $\mu$  on  $\Sigma_2$ , then  $d(H, H_\Sigma) = \mu$  and  $H_\Sigma$  is the unique closest point of  $\Sigma_2$  to  $H$ . In particular,  $d(H, \Sigma_2) = d(H, H_\Sigma)$  holds.*

In the following we show that  $d_H$  has a global minimum on  $\Sigma_2$ . First we take a weaker observation.

**Proposition 133.** *The distance function  $d_H$  has a global minimum on the closure  $\text{cl}(\Sigma_2)$  of  $\Sigma_2$  in  $\text{Herm}(n)$ .*

*Proof.* Actually it is a classical fact for any closed subset  $A$  of  $\mathbb{R}^n$  and a point  $P \in \mathbb{R}^n$  that  $A$  has a point with minimal distance from  $P$ . For completeness we write a proof for our particular situation, which works in general.

Take a closed ball  $\mathcal{B} \subset \text{Herm}(n)$  of radius  $R$  centered at  $H$ , that is,  $\mathcal{B} = \{G \in \text{Herm}(n) \mid d(H, G) \leq R\}$ . The radius  $R$  has to be chosen such that  $\text{cl}(\Sigma_2) \cap \mathcal{B}$  is non-empty, e.g.,  $R > d(H, H_\Sigma)$  is good. If  $d_H$  has a global minimum on  $\text{cl}(\Sigma_2) \cap \mathcal{B}$ , then it is the global minimum on  $\text{cl}(\Sigma_2)$  as well.

$\text{cl}(\Sigma_2) \cap \mathcal{B}$  is a closed and bounded subset of  $\mathbb{R}^n$ , hence it is compact, therefore, any continuous function on it has a global minimum, proving the proposition.  $\square$

**Proposition 134.**  *$H_\Sigma$  is the unique closest point of  $\Sigma_2$  to  $H$ . In particular,  $d(H, \Sigma_2) = d(H, H_\Sigma)$  holds.*

*Proof.* According to Proposition 133, take a point  $K \in \text{cl}(\Sigma_2)$  with minimal distance from  $H$ . Recall from Section 3.2 the disjoint decomposition  $\text{cl}(\Sigma_2) = \Sigma_2 \cup \Sigma_3 \cup \dots \cup \Sigma_n$ , hence,  $K \in \Sigma_k$  holds with a  $k \geq 2$ . Then, by applying the generalization of Corollary 132 to  $\Sigma_k$ , it follows that  $K$  is the projection of  $H$  to  $\Sigma_k$  by contracting the lowest  $k$  eigenvalues of  $H$  to their mean value.

Assume indirectly that  $k > 2$ . The triangle of vertices  $H$ ,  $H_\Sigma$ ,  $K$  has a right angle at  $H_\Sigma$ . Indeed, by Proposition 117, the line  $L_H$  joining  $H$  and  $H_\Sigma$  is orthogonal to  $\Sigma_2$ . Since the line joining  $H_\Sigma$  and  $K$  lies in  $\Sigma_2$ , it is orthogonal to  $L_H$ . See Figure 5. It follows that  $d(H, H_\Sigma) < d(H, K)$ , which contradicts with the premise that  $K$  is the closest point of  $\text{cl}(\Sigma_2)$  to  $H$ .

Therefore,  $k = 2$  and  $K = H_\Sigma$ , which proves the proposition.  $\square$

*Proof of Theorem 3.23 on the distance from  $\Sigma_2$ .* Proposition 134 and Corollary 112 prove Theorem 3.23.  $\square$

**Remark 135.** *If  $H \in \Sigma_{[2, 3]}$ , then  $H_\Sigma$  is not unique, it depends on the choice of the unitary matrix diagonalizing  $H$ , more precisely, on the subspace generated by the 2nd column of  $U$ . However,  $d(H, H_\Sigma)$  is the same for every  $H_\Sigma$ , and it is the global minimum of the distance function  $d_H$  on  $\Sigma_2$ . Therefore,  $d(H, \Sigma_2) = d(H, H_\Sigma)$  holds in this case with any choice of  $H_\Sigma$ .*

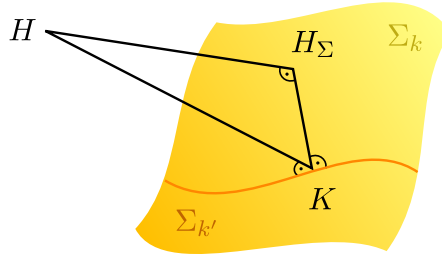


Figure 5: The proof of Proposition 134. Since  $k > 2$ , the closure of  $\Sigma_2$  contains  $\Sigma_2$ . The projections of  $H$  to  $\Sigma_2$  and  $\Sigma_2$ , (obtained by contracting the lowest two and the lowest two eigenvalues of  $H$  to their mean value) is denoted by  $H_\Sigma$  and  $K$ , respectively.  $K$  is also the projection of  $H_\Sigma$  to  $\Sigma_2$  in the same sense. Moreover, the line segment joining  $H_\Sigma$  and  $K$  lies in  $\Sigma_2$ , implying that it is orthogonal to the line segment joining  $H$  and  $H_\Sigma$ , by Proposition 117. Therefore, the right triangle with vertices  $H$ ,  $H_\Sigma$  and  $K$  shows that  $d(H, H_\Sigma) < d(H, K)$ . (The orthogonality of the line segment joining  $H$  and  $K$  to  $\Sigma_2$  and  $H_\Sigma$ , respectively, and  $K$  to  $\Sigma_2$  is not used in the proof.)

### B.3 Parameter-dependent quantum systems and Weyl points

*Proof of Theorem 3.35 on the characterization of Weyl points.* The equivalence of (1) and (2) is a well-known property of transversality, see e.g. [77, pg. 28] or [78, Lemma 4.3.]. To see it in our particular situation, consider a chart on  $M^3$  around  $p_0 = 0$ , and consider the SW chart (Corollary 3.17) on the neighborhood  $\mathcal{V}_0$  of  $H_0$  in  $\text{Herm}(n)$ , with coordinates  $\phi(H) = (x, y) \in \mathbb{R}^{n^2-3} \times \mathbb{R}^3$ . Let  $\phi_y : \mathcal{V}_0 \rightarrow \mathbb{R}^3$  denote the map  $\phi_y(H) = (y_1, y_2, y_3)$ . Obviously,  $h = \phi_y \circ H$ , and the tangent space of  $\Sigma_2$  at  $H_0$  is  $T_{H_0}\Sigma_2 = \ker((d\phi_y)_{H_0})$ . The transversality of  $H$  to  $\Sigma_2$  at  $H(p_0) = H_0$  means that

$$T_{H_0}\Sigma_2 + (dH)_{p_0}(T_{p_0}M^3) = T_{H_0}\text{Herm}(n), \quad (136)$$

or equivalently,

$$\ker((d\phi_y)_{H_0}) + (dH)_{p_0}(T_{p_0}M^3) = T_{H_0}\text{Herm}(n). \quad (137)$$

(Recall the definitions from Section 3.5.) By applying  $(d\phi_y)_{H_0}$  on both sides, we get

$$(d\phi_y)_{H_0} \circ (dH)_{p_0}(T_{p_0}M^3) = (d\phi_y)_{H_0}(T_{H_0}\text{Herm}(n)). \quad (138)$$

On the left side,  $(d\phi_y)_{H_0} \circ (dH)_{p_0} = (dh)_{p_0}$  by the chain rule, and the right side is equal to  $T_0\mathbb{R}^3$ , since  $(d\phi_y)_{H_0}$  is surjective. Therefore, the transversality is equivalent to the fact that  $(d\phi_y)_{H_0}$  is surjective on the the image of  $(dH)_{p_0}$ , which is equivalent to the fact that  $(dh)_{p_0}$  has maximal rank 3. This proves (1)  $\Leftrightarrow$  (2).

Point (3) is clearly equivalent to (2), since it is equivalent to the following: for every  $\gamma$  with  $\gamma(0) = p_0$ ,  $\gamma'(0) \neq 0$ ,  $\gamma'(0) \notin \ker((dh)_{p_0})$ . Point (3) is also equivalent to (4), since the order of energy splitting is equal to the order of  $h(\gamma(t))$ , which is 1 by (3).  $\square$

*Proof of Corollary 3.39 on Weyl points being isolated.* First we show that  $p_0$  has a neighborhood  $\widetilde{\mathcal{W}}_0$  in  $M$  such that the restriction  $H|_{\widetilde{\mathcal{W}}_0}$  is transverse to  $\Sigma_2$ . The differential of  $h$  has maximal rank at  $p_0$ , that is, its determinant is non-zero. But the determinant  $p \mapsto \det((dh)_p)$  is a continuous map, hence  $p_0$  has a neighborhood  $\widetilde{\mathcal{W}}_0$  such that  $\det((dh)_p) \neq 0$  if  $p \in \widetilde{\mathcal{W}}_0$ , that is, the rank of the differential of  $h$  has maximal rank at every point  $p \in \widetilde{\mathcal{W}}_0$ . Then, by point (2) of Theorem 3.35, the restriction  $H|_{\widetilde{\mathcal{W}}_0} : \widetilde{\mathcal{W}}_0 \rightarrow \text{Herm}(n)$  is transverse to  $\Sigma_2$ , i.e., at every  $p \in \widetilde{\mathcal{W}}_0$ , either  $H$  is transverse to  $\Sigma_2$  at  $H(p) \in \Sigma_2$ , or  $H(p) \notin \Sigma_2$ . Then, by the theorem in [77, pg. 30]

(see also [78, Thm. 4.4.]),  $H^{-1}(\Sigma_2) \cap \widetilde{\mathcal{W}}_0$  is a submanifold of dimension  $\dim(M^3) - \text{codim}(\Sigma_2) = 0$  that is, it consists only of isolated points, proving the corollary.  $\square$

*Proof of Corollary 3.40 on Weyl points being stable and generic.* Part (a) is essentially the stability theorem [77, 35], see also [78, pg. 59, exercise (1) (a)]. We formulate the proof in our particular situation.

The perturbation  $H_t$  induces a perturbation  $h_t$  of  $h_{t=0} = h$ , that is, a smooth map  $(p, t) \mapsto h_t(p)$  defined in a neighborhood of  $(p_0, 0)$ . The determinant map  $(p, t) \mapsto \det((dh_t)_p)$  is continuous, hence, it is non-zero in a neighborhood of  $(p_0, 0)$ . It implies that there is an  $\epsilon_1 > 0$  such that for a fixed  $|t| < \epsilon_1$  the map  $p \mapsto H_t(p)$  is transverse to  $\Sigma_2$  in a sufficiently small neighborhood of  $p_0$  in  $M$ . Therefore, the map  $(p, t) \mapsto H_t(p)$  is also transverse to  $\Sigma_2$ , hence the preimage of  $\Sigma_2$  is a smooth manifold  $\Gamma$  in a neighborhood of  $(p, 0)$  in  $M \times \mathbb{R}$  of dimension  $\dim(\Gamma) = \dim(M \times \mathbb{R}) - \text{codim}(\Sigma_2) = 1$ . Let  $\Gamma_0$  be the component of  $\Gamma$  containing  $(p_0, 0)$ . Applying the projection  $(p, t) \mapsto p$  to  $\Gamma_0$  gives the  $\mathcal{C}^\infty$  curve  $\gamma : (-\epsilon_1, \epsilon_1) \rightarrow M$  through  $\gamma(0) = p_0$ , satisfying that  $\gamma(t) \in H_t^{-1}(\Sigma_2)$  is a Weyl point of  $H_t$ .

Other degeneracy points can be avoided by a further restriction of  $t$ , i.e.,  $|t| < \epsilon$  with a suitable  $0 < \epsilon < \epsilon_1$ , defined as follows. Choose a neighborhood  $\mathcal{W}_\gamma$  of the image of  $\gamma$  in  $\mathcal{W}_0$  which does not contain other degeneracy points, that is,  $H_t^{-1}(\Sigma_2) \cap \mathcal{W}_\gamma = \{\gamma(t)\}$  for all  $-\epsilon_1 < t < \epsilon_1$ . Consider the compact set  $\text{cl}(\mathcal{W}_0) \setminus \mathcal{W}_\gamma$ . Observe that there is an  $0 < \epsilon < \epsilon_1$  such that  $H_t(p) \notin \Sigma_2$  for  $p \in \text{cl}(\mathcal{W}_0) \setminus \mathcal{W}_\gamma$  and  $0 < |t| < \epsilon$ . Indeed, otherwise there would be a series  $(p_i, t_i)$  such that  $t_i$  converges to 0 and  $H_{t_i}(p_i) \in \Sigma_2$ , and the limit of a convergent subseries of  $p_i$  would be a point  $q \in \text{cl}(\mathcal{W}_0) \setminus \mathcal{W}_\gamma$  with  $H(q) \in \Sigma_2$ . This proves point (a).

Part (b) follows from the transversality theorem [77, pg 68-69], see also [78, Lemma 4.6.]. Consider a perturbation parametrized by the Hermitian matrices  $M \times \text{Herm}(n) \rightarrow \text{Herm}(n)$ , defined as  $(p, K) \mapsto H_K(p) := H(p) + K$ . This map is transverse to  $\Sigma_2$ , indeed, for a fixed  $p$  it is a translation of  $\text{Herm}(n)$ . By the transversality theorem, those parameter values  $K$  for which the map  $p \mapsto H_K(p)$  is transverse to  $\Sigma_2$  form a dense subset in  $\text{Herm}(n)$ . This proves the theorem.  $\square$

**Remark 139.** *In Corollary 3.40 we formulated the protected nature of the Weyl points in a way which can be deduced from the properties of transversality. The goal is to demonstrate the power of this approach in context of the degeneracy points. However, there are several possible generalizations, whose rigorous proofs are obstructed by technical difficulties.*

1. *In part (b), one may expect a stronger result, namely, the existence of a one-parameter perturbation  $H_t$  of  $H$  which has only Weyl points for  $0 < t < \epsilon$ . This does not follow from the transversality theorems appearing in the literature. Indeed, the set of the ‘wrong’ perturbations (in the particular form  $H_K(p) = H(p) + K$ , the set of those  $K$  matrices for which  $H_K$  is non-transverse) might be very complicated in general, although its complement is a dense set. If the map germ of  $h$  at  $p_0$  is ‘sufficiently nice’, then the stronger statement holds. See the Appendix of [46] for related results and examples.*
2. *For a sufficiently small  $\epsilon$ , the Weyl points of  $H_K$  in  $\mathcal{W}_0$  can be regarded as the Weyl points born from the non-generic degeneracy point  $p_0$  of  $H$ . If there is a one-parameter perturbation  $H_t$  with only Weyl points, then these Weyl points converge to  $p_0$ , as  $t$  tends to 0, and they can be separated from other Weyl points similarly as in the proof of part (a) of Corollary 3.40. In general it is harder to formalize the concept of ‘Weyl points born from  $p_0$ ’.*
3. *Every Weyl point  $p$  of  $H_t$  has a sign  $(\pm 1)$ , defined as the sign of  $\det((dh_t)_p)$ . The sum of the signs for the Weyl points born from  $p_0$  does not depend on the perturbation, it is an*

invariant of the degeneracy point  $p_0$  of  $H$ . Moreover, it is equal to the local degree  $\deg_{p_0}(h)$  of  $h$  at  $p_0$ , and also with the Chern number of the lowest eigenstate (up to sign). This number is the topological charge of the non-generic degeneracy point  $p_0$  of  $H$ .

4. One can consider the global version, i.e., the transversality to the whole degeneracy set  $\Sigma$ . However,  $\Sigma$  is not a manifold. A map  $H : M^3 \rightarrow \text{Herm}(n)$  defined on a 3-manifold  $M^3$  is transverse to  $\Sigma$  if it is transverse to every stratum of  $\Sigma$ . In other words, such map has only isolated transverse two-fold degeneracy points, but not necessarily ground-state. A map which is non-transverse to  $\Sigma$  can have various degeneracy patterns, for example, multifold degeneracy points or non-isolated degeneracies. Every map can be perturbed to a transverse one by an arbitrary small perturbation, hence, any arbitrarily complicated degeneracy splits into transverse two-fold degeneracy points (Weyl points).

## C Birth Quota of Non-Generic Degeneracy Points

In this Appendix, we provide the mathematical background of the results presented in the main text. In the main text, the concept of local multiplicity of a real or a complex map was introduced with a perturbative approach; we provide a detailed description of this perturbative approach in Sec. C.1. On the other hand, often the local multiplicity is defined with a more direct, algebraic approach, which (i) does not rely on deformations (that is, perturbations), and (ii) provides an alternative computational method. We summarize this algebraic description of the local multiplicity and its relation with our approach (without proof) in Sec. C.2. In Sec. C.3, we compute the local multiplicity for various examples.

### C.1 The local multiplicity

In this Appendix, we first prove that in the complex case, the discriminant set does not divide the parameter space into different regions (Sec. C.1). This statement allows us to define the local multiplicity as the number of complex Weyl points of any generic deformation. Then, we prove the conservation of the local degree, which, if applied to the complexification, implies that the local degree of the complexification is equal to the local multiplicity (Sec. C.1). Moreover, it provides a method, which we call ‘constant deformation’, to compute the local degree and the local multiplicity (Sec. C.1).

#### The local multiplicity is well defined

Consider a holomorphic map  $g : \mathbb{C}^n \rightarrow \mathbb{C}^n$ , defined on a neighborhood of the origin, with an isolated root at 0. Such a map is called *finite*. Let the holomorphic map  $\mathcal{G} : \mathbb{C}^n \times \mathbb{C}^k \rightarrow \mathbb{C}^n \times \mathbb{C}^k$  be a  $k$ -parameter unfolding of  $g$ , i.e.  $\mathcal{G}(x, t) = (g_t(x), t)$  and  $g_0 = g$ . The one variable holomorphic function  $x \mapsto g_t(x)$  is called the analytic deformation, or simply deformation of  $g$  with respect to the control parameter  $t$ . Note that we use the terminology ‘deformation’ as a more specified version of the ambiguous term ‘perturbation’. We refer to the two variable function  $(x, t) \mapsto g_t(x)$  as  $\mathcal{G}_1(x, t)$ , i.e. the first component of  $\mathcal{G}$ .

As it is explained in the main text for  $n = 3$ , we restrict  $\mathcal{G}$  to the domain  $B_\epsilon^{2n} \times \mathcal{U}_{\mathbb{C}} \subset \mathbb{C}^n \times \mathbb{C}^k$  satisfying the following conditions:

- $B_\epsilon^{2n} \subset \mathbb{C}^n$  is a closed ball centered at the origin with a radius  $\epsilon$  small enough that the only root of  $g$  in  $B_\epsilon^{2n}$  is the origin.
- $\mathcal{U}_{\mathbb{C}} \subset \mathbb{C}^k$  is an open ball around the origin such that for all  $t \in \mathcal{U}$  the deformation  $g_t$  has no roots in the boundary sphere  $\partial B_\epsilon^{2n} = S_\epsilon^{2n-1}$ , i.e.  $g_t^{-1}(0) \cap S_\epsilon^{2n-1} = \emptyset$ .

As a consequence of these conditions, if  $t$  varies in  $\mathcal{U}$  along a continuous curve through the origin, then the continuous trajectories of the points of  $g_t^{-1}(0)$  do not reach the separator sphere  $S_\epsilon^{2n-1}$ . Hence the points of  $g_t^{-1}(0) \cap B_\epsilon^{2n}$  can be interpreted as the roots of the deformation born from the origin.

Define the discriminant set  $\mathcal{D}_\mathbb{C} \subset \mathcal{U}_\mathbb{C}$  as the set of those  $t \in \mathcal{U}_\mathbb{C}$  control parameter values for which  $g_t$  has a singular root in  $B_\epsilon^{2n}$ , i.e. there exists  $x \in B_\epsilon^{2n}$  with  $g_t(x) = 0$  and  $\det(\text{Jac}_x(g_t)) = 0$ .

Note that the terminology used here is not universal. The name ‘discriminant’ usually denotes the set of the singular values of a map, see [90].  $\mathcal{D}_\mathbb{C}$  is reminiscent of the ‘bifurcation set’ of an unfolding, but it is not that. More detailed analysis shows that  $\mathcal{D}_\mathbb{C}$  coincides with the bifurcation set with respect to contact equivalence. In this work, we call it discriminant set, as it is a straightforward generalization of the discriminant of polynomials in sense described in Section 4.2 and on Figure 6.

It can happen in special cases that  $\mathcal{D}_\mathbb{C} = \mathcal{U}_\mathbb{C}$ , consider for example the unfolding  $\mathcal{G}(x, t) = (x^3 - tx^4, t)$  of  $g(x) = x^3$ . However for generic unfoldings  $\mathcal{D}_\mathbb{C} \neq \mathcal{U}_\mathbb{C}$ , that is, there is at least one control parameter  $t$  such that  $g(t)$  is a generic deformation. From now on all the unfoldings are assumed to be generic in this sense.

To make the multiplicity well defined, a required property of  $\mathcal{D}_\mathbb{C}$  is the following:

*Proposition 1.* For a finite map  $g$ , the complement  $\mathcal{U}_\mathbb{C} \setminus \mathcal{D}_\mathbb{C}$  of  $\mathcal{D}_\mathbb{C}$  is path connected: any two parameter values  $t_1, t_2 \in \mathcal{U}_\mathbb{C} \setminus \mathcal{D}_\mathbb{C}$  can be joined with a continuous curve in  $\mathcal{U}_\mathbb{C} \setminus \mathcal{D}_\mathbb{C}$ .

*Proof:* We have not found this statement in the literature, hence we provide a short proof based on two facts.

(1) A set defined by holomorphic equations in the complex space is called complex analytic set. A complex analytic set has at least 1 complex codimension, hence its real codimension is at least 2, therefore its complement is path connected [97, 98].

(2) Remmert’s Finite Mapping Theorem [98, Chapter V]: The image of a finite map between complex analytic sets is complex analytic.

By (1) it is enough to prove that  $\mathcal{D}_\mathbb{C}$  is an analytic set in  $\mathcal{U}_\mathbb{C}$ . To prove it we use (2).

Observe that  $\det(\text{Jac}_x(g_t)) = 0$  holds at a point  $(x, t) \in B_\epsilon^{2n} \times \mathcal{U}_\mathbb{C}$  if and only if  $\det(\text{Jac}_{(x,t)}(\mathcal{G})) = 0$ . Therefore  $t \in \mathcal{D}_\mathbb{C}$  if and only if  $(0, t)$  is a singular value of  $\mathcal{G}$ , that is, there exists  $x \in B_\epsilon^{2n}$  such that  $\mathcal{G}(x, t) = (g_t(x), t) = (0, t)$  and  $\det(\text{Jac}_{(x,t)}(\mathcal{G})) = 0$ .

To formalize the former description, we define

$$\mathcal{S} = \{(x, t) \in B_\epsilon^{2n} \times \mathcal{U}_\mathbb{C} \mid \det(\text{Jac}_{(x,t)}(\mathcal{G})) = 0, \mathcal{G}_1(x, t) = 0\}. \quad (140)$$

$\mathcal{S}$  is a complex analytic set. Consider the projection map  $\pi : \mathcal{S} \rightarrow \mathbb{C}^k$ ,  $\pi(x, t) = t$ ; for a specific example and visualization, see Fig. 6. Then, since  $g$  is finite, the projection map  $\pi$  is finite from  $(\mathcal{S}, 0)$  to  $(\mathbb{C}^k, 0)$  in the sense that 0 is an isolated point of  $\pi^{-1}(0)$ . By Remmert’s Finite Mapping Theorem, the image of  $\pi|_{\mathcal{S}}$  is complex analytic. On the other hand, the image  $\pi(\mathcal{S})$  is  $\mathcal{D}_\mathbb{C}$ . Therefore  $\mathcal{D}_\mathbb{C}$  is complex analytic.

As a consequence of Proposition 1, the cardinality of the set  $g_t^{-1}(0) \cap B_\epsilon^{2n}$  is the same for any  $t \in \mathcal{U}_\mathbb{C} \setminus \mathcal{D}_\mathbb{C}$ . We call this number the local multiplicity  $\text{mult}_0 g$  of  $g$ . We define the local multiplicity  $\text{mult}_0 h$  of a real analytic map  $h : \mathbb{R}^n \rightarrow \mathbb{R}^n$  as the local multiplicity  $\text{mult}_0 h_\mathbb{C}$  of the complexification  $h_\mathbb{C} : \mathbb{C}^n \rightarrow \mathbb{C}^n$ , where  $h_\mathbb{C}$  is the complex holomorphic map defined with the same power series as  $h$ .

Note that  $\text{mult}_0 h$  is well-defined with this definition if and only if  $h_\mathbb{C}$  is finite at 0. Moreover, the local multiplicity is always a positive integer. We already anticipate that the alternative, algebraic definition of the local multiplicity (see App. C.2) can be applied to any analytic map (i.e., not only finite maps). Furthermore, according to the algebraic definition, non-finite analytic maps will have an infinite local multiplicity.

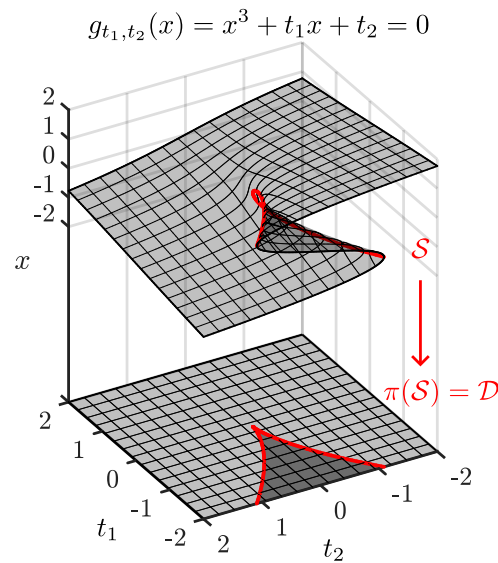


Figure 6: The projection  $\pi$  in the case of the unfolding  $\mathcal{G}_1(x, t_1, t_2) = x^3 + t_1 x + t_2$  of  $g(x) = x^3$ . The surface consists of those points  $(x, t_1, t_2)$  that satisfy  $g_{t_1, t_2}(x) = 0$ . The set  $\mathcal{S}$  is the ‘contour’ of the surface, i.e., the points of the surface where the tangent plane contains a vertical line. The projection of  $\mathcal{S}$  to the  $(t_1, t_2)$  plane is the discriminant set  $\mathcal{D}_{\mathbb{C}}$ . This discriminant set is the same as the zero locus of the discriminant of the degree-3 polynomial  $\mathcal{G}_1$ , cf. main text. Note that in this ‘real picture’ the discriminant set divides the  $(t_1, t_2)$  plane into two parts such that each point of the lighter part has 1 preimage, while each point of the darker part has 3 preimages with respect to the projection. This is not the case in the complex version, where the complement of the discriminant set is connected and every point of it has 3 preimages.

### The local multiplicity is the local degree of the complexification

Consider a point  $P \in \mathbb{R}^m$ , and an analytic map  $h : U_P \rightarrow \mathbb{R}^m$  defined on a neighborhood  $U_P$  of  $P$  on which the Taylor series of  $h$  converges. Assume that  $P$  is an isolated root of  $h$ , i.e.,  $h(P) = 0$ , and  $P$  is an isolated point of the preimage set  $h^{-1}(0)$ .

The *local degree*  $\deg_P h$  of  $h$  at  $P$ , also called the *index* of  $h$ , is defined as follows [86, 87, 88, 89, 90]. Take a sphere  $S_\epsilon^{m-1} \subset U_P \subset \mathbb{R}^m$  around  $P$  with a small enough radius  $\epsilon$  such that  $h$  has no other zeros inside the sphere, and the orientation of the sphere is inherited from  $\mathbb{R}^m$ . Define the map

$$\tilde{h} = \frac{h}{|h|} : S_\epsilon^{m-1} \rightarrow S^{m-1}, \quad (141)$$

which is called ‘pseudospin texture’ in physics, see e.g. [26]. Then the local degree  $\deg_P h$  of  $h$  is defined as the *global degree*  $\deg \tilde{h}$  of  $\tilde{h}$ , defined as follows. Take a *regular value*  $q \in S^{m-1}$  of  $\tilde{h}$ , i.e. the tangent map (the Jacobian) of  $\tilde{h}$  has maximal rank at each preimage  $p \in \tilde{h}^{-1}(q)$ . Each preimage  $p$  is endowed with a sign, which is positive, if  $\tilde{h}$  preserves the orientation around  $p$ , and it is negative, if the orientation is reversed. Then,  $\deg \tilde{h}$  (and hence  $\deg_P h$ ) is defined as the sum of the signs of the the preimages of a regular value  $q$ .

Importantly, the global degree  $\deg \tilde{h}$  does not depend on the choice of  $q$ , and  $\deg_0 h = \deg \tilde{h}$  does not depend on the choice of  $\epsilon$ , see [90, E.3] and [86].

A simple example, which is easy to visualise, is the  $m = 2$  case, when the local degree is also called ‘winding number’. For example, the map

$$\begin{aligned} h & : \mathbb{R}^2 \rightarrow \mathbb{R}^2, \\ h(x, y) & = (\operatorname{Re}(x + iy)^2, \operatorname{Im}(x + iy)^2) = (x^2 - y^2, 2xy), \end{aligned} \quad (142)$$

has local degree  $\deg_0 h = 2$ . In fact,  $h$  maps the unit circle of the domain onto the unit circle of the target, and any value  $q = (X, Y) \in S^1$  is a regular value, which has two preimages, namely,  $x + iy = \pm\sqrt{X + iY}$ . The map  $\tilde{h} = h|_{S^1} : S^1 \rightarrow S^1$  preserves the orientation, hence both preimage has positive sign, implying  $\deg_0 h = 2$ .

In the case of an  $h : \mathbb{R} \rightarrow \mathbb{R}$  function,  $\deg_0 h$  is either  $\pm 1$  or 0 depending on the order of the Taylor series of  $h$ : if the power of the leading term is odd, then the local degree is  $\pm 1$ , and if this degree is even, the local degree is 0.

The local degree  $\deg_P g$  of a complex map  $g : \mathbb{C}^n \rightarrow \mathbb{C}^n$  at an isolated root  $P \in \mathbb{C}^n$  is defined as the local degree  $\deg_P g_{\mathbb{R}}$  of the realification (real-imaginary decomposition)  $g_{\mathbb{R}} : \mathbb{R}^{2n} \rightarrow \mathbb{R}^{2n}$  of  $g$ . For example, consider  $g : \mathbb{C} \rightarrow \mathbb{C}$ ,  $g(z) = z^2$ . Its realification is the map  $h$  in Eq. (142), hence  $\deg_0 g = 2$ . Note that in general, the local degree of a real map is not equal to the local degree of its complexification. In fact, take the function  $h : \mathbb{R} \rightarrow \mathbb{R}$ ,  $h(x) = x^2$ , then  $\deg_0 h = 0$ , while  $\deg_0 h_{\mathbb{C}} = \deg_0 h_{\mathbb{C}, \mathbb{R}} = 2$ .

Consider an unfolding  $\mathcal{H} : \mathbb{R}^m \times \mathbb{R}^k \rightarrow \mathbb{R}^m \times \mathbb{R}^k$ , of  $h : \mathbb{R}^m \rightarrow \mathbb{R}^m$  where  $\mathcal{H}(x, t) = (h_t(x), t)$  and  $h_0 = h$ . Restrict  $\mathcal{H}$  to a domain  $B_\epsilon^m \times \mathcal{U}$  as it is explained in the main text: first we find a domain  $B_\epsilon^{2m} \times \mathcal{U}_{\mathbb{C}}$  for the complexification  $h_{\mathbb{C}}$  (cf. Appendix C.1), and then define  $\mathcal{U} \subset \mathbb{R}^k$  as the set of the real parts of the points of  $\mathcal{U}_{\mathbb{C}}$ , and  $B_\epsilon^m$  as the set of the real parts of the points of  $B_\epsilon^{2m}$ .

*Proposition 2. (Conservation of the local degree.)* The sum of the local degrees at the roots of a deformation  $h_t$  equals the local degree of the original map  $h$  at its single root. Formally:

$$\sum_{p \in h_t^{-1}(0) \cap B_\epsilon^m} \deg_p h_t = \deg_0 h, \quad (143)$$

holds for all  $t \in \mathcal{U}$ .

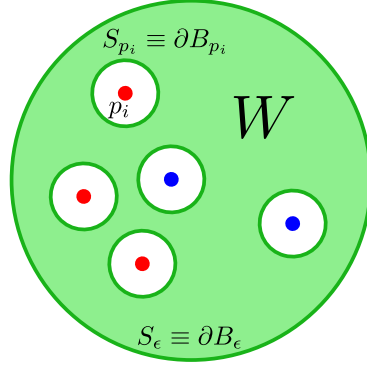


Figure 7: Visual proof of Proposition 2. The boundary of  $W$  consists of the sphere  $S_\epsilon^{m-1}$  and the spheres  $S_p^{m-1}$  around each Weyl point  $p \in h_t^{-1}(0) \cap B_\epsilon^m$  with reversed orientation. Since the degree of the map  $\tilde{h}_t$  is 0 on the whole boundary of  $W$ , the degree on  $S_\epsilon^{m-1}$  is equal to the sum of the signs of the Weyl points inside the sphere.

*Proof:* Take disjoint closed balls  $B_p^m \subset B_\epsilon^m$  around the roots of  $h_t$  with boundary  $S_p^{m-1}$  and interior  $\text{int}(B_p^m)$ . Cut out the interior of these disjoint balls from  $B_\epsilon^m$  to obtain the closed domain

$$W = B_\epsilon^m \setminus \bigcup_{p \in h_t^{-1}(0) \cap B_\epsilon^m} \text{int}(B_p^m). \quad (144)$$

Furthermore, consider the normalized map on  $W$ , defined as

$$\tilde{h}_t = \frac{h_t}{|h_t|} : W \rightarrow S^{m-1}. \quad (145)$$

By a classical topological argument, the global degree of the restriction

$$\tilde{h}_t|_{\partial W} : \partial W \rightarrow S^{m-1} \quad (146)$$

to the boundary  $\partial W$  of  $W$  is 0, see [86, pg. 28]. This global degree is

$$\deg \tilde{h}_t|_{\partial W} = \deg \tilde{h}_t|_{S_\epsilon^{m-1}} - \sum_p \deg \tilde{h}_t|_{S_p^{m-1}}, \quad (147)$$

where the minus sign arises because the boundary components  $S_p^{m-1}$  inherit reversed orientation from  $W$ . Therefore we find

$$\sum_p \deg \tilde{h}_t|_{S_p^{m-1}} = \deg \tilde{h}_t|_{S_\epsilon^{m-1}}. \quad (148)$$

The left hand side is equal to the left hand side of Eq. (143) by definition. The right hand side is equal to  $\deg_0 h$ , since  $\tilde{h}_t|_{S_\epsilon^{m-1}}$  and  $\tilde{h}|_{S_\epsilon^{m-1}}$  are homotopic maps, and the global degree is homotopy invariant [86, pg. 28]. This concludes the proof of Eq. (143).

Now we derive two important corollaries of Proposition 2: (1) An alternative definition of the local degree, which is well suited to calculate the local degree. (2) Local multiplicity is the local degree of the complexification.

As the first step towards (1) and (2), let  $\mathcal{D} \subset \mathcal{U}$  be the discriminant set of  $\mathcal{H}$ , and consider a control parameter vector  $t \in \mathcal{U} \setminus \mathcal{D}$ . The Jacobian of  $h_t$  at each root  $p \in B_\epsilon^m$  has the maximal rank  $m$ , therefore  $\deg_p h_t = \pm 1$ , and its sign is equal to the sign of the determinant of the

Jacobian. By Eq. (143), the local degree  $\deg_0 h$  is equal to the sum of the signs of the roots  $p$  of  $h_t$ .

As the second step toward (1) consider a specific simple deformation, a *constant deformation*  $h_q = h - q$  with a regular value  $q \in \mathbb{R}^m$  close to the origin. More precisely, we consider the one-parameter deformation  $h_t = h - tq$  on the restricted domain  $\mathcal{U}$ , with  $t = 1 \in \mathcal{U} \setminus \mathcal{D}$ . Then  $h_q^{-1}(0) = h^{-1}(q)$ . Therefore,  $\deg_0 h$  is equal to the sum of the signs of the preimages of a small regular value  $q$ , i.e.,

$$\deg_0 h = \sum_{p \in h^{-1}(q) \cap B_\epsilon^m} \operatorname{sgn}(\det(\operatorname{Jac}_p(h))). \quad (149)$$

This result can be used to calculate the local degree  $\deg_0 h$ .

Finally, we derive (2). We apply Proposition 2 for a deformation  $g_t$  of a complex holomorphic map  $g : \mathbb{C}^n \rightarrow \mathbb{C}^n$ , where  $t \in \mathcal{U}_{\mathbb{C}} \setminus \mathcal{D}_{\mathbb{C}}$ . A holomorphic map always preserves the orientation, hence  $\deg_p g_t = 1$  holds for each root  $p$  of  $g_t$ . Therefore the sum at the left side of Eq. (143) is the number of the roots, that is, the multiplicity  $\operatorname{mult}_0 g$ . We conclude that

$$\operatorname{mult}_0 g = \deg_0 g \quad (150)$$

holds for finite complex maps.

## C.2 Algebraic approach: the local algebra

In the singularity-theory literature, multiplicity is often defined in an algebraic way, such that the definition refers to the real map, without referring to its complexification [87, 90, 97]. In fact, the multiplicity  $\operatorname{mult}_0 h$  is the dimension of the local algebra  $Q_0(h)$  associated to  $h$  at 0. In Sec. C.2, we summarize concepts and relations of elementary algebra (ring theory). In Sec. C.2, we introduce the local algebra and use it to provide an alternative definition of the local multiplicity.

### From a ring to a local algebra

An elementary example of a ring is  $(\mathbb{Z}, +, \cdot)$ , the integers equipped with addition and multiplication. The integers with addition form a group. The integers with multiplication form a semi-group, which has an identity element (that is 1), but not every integer is invertible: 0 has no inverse, 1 has an inverse (itself),  $-1$  has an inverse (itself), but other integers do not have their inverse (within  $\mathbb{Z}$ ). In addition, the multiplication is commutative. Actually, the integers form a *commutative ring with an identity element*.

Take, for example, the subset  $I_4 = \{\dots, -8, -4, 0, 4, 8, \dots\}$  of the ring of integers. It contains 0. It is closed under both addition and multiplication. In addition, it is also closed under ‘external multiplication’; that is, under multiplication with ring elements – integers – that are outside  $I_4$ . Such a subset is called an *ideal* of the ring.

A single element of the ring, say  $r = 4$ , can generate a *principal ideal*, which is  $I_r = I_4$  in this case. Formally, the principal ideal generated by  $r \in \mathbb{Z}$  is  $I_r = \{r \cdot r' \mid r' \in \mathbb{Z}\}$ .

Two elements of the ring can also generate an ideal:  $I_{r,q} = \{a \cdot r + b \cdot q \mid a, b \in \mathbb{Z}\}$ . For example,  $I_{2,3} = R = I_1$ . Another example is  $I_{2,4} = I_2$ . The ring of integers is a *principal ideal ring*: every ideal in  $\mathbb{Z}$  is a principal ideal. Furthermore, the ideal generated by a finite set of integers is the ideal generated by their greatest common divisor. The ring of integers is a *Noetherian ring*: every ideal in  $\mathbb{Z}$  is finitely generated. (Every principal ideal ring is a Noetherian ring.)

A ring can be partitioned with an ideal, e.g.,  $\mathbb{Z}/I_4$ . The elements of the ring are assigned to the same partition class (are considered equivalent) if their difference is in the ideal:  $r_1 \sim_I r_2$  if  $r_1 - r_2 \in I$ . That is, partitioning  $\mathbb{Z}$  with  $I_4$  yields 4 classes, the well-known residue classes,  $[0]$ ,  $[1]$ ,  $[2]$ ,  $[3]$ . For example  $[3] = \{\dots, -5, -1, 3, 7, \dots\}$ .

The set of classes is called the *quotient*  $R/I$  of ring  $R$  with respect to its ideal  $I$ , and the elements of the quotient  $R/I$  are often called *residue classes* of  $R \pmod I$ . In fact, the quotient  $R/I$  is a ring. For example,  $[2] + [3] = [1]$ , in the sense that any representative of  $[2]$  plus any representative of  $[3]$  is contained in  $[1]$ . Similarly,  $[2] \cdot [3] = [2]$ .

In certain quotient rings we find pairs which multiply to  $[0]$ , even though neither of them is  $[0]$ . For example, in e.g., in the quotient ring  $\mathbb{Z}/I_6$ , we have  $[2] \cdot [3] = [0]$ . Such pairs are called zero divisors.

A commutative ring is called *domain* (or *integral domain*) if it is free of zero divisors. That is, if  $a \cdot b = 0$  implies  $a = 0$  or  $b = 0$ . For example,  $\mathbb{Z}$  is a domain, but  $\mathbb{Z}/I_n$  is a domain only if  $n$  is a prime.

A ring is called a *real algebra*, if it is also a vector space over  $\mathbb{R}$ , and the multiplication with scalars is compatible with the ring multiplication. In the same way complex algebras are rings which are also vector spaces over  $\mathbb{C}$ . The typical examples are function algebras. In fact, the functions from any set  $A$  to  $\mathbb{R}$  form a real algebra with respect to the pointwise operations, and if a subset of them is closed to the operations, then it is a real algebra as well. In these algebras the ring multiplication is also commutative, and they have identity element, namely, the constant 1 function.

The simplest functions are the polynomials.  $\mathbb{R}[x]$  denotes the real algebra of polynomials of one variable with real coefficients, and similarly  $\mathbb{C}[x]$  is the complex algebra of complex polynomials. The pointwise algebra operations agrees with the formal operations using the coefficients, i.e.

$$\left( \sum_{i=0}^n a_i x^i \right) + \left( \sum_{i=0}^m b_i x^i \right) = \sum_{i=0}^k (a_i + b_i) x^i \quad (151)$$

where  $k = \max(n, m)$ , and

$$\left( \sum_{i=0}^n a_i x^i \right) \cdot \left( \sum_{i=0}^m b_i x^i \right) = \sum_{i=0}^l \left( \sum_{j=0}^i a_j b_{i-j} \right) x^i \quad (152)$$

where  $l = nm$ .

$\mathbb{R}[x]$  and  $\mathbb{C}[x]$  are principal ideal rings as well, it follows from the existence of *greatest common divisor* of polynomials. Moreover these rings has another important common property with  $\mathbb{Z}$ : the unique irreducible decomposition. In  $\mathbb{Z}$  the irreducible elements are the prime numbers, and by the fundamental theorem of number theory, every integer except 0, 1 and  $-1$ , can be decomposed as a product of prime numbers. The prime factors are unique (up to reordering) and their signs. Similarly, in  $\mathbb{C}[x]$  the irreducible polynomials are the degree 1 (i.e., linear) polynomials, and by the fundamental theorem of algebra every polynomial of at least degree 1 can be decomposed as the product of degree 1 polynomials. The irreducible factors are unique (up to reordering and up to scalar factors) – in fact, in  $\mathbb{C}[x]$  the invertible elements are the degree 0 polynomials (i.e. constant polynomials). Referring to this property we say that  $\mathbb{Z}$  and  $\mathbb{C}[x]$  are *unique factorization domains (UFD)*.  $\mathbb{R}[x]$  is also an UFD, the irreducible elements are the degree 1 polynomials and the degree 2 polynomials with negative discriminant. All the real polynomials of degree at least 1 can be decomposed to the product of irreducible ones, and the decomposition is essentially unique.

The multi-variable polynomial algebras  $\mathbb{R}[x_1, \dots, x_m]$ , and  $\mathbb{C}[x_1, \dots, x_m]$  are UFDs as well, but they are not principle ideal rings. In fact, the ideal generated by  $x_1$  and  $x_2$  cannot be generated by only one element. Note that a principal ideal domain is UFD, but the converse is not true,  $\mathbb{R}[x_1, \dots, x_m]$ , and  $\mathbb{C}[x_1, \dots, x_m]$  are counterexamples. On the other hand these algebras are Noetherian by the Hilbert's basis theorem.

Further examples are the algebras of *formal power series*  $\mathbb{R}[[x_1, \dots, x_m]]$  and  $\mathbb{C}[[x_1, \dots, x_m]]$  of  $m$  variables. E.g.  $\mathbb{R}[[x, y]]$  consists of the infinite power series

$$g(x, y) = \sum_{i,j=0}^{\infty} a_{ij} x^i y^j, \quad (153)$$

where  $a_{ij} \in \mathbb{R}$ . Since these power series are not assumed to be convergent, they are not functions. Nevertheless, the ring operations are defined formally, using the coefficients, similarly to Eq. (151) and Eq. (152).

The rings  $\mathbb{R}[[x_1, \dots, x_m]]$  and  $\mathbb{C}[[x_1, \dots, x_m]]$  are Noetherian UFDs as well. Moreover they have an important additional property: they are *local rings*. Consider the power series  $g$  with constant term  $g(0)$  not zero. These are exactly the invertible elements. Indeed, the multiplicative inverse of  $g = g(0) - \tilde{g}$  with nonzero  $g(0)$  reads

$$g^{-1} = \frac{1}{g(0)} \cdot \left(1 - \frac{\tilde{g}}{g(0)}\right)^{-1}, \quad (154)$$

which can be rewritten in the form of a formal power series using the geometric series formula as

$$g^{-1} = \frac{1}{g(0)} \cdot \sum_{k=0}^{\infty} \left(\frac{\tilde{g}}{g(0)}\right)^k. \quad (155)$$

However, a power series with  $g(0) = 0$  does not have a multiplicative inverse.

On the other hand, the collection of power series with  $g(0) = 0$  form an ideal  $\mathfrak{m}_m$ . This  $\mathfrak{m}_m$  is a *maximal ideal*, since the only ideal containing it is the whole ring. Moreover,  $\mathfrak{m}_m$  is the only maximal ideal in  $\mathbb{R}[[x_1, \dots, x_m]]$  (resp. in  $\mathbb{C}[[x_1, \dots, x_m]]$ ). A ring (resp. an algebra) with a unique maximal ideal is called *local ring* (resp. *local algebra*). Being local is equivalent with the fact that the complement of the irreducible elements forms an ideal.

Finally, the algebra in which we will work is  $\mathbb{R}\{x_1, \dots, x_m\} \subset \mathbb{R}[[x_1, \dots, x_m]]$  (resp.  $\mathbb{C}\{x_1, \dots, x_m\} \subset \mathbb{C}[[x_1, \dots, x_m]]$ ), consisting of the power series with nonzero convergence radius. Such a power series defines an analytic function  $g : \mathbb{R}^m \supset U_0 \rightarrow \mathbb{R}$  on a neighborhood  $U_0$  of the origin. Hence  $\mathbb{R}\{x_1, \dots, x_m\}$  (resp.  $\mathbb{C}\{x_1, \dots, x_m\}$ ) can be interpreted as either as the algebra of the locally convergent power series defined in the neighborhood of zero, or as the algebra of the analytic functions defined in a neighborhood of zero. These algebras are Noetherian UFD local algebras as well.

### Local algebra of analytic maps

In what follows, we will consider  $f : \mathbb{R}^m \supset U_0 \rightarrow \mathbb{R}^m$  as an analytic map defined in a neighborhood  $U_0$  of the origin with  $f(0) = 0$ , simply denoted by  $f : (\mathbb{R}^m, 0) \rightarrow (\mathbb{R}^m, 0)$ . We will denote the components as  $f_j : U_0 \rightarrow \mathbb{R}$  with  $j \in \{1, \dots, m\}$ . Note that in the main text we considered the special cases  $1 \leq m \leq 3$ .

Let  $\mathbb{R}\{x_i\}$  ( $i = 1, \dots, m$ ) denote the set of locally convergent power series of  $m$  variables, i.e.  $\mathbb{R}^m \rightarrow \mathbb{R}$  functions that are analytic at the origin. Let  $I_f = I(f_1, \dots, f_m)$  be the ideal generated by the components  $f_j$  of  $f$ . Recall that  $I_f$  consists of all linear combinations of  $f_j$  with coefficients in  $\mathbb{R}\{x_i\}$ . The *local algebra* of  $f$  is the quotient  $Q_0(f) = \mathbb{R}\{x_i\}/I_f$ , i.e. the algebra of the residue classes  $\text{mod } I_f$ .

The local algebra  $Q_0(f)$  of any power series  $f$  (defined in the previous paragraph) is a local algebra (defined in the previous subsection). Indeed, the residue classes of the elements of  $\mathfrak{m}$  form the unique maximal ideal of it.

In this algebraic framework, the *local multiplicity*  $\text{mult}_0 f$  of  $f$  is defined as the dimension  $\dim Q_0(f)$  of the local algebra, cf. [89, Prop. 2.2.].

*Example 1:* Take  $f_1(x, y) = x$  and  $f_2(x, y) = y^2$ . Then, the generated ideal in  $\mathbb{R}\{x, y\}$  is

$$I_f = \left\{ \begin{array}{l} a_1(x, y) \cdot x + a_2(x, y) \cdot y^2 \\ a_1, a_2 \in \mathbb{R}\{x, y\} \end{array} \right\} \quad (156)$$

i.e.  $g \in I_f$  if and only if every term of  $g$  is divisible by  $x$  or  $y^2$ . The local algebra of  $f(x, y) = (x, y^2)$  is formed by the linear combinations  $a[1] + b[y]$  ( $a, b \in \mathbb{R}$ ) of the residue classes of  $[1]$  of 1 and  $[y]$  of  $y$ . Indeed,  $g_1$  and  $g_2$  in  $\mathbb{R}\{x, y\}$  represent the same residue class if and only if each term of  $g_1 - g_2$  is divisible by  $x$  or  $y^2$ , consequently the residue class  $[g]$  of

$$g(x, y) = a_{00} + a_{10}x + a_{01}y + a_{20}x^2 + a_{11}xy + a_{02}y^2 + \dots \quad (157)$$

is  $a_{00}[1] + a_{01}[y]$ . Therefore, in this example, the local multiplicity  $\text{mult}_0 f$  of  $f$  is  $\dim Q_0(f) = 2$ .

*Example 2:* The local multiplicity of a single-variable power series  $f \in \mathbb{R}\{x\}$  is equal to its order  $r$ , for the following reason:

$$f(x) = \sum_{i=r}^{\infty} a_i x^i = x^r \cdot \sum_{j=0}^{\infty} a_{j+r} x^j, \quad (158)$$

hence  $f$  agrees with its leading term  $x^r$  up to an invertible factor. Therefore  $I_f = I(x^r)$ . A basis of the quotient  $Q_0(f) = \mathbb{R}\{x\}/I_f$  is formed by the residue classes  $[1], [x], [x^2], \dots, [x^{r-1}]$ . As a consequence, the local multiplicity of  $f$  is indeed  $r$ . This example also shows that the local multiplicity is a generalization of the order of single-variable power series.

In the rest of this section, we connect this algebraic definition of the local multiplicity with the concepts used in the main text and in App. C.1.

Recall that the complexification of a real analytic map  $f : (\mathbb{R}^m, 0) \rightarrow (\mathbb{R}^m, 0)$  is the holomorphic map  $f_{\mathbb{C}} : (\mathbb{C}^m, 0) \rightarrow (\mathbb{C}^m, 0)$  defined by the same power series. The local algebra  $Q_0(f_{\mathbb{C}}) = \mathbb{C}\{x_i\}/I_{f_{\mathbb{C}}}$  of  $f_{\mathbb{C}}$  is a complex algebra, and in fact,  $Q_0(f_{\mathbb{C}}) \cong Q_0(f) \otimes \mathbb{C}$ . Hence the local multiplicities  $\text{mult}_0 f_{\mathbb{C}} = \dim_{\mathbb{C}} Q_0(f_{\mathbb{C}})$  and  $\text{mult}_0 f = \dim Q_0(f)$  are equal. On the other hand, if  $g_{\mathbb{R}} : (\mathbb{R}^{2m}, 0) \rightarrow (\mathbb{R}^{2m}, 0)$  is the realification of a complex map  $g : (\mathbb{C}^m, 0) \rightarrow (\mathbb{C}^m, 0)$ , then  $(\text{mult}_0 g)^2 = \text{mult}_0 g_{\mathbb{R}}$  holds, see the proof of [89, Prop. 2.4].

A real analytic map  $f$  is called *finite* if its local multiplicity  $\text{mult}_0 f = \dim Q_0(f)$  is finite. This is equivalent with the fact that 0 is an isolated root of the complexification  $f_{\mathbb{C}}$ , which implies that 0 is an isolated root of  $f$  as well, see [90, Thm. D.5.]. For a finite map  $f$  the local degree of the complexification is equal to the multiplicity, i.e.,  $\deg_0 f_{\mathbb{C}} = \text{mult}_0 f$ , see [90, Cor. E.3]. Together with the arguments in Appendix C.1 we conclude the equivalence of the two definitions of the local multiplicity. Namely, the number of roots born from the origin upon a generic deformation  $f_{\mathbb{C}, t}$  is equal to the dimension  $\dim Q_0(f)$  of the local algebra  $Q_0(f)$ .

Moreover, the local degree  $\deg_0 f$  of the real map  $f$  can also be computed from the local algebra: it is the index of a suitably defined symmetric bilinear form on  $Q_0(f)$ , that is, the difference between the number of positive and negative eigenvalues, see [88, 89]. This also implies  $|\deg_0 f| \leq \text{mult}_0 f$ .

### C.3 Computing the local degree and the local multiplicity for a few examples

In the following section we compute the above invariants on several examples using the introduced methods. Since most of them are motivated by physical systems, we use the physical and the mathematical terminology as synonyms. Namely, the roots of a map  $h : (\mathbb{R}^3, 0) \rightarrow (\mathbb{R}^3, 0)$  or a deformation  $h_t$  of  $h$  are called degeneracy points, the generic roots of  $h_t$  are the Weyl points. The local degree of each root is its topological charge, and the local multiplicity  $\text{mult}_0 h$  is the birth quota.

<u>Complexification</u>	<u>Realification</u>
$f : (\mathbb{R}^m, 0) \rightarrow (\mathbb{R}^m, 0)$	$g : (\mathbb{C}^n, 0) \rightarrow (\mathbb{C}^n, 0)$
$\Downarrow$	$\Downarrow$
$f_{\mathbb{C}} : (\mathbb{C}^m, 0) \rightarrow (\mathbb{C}^m, 0)$	$g_{\mathbb{R}} : (\mathbb{R}^{2n}, 0) \rightarrow (\mathbb{R}^{2n}, 0)$
$\text{mult}_0 f \stackrel{1.}{=} \text{mult}_0 f_{\mathbb{C}} \stackrel{2.}{=} \deg_0 f_{\mathbb{C}},$	$\text{mult}_0 g \stackrel{4.}{=} \deg_0 g \stackrel{5.}{=} \deg_0 g_{\mathbb{R}},$
$\deg_0 f \stackrel{3.}{\leq} \deg_0 f_{\mathbb{C}}$	$\text{mult}_0 g_{\mathbb{R}} \stackrel{6.}{=} (\text{mult}_0 g)^2$

Table 2: Summary of the relations between local degree and local multiplicity, complexification and realification. 1.: According to the definition of the local multiplicity introduced in the main text, this equation holds by definition. In fact, both  $\text{mult}_0 f_{\mathbb{C}}$  and  $\text{mult}_0 f$  are defined as the number of the generic roots of a generic deformation of  $f_{\mathbb{C}}$ . On the other hand in Appendix C.2  $\text{mult}_0 f$  is defined as the real dimension of the local algebra  $Q_0(f)$  of  $f$  and  $\text{mult}_0 f_{\mathbb{C}}$  is defined as the complex dimension of the local algebra  $Q_0(f_{\mathbb{C}})$  of  $f_{\mathbb{C}}$ . Based on this, the equation follows from the fact that  $Q_0(f_{\mathbb{C}})$  is the complexification of  $Q_0(f)$ . The equivalence of the two different definitions of the local multiplicity is not proved in this article, we refer to [90]. 2.: The equation is proved in Appendix C.1, see Eq. (150). More precisely the equation is proved for that definition of the local multiplicity we introduced in the main text. 3.: The inequality is proved in the main text (using the definitions introduced there). For singular germs, i.e.  $\text{Jac}_0(f) < m$ , the sharper inequality  $2 \deg_0 f \leq \text{mult}_0 f$  is proved in [89]. 4.: This is equation Eq. (150) in Appendix C.1. 5.: The equation holds by definition. 6.: The equation is proved in [89].

**Example 1**

Consider the effective Hamiltonian map

$$h(x, y, z) = \begin{pmatrix} x \\ y \\ z^n \end{pmatrix}. \quad (159)$$

The case  $n = 3$  is described in [99] as the three-node process, where two Weyl points with the same charge collide with an oppositely charged third one. This suggests that the charge (local degree) is  $+1$  and the local multiplicity is 3.

*Local degree from the constant-deformation method.* For a general  $n$ ,  $\deg_0 h = n \bmod 2$ . Indeed, the constant deformation

$$h_t(x, y, z) = h(x, y, z) - (t_1, t_2, t_3), \quad t_3 < 0 \quad (160)$$

has 1 real root

$$(x, y, z)_{\text{WP}} = (t_1, t_2, \sqrt[n]{t_3}) \quad (161)$$

for  $n$  odd with positive sign (since  $z^n$  is increasing), and there is no solution for even  $n$ . Note that geometrically,  $\deg_0 h$  is the ‘generalized winding number’ of the restricted normalized map  $\frac{h}{|h|}|_{S^2} : S^2 \rightarrow S^2$ .

*Local multiplicity from the constant-deformation method.* Here, we show that  $\text{mult}_0 h = n$ . Indeed,

$$h_{\mathbb{C}}(x, y, z) = (t_1, t_2, t_3), \quad t_3 \neq 0 \quad (162)$$

has  $n$  complex solutions

$$(x, y, z)_{\text{CWP},k} = \left( t_1, t_2, e^{i\frac{2\pi k}{n}} \sqrt[n]{t_3} \right), \quad (163)$$

with  $0 \leq k < n$ , hence  $\deg_0 h_{\mathbb{C}} = n$ , and this is equal to  $\text{mult}_0 h_{\mathbb{C}}$  which is equal to  $\text{mult}_0 h$ . Geometrically,  $n$  is the ‘generalized winding number’ of the restricted normalized map  $\frac{h_{\mathbb{C}}}{|h_{\mathbb{C}}|}|_{S^5} : S^5 \rightarrow S^5$ .

*Local multiplicity from the algebraic method.* We present here the algebraic method step by step, to illustrate it on this simple example. The ideal  $I_h \subset \mathbb{R}\{x, y, z\}$  consists of the (locally convergent) power series of 3 variables such that every term is a multiple of  $x$ ,  $y$  or  $z^n$ . Two elements  $f$  and  $g$  of  $\mathbb{R}\{x, y, z\}$  represents the same residue class  $\bmod I_h$  if and only if  $f - g \in I_h$ , that is, the coefficients of the  $z^k$  terms are the same in  $f$  and  $g$  for  $k < n$ . In other words, the element  $[f] \in \mathbb{R}\{x, y, z\}/I_h$  can be represented by the power series of  $z$  derived from  $f$  by substituting  $x = y = z^n = 0$ . We obtained that  $Q_0(h) = \mathbb{R}\{x, y, z\}/I_h = \mathbb{R}\{z\}/I(z^n)$  is a vector space with a possible choice of a basis is formed by the residue classes of  $1, z, z^2, \dots, z^{n-1}$ . We conclude that  $\text{mult}_0 h = \dim Q_0(h) = n$ .

All the above arguments show that the only essential part of this  $h$  is the third component  $z^n$ . The study of the deformations can also be reduced to study the deformations of the single-variable function  $z^n$  near 0. Adding extra terms of degree less than  $n$  results a degree  $n$  polynomial, which has  $n$  complex roots in general. These complex roots converge to 0 if the coefficients of the extra terms tend to 0. The number of real roots is at most  $n$  and at least 1 if  $n$  is odd, and the signs of the roots alternate. As we already noted in the main text, if we allow higher degree terms in the deformation, more roots appear, but these are coming from the infinity, not from zero, in the following sense. Consider  $z^n - tz^{n+1} = -tz^n \cdot (z - 1/t)$ . As  $t$  tends to zero, the extra root  $1/t$  converges to the infinity.

Notice that previous paragraph remains true if  $z^n$  is replaced by an arbitrary (locally convergent) power series  $f(z)$  of order  $n$ . Any small generic complex deformation of  $f$  has  $n$  roots coming from 0 and any small generic real deformation has at most  $n$  roots, at least 1 in the odd case, and their signs alternate. In this sense the local multiplicity can be considered as the generalization of the order of the single-variable power series to higher dimensions.

### Example 2

The  $n$ -fold Weyl point, including the double ( $n = 2$ ) and triple ( $n = 3$ ) Weyl points, appears in many contexts. See, for example, the electronic band structure of multi-Weyl semimetals, as described in [4]. An  $n$ -fold Weyl point is described by the map

$$h(x, y, z) = \begin{pmatrix} \operatorname{Re}(x + iy)^n \\ \operatorname{Im}(x + iy)^n \\ z \end{pmatrix}. \quad (164)$$

Similarly to the previous example, we can omit the identity component  $z$  for the calculation to obtain a map  $f : (\mathbb{R}^2, 0) \rightarrow (\mathbb{R}^2, 0)$  with the same local degree and local multiplicity as  $h$ . For this reason, the local degree and the local multiplicity of the 3D double Weyl points are the same as those of the 2D double Weyl point in bilayer graphene (see main text). Below, we show that the local degree of the  $n$ -fold Weyl point is  $\deg_0 h = \deg_0 f = n$ , whereas its local multiplicity is  $\operatorname{mult}_0 h = \operatorname{mult}_0 f = n^2$ .

*Local degree from the constant-deformation method.* Let us introduce the complex variable  $w = x + iy$ . The equation  $w^n = t$  ( $t \neq 0$ ) has  $n$  complex solutions, which implies that  $f_t = f - (t, 0)$  has  $n$  real roots, which in turn implies that  $\deg_0 f = \deg_0 h = n$ . Geometrically speaking, this local degree is the winding number of  $w^n$  on the complex plane, or, alternatively, the winding number of the map  $\frac{h}{|h|} : S^2 \rightarrow S^2$ , or, alternatively, the winding number of the map  $\frac{f}{|f|} : S^1 \rightarrow S^1$ .

*Local multiplicity from the constant-deformation method.* Here, we sketch the derivation of the local multiplicity  $\operatorname{mult}_0 h$  as the local degree  $\deg_0 h_{\mathbb{C}}$  of the complexification. To obtain the local multiplicity, we have to find the complex solutions  $x$  and  $y$  of the system of equations

$$\operatorname{Re}(x + iy)^n = t_1, \quad (165a)$$

$$\operatorname{Im}(x + iy)^n = t_2. \quad (165b)$$

These equations can be solved exactly, and the number of complex solutions is  $n^2$ , implying that the local multiplicity of  $h$  is  $n^2$ . For completeness we will provide the explicit solutions of Eq. (165) for  $(t_1, t_2) = (t^n, 0)$ , see Eq. (183), but first we introduce the more effective algebraic methods to compute the local multiplicity directly from  $h$ , without referring to deformations.

*Local multiplicity from the algebraic method.* We can also find  $\operatorname{mult}_0 h$  as the dimension  $\dim Q_0(h)$  of the local algebra associated to  $h$ . We show this calculation only for  $n = 2$ . In this case, it holds that  $\operatorname{Re}(x + iy)^2 = x^2 - y^2$  and  $\operatorname{Im}(x + iy)^2 = 2xy$ . Therefore the ideal  $I_h \subset \mathbb{R}\{x, y, z\}$  is generated by

$$x^2 - y^2, \quad xy \quad \text{and} \quad z. \quad (166)$$

First of all, notice that  $x^3$  and  $y^3$  are in  $I_h$ . Indeed,

$$x^3 = x \cdot (x^2 - y^2) + y \cdot xy, \quad (167)$$

and similarly for  $y^3$ . To identify the residue class

$$[f] \in Q_0(h) = \frac{\mathbb{R}\{x, y, z\}}{I_h} \quad (168)$$

of  $f \in \mathbb{R}\{x, y, z\}$ , we first reduce  $f$  by substituting  $xy = z = x^3 = 0$ , since the residue class of these terms are 0. The resulting power series  $\tilde{f}$  has only pure  $x$  and  $y$  powers up to second degree.

$$\tilde{f} = a_{00} + a_{10}x + a_{20}x^2 + a_{01}y + a_{02}y^2 \quad (169)$$

and

$$\tilde{g} = b_{00} + b_{10}x + b_{20}x^2 + b_{01}y + b_{02}y^2 \quad (170)$$

are in the same residue class if and only if  $\tilde{f} - \tilde{g}$  is divisible by  $x^2 - y^2$ , that is,

$$a_{00} = b_{00}, \quad a_{10} = b_{10}, \quad a_{01} = b_{01} \quad \text{and} \quad a_{20} + a_{02} = b_{20} + b_{02}. \quad (171)$$

These 4 parameters can be chosen independently to determine a residue class. In other words, a possible basis of

$$Q_0(h) = \frac{\mathbb{R}\{x, y\}}{I(xy, x^2 - y^2)} \quad (172)$$

is formed by the residue classes of 1,  $x$ ,  $y$  and  $x^2 + y^2$ , hence the dimension is 4.

The same argument can be presented in a more convenient way, by substituting the elements of the ideal by 0. That is,

$$x^2 - y^2 = 0, \quad xy = 0 \quad \text{and} \quad z = 0. \quad (173)$$

Then we have the 4 nonzero residue classes

$$[1], [x], [y], [x^2] = [y^2], \quad (174)$$

and we can see that the residue class of every higher order term is zero, e.g.

$$[x^3] = [x^2] \cdot [x] = [y^2] \cdot [x] = [y \cdot xy] = [y] \cdot [xy] = 0. \quad (175)$$

The above calculation can be further simplified using the unique factorization in the ring of power series [cite](#). Define

$$f_1 = x, \quad f_2 = y, \quad g_1 = x - y, \quad g_2 = x + y. \quad (176)$$

Then

$$h_1 = xy = f_1 f_2 \quad \text{and} \quad h_2 = x^2 - y^2 = g_1 g_2 \quad (177)$$

are the unique irreducible decompositions of the components of  $h$ . The multiplicity has the following property, known from the theory of complex plane curve singularities, see e.g. [\[100, Chapter 3\]](#):

$$\dim \left( \frac{\mathbb{R}\{x, y\}}{I(f_1 g_1, f_2 g_2)} \right) = \sum_{i,j=1}^2 \dim \left( \frac{\mathbb{R}\{x, y\}}{I(f_i, g_i)} \right). \quad (178)$$

In our case, each of the 4 terms are equal to 1, hence the multiplicity is 4.

This process also works for greater  $n$ , e.g for  $n = 3$

$$\begin{aligned} \operatorname{Re}(x + iy)^3 &= x^3 - 3xy^2 \\ &= x(x - \sqrt{3}y)(x + \sqrt{3}y), \end{aligned} \quad (179)$$

$$\begin{aligned} \operatorname{Im}(x + iy)^3 &= 3x^2y - y^3 \\ &= y(\sqrt{3}x - y)(\sqrt{3}x + y), \end{aligned} \quad (180)$$

hence the multiplicity is  $3 \cdot 3 = 9$ . Compare with [Fig 8](#), where the deformation [Eq. \(184\)](#) pulls apart the zero loci of the components revealing the 9 generic intersection points.

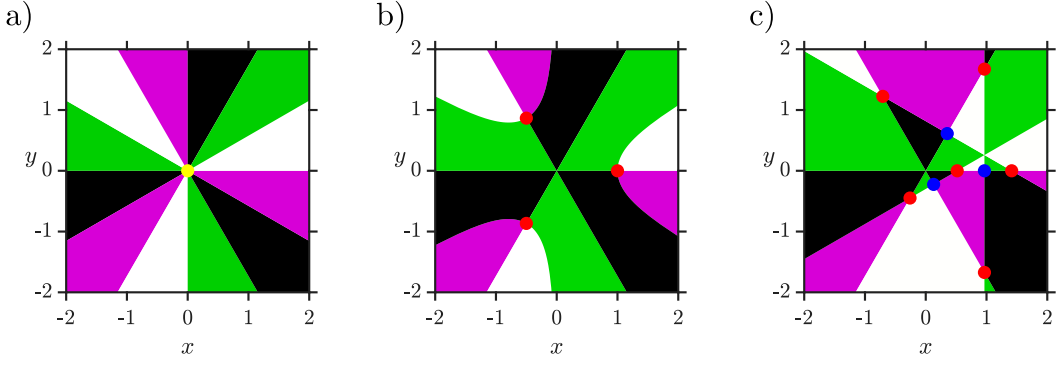


Figure 8: Birth quota of the 3-fold Weyl point. a) 3-fold Weyl point as a non-generic degeneracy point. Colored plane shows the sign pattern of the effective Hamiltonian map  $h \equiv h_{t=0}$  of Eq. (181). For the coloring scheme, see Fig. 1 of the main text. b) Three Weyl points (red) born due to deformation of Eq. (181) with  $t = 1$ . c) Nine Weyl points (red and blue) born due to deformation of Eq. (184) with  $t = 1$ . The multiplicity of the 3-fold Weyl point is 9, i.e., this panel illustrates the case when the number of newborn Weyl points is maximal.

*Local multiplicity from the ‘square rule’.* The third method uses the relation between the multiplicities of a complex map  $g : (\mathbb{C}^m, 0) \rightarrow (\mathbb{C}^m, 0)$  and its realification  $g_{\mathbb{R}} : (\mathbb{R}^{2m}, 0) \rightarrow (\mathbb{R}^{2m}, 0)$ . In this case,  $\text{mult}_0 g_{\mathbb{R}} = (\text{mult}_0 g)^2$  holds by the proof of [89, Prop. 2.4.]. Applying this for the map  $g(w) = w^n$ , we conclude that  $\text{mult}_0 h = n^2$ .

*Example deformations.* Here we provide two special deformations with the explicit location of the Weyl points. The first one is the constant deformation which has the minimal number  $|\deg_0 h|$  of real Weyl points, and the second one has the maximal number  $\text{mult}_0 h$  of real Weyl points, although, in both cases the number of generic complex Weyl points is  $\text{mult}_0 h$ .

*1st deformation.* Consider the simplest complex deformation of the complex function  $w^n = (x + iy)^n$ , namely the constant deformation  $(x + iy)^n - t^n$ , which has  $n$  complex roots. Its realification induces the following real deformation of  $h$ :

$$h_t(x, y, z) = \begin{pmatrix} \text{Re}(x + iy)^n - t^n \\ \text{Im}(x + iy)^n \\ z \end{pmatrix}. \quad (181)$$

Then, the  $n$  complex roots of  $w^n - t^n = 0$  imply  $n$  real Weyl points at

$$\begin{pmatrix} x \\ y \\ z \end{pmatrix}_{\text{WP},k} = t \begin{pmatrix} \cos\left(\frac{2\pi k}{n}\right) \\ \sin\left(\frac{2\pi k}{n}\right) \\ 0 \end{pmatrix}, \quad (182)$$

where  $0 \leq k < n$ , with charge  $+1$ , since the realification of a complex map preserves the orientation.

Furthermore, the complexification of  $h_t$  has  $n^2$  complex roots at

$$\begin{pmatrix} x \\ y \\ z \end{pmatrix}_{\text{CWP},km} = t e^{i\pi \frac{2k-m}{n}} \begin{pmatrix} \cos\left(\frac{\pi m}{n}\right) \\ \sin\left(\frac{\pi m}{n}\right) \\ 0 \end{pmatrix} \quad (183)$$

with  $0 \leq k, m < n$ . The real Weyl points in Eq. (182) are the solutions corresponding to the indices satisfying  $m \equiv 2k \pmod{n}$ , the others are non-real complex Weyl points.

For the  $n = 3$  case, the non-generic degeneracy point corresponding to  $t = 0$  is shown in Fig. 8a as the yellow point, and the 3 Weyl points born from the latter, corresponding to  $t = 1$  are shown in Fig. 8b.

*2nd deformation.* The deformation

$$h_t = \begin{pmatrix} \operatorname{Re} \left( x + iy - te^{i\frac{\pi}{4n}} \right)^n \\ \operatorname{Im}(x + iy)^n \\ z \end{pmatrix} \quad (184)$$

splits the  $n$ -fold Weyl point into  $n^2$  real Weyl points at

$$\begin{pmatrix} x \\ y \\ z \end{pmatrix}_{\text{WP},km} = t \frac{\sin\left(\frac{\pi}{n}\left(k + \frac{1}{4}\right)\right)}{\sin\left(\frac{\pi}{n}\left(k - n + \frac{1}{2}\right)\right)} \begin{pmatrix} \cos\left(\frac{\pi m}{n}\right) \\ \sin\left(\frac{\pi m}{n}\right) \\ 0 \end{pmatrix}, \quad (185)$$

where  $0 \leq k \leq n - 1$  and  $1 \leq m \leq n$ . Their charges are

$$Q_{km} = (-1)^{k+m} \cdot \operatorname{sgn}\left(\frac{1}{2} + k - m\right). \quad (186)$$

Fig. 8c shows the  $n = 3$  case for  $t = 1$ . The non-generic degeneracy point splits to 9 real Weyl points.

### Example 3

The first two examples were  $(\mathbb{R}^3, 0) \rightarrow (\mathbb{R}^3, 0)$  maps where 1 or 2 components were trivial, therefore, those could be treated as  $(\mathbb{R}, 0) \rightarrow (\mathbb{R}, 0)$  and  $(\mathbb{R}^2, 0) \rightarrow (\mathbb{R}^2, 0)$  maps effectively. Moreover, the second example suggests the inequality  $(\deg_0 h)^2 \leq \operatorname{mult}_0 h$ , but this is not true in general. The following example is a  $(\mathbb{R}^3, 0) \rightarrow (\mathbb{R}^3, 0)$  map from [89, Pg. 24], where all 3 components are non-trivial, and it is also a counterexample for the inequality

$$h(x, y, z) = \begin{pmatrix} xyz \\ x^2 - y^2 \\ x^2 - z^2 \end{pmatrix}. \quad (187)$$

This map has local degree  $\deg_0 h = 4$  and local multiplicity  $\operatorname{mult}_0 h = 12$ , as stated in [89]. Note that the inequality  $2|\deg_0 h| \leq \operatorname{mult}_0 h$  is proved in [89] if 0 is a nongeneric root of  $h$ .

Even though example Eq. (187) was presented in [89] in a purely mathematical context, a similar map also arises in the electronic band structure context, highlighted in Eq. (2) of [26]. Denoting the map defined by their Eq. (2) as  $h_{\text{nSOC}}$ , and assigning  $A = B = -1$ , it holds that  $h_{\text{nSOC}} = g \circ h$ , where  $g$  is the linear map

$$g(x, y, z) = \frac{1}{2} \begin{pmatrix} z + y \\ \sqrt{3}(z - y) \\ 2x \end{pmatrix}. \quad (188)$$

It is clear that composing a map with a linear transformation  $g$  with positive determinant preserves the local degree and the local multiplicity, therefore we have  $\deg_0(g \circ h) = \deg_0 h$  and  $\operatorname{mult}_0(g \circ h) = \operatorname{mult}_0 h$ .

*Local multiplicity from the algebraic method.* The result  $\operatorname{mult}_0 h = 12$  can be derived easily using the irreducible decomposition of the components of  $h$ . In fact,

$$I_h = I(xyz, (x - y)(x + y), (x - z)(x + z)), \quad (189)$$

and by the general version of Eq. (178) we have

$$\begin{aligned} \text{mult}_0 h &= \text{mult}_0(x, x - y, x - z) \\ &+ \text{mult}_0(x, x - y, x + z) + \dots \\ &+ \text{mult}_0(z, x + y, x + z). \end{aligned} \quad (190)$$

Here all the 12 terms are 1. For example

$$I(x, x - y, x - z) = I(x, y, z), \quad (191)$$

whose multiplicity is 1, since a basis of  $\mathbb{R}\{x, y, z\}/I(x, y, z)$  is formed by the residue class of 1.

*Example deformations.* Here we provide two special deformations with the explicit location of the Weyl points. The first one is the constant deformation which has the minimal number  $|\text{deg}_0 h|$  of real Weyl points. The second one has the maximal number  $\text{mult}_0 h$  of real Weyl points, although, in both cases the number of generic complex Weyl points is  $\text{mult}_0 h$ .

*1st deformation.* Consider the following constant deformation  $h(x, y, z) - (t^3, 0, 0)$ , reads

$$h_t(x, y, z) = \begin{pmatrix} xyz - t^3 \\ x^2 - y^2 \\ x^2 - z^2 \end{pmatrix}. \quad (192)$$

It has 4 real Weyl points at

$$(x, y, z)_{\text{WP}} = (\pm t, \pm t, \pm t) \mid \text{sgn}(xyz) = 1, \quad (193)$$

Each has charge +1, since the determinant of the Jacobian of  $h_t$  is positive everywhere, except the origin. This observation proves that  $\text{deg}_0 h = 4$ . Furthermore, there are 8 non-real complex Weyl points at

$$\exp(\pm 2\pi i/3) \cdot (x, y, z)_{\text{WP}}. \quad (194)$$

Therefore, the number of complex Weyl points proves that  $\text{mult}_0 h = 12$ .

Fig. 9a shows the 4 real Weyl points at every second corner of a cube with edge length  $2t$  around the origin.

*2nd deformation* The deformation

$$h_t(x, y, z) = \begin{pmatrix} (x - t)(y - 2t)(z - 3t) \\ x^2 - y^2 \\ x^2 - z^2 \end{pmatrix} \quad (195)$$

splits the degeneracy into the maximal number of  $\text{mult}_0 h = 12$  real Weyl points with charges  $Q$  at

$$\begin{aligned} (x, y, z)_{\text{WP}} &= (t, \pm t, \pm t) & Q &= \text{sgn}(yz), \\ (x, y, z)_{\text{WP}} &= (\pm 2t, 2t, \pm 2t) & Q &= -\text{sgn}(z), \\ (x, y, z)_{\text{WP}} &= (\pm 3t, \pm 3t, 3t) & Q &= 1. \end{aligned} \quad (196)$$

The topological charge sum rule is satisfied with the 8 positively charged Weyl points and the 4 negatively charged Weyl points giving the charge of the unperturbed non-generic degeneracy.

Fig. 9b shows the 12 real Weyl points at corners of 3 concentric cubes, each contributes with 4 corners corresponding to 1 face.

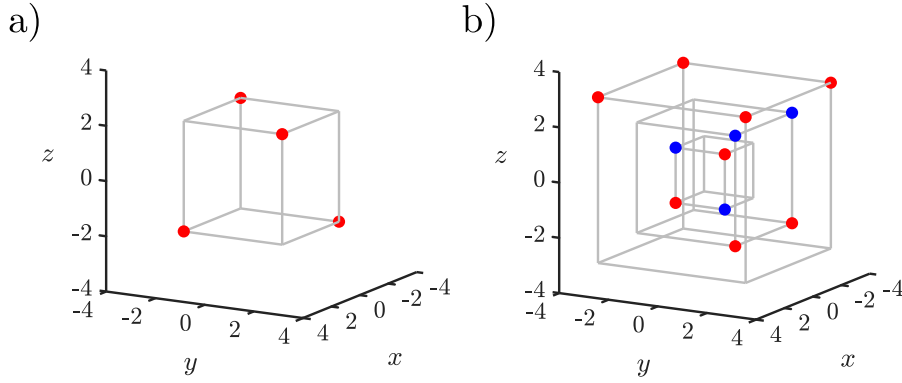


Figure 9: Birth quota of the map defined in Eq. (187). a) The minimal number of  $\deg_0 h = 4$  Weyl points (red) born due to the constant deformation of Eq. (192) with  $t = 2$ . b) The maximal number of  $\text{mult}_0 h = 12$  Weyl points (red and blue) born due to the deformation of Eq. (195) with  $t = 1$ . The sum rule for the topological charge is satisfied with 8 Weyl points with charge +1 (red) and 4 Weyl points with charge -1 (blue).

#### Example 4

In the previous three subsections, we computed the local multiplicities of  $(\mathbb{R}^3, 0) \rightarrow (\mathbb{R}^3, 0)$  maps describing energy degeneracies of quantum systems. In all cases so far, the local multiplicities were finite. In this subsection, we showcase a  $(\mathbb{R}^3, 0) \rightarrow (\mathbb{R}^3, 0)$  map that exemplifies that the local multiplicity of an isolated degeneracy can also be infinite. This example map is the following:

$$h(x, y, z) = \begin{pmatrix} xz \\ yz \\ z^2 - (x^2 + y^2) \end{pmatrix}. \quad (197)$$

*Local multiplicity from the algebraic method.* We show that  $\text{mult}_0 h = \infty$ . This follows from the following observations:

a) Since  $xz$ ,  $yz$  and  $z^2$  are divisible by  $z$  (they are 0 if  $z = 0$ ), the components of  $h$  are contained in the ideal generated by the functions  $z$  and  $x^2 + y^2$ . Therefore  $I_h \subset I(z, x^2 + y^2)$ . We conclude that

$$\text{mult}_0 h = \dim \frac{\mathbb{C}\{x, y\}}{I_h} \geq \dim \frac{\mathbb{C}\{x, y\}}{I(z, x^2 + y^2)}. \quad (198)$$

b) We show that the right hand side of Eq. (197) is infinite. In particular we show that the residue classes

$$[1], [x], [x^2], [x^3], \dots \in \frac{\mathbb{C}\{x, y\}}{I(z, x^2 + y^2)} \quad (199)$$

are linearly independent. Indeed, their finite linear combinations are exactly the residue classes of the one variable polynomials

$$a_n x^n + a_{n-1} x^{n-1} + \dots + a_1 x + a_0, \quad (200)$$

and these polynomials are not contained in the ideal  $I(z, x^2 + y^2)$ .

*Complexification.* According to the infinite multiplicity,  $h_{\mathbb{C}}$  is not finite at 0, i.e. 0 is not isolated in the zero locus  $h_{\mathbb{C}}^{-1}(0)$ . Indeed,  $x^2 + y^2$  in  $\mathbb{C}\{x, y\}$  decomposes as

$$x^2 + y^2 = (x + iy)(x - iy). \quad (201)$$

Therefore the set of the common solutions of  $z = 0$  and  $x^2 + y^2 = (x + iy)(x - iy) = 0$  is the union of the two complex lines  $x + iy = 0$  and  $x - iy = 0$  intersecting at 0.

*Example deformation.* Since in this case  $\text{mult}_0 h = \infty$ , there is no birth quota for the number of Weyl points.

The deformation

$$h_t(x, y, z) = \begin{pmatrix} xz \\ yz \\ z^2 - (x^2 + y^2) + t^2 \end{pmatrix} \quad (202)$$

splits the degeneracy point at the origin into a nodal loop

$$\begin{pmatrix} x \\ y \\ z \end{pmatrix}_{\text{loop}} = t \begin{pmatrix} \cos \varphi \\ \sin \varphi \\ 0 \end{pmatrix}, \quad 0 \leq \varphi < 2\pi, \quad (203)$$

which is *continuously* many degeneracies (see Fig. 10a). This can be further splitted to *discrete* number of Weyl point without upper limit with the following deformation (compare with Eq. (181))

$$h_{t,s}^n(x, y, z) = \begin{pmatrix} xz \\ yz \\ z^2 - (x^2 + y^2) + t^2 \\ +s \begin{pmatrix} \text{Re}(x + iy)^n - t^n \\ \text{Im}(x + iy)^n \\ 0 \end{pmatrix} \end{pmatrix}. \quad (204)$$

The second deformation splits the loop everywhere except where the deformation is zero

$$\begin{pmatrix} x \\ y \\ z \end{pmatrix}_{\text{WP},k} = t \begin{pmatrix} \cos\left(\frac{\pi k}{n}\right) \\ \sin\left(\frac{\pi k}{n}\right) \\ 0 \end{pmatrix}, \quad 0 \leq k < n. \quad (205)$$

This leaves  $n$  Weyl points at the former loop. Setting  $s = t$  and increasing it from 0 to 1 describes a process where the degeneracy point directly splits into at least  $n$  Weyl points.

In this case the location of the Weyl points outside the loop is not analytically solvable. By numerical calculations we found that every point has an oppositely charged pair nearby where the condition  $h_{t,s}^n(x, y, z) = 0$  is satisfied, thus, the total number of Weyl points is  $2n$ . The topological charge is distributed among the Weyl points in a non-trivial fashion. See Fig. 10b.

*Local degree.*  $\text{deg}_0 h = 0$  which can be proven with the deformation

$$h_t(x, y, z) = \begin{pmatrix} xz + ty \\ yz - tx \\ z^2 - (x^2 + y^2) + t^2 \end{pmatrix}. \quad (206)$$

This deformation splits the degeneracy into nothing because  $h_t(x, y, z) = 0$  has no real-valued solution, meaning that the local degree is indeed zero.

### Example 5 – counterexample

Here, we provide a perturbation of the one-variable real function  $h(x) = x$ , with the number of newborn Weyl points being greater than  $\text{mult}_0 h = 1$ . This example does not invalidate the results of this chapter, rather it shows that the analytic condition (or the weaker  $C^\infty$ -condition)

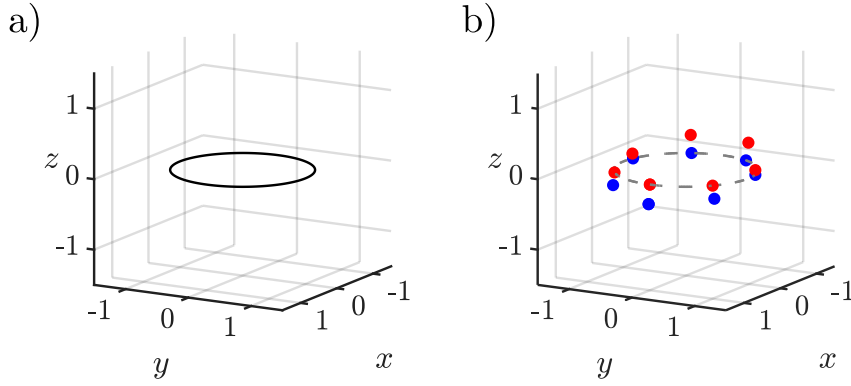


Figure 10: Splitting a degeneracy point without a birth quota. The map defined in Eq. (197) has multiplicity infinity, thus, it has no birth quota. a) The deformation Eq. (202) with  $t = 1$  splits the degeneracy point into a nodal circle (black solid line) in the  $xy$  plane with radius 1. b) The nodal circle is further splitted into Weyl points (red and blue points) with the deformation Eq. (204) with  $n = 7$  and  $s = 1$ . This deformation leaves 7 Weyl points on the former circle (chopped gray line) with additional 7 Weyl points nearby giving 14 Weyl points together. It is possible to split the degeneracy directly into  $2n$  Weyl points with applying the two deformations together with  $s = t$  going from 0 to 1.

*assumed for the deformation* is indeed required for respecting the birth quota. Indeed, in this (counter)example the perturbation  $(x, t) \mapsto h_t(x)$ , considered as a map of both the configurational and the control parameters, is not analytic, what is more, it is not continuously differentiable.

Consider the perturbation

$$h_t(x) = x - \frac{2t^2x}{t^2 + x^2} = \frac{x(x^2 - t^2)}{x^2 + t^2}. \quad (207)$$

*Extending to  $t = 0$  and  $x = 0$ .* For a fixed  $t \neq 0$ ,  $h_t(x)$  is an analytic function of  $x$  defined in a neighborhood of  $x = 0$ . For  $t = 0$ ,  $h_0(x)$  is not defined at  $x = 0$ . However, if  $t \rightarrow 0$ , then  $h_t(x)$  converges to  $x$  uniformly:

$$\lim_{t \rightarrow 0} h_t(x) = h(x) = x, \quad (208)$$

Hence we can define  $h_0(0) = 0$  using this limit, consequently  $h_0(x) = h(x) = x$  everywhere. Therefore, we could consider  $h_t(x)$  as a perturbation of  $h(x)$ .

*Roots.*  $h_t(x)$  has 3 generic roots at

$$x_{\text{WP}} \in \{0, \pm t\}, \quad (209)$$

therefore the number of the newborn Weyl points from the origin is bigger than the birth quota  $\text{mult}_0 h = 1$ . Why does our argument fail in this example? Obviously this perturbation does not satisfy the conditions required for respecting the birth quota. Which condition is not satisfied? Is  $h_t(x)$  an analytic deformation of  $h(x)$ ? We provide here a detailed analysis of these questions.

*Taylor series of  $h_t$  around 0.* One can show that the Taylor series of  $h_t(x)$  fails to converge to  $x$ . Observe that

$$h_t(x) = t \cdot h_1\left(\frac{x}{t}\right), \quad (210)$$

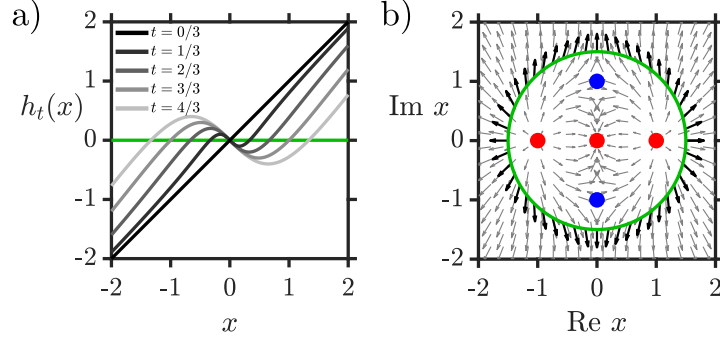


Figure 11: Perturbation defined in Eq. (207) of the function  $h_0(x) = x$  does not respect the birth quota. a) The function  $h_t(x)$  uniformly goes to  $x$  as  $t$  goes to 0. However, the first derivative is  $-1$  for every  $t \neq 0$ , and  $+1$  for  $t = 0$ . In such a process, 3 roots merge in the origin, while keeping the total topological charge (sign)  $+1$ . b) The complexification  $h_{Ct}(x)$  has 2 poles (blue) on the imaginary axis, in addition to the 3 roots (red) on the real axis, for  $t \in \mathbb{R} \setminus \{0\}$ . Note that the birth quota is respected in a generalized sense: if we assign negative multiplicity to the poles, then the sum of the multiplicities of the newborn complex roots and poles together equals the original multiplicity.

meaning that varying  $t$  scales up the graph of  $h_t(x)$ . Using this property, the derivatives of  $h_t$  at 0 reads

$$h_t^{(n)}(0) = t^{1-n} \cdot h_1^{(n)}(0), \quad (211)$$

for all  $t \neq 0$ . The first derivative of the perturbed function at 0 is  $h_t'(0) = -1$  independently of  $t$ . This is not equal to the derivative of the unperturbed function  $h_0'(0) = 1$ . Higher derivatives of the perturbed function even diverges as  $t$  goes to 0. Therefore, the Taylor series expansion of  $h_t(x)$  at  $x_0 = 0$  (with respect to  $x$ ) does not converge to the Taylor series of  $h$  at 0. Practically this shows the problem with the perturbation  $h_t(x)$  of  $h(x)$ .

*Continuity and partial differentials.* For a more fundamental analysis consider the two variable function  $\mathcal{H}_1 : (x, t) \mapsto h_t(x)$ . The problem is that  $\mathcal{H}_1$  is not analytic around zero as a two-variable function. Although it is continuous (if we define  $\mathcal{H}_1(0, 0) = 0$ ), it is not continuously differentiable.

To see the continuity, introduce the polar coordinates  $x = r \cos(\alpha)$  and  $t = r \sin(\alpha)$ , then

$$\mathcal{H}_1(r, \alpha) = r \cos(\alpha) \cos(2\alpha), \quad (212)$$

and

$$\lim_{(x,t) \rightarrow 0} \mathcal{H}_1(x, t) = \lim_{r \rightarrow 0} \mathcal{H}_1(r, \alpha) = 0. \quad (213)$$

To see that  $\mathcal{H}_1$  is not continuously differentiable, we show that its partial derivative with respect to  $x$  is not continuous at  $(0, 0)$ . Indeed, we find

$$\partial_x \mathcal{H}_1(x, t) = \frac{x^4 + 4x^2t^2 - t^4}{(x^2 + t^2)^2}, \quad (214)$$

and writing this in polar coordinates yields

$$\partial_x \mathcal{H}_1(r, \alpha) = \cos(2\alpha) + \sin^2(2\alpha). \quad (215)$$

This derivative depends on  $\alpha$ , but it is independent of  $r$ . Therefore, the limit

$$\lim_{(x,t) \rightarrow (0,0)} (\partial_x \mathcal{H}_1(x,t)) = \lim_{r \rightarrow 0} (\partial_x \mathcal{H}_1(r,\alpha)) \quad (216)$$

does not exist.

Recall that by definition,  $h_t$  is an analytic deformation of a map  $h$  if it is the first component  $\mathcal{H}_1$  of an analytic unfolding  $\mathcal{H}$  with a fixed control parameter value  $t$ , considered as the function of  $x$ , see Section *Birth quota* in the main text and Sec. C.1. The analytic property of  $\mathcal{H}$  is used in the proof of Proposition 1. Note that smoothness ( $C^\infty$ ) is also enough to respect the birth quota. Since in this example  $\mathcal{H}_1(x,t)$  is not analytic (neither smooth), the perturbation  $h_t(x)$  is not an analytic deformation of  $h(x)$  according to our definition.

*Complexification.* It is instructive to investigate the complexification of  $h_t(x)$  for  $t \neq 0$ . It is a meromorphic one-variable function with the 3 generic real roots and two first-order poles at

$$x_P = \pm it. \quad (217)$$

The equation  $3 - 2 = 1 = \text{mult}_0 h$  suggest that the poles can be considered as ‘complex Weyl points with negative sign’, and in fact this is the case, as we can see as follows. The function  $f(z) = 1/z^k$  has a pole of order  $k$  at zero. On the unit circle  $1/z^k = \bar{z}^k$  (with overline denoting complex conjugation), hence we can change  $f$  to  $\bar{z}^k$  inside the unit circle to get a continuous function (which can be smoothed along the unit circle). The local degree of this modified function at the origin is  $-k$ . This result can be interpreted as a pole of order  $k$  can be replaced with a root of local degree  $-k$ .

Therefore, by this observation, the birth quota  $\text{mult}_0 h = 1$  is respected in a generalized sense. Note that this does not hold in general. Indeed, this example is specific for two reasons: (1) the 1-dimensionality is required for having the isolated poles in the sense used here, and (2) neither the roots nor the poles cross the separator for small values of  $t$ .